THEORETICAL AND NUMERICAL STUDIES OF PLUME FLOWS IN VACUUM CHAMBERS

by

Chunpei Cai

A dissertation submitted in partial fulfillment
of the requirements for the degree of
Doctor of Philosophy
(Aerospace Engineering)
in The University of Michigan
2005

Doctoral Committee:

Professor Iain D. Boyd, Chairperson
Professor Alec D. Gallimore
Professor Bram van Leer
Assistant Professor Andrew J. Christlieb

Dedicated to my family for years of encouragement and support,
and to my friends.

ACKNOWLEDGEMENTS

First and foremost, I would like to express my sincere thanks to my advisor, Professor Iain D. Boyd, for his guidance throughout this research, for his insight into many questions, and for his generous support and constant encouragement. The lessons I have learned from him will stay with me for the rest of my professional career.

I also wish to thank the other members of my doctoral committee, Professor Andrew Christlieb, Professor Alec D. Gallimore and Professor Bram van Leer, for their comments and participations.

My special thanks goes to Dr. Quanhua Sun for his help and collaboration throughout this research, his suggestions are quite important to several parts of the work in this thesis. I wish to thank Anton VanderWyst for his constant companionship in our office, especially at weekends, and his very helpful training of Latex and Lyx. I also appreciate the help from Dr. Mitchell R. Walker and Dr. Brian Beal for providing experimental measurement data from their work.

I would like also to thank my supervisor Mr. Paolo Sansalvadore in Altair Engineering Inc., for teaching me software engineering, computational geometry and sheet metal forming. Working with him in the past six years is a very happy and invaluable experience of my life. The programming skills I learned from him are quite useful in the research for this Ph.D. study. I also wish to thank the support from Altair Engineering Inc., especially Mr. James P. Dagg, for offering me an absence

leave of ten months from the company, hence I can concentrate on my study. Most of the work in this thesis and the drafting of this thesis are finished during this period.

My sincere appreciation goes to my other friends, research group members and officemates: Dr. Gang Chen, Ying Zhang, Dr. Jing Fan, Weixiang Zhang, Yongxian Gu, Li Qiao, Dr. Li Liu, Peihua Zhou, Dr. Xiaochun Shen, Dazhi Liu, Dr. Jian Tang, Dr. Fang Xu, Xiaoyun Gong, Dr. William W. McMillan, Qingmei Jiang, Dr. Wenglan Wang, Dongqi Zhang, Haoyu Gu, Dr. Michael Keidar, Dr. Justin Koo, Matthew McNenly, Dr. Jerry W. Emhoff, Michael Martin, Jon Burt, Jeremy Boerner, Jose Padilla, John Yim, Tom Schwartzentruber, Youngjun Choi and Kevin Scavezze. Thanks for making my stay at the University of Michigan a memorable and enjoyable one, and for much help in both technical and mundane matters.

I would like to thank our graduate secretaries Margaret Fillion, Denise Phelps and other staff as well as other friends, who always offered me their generous help when in need.

I am greatly indebted to my wife, Jie Luo, my daughter, Helen S. Cai and my parents for their unending care, support, understanding, love and encouragement throughout my doctoral program. Their love and patience have been always helped me in many ways.

Finally, I would like to acknowledge the financial support I have received from the Air Force Office of Scientific Research under grant F49620-03-1-0123 and FA9550-05-1-0042. Without financial support, this study would have not been possible.

TABLE OF CONTENTS

LIST OF FIGURES

Figure

LIST OF TABLES

Table

LIST OF APPENDICES

Appendix

CHAPTER I

INTRODUCTION

1.1 Motivation and Problems

Electric Propulsion (EP) devices have several important merits over traditional chemical thrusters and they have been widely used in space for primary propulsion and on-orbit applications such as station-keeping. There have been active research efforts on EP devices since the mid 1950's, one of the introductory book by Stuhliger [52]. Among the active research topics, spacecraft integration and plume impingement are two important issues for EP devices. In this study, several problems related with plume flows from EP devices will be investigated analytically and numerically.

The major problem studied in this thesis is three-dimensional particle simulations of plasma plume flows from a cluster of Hall thrusters. During the past decade, plasma plume flows from a single thruster have been simulated widely with particle methods [46, 55]. These simulations adopted simplified axi-symmetric configurations and the plasma potential was usually solved by the simplest Boltzmann relation. There are several problems associated with these simplifications:

1. With multiple thrusters in operation, plasma plume flows from different thrusters may interact with each other. Hence, the flowfield is completely three-dimensional.

2. There are some detailed near-field objects, such as thruster cathode-neutralizers and conic protection caps on the front of some Hall thrusters. These three-dimensional objects have significant effects on the near field flow properties and cannot be well represented with axi-symmetric simplifications.

3. The simple electron model, the Boltzmann relation, cannot predict some detailed electron properties in the near field. Some important electron properties, such as the electron temperature distributions, change rapidly in the flow field, while the Boltzmann relation assumes that this property follows a constant distribution in the whole flowfield.

As the most important work of this thesis, several three-dimensional particle simulations are performed to understand the plume flowfield in front of a cluster of Hall thrusters. An advanced detailed electron model will be used in these simulations. This model is expected to be capable of predicting important electron properties in the whole flowfield. Three-dimensional effects, such as thruster clustering effects and cathodes effect, will be demonstrated with the simulation results. Several implementation issues associated with unstructured meshes will be discussed. While performing these particle simulations of the three-dimensional plasma plume flows from a cluster of thrusters, another two related issues were identified and are included in this thesis as well.

One important issue is facility effects of large vacuum chambers. To the EP community, including people working on experiments or numerical simulations, this problem is quite important [9]. EP devices are designed for usage in space, where nearly perfect vacuum exists, but they are tested in large vacuum chambers on the ground. The finite background pressure in the large vacuum chambers may have

adverse effects on the performance of EP devices in experiments and on particle simulations of plume flows. One fundamental concern to the EP community is to estimate the facility effects on the background pressure and velocity in the vacuum chamber. More specifically, this thesis will provide answers to the following questions:

1. With given fixed facility parameters and given electric thrusters in a large vacuum chamber, what average background pressure and average background velocity will be expected in this chamber? These two properties contribute to the performance difference between experiments in a chamber and real operation in space. Having a clear understanding of this problem is crucial to both experiments and numerical simulations.

2. What are the exact effects on the background gas that a change of facility properties will result in? Possible facility properties include the pump sticking coefficient, the pump temperature, the pump size, the chamber wall temperature and the chamber side wall length. Answering this question can provide guidelines for designing new chambers and improving old chambers.

In the literature, there is little prior work on these problems. This thesis will provide several sets of analytical models to answer these questions. Several analytical results from these models are also used to aid the three-dimensional particle simulations of plasma plume flows.

Another important issue is to analytically investigate the plasma plume flows in space. Plume flows from EP devices are complex, but by omitting electric field effects and collisions, the plasma plumes can be approximated with a mixture of free molecular flows of ions and neutrals out of exits with different shapes. In the literature, there are essentially no reports of similar analytical work on electric plasma

plume flows previously. This thesis represents an initial effort to analytically study plasma plume flows in vacuum.

1.2 Background for Electric Propulsion

1.2.1 Historical Background

The idea of electric propulsion can be traced back to Robert Goddard. He noticed an important fact that in several of his experiments, a quite high exhaust velocity was achieved with a still cool tube. He pointed out the fact that electrostatic propulsion has no limitation of speed by the specific heat of combustion with several papers in the 1920's [24]. Another EP pioneer, Hermann Oberth, expanded on the concept of EP, and several theoretical studies were published from 1945 to the mid 1950's.

While Oberth and Goddard recognized the potential payoff electric propulsion could have to interplanetary flight, it was Wernher von Braun who sanctioned the first serious study on EP. In 1947, at Fort Bliss, von Braun assigned a young engineer named Ernst Stuhlinger the task of giving Professor Oberth's early concepts of electric spacecraft propulsion "some further study". Fifteen years later, Stuhlinger published a book entitled *Ion Propulsion for Space Flight* and directed NASA Marshall Space Flight Center's work on arcjet and ion propulsion systems.

One drawback cited by people who had doubts about EP was the low inherent thrust-to-weight ratios of electric engines. EP systems are expected to have thrust-to-weight values thousands of times smaller than chemical propulsion systems. In 1953, H.S. Tsien designed trajectories and thrust alignment procedures for low-thrust, EP-propelled spacecraft. In his work, it was shown that thrust-to-weight ratios as low as 1×10^{-5} are sufficient to change the trajectory of a space vehicle over a realistic period of time.

With the beginning of the "Space Race" in the late 1950's between the U.S.S.R and the U.S.A, experimental work on EP began to flourish. In the United States, RocketDyne(1958), NACA Lewis Flight Laboratory(1959, now NASA Glenn), and Princeton University(1961) began their EP experimental programs.

In the early 1990's, the advent of new, high-power spacecraft architectures made EP more attractive to mission planners. At the same time, an influx of Russian Hall thruster technology to the west and an aggressive new technology push at NASA began to advocate the use of ion engines in interplanetary probes.

As of today, EP devices are widely used as primary interplanetary propulsion and for on-obit applications such as station keeping, attitude control and orbit transfer [38].

1.2.2 Advantages of Electric Propulsion

Compared with traditional chemical rockets, EP devices have several advantages. First, the exhaust velocity is much higher. Chemical rockets have a limit for the exhaust velocity, typically of a few kilometers per second:

$$u_{ex} \leq \sqrt{2h_c/m} \tag{1.1}$$

where h_c is the combustion enthalpy and m is the mean mass of the exhaust products. EP devices, on the other hand, can readily exhaust velocities as high as 110 km/s. Second, no oxidizer is needed and electricity can be obtained in space via solar cells, hence there is more room for payload. Third, EP devices can use inert easily stored propellants which are much safer than chemical propellants. Detailed discussion of these advantages can be found in many EP books and several Ph.D. theses such as [50].

1.2.3 Types of Thrusters

Electric propulsion mechanisms were first divided into three canonical categories by Stuhlinger [52]:

1. Electrothermal devices heat a propellant gas with electrical current or electromagnetic radiation. The resulting thermal energy is converted to directed kinetic energy by expansion through a nozzle. Resistojets, arcjets and cyclotron resonance thrusters are examples of electrothermal devices.

2. Electrostatic devices accelerate charge-carrying propellant particles in a static electric field. These devices typically use a static magnetic field that is strong enough to retard electron flow, but too weak to materially affect ion trajectories. Ion engines and Hall thrusters are examples of electrostatic thrusters.

3. Electromagnetic devices accelerate charge-carrying propellant particles in interacting electric and magnetic fields. The magnetic field strength in these devices is typically high enough to significantly affect both ion and electron trajectories. Examples include pulsed plasma thrusters(PPT), Magnetohydrodynamic (MPD) thrusters, Hall thrusters and traveling-wave accelerators.

The work in this thesis involves one specific Hall thruster, the BHT200 [8].

1.3 Objectives and Thesis Organization

There are three primary objectives in the thesis.

1. Investigate the facility effects on the background flow in large vacuum chambers.

2. Develop analytical solutions to free molecular flows out of exits with different shapes.

3. Perform particle simulations of plasma plume flows from a cluster of Hall thrusters with a detailed electron model on unstructured meshes.

Chapter II reviews the background of a dilute gas and simulation methods, including two specific particle simulation techniques that are to be used in the plasma plume simulations.

Chapter III discusses vacuum chamber facility effects. It includes five free molecular models and comparisons with experimental measurements and numerical simulation results. This chapter addresses the first objective.

Chapter IV discusses six free molecular flows out of exits with different shapes. Their exact solutions or exact expressions are obtained and compared with numerical simulation results. This chapter addresses the second objective.

Chapter V reports several three-dimensional particle simulations of plasma plume flows from a cluster of Hall thrusters with a detailed electron model on unstructured meshes. Some important three-dimensional effects, due to the clustering and cathodes are demonstrated with the simulation results. This chapter addresses the third objective.

Chapter VI presents summaries and conclusions for the three pieces of work in this thesis. This chapter ends with some recommendations for future work.

Several appendixes at the end of the thesis include all important mathematical integrals used in this study and several code implementation issues.

CHAPTER II

REVIEW OF NUMERICAL METHODS

In Chapters Three and Four, the direct simulation Monte Carlo(DSMC) method will be used to provide numerical simulation results to validate some analytical work obtained in this study. In Chapter Five, the DSMC and Particle-In-Cell(PIC) methods will be used to simulate three-dimensional plasma plume flows from a cluster of Hall thrusters. Hence this chapter is devoted to background introduction and methodology review.

In this study, gaseous xenon is used for all simulation work.

2.1 Molecular Models and Several Characteristic Lengths

Dilute gases are generally described as a myriad of discrete molecules(monatomic, diatomic, or polyatomic) with inner structures. In view of the large number of molecules in most cases, it is impossible to address all the details of molecules and their interactions. For practical applications, several simplified molecular models have been suggested, such as the simplest Hard Sphere(HS) model and a recently proposed generalized soft sphere(GSS) model [25]. These models treat molecules as small balls with a fixed or variable diameter d, and molecular interactions occur only when two molecules are close enough.

There are three characteristic length scales associated with molecules in the microscopic viewpoint of fluids: the molecule diameter d, the mean molecular spacing δ, and the mean free path λ.

If $d < \delta$, only a small part of the space is occupied by molecules and the dilute assumption is correct. This means that effects on a molecule from other molecules are small, and it is highly probable that only one other molecule interacts(collides) with a molecule in which case there is a strong effect. Hence, for a dilute gas, molecular interactions are commonly treated as binary collisions.

The ratio of the mean free path to the characteristic dimension, defined as the Knudsen number, $Kn = \lambda/L$, is a quite important parameter to indicate the validity of continuum approaches. Generally, it is accepted that $Kn < 0.01$ represents a flow where the continuum assumption is valid; $Kn > 1$ represents a free molecular flow where intermolecular effects are quite insignificant since essentially no collisions happen and the continuum assumption is not applicable; $0.01 < Kn < 1$ represents a transition region between the continuum and free molecular regions.

Most problems studied in this thesis are in the free molecular flow region.

2.2 Simulation Methods for Fluid Flow Problems

In essence, numerical simulation methods for fluid flow problems can be classified into two categories: continuum methods and kinetic methods.

A continuum method is a "top-down" method, which is based on macroscopic conservation equations of fluids, such as the mass equation, momentum equation and energy equation. It uses the continuum assumption and its primary variables are macroscopic properties, such as density, velocities, pressure and temperature. This type of method is successful in solving a large range of flow problems but has

difficulties in solving flows with strong non-equilibrium phenomena.

A kinetic method is a "bottom-up" approach, which is based on more fundamental, microscopic kinetic relations, such as the Boltzmann equation. A kinetic method concentrates on low level microscopic interactions with a force field or between molecules or atoms, by analyzing the molecular momentum and energy redistribution after collisions. Such methods are useful in simulating non-equilibrium flows. Another difference from the continuum method is macroscopic properties such as velocities and pressure are evaluated using moments of velocity distribution functions or statistical sampling.

The Molecular Dynamics(MD) method, the DSMC method and the PIC method belong to the class of particle methods, a subtype of kinetic simulation methods. The MD method is effective in simulating dense gas, the DSMC method is effective in simulating dilute neutral gas flow while the PIC method is effective in simulating dilute flows with charges and electric/magnetic field effects called plasma.

2.3 The Molecular Dynamics Method

To study gas flow, there are several particle approaches. The MD method is considered to be the first particle method and related to the DSMC method, proposed by Alder and Wainwright in the late 1950's [2, 3] to study the interactions of hard spheres. A detailed introduction of this method is provided by Haile [30].

A MD simulation involves simultaneous tracking of a large number of simulated molecules within a region of simulated physical space and a potential energy function is generally used to determine the force on a molecule due to the presence of other molecules. This potential energy function is modeled with two-body or many-body potentials or an empirical choice. At the same time, the time evolution of a set of in-

teracting molecules is followed by integrating Newton's classical equations of motion. Macroscopic flow properties are obtained by averaging the molecule information over a space volume. This space volume should be larger than the mean molecular spacing and much smaller than the characteristic dimensions.

The major disadvantage of this method is that it is highly inefficient to use for most practical applications, because a large number of molecules must be simulated, and the computation of an element of trajectory for any molecule requires consideration of all other molecules as potential collision partners. As a result, molecular dynamics is limited to flows where the continuum and statistical approaches are inadequate.

2.4 The Direct Simulation Monte Carlo Method

The most commonly used particle method for simulating a rarefied gas flow is the DSMC method [12]. This method was first introduced by Bird in the 1960's and has been developed to the state where it is very reliable and accurate, and has gained wide acceptance in the scientific community. Each simulated particle in the DSMC method represents a large number of real molecules which makes a DSMC simulation much more efficient than a molecular dynamics simulation. Many review papers describing the DSMC method can be found in the literature(Bird [11] [10], Muntz [37], Oran et al [43], Ivanov and Gimelshein [31]). Among its many effective applications in simulating rarefied, nonequilibrium gas flows, one of the most successful applications was its successful prediction of the inner structure for normal shock waves.

By limiting the time step, the DSMC method decouples collisions and movement of the particles. The DSMC method emulates the nonlinear Boltzmann equation by simulating the real molecule collisions with collision frequencies and scattering

velocity distributions determined from the kinetic theory of a dilute gas. With a sufficiently large number of simulated particles, Bird [14] has shown that the Boltzmann equation can be derived through the DSMC procedures.

2.4.1 Algorithm of the DSMC Method

For the DSMC method, the computational domain is divided into a network of cells, where each cell serves as a separate region for molecular interaction and as a space element for sampling flow information. In order to decouple the movement of particles and the interaction between particles, the time step employed in the DSMC method is smaller than the mean collision time of gas molecules. The state of the system is described by the positions and velocities of particles. After an initial setup of cells and distribution of particles into cells, several essential steps in a time step are:

1. Select collision pairs. Some particles are randomly selected to collide. The rules of this random selection are developed from kinetic theory, so as to replicate the correct collision frequency.

2. Perform binary collisions, including redistribution of all types of energies and chemical reactions. Momentum and energy are conserved in the collision process.

3. Inject new particles at inlet boundaries. The number of particles is decided by kinetic theory.

4. Move particles and compute interactions with other boundaries. The particles are first allowed to translate at constant velocity as if they did not interact with each other, that is, they are moved according to their own trajectories

and their positions are updated deterministically. Some particles may travel from cell to cell. Some particles may escape from the computational domain or hit a solid wall and bounce back.

5. Sample flow properties.

For a steady dilute flow simulation, the above steps are repeated until a prescribed time is reached.

2.4.2 Collisions

In Step 1, to evaluate the collisions in a DSMC simulation, pairs of particles in a cell are randomly selected, regardless of their relative positions and velocities. In Bird's "No Time Counter" (NTC) scheme [12], a total number of

$$\frac{1}{2}n\bar{N}(\sigma g)_{\max}\Delta t$$

pairs are sampled from the cell at each time step and a collision actually takes place if a candidate pair satisfies

$$(\sigma g)/(\sigma g)_{\max} > \mathfrak{R}.$$

where $\mathfrak{R}$ is a random number uniformly distributed in $[0, 1)$. The average number of particles in the cell is denoted by $\bar{N}$. The parameter $(\sigma g)_{\max}$ is stored for each cell and is best set initially to a reasonably large value, but with provision for it to be automatically updated if a larger value is encountered during the sampling.

The NTC scheme is employed throughout the DSMC simulations in this thesis.

2.4.3 Variable Hard Sphere Model

In step 2, after a collision, conservation of momentum and energy provide four out of the six equations required to determine the post-collision velocities. The remaining two conditions are made with the assumption of isotropic scattering.

In determining the collision frequency of a gas molecule, the use of the typical inverse power law potential model is inadequate because the model gives an infinite total cross-section. To overcome this difficulty, Bird [15] introduced the Variable Hard Sphere (VHS) model as a practical approximation to the inverse power law potential model. In the VHS model, isotropic scattering is also assumed and its total cross-section, σ, is allowed to vary with the relative speed of the two colliding molecules, g, as follows

$$\sigma/\sigma_r = g^{1-2\omega}/\overline{g_r^{1-2\omega}}. \tag{2.1}$$

Here, g_r is the relative collision speed at the reference temperature T_r. In Equation (2.1), σ_r is the reference cross section and is written as $\sigma_r = \pi d_{\text{ref}}^2$, where d_{ref} denotes the reference molecular diameter. Data for ω and d_{ref} at $T_r = 273$ K for several major species can be found in Reference [12].

The VHS model is used throughout this thesis for all flow simulations involving neutral-neutral collisions.

2.4.4 Boundary Conditions

In Step 4, the velocity distribution for simulated particles reflecting from a solid wall varies with the type of the wall they hit. Specular and diffuse walls are the two most common types considered in DSMC. When a particle collides with a specular wall, its component of velocity tangential to the wall remains the same and the component normal to the wall changes its sign. When a particle bounces back from a diffuse wall at temperature T_w, its velocity components tangential to the wall are sampled from the standard Maxwellian distribution

$$f(c_t)\, dc_t = \frac{1}{\sqrt{2\pi R T_w}} \exp\left(\frac{-c_t^2}{2RT_w}\right) dc_t, \tag{2.2}$$

while its normal component is sampled from the biased-Maxwellian distribution

$$f(c_n)\,dc_n = \frac{1}{RT_w} c_n \exp\left(\frac{-c_n^2}{2RT_w}\right) dc_n. \tag{2.3}$$

A wall with accommodation coefficient ν means that a fraction ν of all the particles colliding with the wall are thermalized by the wall and the remaining fraction $(1-\nu)$ of the particles are specularly reflected by the wall. In this thesis, a full accommodation coefficient $\nu = 1$ is used in all simulations.

The internal energy of a reflecting particle can be handled in the same manner. However, for atomic xenon, which is exclusively used in all simulations in the thesis, no internal energy is considered.

In Chapter III, sticking wall boundaries are used to represent cryogenic pump plates. The pumps are characterized by a low pump temperature T_p and a pump sticking coefficient α. When particles hit such cold pumps, by a probability of α they stick on the plates, and with a probability of $1-\alpha$ they reflect diffusely with a speed characterized by the low pump temperature T_p.

2.4.5 Limitations of DSMC

Two principal limitations of the DSMC method are the assumption of molecular chaos and the requirement of a dilute gas. The molecular chaos assumption means that particles undergoing a collision will not meet again before colliding with other particles many times. The velocities of a collision pair are, therefore, totally uncorrelated. The dilute gas assumption prevents this method from being used for dense gases or for highly ionized plasmas that are dominated by long-range interactions [12].

Another fundamental assumption for DSMC is that particle motion and particle collisions can be decoupled. This assumption requires that the simulation time-step (Δt) should smaller than the local mean collision time (τ).

Compared with continuum Computational Fluid Dynamics(CFD) methods, all particle methods, including the DSMC method, are quite expensive in simulation cost.

2.4.6 MONACO

The particular DSMC code, named MONACO, employed in this study was first developed by Dietrich and Boyd [23] in 1996. Since then, MONACO has been further modified and applied to a wide variety of rarefied gas problems. MONACO-V3.0 is a general-purpose DSMC simulation package written in C for simulating two-dimensional, axi-symmetric, or three-dimensional rarefied gas flows. It contains some object-oriented features and different functionalities are separated for easy maintenance and update.

Its major structure is a double pointer for cell data, which enables an excellent performance on parallel machines. Inside each cell, the major data structures are two linked lists for particles, and these linked lists toggle as a current list and a backup list. When particles move, they move from the current list to the backup list. This linked list treatment achieves great efficiency. Besides the two linked list of particles, neighboring cell information and boundary information, are saved in the cell structure as well. These data structures make MONACO capable of simulating problems with complex geometry.

MONACO employs the VHS or Variable Soft Sphere [33] (VSS) collision models, the variable rotational energy exchange probability model of Boyd [19, 20], and the variable vibrational energy exchange probability model of Vijayakumar *et al.* [58] although these models are turned off in all simulations of this thesis due to the fact that xenon is monatomic. Cell weighting factors and time-steps may be set uniquely

for each cell in the grid. A sub-cell scheme is implemented for selection of collision pairs where the number of sub-cells is scaled by the local mean free path.

2.5 The Particle In Cell Method

Analogous to dilute gas flow which can be simulated effectively by the DSMC method, plasmas can be modeled by a particle method with considerations of electric and magnetic field effects. The PIC method is such a kinetic particle method that tracks the motion of collections of charged particles similar to the DSMC method.

The PIC method is well developed, and a detailed description can be found in the book by Birdsall and Langdon [16]. This method has been applied to magnetically and inertial confined fusion plasmas, electron and ion guns, microwaves devices, and plasma propulsion. Work by Roy [46] [47] and VanGilder [55] employed the PIC method to model ion thruster plumes.

Similar to the DSMC method, the PIC method moves particles which represent neutrals, ions and electrons through space. Usually, the plasma potential and electric field are evaluated on nodes forming cells. In simulating plasma, the cell size, time scale, and number of particles per cell must be adequate to represent the essence of the plasma physics. To update the particles' properties properly according to the physics, the time scale should correspond to the inverse of the plasma frequency:

$$\omega_p = \sqrt{\frac{ne^2}{\epsilon_0 m}} \tag{2.4}$$

If inter-particle effects are significant in the plasma flow, the cell size should be the order of or less than the Deybe length, which is the shielding distance around a test charge and the scale length inside which inter-particle effects are most significant:

$$\lambda_d = \sqrt{\omega_p} v_{th} \tag{2.5}$$

Generally, in quasi-neutral plasmas where collective behavior is more significant, larger cells can be used.

2.5.1 Major Steps in the PIC Method for Plasma Plume Simulations

For particle simulations of plasma plume flow, which consist of neutrals, ions and electrons, heavy neutrals and ion particles are simulated with the DSMC and the PIC methods, while the electrons are modeled as a fluid because electrons can adjust themselves more quickly.

The major difference in the PIC method from the DSMC method is, due to the presence of the electric field, accelerations on charged particles must be considered. Hence, there are a few extra steps in the PIC method:

1. Calculate electric potential field ϕ, and magnetic field if it is included. Usually the process needs to obtain the charge density distribution, which requires a process to allocate ion particle charges onto the mesh.

2. Calculate the electric field from $\overrightarrow{E} = - \bigtriangledown \phi$.

3. Interpolate the ion acceleration in a cell from the coordinates of the ion particle and the nodes forming the cell, and the electric field on the nodes.

4. Accelerate ion particles over a small time step Δt. The PIC method can consider the magnetic field effect by a leapfrog scheme that applies the magnetic field acceleration from the cluster at a mid step [16]. However, in most situations of plume flows, the magnetic field leakage from the thruster is not strong in the plume near field, hence in this study, magnetic field effects are neglected.

5. Perform collisions. Besides Momentum Exchange (MEX) between neutral particles, there are two other groups of collisions that must be considered in plasma

plume flows: MEX between a neutral particle and an ion particle, and Charge Exchange(CEX) between a neutral particle and an ion particle. The latter type of collision happens when a fast ion particle passes a slow neutral particle. With an electron transferred from the neutral to the fast ion, a CEX collision will result in a fast neutral and a slow ion.

A complete list of steps for the DSMC-PIC methods can be found in Chapter V for particle simulations of plasma plume flows from a cluster of Hall thrusters.

2.6 The Detailed Fluid Electron Model

In the first PIC step to compute the plasma potential, the most widely used and the simplest fluid electron model is the Boltzmann relation, which is obtained from the electron momentum equation:

$$\phi = \phi_{ref} + \frac{kT_{ref}}{e} \log(\frac{n_e}{n_{ref}}) \tag{2.6}$$

This equation is derived using several strong assumptions. These assumptions include that the fluid electron flow is isothermal, collisionless, the electron pressure obeys the ideal gas law and the magnetic field is neglected. However, in plasma plumes, especially in the near field, there are significant gradients and the approximation may be inappropriate.

To improve the understanding of the plume flow characteristics, recently a detailed electron model was proposed [17] and illustrated with an axi-symmetric plume simulation. Chapter V reports an implementation of this detailed electron model on a three-dimensional unstructured mesh. The major results in [17] are summarized here for reference.

In the detailed model, an equation for the electron stream function ψ can be derived from the steady mass conservation law for electrons with ionization effects,

the final expression is:

$$\nabla^2\psi = n_e n_a C_i \tag{2.7}$$

where $n_e\overrightarrow{v_e} = \nabla\psi$ and the ionization rate coefficient C_i is expressed as a function of electron temperature using a simple relation proposed by Adeho et al. [1]:

$$C_i = \sigma_i c_e (1 + \frac{T_e\epsilon_i}{(T_e+\epsilon_e)^2}) \exp(-\frac{\epsilon_i}{T_e}) \tag{2.8}$$

From a generalized Ohm's law:

$$\overrightarrow{j} = \sigma[-\nabla\phi + \frac{1}{en_e}\nabla(n_e k T_e)] \tag{2.9}$$

with given n_e, $\overrightarrow{v_e}$, T_e and the charge continuity condition:

$$\nabla \cdot \overrightarrow{j} = 0 \tag{2.10}$$

a generalized Poisson's equation describing the electron potential is obtained:

$$\begin{aligned}\nabla\cdot(\sigma\nabla\phi) = \quad & \nabla\cdot(\tfrac{k\sigma}{en_e}\nabla(n_eT_e)) = \tfrac{k}{e}(\sigma\nabla^2T_e + \sigma T_e\nabla^2(\ln(n_e)) + \sigma\nabla(\ln n_e)\cdot\nabla T_e \\ & + T_e\nabla\sigma\cdot\nabla(\ln(n_e)) + \nabla\sigma\cdot\nabla T_e)\end{aligned} \tag{2.11}$$

The electron temperature equation is obtained from the steady-state electron energy equation:

$$\begin{aligned}\nabla^2T_e \quad & = -\nabla\ln(\kappa_e)\cdot\nabla T_e + \tfrac{1}{\kappa_e}(-\overrightarrow{j}\cdot\overrightarrow{E} + \tfrac{3}{2}n_e(\overrightarrow{v_e}\cdot\nabla)kT_e + p_e\nabla\cdot\overrightarrow{v_e} \\ & + 3\tfrac{m_e}{m_i}\nu_e n_e k(T_e - T_h) + n_e n_a C_i\epsilon_i)\end{aligned} \tag{2.12}$$

The electron number density n_e is set equal to the ion number density n_i based on the plasma quasi-neutral assumption. The electron conductivity σ, the electron thermal conductivity κ_e, the ion-electron collision frequency ν_{ei}, and the neutral electron collision frequency ν_{en} can be found in [36] and its references:

$$\sigma = \frac{e^2 n_e}{m_e v_e} \tag{2.13}$$

$$\kappa_e = \frac{2.4}{1 + \frac{\nu_{ei}}{\sqrt{2}\nu_e}} \frac{k^2 n_e T_e}{m_e \nu_e} \tag{2.14}$$

where $\nu_e = \nu_{ei} + \nu_{en}$, ν_{ei} is the ion-electron collision frequency, and ν_{en} is the neutral electron collision frequency.

By treating the right hand side terms as known sources and solving Equations (2.7), (2.11), and (2.12), three fundamental electron properties are obtained, i.e., electron velocity, plasma potential, and electron temperature. With these detailed properties, the plasma plume simulation yields much improved results in comparison to the Boltzmann relation.

CHAPTER III

VACUUM CHAMBER FACILITY EFFECTS

3.1 Background and Assumptions

Vacuum chambers have wide applications for a variety of purposes such as materials processing and spacecraft electric propulsion experiments. The goal of vacuum chambers is to maintain a low pressure. For example, in the experiments of testing a cluster of high power electric plasma thrusters inside vacuum chambers [60] [29] [8], the backpressure was maintained at about 10^{-3}–10^{-4} Pa with thrusters in operation. In such experiments, a high backpressure will distort the exhaust plume flow and affect the width of the ion energy distribution function through collisions between beam ions and neutral background particles. The presence of a high backpressure misrepresents the real situation in space and may adversely affect the experiments.

One fundamental concern about the vacuum chamber is to understand the facility effects on the chamber performance. There are several facility effects that have significant impact on the vacuum chamber backpressure [9]. For vacuum chambers used for electric propulsion experiments, large cryo-genic pumps are usually employed as the primary pumps. A cryogenic pump typically has a steel plate that is maintained at a low temperature by gaseous helium. The pump sticking coefficient has a significant effect on the backpressure [9]. Generally, propellant frost will build up

on cryopump surfaces and eventually limit the pumping speed, hence, even though the nominal sticking coefficient for gas on steel pump plates at low temperature is high, in real experimental operations, the sticking coefficient for pumps may be much lower. Other important facility considerations include pump size and chamber side-wall length. In [60], different backpressures were measured with different numbers of pumps in operation and different mass flow rates from one or two 5 kW Hall thrusters. However, compared with this experimental work, there is little theoretical analysis about the facility effects in the literature. An analytical study of the facility effects and the background flow will benefit not only numerical simulations but also experimental work associated with vacuum chambers.

Vacuum chambers have different configurations based on the pump locations. In this chapter, two kinds of chambers are discussed. The first type of chamber is equipped with two-sided pumps. The other type of chamber is equipped with one-sided pumps located at one chamber end. Compared with a vacuum chamber equipped with one-sided pumps, the flowfield in a vacuum chamber equipped with two-sided pumps is more complex: there exists a pre-pump region and a post-pump region and the pressures in these two regions are different. The major purposes of this chapter are to investigate the background flow inside these two types of vacuum chambers and to study the facility effects on their background flow.

The Large Vacuum Test Facility (LVTF) at the Plasmadynamics and Electric Propulsion Laboratory (PEPL) in the University of Michigan is a typical vacuum chamber equipped with two-sided vacuum pumps. The LVTF is used for studying spacecraft electric plasma thrusters and Figure 3.1 illustrates its configuration. It is a stainless steel-clad vacuum chamber that has a cylindrical volume of 280 m^3 with a length of 9 m and a diameter of 6 m. Near one end of the chamber, there are seven

CVI TM-1200 nude cryopumps with a total surface area of 7.26 m^2. In operation, two, four or seven cryopumps can be turned on, hence in different situations, the total pump area can be varied. The pumps are maintained at an estimated low temperature of 15 K with gaseous helium. When particles such as xenon atoms or ions hit the pumps, a fraction of the particles stick to the plates and the rest reflect diffusely with a thermal speed characterized by the pump temperature of 15 K. The configuration of the LVTF can be simplified as Figure 3.2, where only the thrusters and the pumps are preserved and their relative positions are clearly reflected.

The pump performance is of significant importance and the pump sticking coefficient has a decisive influence on the final rarefied background flow in the chamber. Usually in LVTF, there is one thruster or a cluster of thrusters mounted on a test station in front of the pumps. In the present study, Hall thrusters employing xenon propellant are considered. The pump plates are aligned parallel to the plume flow direction, hence both sides of the pumps are equally exposed to the plume flow.

In operation, a low-density plasma flow is exhausted from the thruster towards the other chamber end without pumps. Though there are ions in the plume flow field, the ion number density is far lower than the neutral number density and when these ions hit the chamber wall, they lose their charge and rebound diffusely as neutrals with a thermal speed characterized by the wall temperature of 300 K. It is reasonable to assume neutrals move slowly from one chamber end towards the other end where the pumps are located.

Inside the LVTF, because the background gas flow is highly rarefied, it is reasonable to separate the chamber gas pressure into two parts: a universal background pressure and a plume pressure that only exists inside the plume. The study of the first part is the primary concern of this chapter.

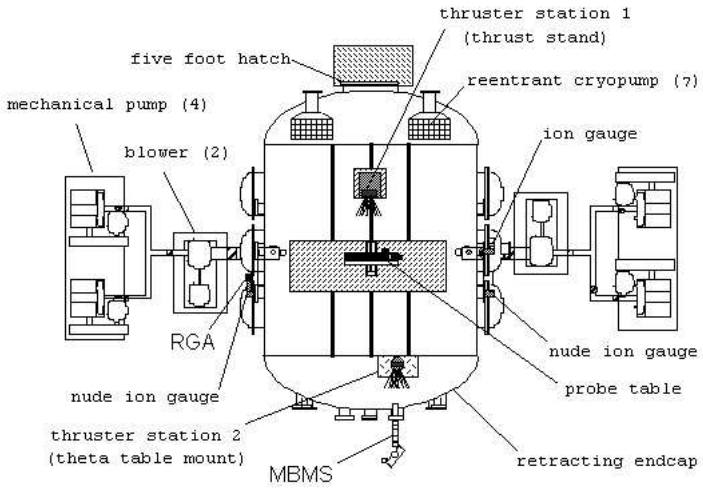

Figure 3.1: Large Vacuum Test Facility at the University of Michigan(Courtesy of PEPL).

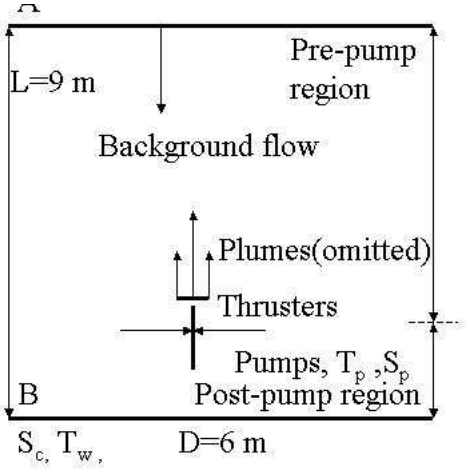

Figure 3.2: Simplified Configurations for the LVTF.

In the experiments [60] [29] [8], the backpressure of neutral xenon is calculated using the ideal gas law $P_b = nkT_w$, where n is the xenon number density measured using an ionization gauge and T_w is the chamber wall temperature. One possible ideal location to measure the background density is on the centerline of the chamber and between the pumps and the thrusters. Locations inside the plume(s) or close to the chamber walls should be avoided because of possible plume pressure effects and wall effects.

General Assumptions Based on the LVTF working conditions, several general assumptions can be made, and these assumptions are applicable to chambers equipped with one-sided pumps as well:

1. Pumps work effectively and create a low-density environment. This assumption results in a free molecular flow at the final steady state. With a typical final xenon backpressure of 10^{-3} Pa in the chamber, the mean free path of xenon atoms is about 2.86 m.

2. The chamber wall temperature is 300 K.

3. The background flow is simplified as one-dimensional flow.

4. The plume flow is neglected. This study concerns the background flow, and no matter whether the flow from the thruster is hot or cold, all heavy particles, such as neutrals and ions reflect at the chamber wall as background neutrals. The reflection of plume flow from one chamber end can be considered as neutral xenon coming into the chamber through that chamber end with an area, S_c, at the thruster mass flow rate, $\dot{m}$, and wall temperature, T_w. This end of the chamber is considered as a source.

5. All pumps have the same sticking coefficient, α, the same pump temperature, T_p, and a total pump area, S_p. Suppose for simplicity, the total pump area, S_p, is smaller than the chamber cross-section area, S_c, (this is correct for the LVTF). When xenon atoms and ions hit one of the pumps, by a probability of α they stick to the pumps and by a probability of $1-\alpha$ they rebound with a thermal speed characterized by T_p. Hence the pumps can be treated as a sink with a temperature, T_p, and an area, S_p, which is smaller than S_c. Because the flow is highly rarefied, the particles reflected from the pumps cannot hit the same pumps immediately without the necessary change of velocity direction by collisions with the other chamber end or the chamber sidewalls.

With the above assumptions, the background flow in the vacuum chamber can be simplified as one free molecular flow with a source at one chamber end and a sink for the pumps on or close to the other chamber end.

For any dilute gas flow in equilibrium, the velocity distribution in any coordinate direction can be described as a full Maxwellian distribution. For a temperature T, the velocity distribution function is:

$$f(C)dC = \left(\frac{m}{2\pi kT}\right)^{1/2} \exp(-mC^2/(2kT))dC \tag{3.1}$$

The mass flux in one direction across an area S normal to flow direction is:

$$\dot{m} = mnS\int_0^\infty C_n f(C_n)dC_n = \frac{1}{4}mnS\sqrt{8kT/(\pi m)} = mn_+S\sqrt{2kT/(\pi m)} \tag{3.2}$$

where $n_+ = \frac{1}{2}n$ is the number density of particles moving in one direction.

Another important relation for this study is the number density for a group of particles reflected from a plate with a different temperature. Directly from Equation (3.2), to preserve the mass flux, the following relation must hold:

$$n_1\sqrt{T_1} = n_2\sqrt{T_2} \tag{3.3}$$

where the subscripts 1, 2 represent the incoming and reflected groups of particles, respectively. Equation (3.1)– (3.3) can be found in general kinetic theory books [12] [27] [56].

3.2 Model 1: From Mass Conservation Law

Assuming a spatially constant density distribution in the vacuum chamber, which is equipped with one-sided or two-sided vacuum pumps, using the mass conservation law for the gas inside the vacuum chamber, the following relation must hold:

$$\frac{d\rho}{dt} = \frac{d(\int \rho dv)}{V dt} = \frac{1}{V}(\dot{m} - \frac{1}{4}\rho\alpha S_p\sqrt{\frac{8kT_w}{\pi m}}) \tag{3.4}$$

Two boundary conditions can be used to solve this ordinary differential equation:

1. At $t = 0$, the pump and thrusters begin to work, and the average background density in the large vacuum chamber is ρ_0, hence $\rho(t = 0) = \rho_0$.

2. At sufficiently long time, a steady background flow is established: $d\rho(t \to \infty)/dt = 0$.

The solution for this equation consists of one unsteady term and one steady term:

$$\rho(t) = (\rho_0 - \sqrt{\frac{2\pi m}{kT_w}}\frac{\dot{m}}{\alpha S_p})\exp(-\frac{\alpha S_p}{V}\sqrt{\frac{kT_w}{2\pi m}}t) + \sqrt{\frac{2\pi m}{kT_w}}\frac{\dot{m}}{\alpha S_p} \tag{3.5}$$

The mean background flow velocity in the chamber is:

$$U(t) = \frac{\dot{m}}{S_c\rho(t)} \tag{3.6}$$

The pressure corresponding to the experimental measurements is:

$$P_b(t) = (\rho_0 RT_w - \sqrt{2\pi RT_w}\frac{\dot{m}}{\alpha S_p})\exp(-\frac{\alpha S_p}{V}\sqrt{\frac{kT_w}{2\pi m}}t) + \sqrt{2\pi RT_w}\frac{\dot{m}}{\alpha S_p} \tag{3.7}$$

At steady state, the normalized pressure and the speed ratio are:

$$\frac{P_b S_c}{\dot{m}\sqrt{\gamma R T_w}} = \frac{(2\pi/\gamma)^{1/2}}{\alpha s} \tag{3.8}$$

$$\frac{U}{\sqrt{2RT_w}} = \frac{\alpha s}{2\sqrt{\pi}} \tag{3.9}$$

If the backpressure is known, then the pump sticking coefficient can be calculated using:

$$\alpha = \frac{\dot{m}(2\pi R T_w)^{1/2}}{P_b S_p} \tag{3.10}$$

This crude model, especially Equation (3.7), relates several properties from the chamber, the pumps, the thruster and the propellant; only the pump temperature is not included. There are three conclusions from this model:

1. It is evident from Equation (3.7) that if the pumps work efficiently, the pressure will decrease and reach a final steady state. However, Equation (3.7) also indicates that the unsteady term will take a finite time to decay significantly. For example, with the following LVTF parameters: V=280 m^3, T_w=300 K, S_p=7.26 m^2, and an assumption of α=0.40, the decaying term is:

$$P_b(t) = C\exp(-0.57t) = C\exp(-t/1.75) \tag{3.11}$$

where C is a constant.

The significant term in this expression is the semi-decaying period τ_d= 1.75 seconds. In experiments, usually the pumps operate for several hours, and steady background flows are well established. However, in particle simulations of the rarefied plasma plume flow field inside a vacuum chamber, usually the simulations develop as an unsteady process with a time step around 1×10^{-7} second. This requires over 50 million time steps for three semi-decaying periods

to reach a steady flow state. This presents a challenge to the numerical particle simulation and usually a full three-dimensional simulation of the whole chamber flow is too expensive.

2. The background gas flows towards the pump because of the velocity is positive velocity, and the average velocity increases as the pump sticking coefficient or the pump area increases.

3. No matter how efficiently the pumps work, there is a certain amount of finite backpressure in the vacuum chamber. This backpressure is represented by the second term of Equation (3.7). The same equation also indicates that for a specific chamber with fixed pump parameters, at the final steady state, the background pressure is proportional to the mass flux rate from the thrusters, no matter whether the flow is hot or cold. Although this is a crude approximation, experimental measurements [60] support this conclusion. Different backpressures and flow rates in [60] are tabulated in Table 3.1 and illustrated in Figure 3.3. The plot clearly displays the linear relation between backpressure and mass flow rate and the effect of pump area is evident. Table 3.1 contains the sticking coefficients calculated with Equation (3.10). For several cases with two pumps in operation, the calculated sticking coefficients are greater than one. There are two reasons for this problem: this model is crude and the cases with two pumps in operation are actually not quite free molecular, which will be illustrated later. Compared with this model, the next two models make it possible to evaluate the sticking coefficient for the vacuum pump more accurately.

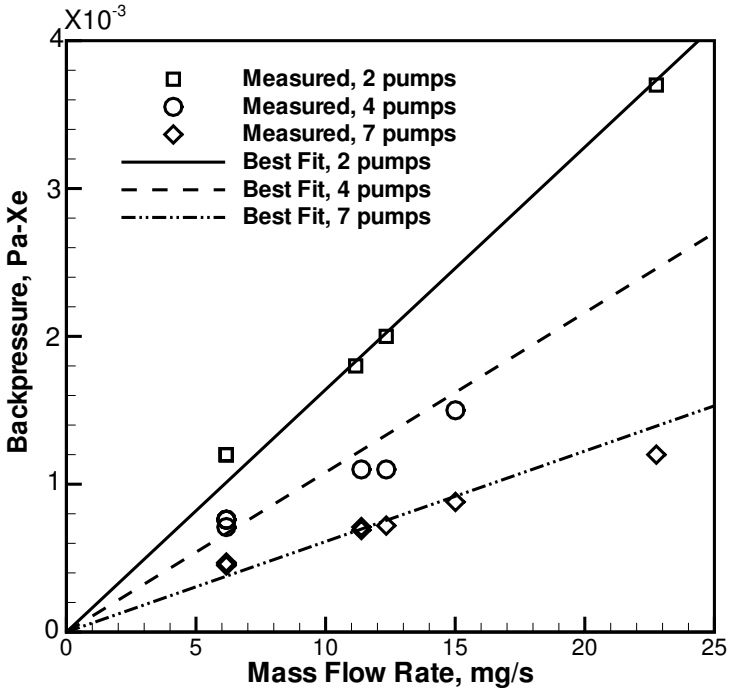

Figure 3.3: Measurements of Flow Rate and Backpressure in LVTF, PEPL.

The background pressure can be calculated from Equation (3.8) with a known sticking coefficient and a given mass flow rate. In general, for this model, the steady state background pressure decreases as the sticking coefficient increases. At small values of α, a 1% difference in the coefficient may result in a significant backpressure difference, while for large values the normalized pressure is not very sensitive to this parameter. For a numerical simulation of flows inside vacuum chambers, a correct sticking coefficient is critical.

3.3 Models for Chambers Equipped with Two-Sided Pumps

In this section, two free molecular flow models are presented to discuss the rarefied background flow in a vacuum chamber equipped with two-sided pumps.

No.	Pumps	Thrus -ters	Anode Flux (mg/s)	Flux (mg/s)	Pressure (mPa-Xe)	α (3.10)	Kn (3.47)
1	2	1	5.25(H)	6.17	1.20	0.856	0.784
2	2	1	10.24(H)	11.16	1.80	1.030	0.525
3	2	1	5.25(H)	12.34	2.00	1.028	0.473
4	2	1	10.46(H)	22.76	3.70	1.028	0.255
5	4	1	5.25(C)	6.17	7.60	0.676	1.247
6	4	1	10.46(C)	11.38	1.10	0.862	0.863
7	4	1	14.09(C)	15.01	1.50	0.833	0.632
8	4	1	5.25(H)	6.17	0.71	0.723	1.334
9	4	1	5.25(H)	12.34	1.10	0.934	0.846
10	7	1	5.25(C)	6.17	0.47	0.625	2.047
11	7	1	10.46(C)	11.38	0.69	0.785	1.395
12	7	1	14.09(C)	15.01	0.88	0.812	1.092
13	7	1	5.25(H)	6.17	0.45	0.652	2.142
14	7	1	5.25(H)	6.17	0.46	0.633	2.078
15	7	1	10.46(H)	11.38	0.71	0.763	1.088
16	7	1	5.25(H)	12.34	0.72	0.815	1.334
17	7	1	10.46(H)	22.76	1.20	0.903	0.801
Ave						0.821	

Table 3.1: Measured Backpressure and Calculated Sticking Coefficients for the LVTF (H: hot flow, C: cold flow. For all cases the cathode flux= 0.92 mg/s).

3.3.1 Model 2: Two-Sided Pump, Kinetic Model with Specular Reflection

Figure 3.4 illustrates the configuration of this model. Pumps are located on a chamber end and both sides of the pumps are exposed to the background flow. There is a pre-pump region AC and a post-pump region DB. The densities in these two regions are not equal. This is exactly the configuration for LVTF.

To simplify the analysis, in this model the sidewall effects are neglected. Further

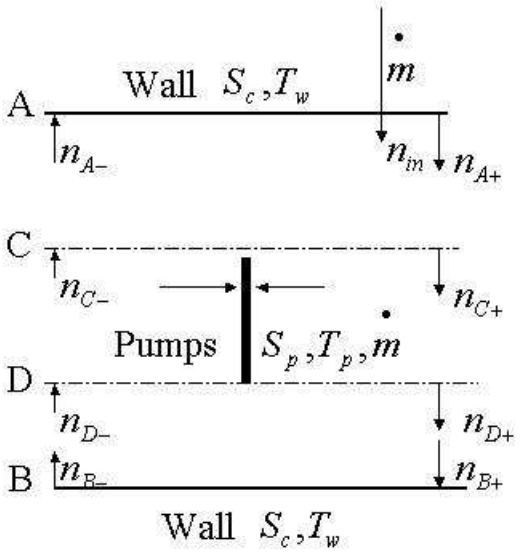

Figure 3.4: Illustration of Models 2 and 3.

for simplicity, suppose the reflected particles from the pumps maintain their original flow directions. The second assumption is quite close to a specular reflection pump wall situation and in the next model this assumption will be relaxed.

The analysis of this model is based on the flux and number density relations along two directions. At section D, consider the mass flux relation for the group of particles traveling from A to B:

$$F_{D+} = mn_{C+}S_cV_w - mn_{C+}S_pV_w + (1-\alpha)\sqrt{\frac{T_w}{T_p}}n_{C+}mS_pV_p \tag{3.12}$$

$$n_{B+} = n_{D+} = (1-s)n_{C+} + (1-\alpha)sn_{C+}\sqrt{\frac{T_w}{T_p}} \tag{3.13}$$

The second term on the right hand side represents the slow particles reflected from the pumps. These slow particles resume high speed after they reflect from chamber end B:

$$n_{B-} = n_{D-} = (1-s)n_{C+} + (1-\alpha)sn_{C+} = (1-\alpha s)n_{C+} \tag{3.14}$$

The pumps further absorb a fraction of these particles:

$$F_{C-} = mn_{B-}S_cV_w - mn_{B-}S_pV_w + (1-\alpha)\sqrt{\frac{T_w}{T_p}}n_{B-}mS_pV_p \tag{3.15}$$

$$n_{A-} = n_{C-} = (1-s)n_{B-} + (1-\alpha)sn_{B-}\sqrt{\frac{T_w}{T_p}} \tag{3.16}$$

The slow particles of the second term on the right hand side resume high speeds after reflection from wall A:

$$n_{A+} = n_{C+} = n_{in} + (1-\alpha s)n_{B-} \tag{3.17}$$

From Equations (3.17) and (3.14), the following relation can be obtained:

$$n_{A+} = n_{C+} = \frac{n_{in}}{\alpha s(2-\alpha s)} \tag{3.18}$$

The above relation can be obtained consistently with the aid of the fluxes in and out of the chamber as well:

$$\dot{m} = mn_{in}S_cV_w = \alpha mn_{C+}S_pV_w + \alpha mn_{B-}S_pV_w \tag{3.19}$$

With an intermediate result obtained from Equations (3.18), (3.14) and (3.18):

$$n_{A-} = n_{C-} = \left(1 - s + (1-\alpha)s\sqrt{T_w/T_p}\right)\frac{(1-\alpha s)}{\alpha s(2-\alpha s)}n_{in} \tag{3.20}$$

The final solutions for this free molecular flow model are:

$$n_A = n_{A+} + n_{A-} = \frac{\left(1 + (1 - s + (1-\alpha)s\sqrt{T_w/T_p})(1-\alpha s)\right)}{\alpha s(2-\alpha s)}n_{in} \tag{3.21}$$

$$n_B = n_{B+} + n_{B-} = \frac{(2 - \alpha s - s + (1-\alpha)s\sqrt{T_w/T_p})n_{in}}{\alpha s(2-\alpha s)} \tag{3.22}$$

$$f_A(C) = \begin{cases} \frac{n_{in}}{\alpha s(2-\alpha s)}\sqrt{\frac{1}{2\pi RT_w}}\exp(-\frac{mC^2}{2kT_w}), & \text{if } C > 0; \\ \frac{s(1-\alpha)(1-\alpha s)\sqrt{T_w/T_p}n_{in}}{\alpha s(2-\alpha s)}\sqrt{\frac{m}{2\pi kT_p}}\exp(-\frac{mC^2}{2kT_p}) & \\ +\frac{(1-s)(1-\alpha s)n_{in}}{\alpha s(2-\alpha s)}\sqrt{\frac{m}{2\pi kT_w}}\exp(-\frac{mC^2}{2kT_w}), & \text{if } C < 0. \end{cases} \tag{3.23}$$

$$f_B(C) = \begin{cases} \frac{s(1-\alpha)\sqrt{T_w/T_p}n_{in}}{\alpha s(2-\alpha s)}\sqrt{\frac{m}{2\pi kT_p}}\exp(-\frac{mC^2}{2kT_p}) \\ +\frac{(1-s)n_{in}}{\alpha s(2-\alpha s)}\sqrt{\frac{m}{2\pi kT_w}}\exp(-\frac{mC^2}{2kT_w}), & \text{if } C>0; \\ \frac{(1-\alpha s)n_{in}}{\alpha s(2-\alpha s)}\sqrt{\frac{m}{2\pi kT_w}}\exp(-\frac{m}{2kT_w}C^2), & \text{if } C<0. \end{cases} \tag{3.24}$$

The normalized pressure corresponding to the experimental measurements [60] [8] and the mean velocities for these two regions are:

$$\frac{P_b(A)S_c}{\dot{m}\sqrt{\gamma RT_w}} = \frac{1}{\alpha s(2-\alpha s)}\sqrt{\frac{\pi}{2\gamma}}\left(1+(1-s+(1-\alpha)s\sqrt{\frac{T_w}{T_p}})(1-\alpha s)\right) \tag{3.25}$$

$$\frac{P_b(B)S_c}{\dot{m}\sqrt{\gamma RT_w}} = \frac{1}{\alpha s(2-\alpha s)}\sqrt{\frac{\pi}{2\gamma}}\left(2-\alpha s-s+(1-\alpha)s\sqrt{\frac{T_w}{T_p}}\right) \tag{3.26}$$

$$\frac{U_A}{\sqrt{2RT_w}} = \frac{\alpha s(2-\alpha s)}{\sqrt{\pi}\left(1+(1-s+(1-\alpha)s\sqrt{\frac{T_w}{T_p}})(1-\alpha s)\right)} \tag{3.27}$$

$$\frac{U_B}{\sqrt{2RT_w}} = 0 \tag{3.28}$$

The above discussion neglects the sidewall effects and the model is essentially for a short chamber situation. If the sidewall is long enough, the slow particles reflected from the cold pumps will hit the sidewall first before they reach a chamber end. In a cylinder with a length of 9 m and a diameter of 6 m, calculation indicates that on average only about 5% of the particles from one chamber end can reach the other end without any collisions on the sidewall, the pump effects are confined in a small local region close to the pump. Hence, simply replacing T_w/T_p with unity in the above formulas may approximate a long chamber situation. It should be pointed out that this is the most convenient treatment but not an accurate treatment. The same treatment for vacuum chambers equipped with one-sided pumps, which is presented and validated by numerical simulations in the next section, yields the best match of average number density and average velocities between analytical results

and numerical simulations. It is therefore reasonable to apply this same treatment to the analytical results for two-sided pumps.

Using T_p/T_w=1, the simplified formulas for normalized pressure are:

$$\frac{P_b(A)S_c}{\dot{m}\sqrt{\gamma RT_w}} = \frac{2-2\alpha s+\alpha^2 s^2}{\alpha s(2-\alpha s)}\sqrt{\frac{\pi}{2\gamma}} \tag{3.29}$$

$$\frac{P_b(B)S_c}{\dot{m}\sqrt{\gamma RT_w}} = \frac{2-2\alpha s}{\alpha s(2-\alpha s)}\sqrt{\frac{\pi}{2\gamma}} < \frac{P_b(A)S_p}{\dot{m}\sqrt{\gamma RT_w}} \tag{3.30}$$

Figure 3.5 gives some calculated LVTF pump sticking coefficients with Equations (3.25) and (3.29) based on the experimental measurement data in [60]. It should be noted that in [60], the ionization gauges are placed quite close to chamber wall; hence the measurements actually include the whole background pressure instead of just one direction of background flow. Figure 3.5 shows that these two formulas yield significant difference, and Equation (3.29) yields smaller but smoother results. Later comparisons of numerical simulations and experimental measurements indicate the results from Equation (3.29) are more accurate.

3.3.2 Model 3: Two-Sided Pump, Kinetic Model with Diffuse Reflection

One key assumption in the above derivation is that the particles reflected from the pump keep their original direction, which simplifies the analysis. In the other limit, particles reflect from pumps diffusely. Though the derivation is much more complex, the corresponding results are similar to the results from Model 2. This model is illustrated in Figure 3.4 as well.

From the diffuse wall condition, after reflection from the pump, half of the particles travel along the original direction while the other half travel along the opposite direction:

$$F_{D+} = mn_{C+}S_cV_w - mn_{C+}S_pV_w + \frac{1-\alpha}{2}\sqrt{\frac{T_w}{T_p}}(n_{C+}mS_pV_p + n_{D-}mS_pV_p) \tag{3.31}$$

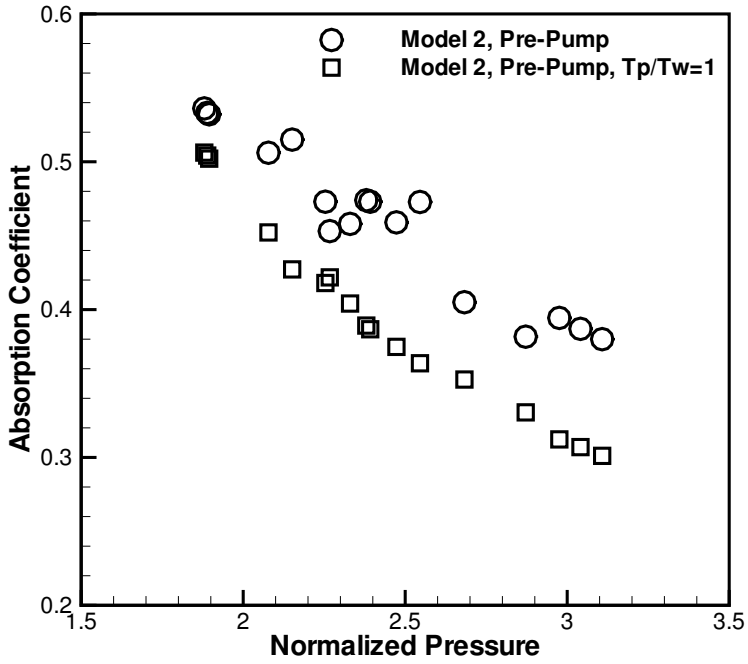

Figure 3.5: Normalized Pressure vs. Calculated Pump Sticking Coefficient.

$$F_{C-} = mn_{B-}S_cV_w - mn_{B-}S_pV_w + \frac{1-\alpha}{2}\sqrt{\frac{T_w}{T_p}}(n_{B-}mS_pV_p + n_{C+}mS_pV_p) \quad (3.32)$$

The various number density relations have the following expressions:

$$n_{B+} = n_{D+} = (1-s)n_{C+} + \frac{1-\alpha}{2}sn_{C+}\sqrt{\frac{T_w}{T_p}} + \frac{1-\alpha}{2}sn_{D-}\sqrt{\frac{T_w}{T_p}} \quad (3.33)$$

$$n_{B-} = n_{D-} = (1-s)n_{C+} + \frac{1-\alpha}{2}sn_{C+} + \frac{(1-\alpha)}{2}sn_{D-} \quad (3.34)$$

$$n_{A-} = n_{C-} = (1-s)n_{B-} + \frac{1-\alpha}{2}sn_{B-}\sqrt{\frac{T_w}{T_p}} + \frac{1-\alpha}{2}sn_{C+}\sqrt{\frac{T_w}{T_p}} \quad (3.35)$$

$$n_{A+} = n_{C+} = n_{in} + (1 - \frac{s}{2} - \frac{\alpha s}{2})n_{B-} + \frac{1-\alpha}{2}sn_{C+} \quad (3.36)$$

The final solutions for this free molecular flow model are:

$$n_A = n_{A+} + n_{A-} = \left(2 - 2s + \frac{1}{2}s^2 + \frac{1}{2}\alpha s^2 + (1-\alpha)s(1-\frac{s}{2})\sqrt{\frac{T_w}{T_p}}\right)\frac{1}{\alpha s(2-s)}n_{in} \quad (3.37)$$

$$n_B = n_{B+} + n_{B-} = \left(2 - 2s + \frac{1}{2}s^2 - \frac{1}{2}\alpha s^2 + (1-\alpha)s\sqrt{\frac{T_w}{T_p}}(1-\frac{s}{2})\right)\frac{1}{\alpha s(2-s)}n_{in} \quad (3.38)$$

$$f_A(C) = \begin{cases} \frac{(2-s+\alpha s)n_{in}}{\alpha s(2-s)}\sqrt{\frac{m}{2\pi kT_w}}\exp(-\frac{m}{2kT_w}C^2), & \text{if } C>0; \\ \frac{(1-\alpha)\sqrt{T_w/T_p}n_{in}}{\alpha}\sqrt{\frac{m}{2\pi kT_p}}\exp(-\frac{m}{2kT_p}C^2) & \\ +\frac{(1-s)(2-s-\alpha s)n_{in}}{\alpha s(2-s)}\sqrt{\frac{m}{2\pi kT_w}}\exp(-\frac{m}{2kT_w}C^2), & \text{if } C<0. \end{cases} \tag{3.39}$$

$$f_B(C) = \begin{cases} \frac{(1-\alpha)\sqrt{T_w/T_p}n_{in}}{\alpha}\sqrt{\frac{m}{2\pi kT_p}}\exp(-\frac{m}{2kT_p}C^2) & \\ +\frac{(1-s)(2-s+\alpha s)n_{in}}{\alpha s(2-s)}\sqrt{\frac{m}{2\pi kT_w}}\exp(-\frac{m}{2kT_w}C^2), & \text{if } C>0; \\ \frac{(2-s-\alpha s)n_{in}}{\alpha s(2-s)}\sqrt{\frac{m}{2\pi kT_w}}\exp(-\frac{m}{2kT_w}C^2), & \text{if } C<0. \end{cases} \tag{3.40}$$

The balanced flow rate condition, Equation (3.19), is completely compatible with the solution set Equations (3.37)- (3.40). The normalized pressure corresponding to the experimental measurements [8] [60] and the mean velocities for these two regions are:

$$\frac{P_b(A)S_c}{\dot{m}\sqrt{\gamma RT_w}} = \frac{1}{\alpha s(2-s)}\sqrt{\frac{\pi}{2\gamma}}\left(2-2s+\frac{1}{2}s^2+\frac{1}{2}\alpha s^2+(1-\alpha)s\sqrt{\frac{T_w}{T_p}}(1-\frac{s}{2})\right) \tag{3.41}$$

$$\frac{P_b(B)S_c}{\dot{m}\sqrt{\gamma RT_w}} = \frac{1}{\alpha s(2-s)}\sqrt{\frac{\pi}{2\gamma}}\left(2-2s+\frac{1}{2}s^2-\frac{1}{2}\alpha s^2+(1-\frac{s}{2})(1-\alpha)s\sqrt{\frac{T_w}{T_p}}\right) \tag{3.42}$$

$$\frac{U_A}{\sqrt{2RT_w}} = \frac{\alpha s(2-s)}{\sqrt{\pi}\left(2-2s+\frac{1}{2}s^2+\frac{1}{2}\alpha s^2+(1-\frac{s}{2})(1-\alpha)s\sqrt{\frac{T_w}{T_p}}\right)} \tag{3.43}$$

$$U_B = 0 \tag{3.44}$$

The formulas for normalized pressure with T_w/T_p =1 are:

$$\frac{P_b(A)S_c}{\dot{m}\sqrt{\gamma RT_w}} = \sqrt{\frac{\pi}{2\gamma}}\frac{\left(2-2s+\frac{1}{2}s^2+\frac{1}{2}\alpha s^2+(1-\alpha)s(1-\frac{s}{2})\right)}{\alpha s(2-s)} \tag{3.45}$$

$$\frac{P_b(B)S_c}{\dot{m}\sqrt{\gamma RT_w}} = \sqrt{\frac{\pi}{2\gamma}}\frac{\left(2-2s+\frac{1}{2}s^2-\frac{1}{2}\alpha s^2+(1-\frac{s}{2})(1-\alpha)s\right)}{\alpha s(2-s)} < \frac{P_b(A)S_c}{\dot{m}\sqrt{\gamma RT_w}} \tag{3.46}$$

3.3.3 Discussions of Models 2 and 3

There is some difference between Equations (3.23), (3.24) and Equations (3.39) and (3.40), for example, the denominators are different. However, the differences between these two sets of results are essentially minor and can be illustrated with calculations of the pump sticking coefficient in LVTF. Table 3.2 summarizes the sticking coefficients computed by the two sets of formulas and it clearly indicates that there are only minor differences between the results from Equations (3.25), (3.26) and Equations (3.41), (3.42), and the same conclusion holds for the results from Equations (3.27), (3.28) and Equations (3.43), (3.44). Models 2 and 3 treat the pump plates as specular and diffusive walls, which are the two extreme situations that bound all real surface reflection conditions. Based on the fact that these two models produce quite close results, the following discussions concentrate on the results from Model 2. All the conclusions apply to Model 3 as well.

There are two possible reasons for the scattered results for the pump sticking coefficients. First, under different working conditions with different mass flow rates and number of pumps in operation, different amounts of propellant frost may build up on the pumps. Hence, the performance of the pumps may be different under different working conditions. Second, there are some fluctuations in the experimental measurements in [60]. Due to these two reasons, the calculated sticking coefficient for a vacuum pump may vary within a small range. For the LVTF, the pre-pump region is larger than the post-pump region and the thrusters are located in the pre-pump region. Hence the results from the pre-pump region are of primary interest. Surprisingly, as indicated in Table 3.2, the calculations for both the pre-pump region and the post-pump region yield quite close results and it can be concluded that the average pump sticking coefficient for the LVTF is close to a value

Case No.	$\alpha(A)$ (3.25)	$\alpha(B)$ (3.26)	$\alpha(A)$ (3.29)	$\alpha(B)$ (3.30)	$\alpha(A)$ (3.41)	$\alpha(B)$ (3.42)	$\alpha(A)$ (3.45)	$\alpha(B)$ (3.46)
1	0.453	0.450	0.422	0.421	0.451	0.451	0.428	0.429
2	0.536	0.537	0.506	0.507	0.537	0.537	0.507	0.506
3	0.533	0.535	0.504	0.504	0.534	0.534	0.504	0.504
4	0.532	0.532	0.502	0.503	0.532	0.532	0.503	0.502
5	0.382	0.382	0.331	0.329	0.381	0.382	0.331	0.329
6	0.473	0.475	0.418	0.417	0.475	0.473	0.418	0.417
7	0.458	0.461	0.404	0.404	0.474	0.472	0.418	0.421
8	0.405	0.406	0.353	0.352	0.406	0.405	0.353	0.352
9	0.506	0.501	0.452	0.451	0.509	0.507	0.453	0.451
10	0.380	0.386	0.301	0.301	0.385	0.382	0.302	0.300
11	0.459	0.467	0.375	0.373	0.465	0.462	0.377	0.372
12	0.473	0.479	0.387	0.385	0.479	0.473	0.389	0.383
13	0.394	0.401	0.312	0.313	0.399	0.395	0.315	0.311
14	0.387	0.391	0.307	0.306	0.392	0.388	0.308	0.305
15	0.473	0.478	0.364	0.362	0.455	0.449	0.366	0.361
16	0.474	0.481	0.389	0.387	0.481	0.475	0.391	0.384
17	0.515	0.522	0.427	0.425	0.521	0.511	0.431	0.424
Ave	0.461	0.464	0.397	0.396	0.463	0.460	0.400	0.397

Table 3.2: Calculated Pump Sticking Coefficients for the LVTF.

of 0.46 by Equations (3.25) (3.26) (3.41) and (3.42) or a value of 0.40 by Equations (3.29) (3.30) (3.45) and (3.46).

Several observations can be made based on Equations (3.23), (3.24) and Equations (3.39), (3.40):

1. The velocity distribution in general is not a zero-centered Maxwellian distribution. Figure 3.6 shows typical asymmetric velocity distribution profiles from Equation (3.23) for several coefficient combinations.

2. The number density in the chamber varies spatially and may be affected by various effects from the chamber, the pumps, the thruster and the propellant. Figures 3.7 and 3.8 show the normalized pressure contours, $P_b S_c/(\dot{m}\sqrt{\gamma RT})$, as a function of $s = S_p/S_c$ and α. The temperature ratio is set to T_p/T_w=15/300. The post-pump region pressure is always smaller than the pre-pump region pressure. When α is too small, the model is not valid because the flow is no longer free molecular. P_A and P_B decrease when α increases. An increase in pump area or pump sticking coefficient always results in a lower backpressure for both chamber ends.

3. Figure 3.9 shows the average velocity normalized by $\sqrt{2RT_w}$ for the pre-pump region. The velocity in the pre-pump region is always greater than zero meaning gas flows towards the pump, but the velocity in the post-pump region is always zero because of a net zero flux. The combination of α=1 and $s = S_p/S_c$=1 results in n_B =0, U_B =0, and $n_A = n_{in}$, $U_A = \sqrt{2RT_w/\pi}$. For this situation, all particles hitting the pumps are absorbed and a vacuum exists in the post-pump region. Because no particles are reflected from the post-pump region, the number density in the pre-pump region is equal to the inlet number density.

All of these conclusions are applicable to Model 3 as well.

Figures 3.10– 3.12 show three measured pressure profiles [60] inside the LVTF and three series of axi-symmetric particle simulation results with different pump sticking coefficients [59]. They correspond to Cases 5, 6 and 11 in Tables 3.1 and 3.2. From the interpolation of computed results in Figure 3.10, a sticking coefficient of 0.30–0.40 will result in good agreement between the experimental measurements and numerical simulation for Case 5, and from Table 3.2, the analytical formulas predict a value of

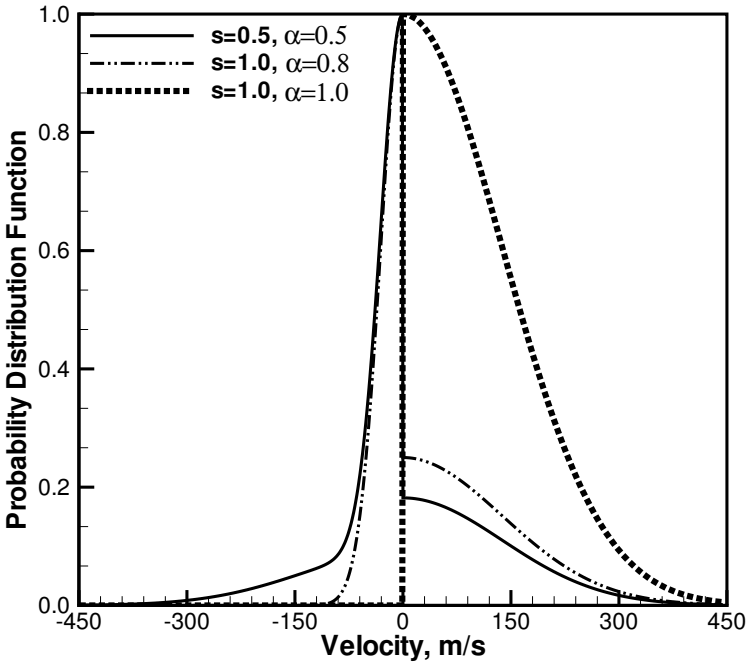

Figure 3.6: Velocity Distribution Function Examples.

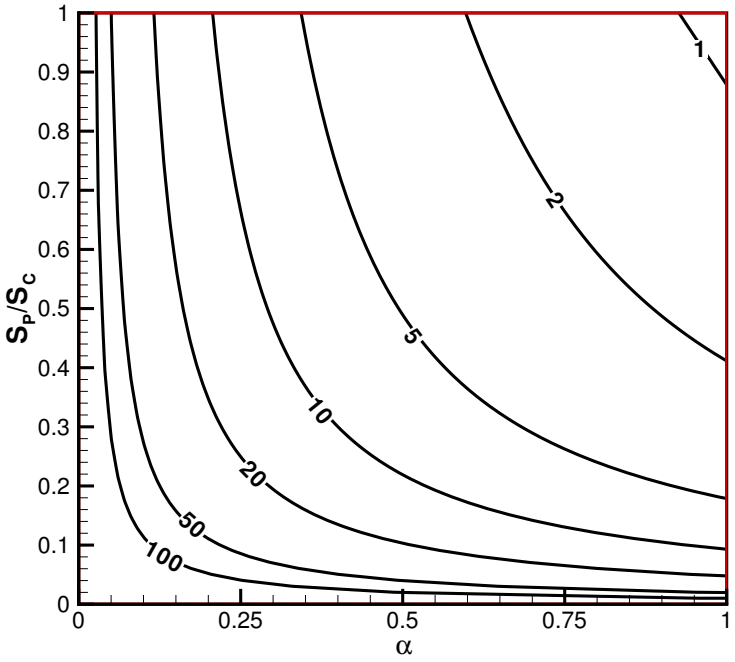

Figure 3.7: Normalized Backpressure in the Pre-Pump Region: $P_b S_c/(\dot{m}\sqrt{2RT_w})$.

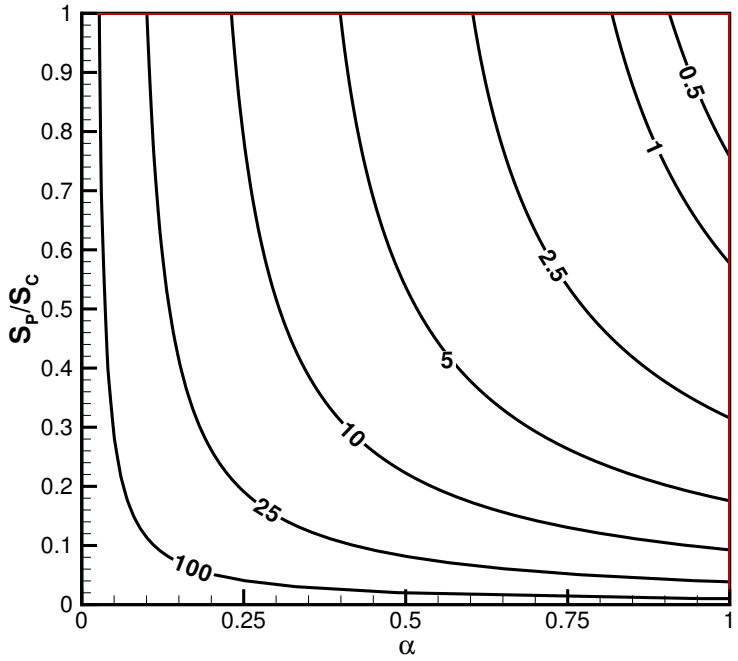

Figure 3.8: Normalized Backpressure in the Post-Pump Region: $P_b S_c/(\dot{m}\sqrt{2RT_w})$.

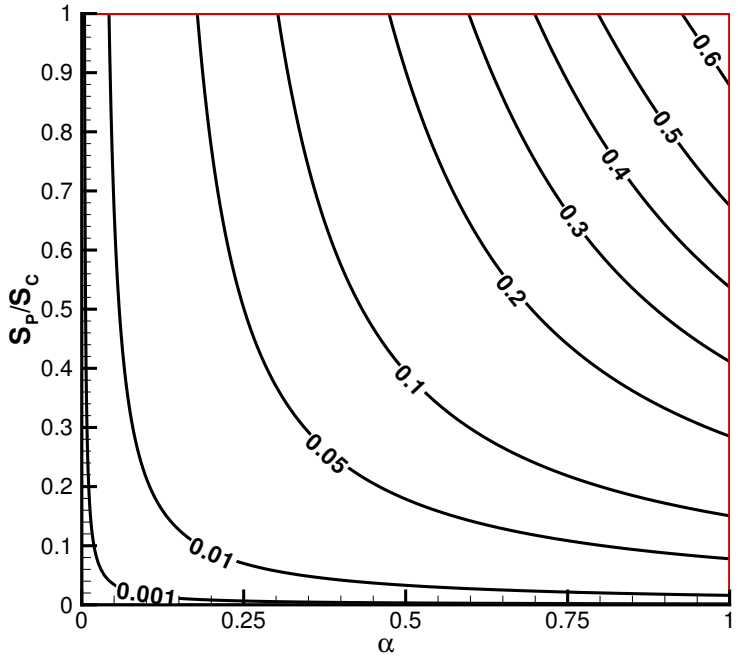

Figure 3.9: Average Velocity in the Pre-Pump Region(normalized by $\sqrt{2RT_w}$).

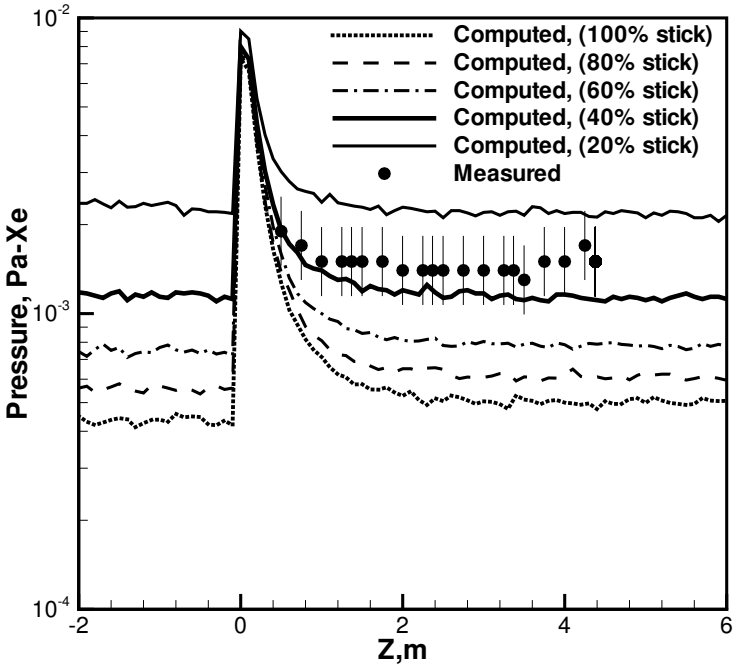

Figure 3.10: Comparisons of Simulated and Measured Pressure Distribution within LVTF with Cold Flow Rate = 5.25 mg/s, 4 Pumps and 1 Thruster in Operation.

0.38 by Equations (3.25) or (3.26), a value of 0.33 from Equations (3.29) or (3.30), a value of 0.38 from Equations (3.41) or (3.42) and a value of 0.33 from Equations (3.45) and (3.46). These formulas predict similar values for Cases 6 (Figure 3.11) and 11 (Figure 3.12) as well. Because the chamber is long, and the wall side effect is significant, the formulas with T_w/T_p =1 may yield sticking coefficients that agree better with the experimental measurements. Obviously the analytical predictions, especially those from Equations (3.29), (3.30), (3.45) and (3.46), match experimental measurement and numerical simulations quite well.

It is appropriate to discuss the range of validity of the above formulas. These formulas are based on a free molecular flow assumption, hence for a specific mass flux and a specific propellant, it is not difficult to evaluate whether the assumption is correct. Because the pre-pump region is the major concern, the number density n_A,

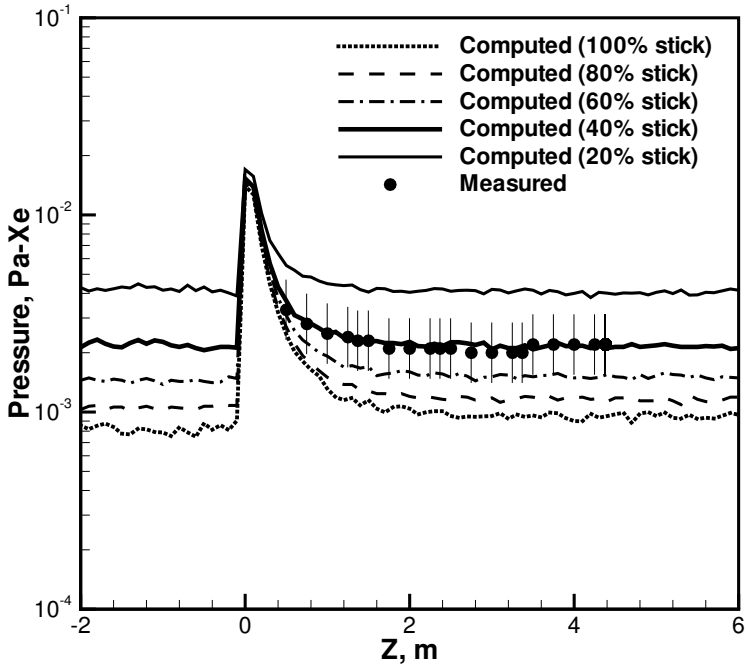

Figure 3.11: Comparisons of Simulated and Measured Pressure Distribution within LVTF with Cold Flow Rate =10.46 mg/s, 4 Pumps and 1 Thruster in Operation.

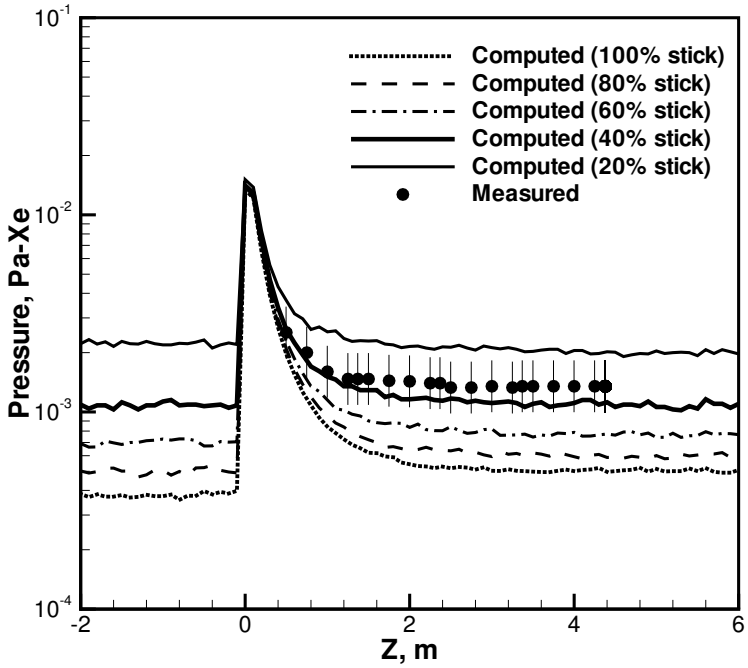

Figure 3.12: Comparisons of Simulated and Measured Pressure Distribution within LVTF with Cold Flow Rate =10.46 mg/s, 7 Pumps and 1 Thruster in Operation.

from Equation (3.25), and the chamber end radius are selected as the characteristic quantities for the evaluation of Knudsen number:

$$Kn = \frac{\lambda}{\sqrt{S_c/\pi}} = \frac{\alpha s(2-\alpha s)m\sqrt{RT_w S_c}}{\pi d^2 \dot{m}\left(1+(1-s+(1-\alpha)s\sqrt{T_w/T_p})(1-\alpha s)\right)} \tag{3.47}$$

where the sticking coefficient in this formula should be computed from (3.25) if not given as a known quantity. Tabulated values of Knudsen number calculated from Equation (3.47) are given in Table 3.2, from which it can be observed that the cases with two pumps in operation are not quite free molecular as they do not satisfy $Kn > 1$.

Another interesting factor is the temperate ratio T_p/T_w. Usually, the cryopumps in a large vacuum chamber are maintained at low temperature, for example, the temperature of pumps in LVTF is about 12–15 K. Generally, this temperature ratio does not have significant effects on large vacuum chambers. As mentioned previously, the large amount of slow particles reflected from the cold pumps are concentrated around the pumps. Once these particles hit the chamber sidewall, these particles resume faster speeds and diffuse quickly. Hence, most of the volume of long chambers is dominated by faster particles, and the pump temperature effects are not significant. Another reason accounting for the unimportance of the temperature ratio is, in the formulas obtained in this study, the temperature ratios are offset by square roots, and in front of these square roots, there are always small coefficients. Hence, in this study, the pump temperature is set to 15 K and no further discussion is necessary.

The final comment about these two models is to note that the results in the two models are obtained with an assumption of one-dimension flow, and the model has essentially a constant density in the pre-pump and post-pump regions. In fact, Equations (3.29), (3.30), (3.45) and (3.46) are extrapolations of this one-dimensional

model. More accurate results could be obtained with careful consideration of the flux relations and different solid angles between the chamber ends and chamber sidewalls. Because both models 2 and 3 consist of two regions and the derivation is significantly more complex, the details are omitted here. However, Figures 3.10– 3.12 indicate that these two simple analytical one-dimensional models yield good agreement with the numerical simulations and experimental measurements.

3.4 Models for Chambers Equipped with One-Sided Pumps

Compared with the models for chambers equipped with two-sided pumps, models for vacuum chambers equipped with one-sided pumps are simpler, hence it is more convenient to investigate chamber sidewall effects. Unlike the previous discussion, which is based on available experimental measurements [60] and three series of simulations [59], there are no experimental data available for chambers equipped with one-sided pumps yet. Hence the validity of the models in this section will be assessed using comparisons with numerical simulations. In this section, the one-sided pumps are located on one chamber end, hence there is no post-pump region and this greatly simplifies the analysis.

3.4.1 Model 4: One-Sided Pump, Kinetic, without Sidewall Effects

In this model, a vacuum chamber is equipped with one-sided pumps located on one chamber end, as illustrated in Figure 3.13. This model represents a practical and well-defined free molecular flow problem.

In the first step, Model 4 still assumes a constant density distribution without strict treatment of wall effects. This treatment is valid for a short chamber situation. In the next model, this assumption will be relaxed.

When the flow reaches a final steady state, the flux must be balanced everywhere

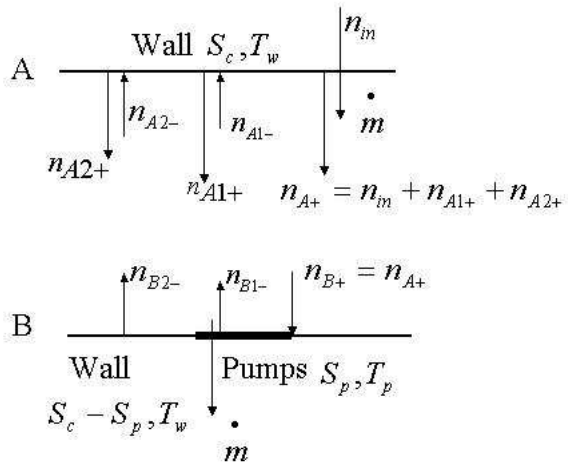

Figure 3.13: Illustration of Model 4.

along two directions and this condition leads to several number density relations. Analysis of these flux and number density relations is the key step to analyze this problem. At chamber end A without pumps, a group of particles moves from A to B with a number density relation: $n_{A+} = n_{in} + n_{A1+} + n_{A2+}$.

At end B, there are three number density relations from the flux relations:

1. Particles reflected at the chamber end B with pumps but not from the pumps:

$$n_{B2-} = n_{A+}(1 - S_p/S_c) = n_{A+}(1 - s) \tag{3.48}$$

2. Mass flux relation: flux out of the chamber through the pumps equals the mass flux into the chamber at the other chamber end:

$$\dot{m} = \alpha m n_{A+} S_p V_w = m n_{in} S_c V_w \tag{3.49}$$

3. Particles reflected from the pumps:

$$n_{B1-} = (1 - \alpha) n_{A+} \frac{S_p}{S_c} \sqrt{\frac{T_w}{T_p}} = (1 - \alpha) s n_{A+} \sqrt{\frac{T_w}{T_p}} \tag{3.50}$$

The above relations yield the following expressions:

$$n_{A1-} = n_{B1-} = \frac{(1-\alpha)}{\alpha}\sqrt{\frac{T_w}{T_p}}n_{in} \tag{3.51}$$

$$n_{A2+} = n_{A2-} = n_{B2-} = \frac{1-s}{\alpha s}n_{in} \tag{3.52}$$

$$n_{A1+} = n_{B1-}\sqrt{\frac{T_p}{T_w}} = \frac{1-\alpha}{\alpha}n_{in} \tag{3.53}$$

$$n_{A+} = \frac{n_{in}}{\alpha s} \tag{3.54}$$

With the above relations, the full solutions for this model are:

$$n_A = n_B = \frac{2-s+s(1-\alpha)\sqrt{\frac{T_w}{T_p}}}{\alpha s}n_{in} = \frac{\dot{m}}{S_c}\sqrt{\frac{\pi}{2kmT_w}}\frac{2-s+s(1-\alpha)\sqrt{T_w/T_p}}{\alpha s} \tag{3.55}$$

$$f(C) = \begin{cases} \frac{2(1-\alpha)s\sqrt{\frac{T_w}{T_p}}n_{in}}{\alpha s}\sqrt{\frac{m}{2\pi kT_p}}\exp(-\frac{mC^2}{2kT_p}) & \\ +\frac{2(1-s)n_{in}}{\alpha s}\sqrt{\frac{m}{2\pi kT_w}}\exp(-\frac{mC^2}{2kT_w}), & \text{if } C>0 \\ \frac{2n_{in}}{\alpha s}\sqrt{\frac{m}{2\pi kT_w}}\exp(-\frac{m}{2kT_w}C^2), & \text{if } C>0 \end{cases} \tag{3.56}$$

The normalized mean velocity, the pressure corresponding to experimental measurements, the pump sticking coefficients and the Knudsen number are as follows:

$$\frac{U}{\sqrt{2RT_w}} = \frac{\alpha s}{\sqrt{\pi}\left(2-s+(1-\alpha)s\sqrt{\frac{T_w}{T_p}}\right)} \tag{3.57}$$

$$\frac{P_b(A)S_c}{\dot{m}\sqrt{\gamma RT_w}} = \sqrt{\frac{\pi}{2\gamma}}\frac{2-s+s(1-\alpha)\sqrt{T_w/T_p}}{\alpha s} \tag{3.58}$$

$$\alpha = \frac{2-s+s\sqrt{T_w/T_p}}{s\sqrt{T_w/T_p}+P_bS_p/(\dot{m}\sqrt{\pi RT_w/2})} \tag{3.59}$$

$$Kn = \frac{\lambda}{\sqrt{S_c/\pi}} = \frac{1}{\sqrt{2}\pi d^2 n_A\sqrt{S_c}} = \frac{\alpha sm\sqrt{RT_wS_c}}{\pi d^2\dot{m}(2-s+(1-\alpha)s\sqrt{T_w/T_p})} \tag{3.60}$$

Model 4 leads to exact solutions to a classical free molecular flow problem. Generally, a vacuum system consistent with Model 4 works less efficiently than a vacuum

chamber equipped with two-sided pumps, which was discussed in the previous section, because only the particles moving towards the pumps have a chance to be absorbed.

Though Equation (3.56) has a different format when compared with Equation (3.39), it indicates that there are three groups of particles moving inside the chamber. One group of particles travels towards the vacuum pump, while the other two groups travel from the pump direction, one of which is directly reflected from the pumps. It is evident that the background flow cannot be described as a Maxwellian distribution, and the average velocity is not zero.

It is critical to consider the wall effects because many vacuum chambers are quite long and the sidewall effects are dominant. With the same treatment of setting the ratio T_p/T_w to unity, which is used in the previous section, Equations (3.55) and (3.57) take new formats:

$$n_A = n_B = \frac{(2 - s\alpha)\dot{m}}{\alpha s S_c}\sqrt{\frac{\pi}{2kmT_w}} \tag{3.61}$$

$$\frac{U}{\sqrt{2RT_w}} = \frac{\alpha s}{\sqrt{\pi}(2 - s\alpha)} \tag{3.62}$$

Model 4 is a constant density model and a special case of the next general model.

3.4.2 Model 5: One-Sided Pump, Kinetic, with Sidewall Effects

Different from the previous treatment of considering sidewall effects by setting the temperature ratio to unity, the following non-constant density model considers sidewall effects more generally. Figure 3.14 illustrates this model.

First, from the relation of the mass flow into the chamber at chamber end denoted as A and that out of the chamber through the pump at chamber end denoted as B:

$$\dot{m} = mn_{in}S_cV_w = \alpha mn_{B+}S_pV_w \tag{3.63}$$

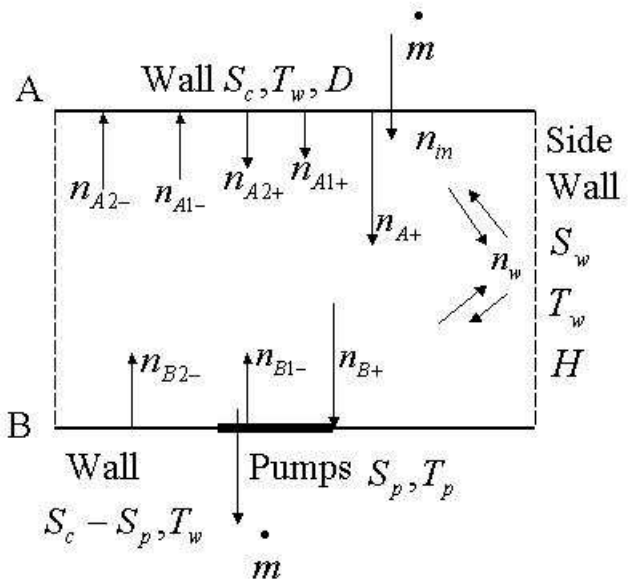

Figure 3.14: Illustration of Model 5.

the following relation is obtained:

$$n_{B+} = \frac{n_{in}}{\alpha s} \tag{3.64}$$

At chamber end B, the following relations exist for the mass flux towards the pumps and other regions of end B:

$$n_{B1-} = n_{B+}(1-\alpha)s\sqrt{\frac{T_w}{T_p}} = \frac{1-\alpha}{\alpha}\sqrt{\frac{T_w}{T_p}}n_{in} \tag{3.65}$$

$$n_{B2-} = (1-s)n_{B+} = \frac{1-s}{\alpha s}n_{in} \tag{3.66}$$

At both ends, the incoming particles are composed of two groups: one group of particles travels from the other end without any collisions with the sidewalls, while the other group of particles travels from the sidewalls. In this study, a variable χ is introduced to represent the percentage of particles travel from one chamber end finally arrive at the other end without any collision with the chamber wall. Another variable, ϵ, is introduced to represent the percentage of particles travel from the

chamber sidewall and finally arrive one chamber end. Further assuming the particles close to the sidewall may drift to both ends with equal probability because of the diffuse wall reflection assumption, the following equations are obtained:

$$n_{B+} = \chi n_{A+} + \epsilon n_w \tag{3.67}$$

$$n_{A-} = \chi n_{B1-} + \chi n_{B2-} + \epsilon n_w \tag{3.68}$$

$$n_{A+} = n_{in} + \epsilon n_w + \chi n_{B2-} + \chi n_{B1-}\sqrt{T_p/T_w} \tag{3.69}$$

The above equations yield the following intermediate results:

$$n_{A+} = \frac{(1+\chi+\alpha s-\alpha\chi s)n_{in}}{\alpha s(1+\chi)} \tag{3.70}$$

$$n_{A-} = \frac{\chi s(1-\alpha)(1+\chi)\sqrt{\frac{T_w}{T_p}}+1+\chi-\chi s-\chi^2 s-\alpha\chi s+\alpha\chi^2 s}{\alpha s(1+\chi)} n_{in} \tag{3.71}$$

The complete solutions for this model do not contain the factor ϵ, but involve an extra geometry parameter χ, which is completely determined by the chamber length and the chamber base radius:

$$n_A = \frac{\chi s(1-\alpha)(1+\chi)\sqrt{T_w/T_p}+2+2\chi-\chi s+\alpha s-\chi^2 s-2\alpha\chi s+\alpha\chi^2 s}{\alpha s(1+\chi)} n_{in} \tag{3.72}$$

$$n_B = \frac{\left(s(1-\alpha)\sqrt{T_w/T_p}+2-s\right)n_{in}}{\alpha s} \tag{3.73}$$

$$n_{ave} = \frac{s(1-\alpha)(1+\chi)^2\sqrt{T_w/T_p}+4+4\chi+\alpha s-s-2\chi s-\chi^2 s-2\alpha\chi s+\alpha\chi^2 s}{2\alpha s(1+\chi)} n_{in} \tag{3.74}$$

$$f_A(C) = \begin{cases} \frac{2(1+\chi+\alpha s-\alpha\chi s)n_{in}}{\alpha s(1+\chi)}\sqrt{\frac{m}{2\pi kT_w}}\exp(-\frac{m}{2kT_w}C^2), & \text{if } C>0 \\ \frac{2\chi s(1-\alpha)(1+\chi)\sqrt{T_w/T_p}n_{in}}{\alpha s(1+\chi)}\sqrt{\frac{m}{2\pi kT_p}}\exp(-\frac{m}{2kT_p}C^2) & \\ +\frac{2(1+\chi-\chi s-\chi^2 s-\alpha\chi s+\alpha\chi^2 s)n_{in}}{\alpha s(1+\chi)}\sqrt{\frac{m}{2\pi kT_w}}\exp(-\frac{m}{2kT_w}C^2), & \text{if } C<0 \end{cases} \tag{3.75}$$

$$f_B(C) = \begin{cases} \frac{2s(1-\alpha)\sqrt{T_w/T_p}n_{in}}{\alpha s}\sqrt{\frac{m}{2\pi kT_p}}\exp(-\frac{m}{2kT_p}C^2) & \\ +\frac{2(1-s)n_{in}}{\alpha s}\sqrt{\frac{m}{2\pi kT_w}}\exp(-\frac{m}{2kT_w}C^2), & \text{if } C<0 \\ \frac{2n_{in}}{\alpha s}\sqrt{\frac{m}{2\pi kT_w}}\exp(-\frac{m}{2kT_w}C^2), & \text{if } C>0 \end{cases} \tag{3.76}$$

The normalized mean velocities, the normalized pressures corresponding to experimental measurements and the Knudsen number are:

$$\frac{U(A)}{\sqrt{2RT_w}} = \frac{\alpha s(1+\chi)}{\sqrt{\pi}\left(\chi s(1-\alpha)(1+\chi)\sqrt{\frac{T_w}{T_P}}+2+2\chi+\alpha s-\chi s-\chi^2 s-2\alpha\chi s+\alpha\chi^2 s\right)} \tag{3.77}$$

$$\frac{U(B)}{\sqrt{2RT_w}} = \frac{\alpha s}{\sqrt{\pi}\left(s(1-\alpha)\sqrt{T_w/T_p}+2-s\right)} \tag{3.78}$$

$$\frac{P_b(A)S_c}{\dot{m}\sqrt{\gamma RT_w}} = \sqrt{\frac{\pi}{2\gamma}}\frac{\chi s(1-\alpha)(1+\chi)\sqrt{\frac{T_w}{T_P}}+2+2\chi+\alpha s-\chi s-\chi^2 s-2\alpha\chi s+\alpha\chi^2 s}{\alpha s(1+\chi)} \tag{3.79}$$

$$\frac{P_b(B)S_c}{\dot{m}\sqrt{\gamma RT_w}} = \sqrt{\frac{\pi}{2\gamma}}\frac{2-s+(1-\alpha)s\sqrt{T_w/T_p}}{\alpha s} \tag{3.80}$$

$$Kn = \frac{\alpha s(1+\chi)m\sqrt{RT_w S_c}}{\pi d^2\dot{m}(\chi s(1-\alpha)(1+\chi)\sqrt{T_w/T_p}+2+2\chi+\alpha s-\chi s-\chi^2 s-2\alpha\chi s+\alpha\chi^2 s)} \tag{3.81}$$

There are several significant observations from the above relations:

1. The formulas for the chamber end with pumps are the same as the results from Model 4.

2. Generally the number densities for the two chamber ends are different, and a non-constant density distribution occurs. Either chamber end can have a higher density with a proper combination of parameters.

3. The background gas flows towards the pump and the flow velocity increases as the pump size of the pump sticking coefficient increases.

4. This model can be considered as a finite chamber length model, and the parameter χ reflects the effect of chamber sidewall length. The constant density Model 4 is a special case of this model. When χ=1, which means the sidewall is quite short, Equation (3.75) degenerates to the constant density distribution of Model 4.

5. The highest average velocity is the same as Model 4, and happens at both ends with a special combination of parameters $\alpha = \chi = s$=1.

The number density in the chamber varies spatially and may be affected by various effects from the chamber, the pumps, the thruster and the propellant. Figures 3.15 and 3.16 show results of normalized pressure and average velocity for end A. In both cases, the parameter χ is set to 0.05 representing a long chamber situation. Mathematically, $\partial P/\partial s \propto (-s^{-2})$ and $\partial P/\partial \alpha \propto (-\alpha^{-2})$, hence, the pressure is a decreasing function of s and α, and Figure 3.15 illustrates these trends. Because the average velocity has an inverse relation with number density to maintain a fixed net mass flow rate, Figure 3.16 illustrates an exact reverse trend in velocity when compared with density. When α is quite small, the model is not valid because the flow is no longer free molecular. The background pressure decreases when α or s increases.

The velocity near the pump is always greater than zero, which means that gas flows towards the pump. The parameter combination of α=1, χ=1 and s=1 results in $n_A = n_B = n_{in}$, $U_A = U_B = \sqrt{RT_w/\pi}$. For this situation, all particles hitting the pumps are absorbed. Because no particles are reflected from the post-pump region, the number densities at chamber ends A and B are equal to the inlet number density. For a short chamber situation χ=0.63, the trends in pressure and velocity are the

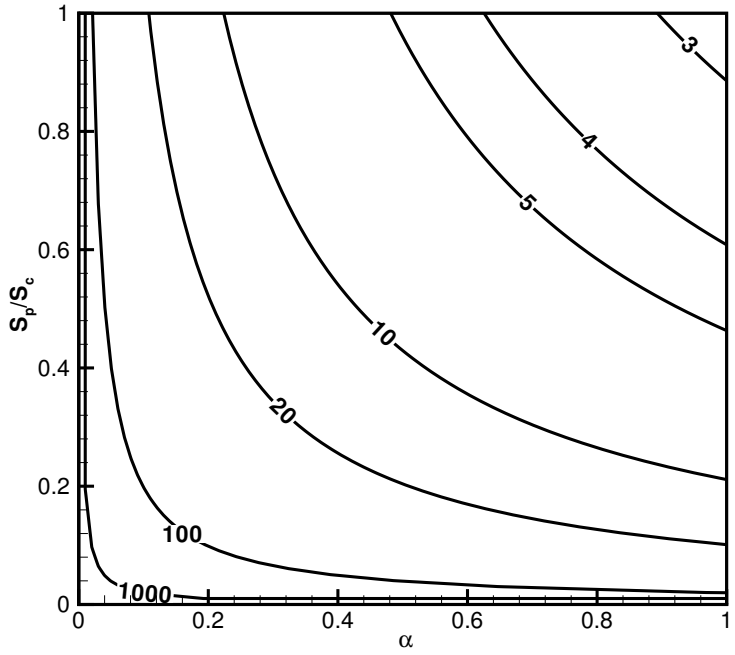

Figure 3.15: Normalized Average Backpressure $\frac{P_b S_c}{\dot{m}\sqrt{\gamma R T_w}}$ at Chamber End without Pumps (Model 5, χ=0.05).

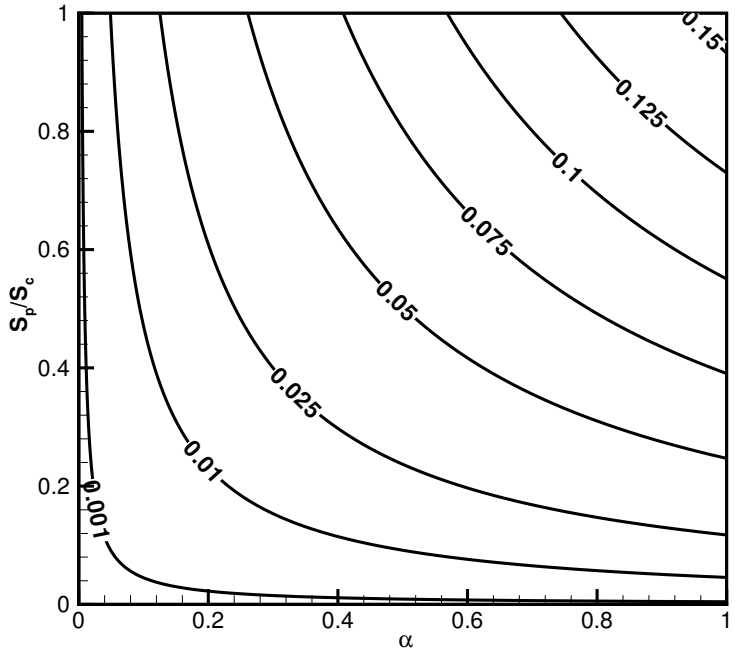

Figure 3.16: Average Velocity $\frac{U}{\sqrt{2RT_w}}$ at Chamber End without Pumps (Model 5, χ=0.05).

same as Figures 3.15 and 3.16, though there are some difference in values.

It is interesting to examine the sidewall effects considered in this model. Figures 3.17 and 3.18 show contours of normalized pressure and speed ratio for the chamber end without pumps using α and χ as variables. For both cases, the parameter s is set to 0.4. Mathematically, $\partial P/\partial\chi$ has different signs depending on α. Hence, the sidewalls have different effects on the final average stage in a chamber. A small α results in a large amount of slow particles reflected from the pumps; within a long chamber where χ is small, these particles cannot reach the other chamber end without collisions with the chamber wall, and particles accumulate at both chamber ends. For a short chamber where χ is greater, these particles are capable of reaching the other chamber end, hence a uniform, higher average density results. With a large α, very few particles are reflected back towards the other end, and a short chamber is effective at absorbing slow particles, hence a lower average density occurs. In Figure 3.17, the condition $\partial P/\partial\chi$ =0 occurs close to α=0.65, and this result will be confirmed later by numerical simulations. For the average velocities illustrated by Figure 3.18, they share the same contour line shapes but reverse trends as Figure 3.17 to maintain a fixed net mass flow rate.

Evaluation of Transport Coefficient χ

A key parameter for this model is the transport coefficient χ, which controls the probability that a particle traveling from one chamber end can reach the other chamber end without any collisions with the chamber sidewall. The evaluation of this parameter involves two steps: first, calculate the solid angle at one specific point on one chamber end subtended by the other chamber end. The solid angle formula is:

$$\Omega = \int_s \frac{\overrightarrow{r}\cdot\overrightarrow{n}dS}{r^3} = \int_0^{2\pi} Hd\phi \int_0^R \frac{\eta^2 d\eta}{(r^2+H^2-2r\eta cos\phi+\eta^2)^{3/2}} \tag{3.82}$$

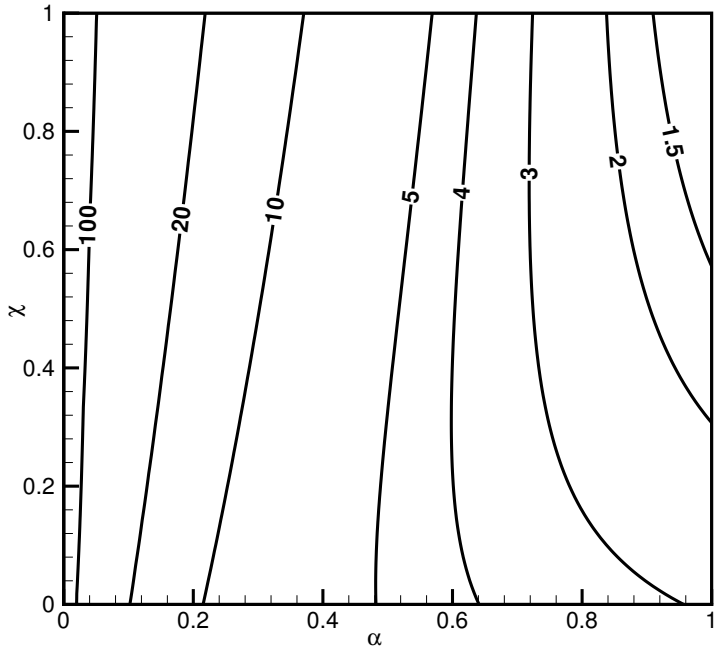

Figure 3.17: Normalized Average Backpressure at Chamber End without Pumps (Model 5, s=0.4).

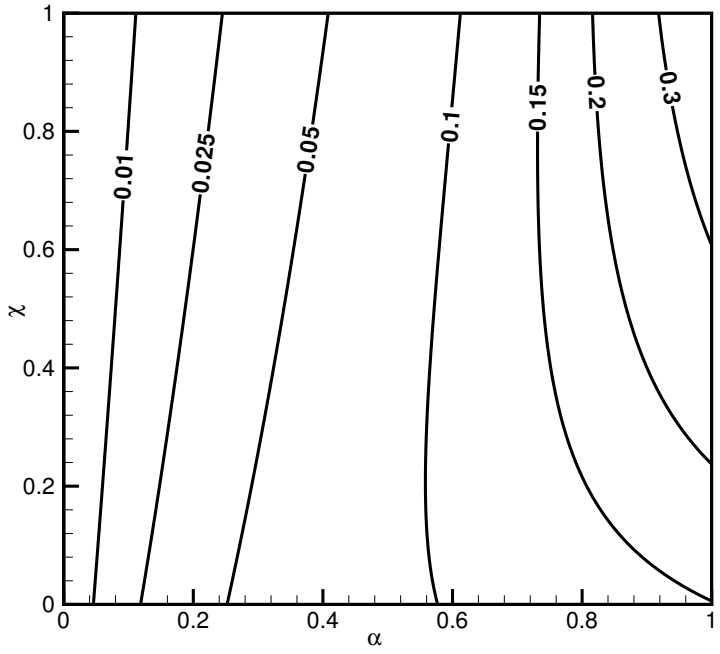

Figure 3.18: Average Speed Ratio $\frac{U}{\sqrt{2RT_w}}$ at Chamber End without Pumps (Model 5, s=0.4).

The final format of this integral involves the Heuman's Lambda function and the complete elliptic integral of the first kind [39] [41]. The second step is to average the solid angles over all points on this chamber end. Though there is an analytical result for the first step, it is extremely difficult to obtain an analytical expression for the second step, which is required to evaluate the analytical results from Model 5. In this study, the transportation coefficient χ is evaluated numerically. Figure 3.19 illustrates the numerical results of χ for different chamber stations at different distances from one chamber end. It shows that as x/R increases, the percentage of particles reaching the stations from one chamber end drops rapidly. For a chamber with L/R=0.9/3, about 63% of particles starting from one chamber end can reach the other chamber end; while for L/R=9/3, only about 5% of particles starting from one chamber end arrive at the other end without hitting the chamber sidewall. Hence, for a large vacuum chamber with a length of 9 meters and a diameter of 6 meters, like the LVTF, the sidewall effect is significant.

3.4.3 Comments on Models 1, 4 and 5

There are three models applicable to the background flow in a vacuum chamber with one-sided pumps: Model 1, Model 4 and Model 5. Among these three models, Model 1 is the crudest one-dimensional model without any consideration of sidewall effects. Model 4 is a relatively accurate model with considerations of two chamber ends and pumps, and the sidewall effect is partially considered by setting the temperature ratio to unity. This model is actually a one-dimensional model with a constant density distribution. Model 5 is the most advanced and complete model that considers sidewall effects, and it can predict a non-constant density distribution along different chamber stations. Model 4 can be considered as one special case of

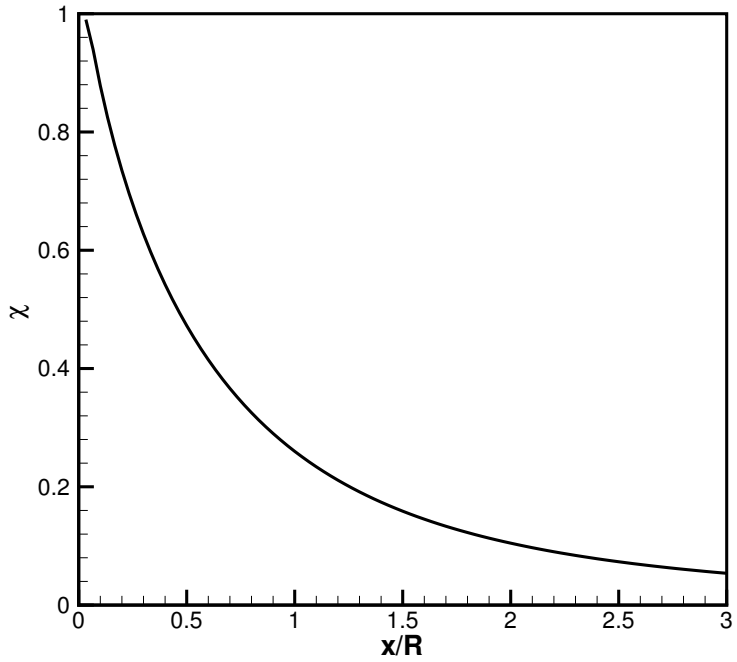

Figure 3.19: χ Distribution at Different Stations in a Cylindrical Chamber.

Model 5.

In experiments, it is not desirable to accumulate a large amount of particles at the chamber end equipped with pumps. Model 5 can predict a threshold value for the sticking coefficient that results in a higher density accumulation around the chamber end equipped with pumps. For example, to satisfy $n_A > n_B$, from Equations (3.72) and (3.73), it can be shown that:

$$\alpha > \frac{\chi^2 - 1 + (1-\chi^2)\sqrt{T_w/T_p}}{1 - 2\chi + \chi^2 + (1-\chi^2)\sqrt{T_w/T_p}} \tag{3.83}$$

A parameter combination of χ=0.05 and T_w/T_p=300/15 results in $\alpha > 0.65$ according to the above relation. It is interesting to observe that this relation is independent of s.

3.4.4 Numerical Simulations

For vacuum chambers equipped with one-sided pumps, there are no experimental measurements available; hence the validity of these models is depended on comparisons with numerical simulations. About 70 DSMC simulations using MONACO [23] are performed to compare with the analytical results. In these simulations, xenon gas flows through a cylindrical chamber with a fixed base radius of 3 meters. In all the simulations, the mass flow rates into and out of the chamber ends are set to 6.17 mg/sec, which is the mass flow rate out of four Hall thrusters studied in Reference [8]. All the simulation results are carefully examined to confirm the mean free path in the flow field is over 3 meters, hence the flow is close to free molecular for each case. These simulations are made physically accurate by including collisions, even though collisions occur very infrequently.

Boundary conditions

Figure 3.20 illustrates the axi-symmetric simulation domain used in this study. It is a cylindrical chamber with a length of 9 m or 0.9 m and a radius of 3 m. These simulations with a long chamber sidewall and a short chamber sidewall provide numerical results to test the performance of the analytical results.

There are four kinds of boundary conditions adopted in these simulations:

1. OO_1: axis of symmetry.

2. OA: mixed inlet and diffuse wall boundary condition. When particles hit this boundary from the inner domain, they reflect diffusely with a speed characterized by a wall temperature T_w =300 K. At the same time, this side also serves as an inlet boundary condition and an extra fixed mass flow rate of 6.17 mg/sec into the chamber is maintained. A uniform inlet on this side is consistent with

the treatment in Models 4 and 5.

3. AB: diffuse wall boundary condition with T_w=300 K.

4. BO_1: mixed outlet and diffuse wall boundary condition. This study attempts to perform simulations without any effects from pump locations, hence, no special location of pumps on this chamber end is specified. Instead, the finite area pump on the chamber end is achieved by the following process: when particles hit this wall, by a probability of $1 - S_p/S_c$ they reflect diffusely with a speed characterized by the wall temperature of 300 K; by a chance of $\alpha S_p/S_c$ they are absorbed by the pumps and hence removed from simulation; by a chance of $(1 - \alpha)S_p/S_c$ they reflect diffusely with a speed characterized by the pump temperature of 15 K. Whether a particle sticks to the pump or reflects on the wall or pumps is decided by comparing two random numbers and the assumed values of α and s. This "No Concrete Pump" treatment has two merits: it is effective to simulate pumps of all size, including quite small pumps, and it is not necessary to regenerate a new mesh for a new simulation with a different pump size.

A mesh of 45 by 15 cells along the axial and radial directions is adopted in these simulations. The flows are almost free molecular, there are very few collisions happening inside the domain, and such a mesh size provides enough resolution while minimizing the simulation cost. The time steps adopted in the final stages of these simulations vary from 1×10^{-4} second to 1×10^{-6} second to reduce multiple reflections for a particle in one time step. Typically, a simulation starts with a relatively large time step and a small number of particles to reach a steady state then the time step is reduced and the particle number increased. For all simulation cases, approximately

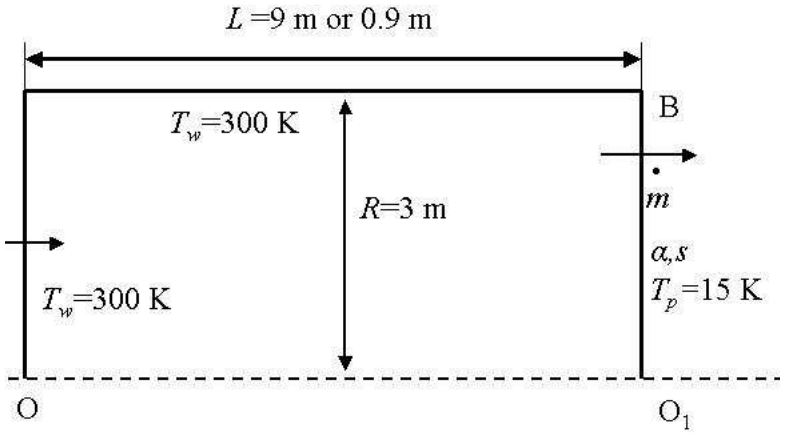

Figure 3.20: Illustration of Simulation Domain(Not in Scale).

one million particles are preserved in the final sampling stage and each case takes less than 30 minutes on a SUN workstation.

Evaluation of Average Quantities

Models 1 and 4 are essentially one-dimensional models with constant distribution at different stations and Model 5 can be considered as one-dimensional with a proper interpolation of the properties at both chamber ends. The primary concern of the numerical simulations is to compute the averaged properties throughout the flow fields. At each time step, an average density and an average velocity for the whole domain are computed by counting all particles in the simulation domain and averaging their velocities:

$$\rho(t) = (\sum(w_i N_i))m/V \tag{3.84}$$

$$U(t) = (\sum U_j)/N \tag{3.85}$$

where N_i and w_i are the total number of particles and the particle weight in the ith cell and V is the whole chamber volume, U_j and N are the jth particle velocity and total number of particles in the domain. The flow evolution history can be computed

through these two expressions.

Comment about Accuracy

The major purposes of these simulations are to provide accurate average background pressure and average background velocity with a combination of different facility effects. The DSMC method is an accurate simulation method to simulate rarefied gas flows; by counting all particles in the chamber and averaging their velocities, Equations (3.84) and (3.85) provide accurate calculations of the average properties. By including collisions between particles and with walls, the DSMC simulations are expected to yield more physically accurate results than the analytical results. Hence, these particle simulation results will be used to compare the effectiveness of the analytical models. The detailed distributions in these two-dimensional simulations may be effected by subtle changes in boundary treatments, but the average number density and average velocity in the chamber are not sensitive to these changes in boundary treatment.

Though the detailed two-dimensional distributions are not the major interest of this study, observations of these results may be quite informative. Figures 3.21 and 3.22 show contours of number density and velocity at a steady flow state for the case of L/R=9/3, S_p/S_c=0.4, α=0.4, and the pumps are located on the right chamber end. Figure 3.21 indicates clearly that for this case there is a large amount of particles reflected from the pump towards the other end. However, after colliding with the long chamber wall, these particles resume a faster speed and the density drops rapidly along one direction though another direction is heavily blocked. Hence, the high density is confined to small regions around the two ends. Figure 3.22 illustrates that the velocity does not change significantly throughout the flowfield, and an overall average velocity can represent the velocity field quite well. For other

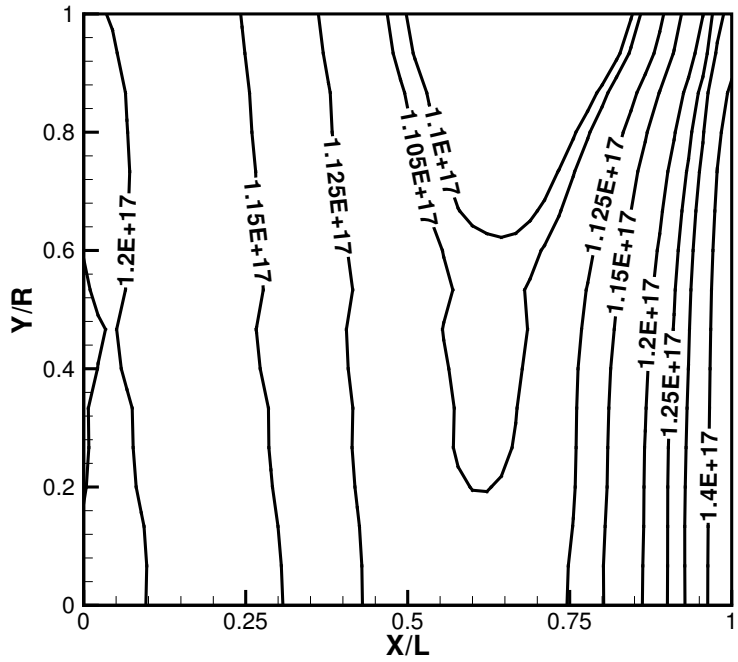

Figure 3.21: Contours of Number Density (m^{-3})(L/R=9/3, S_p/S_c=0.4, α=0.4, pumps located on the right chamber end).

simulation cases, the flowfields are quite similar but with a higher pump area or a higher sticking coefficient, the diffusion from the chamber end with pumps decreases and for the short chamber cases, gradients are distributed more evenly.

It should be mentioned that Model 5 could be used to study the one-dimensional variation of density or velocity distribution at different chamber stations. Model 5 provides two different values at the two chamber ends. With the aid of χ shown in Figure 3.19, it is possible to construct a nonlinear distribution of density or velocity at different chamber stations. However, this will introduce a numerical distribution into the analytical results and is not the major concern of this study. Numerically, the one-dimensional density and velocity can be calculated by averaging particles at different chamber stations. Figure 3.23 shows variations of steady one-dimensional density and speed results for the case L/R=9/3, S_p/S_c=0.4 and α=0.4. For this case,

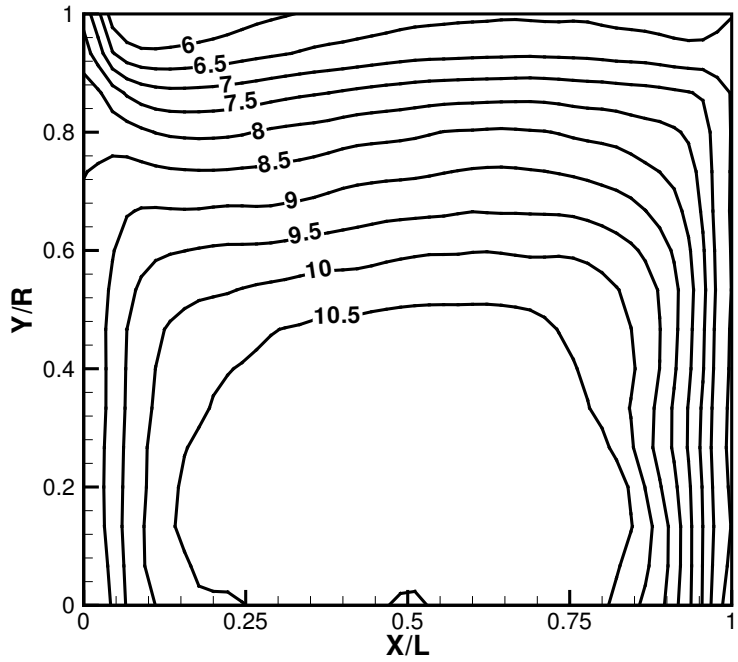

Figure 3.22: Contours of Velocity(m/s)(L/R=9/3, S_p/S_c=0.4, α=0.4, pumps located on the right chamber end).

the diffusion from the chamber end with pumps is more significant than that from the other chamber end. This indicates that the diffusion effect is confined closely to both ends; hence a lower value of density results for this long chamber case. The velocity varies inversely with the density to maintain a fixed net flow rate.

Comparison of Numerical and Analytical Evolution History

Model 1 provides the average density evolution history through Equation (3.5). The semi-decaying period for a cylindrical chamber is:

$$\tau_d = \frac{V\sqrt{2\pi m}}{\alpha S_p \sqrt{kT_w}} = \frac{L\sqrt{2\pi}}{\alpha s \sqrt{RT_w}} \tag{3.86}$$

where V and L are the chamber volume and length.

With parameters S_p/S_c=0.4, α=0.4, T_w=300 K and a chamber length of 9 m or 0.9 m, the semi-decaying periods for the unsteady term are τ_d=1.0 second and 0.10 second, respectively.

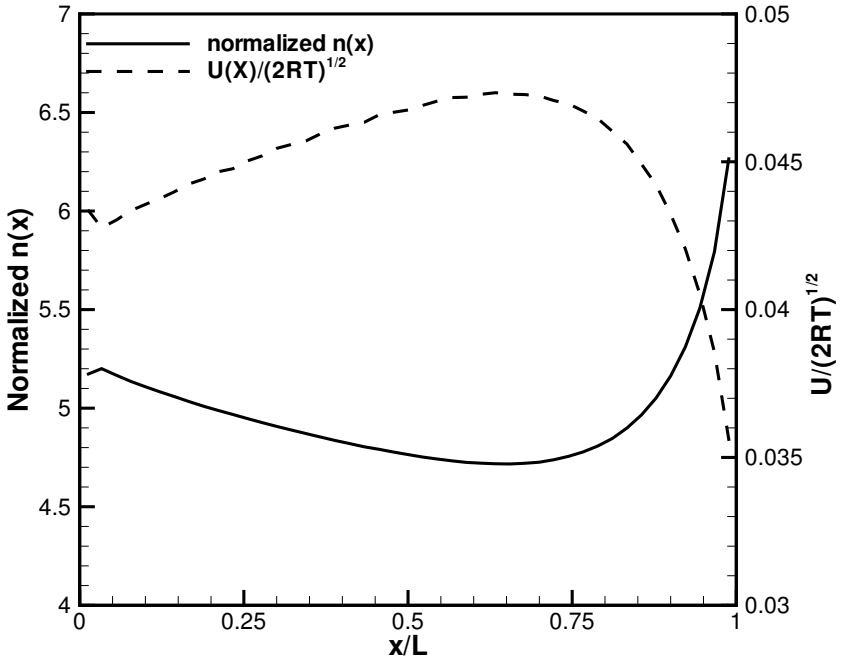

Figure 3.23: 1D Number Density and Velocity Distribution along Chamber Axial Direction(S_p/S_c=0.4, α=0.4, pumps located on the right chamber end).

The density evolution process can be compared with numerical simulations. Figures 3.24 and 3.25 show two comparisons of analytical and numerical simulation results for the cases of L/R=9/3 and L/R=0.9/3 respectively. A common feature in these two pictures is the lower steady state average pressure than the corresponding analytical value. This difference is mainly because the analytical results do not include any collision effects, while in the DSMC simulation results, the collisions between particles and with chamber walls are honestly included. Because the collision effects are always tend to result in a uniform distribution among particles, hence, a lower background pressure is resulted. Several comments can be drawn from these results:

i) The periods required to reach a steady state from the numerical simulation and analytical results are quite close. For all cases, it takes approximately 4 semi-decaying

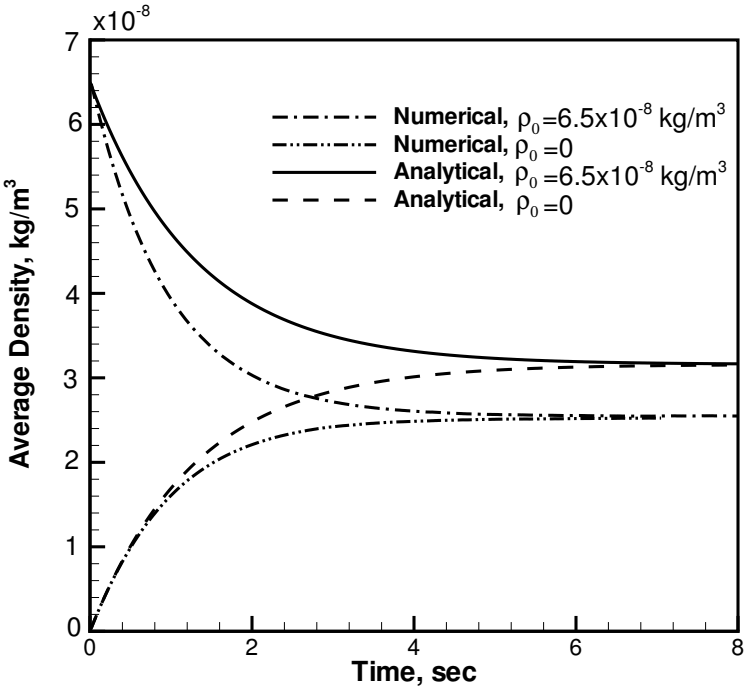

Figure 3.24: Average Density Evolution History(L/R=9/3, S_p/S_c=0.4, α=0.4).

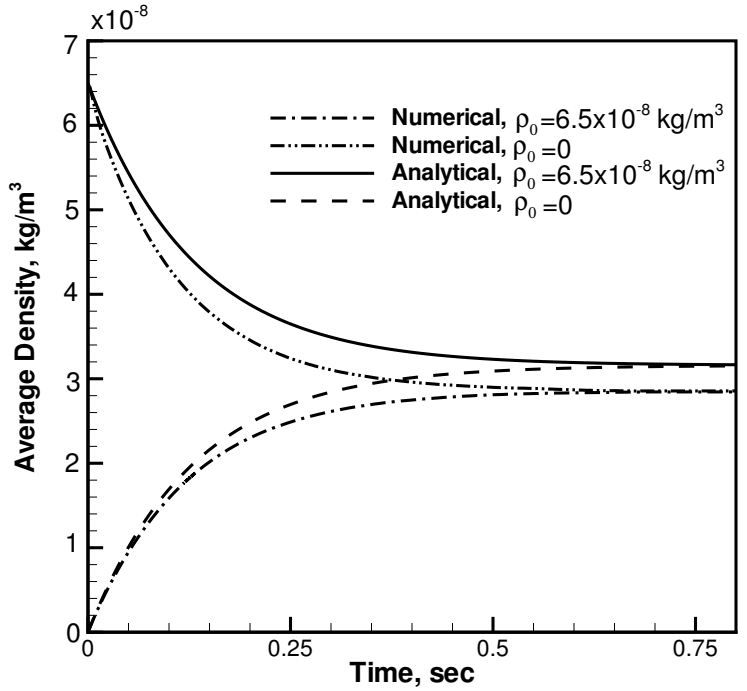

Figure 3.25: Average Density Evolution History(L/R=0.9/3, S_p/S_c=0.4, α=0.4).

periods to reach a steady state. There is some subtle difference between the analytical results and numerical simulation results. The analytical results assume the backpressure is homogenous and there is no preferential direction for gas to enter the chamber; but in the numerical simulations, at time zero, through one chamber end, gas begins to enter the chamber which is initialized by either a uniform background pressure or a vacuum state. Because of this effect, all simulation results include a short startup time which can be estimated as $L/\sqrt{\gamma RT_w} = 9/\sqrt{5/3 \times 8314/131.25 \times 300}$=0.05 sec. However, even with this extra startup time, the numerical simulations converge a little faster than the theoretical results possibly because of collisions among particles and with chamber walls.

ii) For situations that start with a finite initial ambient environment and a vacuum initial ambient environment, the decaying time to reach a steady state is the same.

iii) The long chamber case results in a lower steady state average density for the reason mentioned previously when discussing Figures 3.17 and 3.23.

Comparison of Averaged Density

The pump sticking coefficient has an important effect on the final steady state. Figures 3.26 and 3.27 show the comparison of analytical results from Models 1, 4, 5 and 34 numerical simulations with a varying α, fixed S_p/S_c=0.4 and 0.8, respectively. The number density is normalized by $\dot{m}/(mS_c)\sqrt{2\pi/(RT_w)}$. There are two series of simulation results and two cases of analytical results from Model 5 with χ=0.05 and χ=0.63, corresponding to the situations of L/R=9/3 and L/R=0.9/3. In Figure 3.26, the analytical result from Model 5 with χ=0.05 is equivalent to a horizontal intersection from Figure 3.17. The simulations are divided into two groups of a long chamber wall (L=9 m) and a short chamber wall (L=0.9 m) providing two bounding lines. Because models 1 and 4 do not consider wall effects at all, and all models do

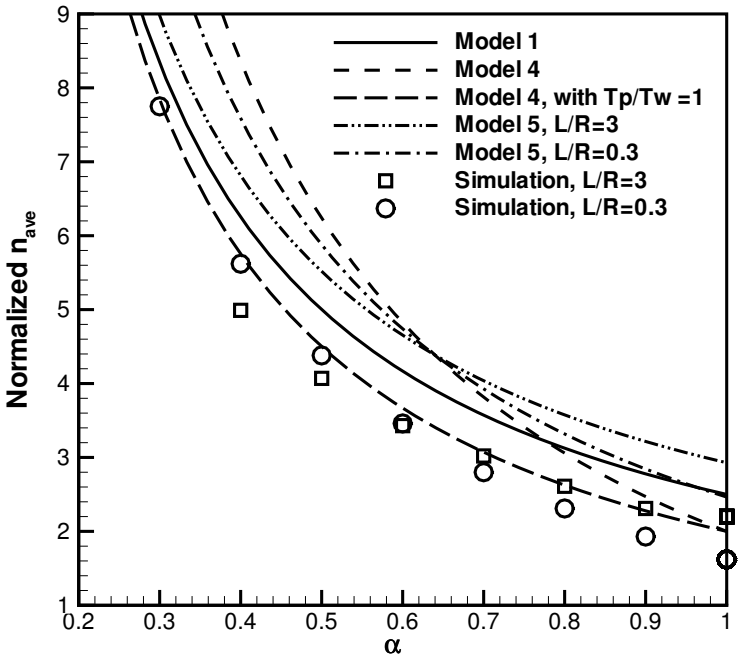

Figure 3.26: Average Density (normalized by $\dot{m}/(mS_c)\sqrt{2\pi/(RT_w)}$, S_p/S_c =0.4).

not include the particle collision effects, the analytical results are less accurate than the numerical simulations. Several observations can be made from these results in Figure 3.26 and 3.27:

i) For fixed S_p/S_c, the difference between analytical results decreases and the analytical results fit the simulations better as α increases;

ii) Two series of numerical simulations yield an intersection point close to α=0.65, which is illustrated in Figure 3.19 as well. Hence, Model 5 has some superiority over the other models by predicting the trends of backpressure with an extra parameter of χ;

iii) The S_p/S_c=0.8 case yields better comparison between the numerical and analytical results than the situation of S_p/S_c=0.4;

iv) Model 4 with T_p/T_w=1 yields the best performance.

The pump area has an important effect on the final steady state as well. Fig-

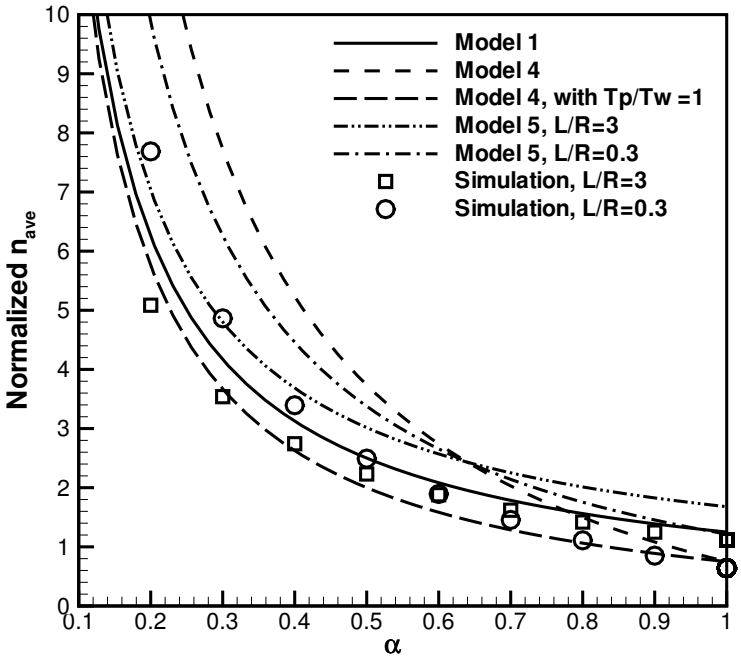

Figure 3.27: Average Density (normalized by $\dot{m}/(mS_c)\sqrt{2\pi/(RT_w)}$, S_p/S_c =0.8).

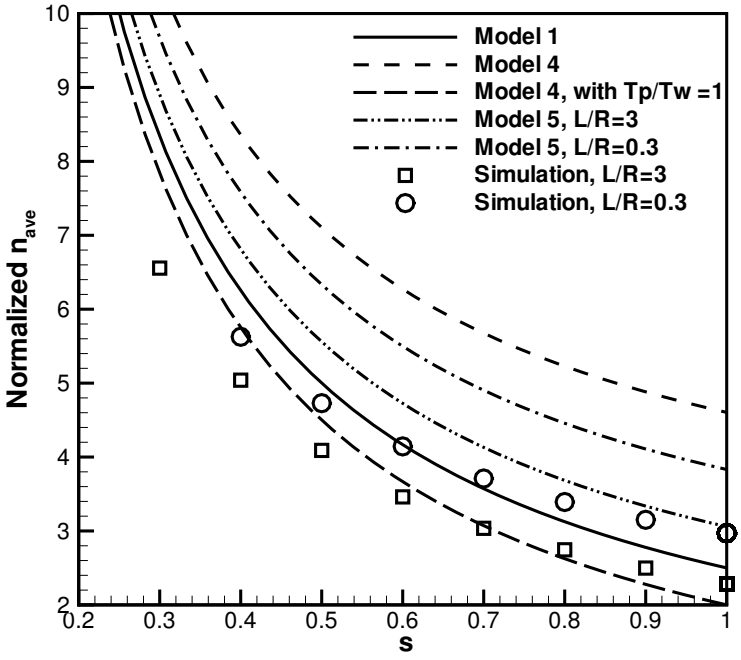

Figure 3.28: Average Density (normalized by $\dot{m}/(mS_c)\sqrt{2\pi/(RT_w)}$, α =0.4).

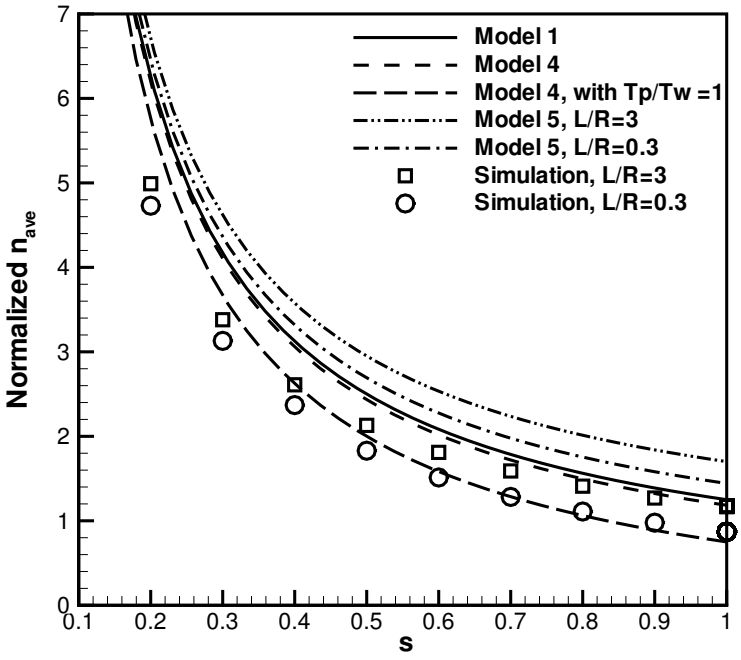

Figure 3.29: Average Density (normalized by $\dot{m}/(mS_c)\sqrt{2\pi/(RT_w)}$, α =0.8).

ures 3.28 and 3.29 show the comparison of analytical results and another 34 simulations with a variation of S_p/S_c, fixed α=0.4 and α=0.8 respectively. In Figure 3.28, the analytical result χ=0.05 from Model 5 with α=0.4 is equivalent to a vertical intersection line in Figure 3.17. From the results in Figures 3.28 and 3.29, it can be observed that:

i) For fixed α, when s increases, the difference among analytical results increases, some analytical results fit the simulation better and the difference between the two series of numerical simulation results is more pronounced;

ii) The two series of numerical simulations do not have a cross point which again is quite consistent with the result shown in Figure 3.17;

iii) The S_p/S_c=0.8 case shows better agreement between analytical results and particle simulations than the situation of S_p/S_c=0.4, the difference among the analytical results decrease, and the performance of Model 4 improves greatly with less

particles reflected from the chamber wall, hence, the S_p/S_c=0.8 case is more comparable to the no-wall assumption for Model 4;

iv) Model 4 with a modification of T_p/T_w=1 has the best performance.

Comparison of Averaged Velocity

Figures 3.30 and 3.31 show the comparison of average velocities for variation of α and fixed S_p/S_c=0.4 and 0.8, respectively. Compared with the average number density, the agreement of average velocity results is more challenging because velocity is a higher order moment of the velocity distribution function. From the results in Figures 3.30 and 3.31, it can be observed that:

i) Models 1 and 4 with T_p/T_w=1 yield the best performance;

ii) The performance of Model 4 improves greatly for S_p/S_c=0.8;

iii) In these two plots, two series of numerical simulations intersect at α=0.65 as indicated in Figure 3.18. Again, Model 5 predicts this intersection point successfully.

Figures 3.32 and 3.33 show the comparison of the average velocity distributions for a variation of S_p/S_c and fixed α=0.4 and 0.8, respectively. It can be observed that:

i) When α=0.4, the long chamber has higher average velocities while for α=0.8 the short chamber has higher average velocities;

ii) Model 1 and Model 4 with T_p/T_w=1 give the best performance;

iii) Model 4 improves significantly with a larger α.

3.5 Effects on Particle Simulations

The analytical results discussed in this chapter have significant effects for particle simulations of plume flows inside a vacuum chamber.

To simulate a rarefied plume flow inside a vacuum chamber, usually the DSMC method is adopted and an axi-symmetric simplification substitutes an expensive

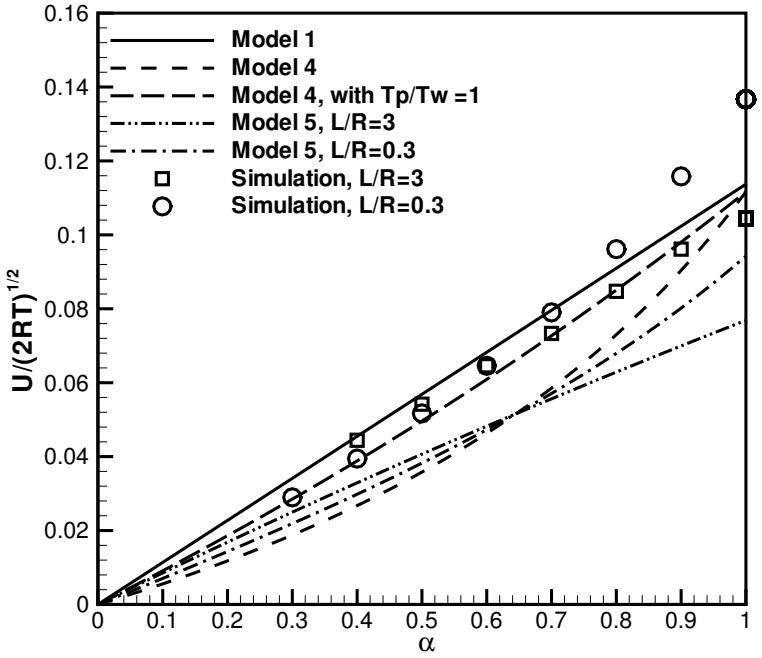

Figure 3.30: Average Velocity Inside Chamber (S_p/S_c=0.4).

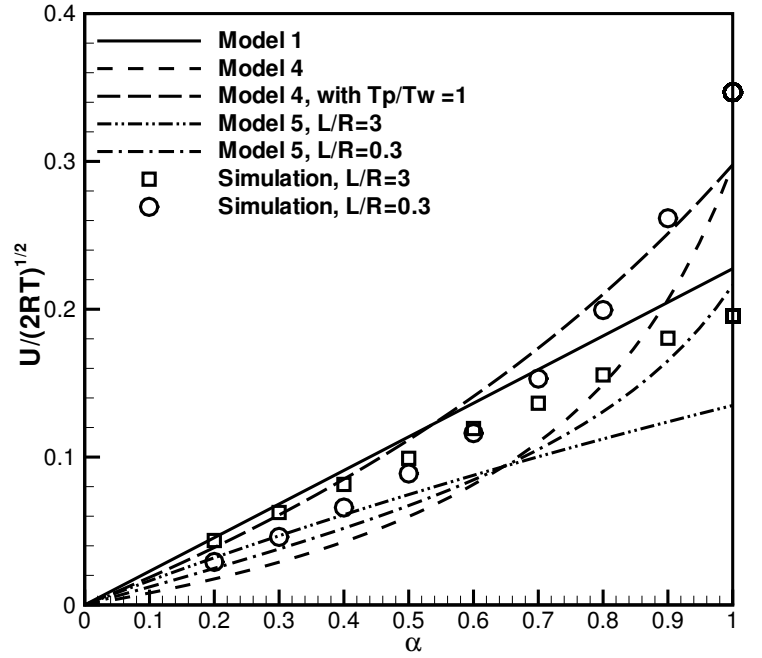

Figure 3.31: Average Velocity Inside Chamber (S_p/S_c=0.8).

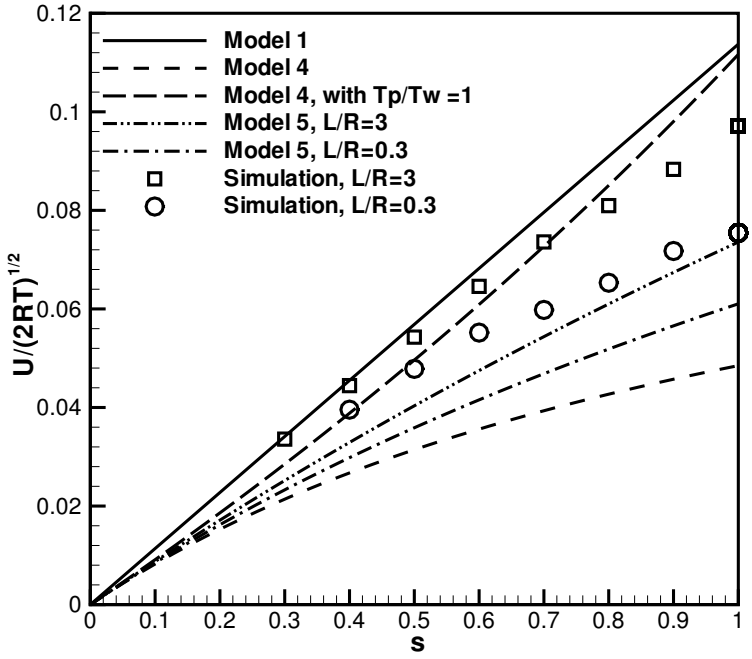

Figure 3.32: Average Velocity Inside Chamber (α=0.4).

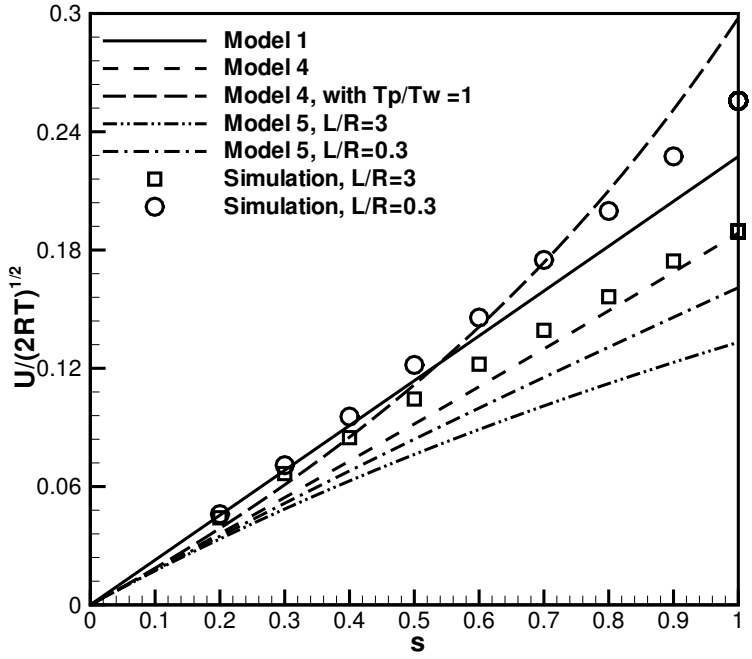

Figure 3.33: Average Velocity Inside Chamber (α=0.8).

full-scale three-dimensional simulation. Traditionally, the background flow effects are either omitted or approximated by a few static background particles in each cell. The velocities of these static background particles are randomly assigned from a zero-centered Maxwellian velocity distribution. However, from the above discussions, it is demonstrated that essentially there are three groups of particles inside a vacuum chamber: two groups diffuse from the chamber end with the vacuum pumps, while the last group diffuses from the other chamber end. The velocities of the background particles are highly affected by various factors. The plasma plume flow inside a vacuum chamber is more like firing a plume flow into another uniform background flow towards the pump. The velocity distribution for the rarefied background flow can be far from a full Maxwellian distribution, the mean velocity of the background flow can be far from zero and can reach $\sqrt{2RT_w/\pi}$, which is over 100 m/s for xenon at room temperature.

The influence on numerical simulations varies with several parameters. For example, in a simulation of electric plumes firing from 4 Hall thrusters inside the LVTF, with a combination of parameters of α=0.39 and s=0.1460 (4 pumps in operation), the average background velocity inside the chamber is only 6.0 m/s and the background number density calculated with formulas for two-sided pumps is only slightly lower than the number density calculated by $n = P_b/(kT_w)$. For this situation, the traditional approximation of background flow by using static particles with velocities sampled from a zero-centered Maxwellian distribution is quite acceptable. However, for other situations where α or s is quite large, the background flow may have a significant effect. Hence, before performing a simplified simulation of gas flow inside a vacuum chamber, it is important to first evaluate the facility parameters and estimate the background flow in the chamber.

To accurately account for the rarefied background flow, there are several options:

1. Represent the backpressure by static background particles, but assign the background particles with velocities sampled from the complete analytical velocity distribution functions obtained in this study.

2. Consider the background flow with inflow boundary conditions. The front and back sides of the simulation domain use different branches of the Maxwellian distributions obtained in this study.

3. Consider the background flow with a general inflow boundary condition for all sides. This approach will need to calculate a new number density, a new mean velocity and a new temperature from the velocity distributions obtained in this study, and reconstruct a new Maxwellian distribution with the above information.

3.6 Conclusions

In this chapter, five free molecular flow models were presented for the rarefied background flow inside vacuum chambers equipped with one-sided or two-sided pumps. Experimental measurements and results from four series of numerical simulations were used to test the validity of these analytical models.

The first model was a crude model with a strong assumption of a constant density distribution inside the vacuum chamber, and led to a set of crude but important relations. This model provided an expression of the semi-decaying period for the unsteady process, and the average background density and velocity fit the numerical simulation results reasonably well of background flows in a vacuum chamber equipped with one-sided pumps.

The second and third models were free molecular flow models that treated the two-sided pump plates as specular and diffusive with selective sticking cold walls. Analyzing the flux and number density relations led to detailed velocity distributions for the background flow, and based on these distributions, the mean velocities and pressures can be computed. With the experimental measurements in [60], the LVTF pump sticking coefficients were calculated. On average the coefficient was close to 0.40, while for different working conditions, the coefficient can vary within a small range. Compared with numerical simulations of specific flows inside the LVTF, the analytical formulas predicted a very similar sticking coefficient.

The fourth and fifth models were free molecular flow models for the background flows inside vacuum chambers equipped with one-sided pumps. Analyzing the flux relations and number density relations led to detailed velocity distributions for the background flow, and based on these distributions, the mean velocities and pressures were obtained. About 70 numerical simulations were performed to test the correctness of the analytical results applicable for chambers equipped with one-sided pumps. Generally, the performance of these analytical models improved greatly as pump area or sticking coefficient increased; Model 4 with T_p/T_w=1 yielded the best performance for average density; Model 4 with T_p/T_w=1 and Model 1 yielded the best performance in predicting the average velocities inside the chamber. Model 5 generally gave relatively poorer performance, although it is the most complete model, with the complex factors of α, χ and s; it predicted the correct trend change for a long chamber and a short chamber; it can create a non-constant distribution between two chamber ends, which is more physically reasonable.

The solutions of these models were five sets of analytical formulas, including comprehensive velocity distribution functions, and the pump sticking coefficient can

be computed with these formulas. These formulas connect different properties from the pumps, the chamber, the propellant and the thruster. These models indicated that the background flow in a chamber was quite different from vacuum, and it cannot be simply treated as a static gas field. The highest speed is over 100 m/s for xenon and the velocity distribution function can deviate far from a Maxwellian distribution. The formulas for the background gas obtained from this study can be used to not only evaluate or predict the performance of a vacuum chamber, but also establish a correct background flow field for numerical simulations.

It is worthy to mention that these models and formulas are applicable to other vacuum chambers with different cross-sections other than cylinders and different applications such as materials processing. The basic principles discussed in the chapter can be used as guidelines to analyze other types of large vacuum chamber with more complicated geometry configurations.

CHAPTER IV

ANALYTICAL FREE MOLECULAR EFFUSION FLOW SOLUTIONS

4.1 Introduction

Free molecular flows passing through small holes are fundamental and important problems in various practical applications. Such applications can be found in materials processing in high vacuum chambers [6], spacecraft design [32], metrology of gas flow [53], and many other applications. Several investigators, such as Liepman [34], Varsigma [39] [41], Willis [61], Rotenone and Weizner [42] have proposed analytical expressions for the mass flow rate near the free-molecular regime in the case of outflow from an orifice into vacuum, which are valid in a very small range of gas rarefaction. Recently, several simulations of rarefied gas flow through a thin orifice [49] were reported.

This study is an initial attempt to analytically investigate the plume flows from electric propulsion systems. Electric propulsion systems, such as Hall thrusters, have several merits over traditional chemical thrusters and they are designed to operate in space for purposes of primary propulsion and on-orbit applications such as station keeping. For electric thrusters, their plume flows are of major interest because of several reasons. First, plume flows can be used to study the performance of a thruster;

second, plume impingement onto a spacecraft can have significant adverse effects. The plume impingement is usually caused by the Charge Exchange(CEX) effect. When a fast ion collides with a slow neutral, an electron may transfer from the slow neutral to the fast ion and results in a fast neutral and a slow ion. Under the electric field effect, this slow ion can drift to large plume angles where sensitive surfaces such as solar cells may be located. Impingement and deposition on such sensitive surfaces may result in eventual failure of the devices. Hence, plume flows are always important research topics for development of electric propulsion thrusters.

Due to its importance, there are many experimental measurements and numerical simulations of plasma plumes of electric thrusters. However, in the literature there are very few reports of analytical studies. Most related previous kinetic work in the literature was concentrated with free molecular flows out of a simplified geometry such as an orifice [39] [41]. Obviously, further analytical results of the plume flow field with more detailed geometries can provide insights and aid in the understanding of the plume flows out of electric thrusters.

There are several fundamental aspects of for a plume flow out of an electric thruster. First, most electric plume flows are free molecular. The mean free path for gas propellant out of a thruster can be estimated with the following hard sphere equation:

$$\lambda = \frac{1}{\sqrt{2}\pi d^2 n_0} \tag{4.1}$$

With a typical number density of $5 \times 10^{18}\ m^{-3}$ at a thruster exit, the mean free path for xenon is $0.268\ m$, which is wider than a typical Hall thruster acceleration channel. Second, the average velocity at a thruster exit plane is greater than zero. The average neutral speed at the thruster exit plane is usually sonic, and the average ion speed is always supersonic due to electric acceleration inside the acceleration

channel. Third, electric field effects in the plume are important for ions. Fourth, collision effects, including elastic collisions and CEX collisions, may have important effects on the plume density and velocity distribution outside the thruster exit.

This study does not intend to provide solutions with considerations of all the above four effects. As an initial effort, by neglecting the electric field and all collision effects, six different free molecular gas flows out of an exit with different geometries are investigated. The exact solutions to the six problems provide first order approximations to cold plume flows, and in a future study, electric field effects and collision effects can be included based on the analytical solutions. Further, in this study, discussions are concentrated on effusion problems with zero exit velocities, which simplifies the situation and provides a solid base for further study.

In the rest of this chapter, section 4.2 presents the problems to be studied and a general solution method; sections 4.3– 4.8 present six free molecular flow problems, their analytical solutions, discussions of their properties or simplifications of the solutions and comparisons with DSMC simulation results; section 4.9 summarizes this chapter.

4.2 Free Molecular Flow Problems and General Treatment

The flows considered in this chapter are six different problems of free molecular gas flows out of an exit into vacuum with a given average speed. The geometry configurations for the exit and the average exit speed are different:

1. A two-dimensional thin slit with a width of $2H$, average exit velocity U_0 is zero.

2. A rectangular slit with a width of $2L$ and a height of $2H$, average exit velocity U_0 is zero.

3. A slit formed by two concentered rectangles with widths and heights $2L$ by $2H$, and $2L_1$ by $2H_1$, average exit velocity U_0 is zero.

4. A circular exit characterized by a radius of R, average exit velocity U_0 is zero.

5. An annulus characterized by an inner radius R_1 and an outer radius R_2, average exit velocity U_0 is zero.

6. A two-dimensional thin slit with a width of $2H$, average exit velocity U_0 is greater than zero.

Suppose the gas at the exit is in equilibrium with a uniform static temperature T_0 and a uniform number density n_0. Denote the plume direction as the x-axis direction, the direction normal to the x-axis as the y-axis direction, and the middle point of the slit/circle center/annulus center is the origin. The objective of this study is to obtain the analytical plume field flow solutions, especially the number density and velocities at any point downstream of the exit.

4.2.1 General Methods

For a dilute gas flow at rest in equilibrium, the velocity distribution is described as a full Maxwellian distribution [12] [27] [56]. With a total number density n and a temperature T_0 the velocity distribution function at any point is:

$$f(u,v,w) = \left(\frac{\beta}{\pi}\right)^{3/2} \exp(-\beta(u^2+v^2+w^2)) \tag{4.2}$$

where $\beta = \frac{1}{2RT_0}$. The highest velocity probability occurs at phase point $(u,v,w) = (0,0,0)$. For a velocity with a nonzero average value of U_0 along the X direction but a zero average value along the Y and Z directions, the distribution Equation (4.2) is shifted along the u-axis by a value of U_0.

With a known velocity distribution $f(u,v,w)$ at a point (X,Y,Z), the average number density normalized by a reference value and velocities at (X,Y,Z) can be evaluated using the velocity distribution function:

$$n(X,Y,Z) = \int_{\Omega} f(u,v,w)dudvdw \tag{4.3}$$

$$U(X,Y,Z) = \frac{1}{n(X,Y,Z)} \int_{\Omega} uf(u,v,w)dudvdw \tag{4.4}$$

$$V(X,Y,Z) = \frac{1}{n(X,Y,Z)} \int_{\Omega} vf(u,v,w)dudvdw \tag{4.5}$$

$$W(X,Y,Z) = \frac{1}{n(X,Y,Z)} \int_{\Omega} wf(u,v,w)dudvdw \tag{4.6}$$

Hence, the critical step is to obtain the velocity distribution function and the integral domain.

During investigating the free molecular flowfield before an orifice exit, [39] observed an important fact when studying a free molecular flow of gas escaping from an orifice:

Observation: For any point (X,Y,Z) in front of the slit, its velocity space can only have non-zero velocity within a specific solid angle Ω subtended by the specific point and exit edges:

$$f(u,v,w) = \begin{cases} \left(\frac{\beta}{\pi}\right)^{3/2} \exp(-\beta(u^2+v^2+w^2)), & u,v,w \in \Omega; \\ 0, & u,v,w \notin \Omega. \end{cases} \tag{4.7}$$

where $\beta = \frac{1}{2RT_0}$ and Ω represents the integral domain in the velocity space.

This observation can be viewed as a velocity-positions relation, which is important to this study: From a given point on the exit, only particles with specific velocity components can arrive at a specific point (X,Y,Z) in front of the exit. This relation takes different forms in the six cases and will be illustrated later as Equations (4.8), (4.18), (4.39) and (4.57). These equations actually have three effects:

First they guarantee a one-to-one mapping relation between velocity phases and provide a complete support to Equation (4.7); Second, they can provide boundaries for the integral domain; Third, they may simplify the integral process by changing velocity integral variables to geometry parameters of the exit.

In this study, many integral formulas are used, and some of them can be found in mathematical handbooks while some of them need careful derivations. For convenience, the integral formulas are summarized as Appendix B at the end of this dissertation.

4.3 Problem One: Free Molecular Effusion Flow from a Thin Slit with a Zero Average Velocity (U_0=0)

4.3.1 Analytical Results

In this case, the previous velocity-positions relation takes the following format: from a point $(0, h)$ on the slit, particles can reach the point (X, Y) if their two velocity components (u, v) satisfy the following relations:

$$\tan(\theta) = \frac{Y - h}{X} = \frac{v}{u}, -H < h < H \tag{4.8}$$

On the other hand, particles from point $(0, h)$ cannot arrive at the point (X, Y) if their two velocity components do not satisfy the above relation. Hence, a correct velocity component relation is the necessary and sufficient condition that a particle can travel from a point on the exit to a specific point in front of the exit. This important relation shows that there is a one to one mapping relation between velocity space for the point on the slit and the velocity space of the point (X, Y). A slice of the velocity space for point $(0, h)$ is strictly mapped onto the velocity space of point (X, Y). There is neither loss nor gain during the mapping. Figure 4.1 illustrates the velocity spaces for two points in front of the exit. One point is outside the plume

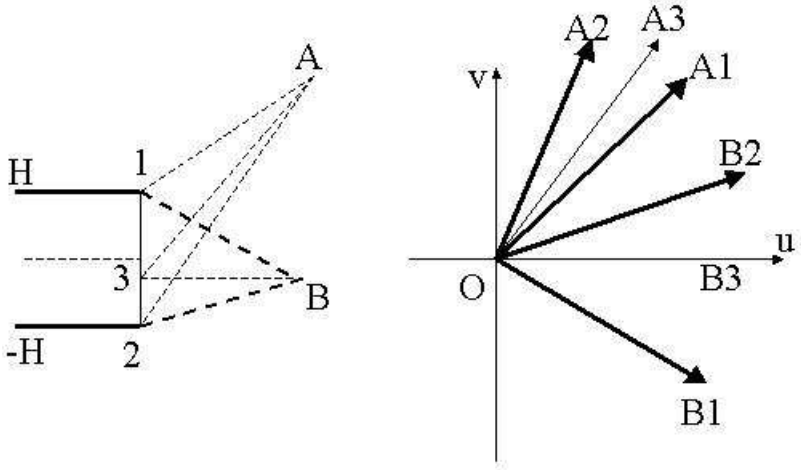

Figure 4.1: Velocity Spaces for Points Inside or Outside Plume Core.

core region, while the other one is inside the plume core. Velocity space "A1-O-A2" represents the first point's integral domain while "B1-O-B2" represents the second point's integral domain. Line O-A3 represents the velocity contributed by particles starting from point 3, while the particle starting at point 3 can arrive at point B is represented by the positive x-axis.

The non-zero values in the velocity space of point (X, Y) form a pie shape bounded by two lines from the slit edge points to the point (X, Y), and the number density and velocities at the point (X, Y) can be obtained by integrating the probability distribution function within the two lines:

$$\tan(\theta_1) = \frac{Y - H}{X} \tag{4.9}$$

$$\tan(\theta_2) = \frac{Y + H}{X} \tag{4.10}$$

With this simple integral domain in the velocity phase space, the integrals can

be simplified with the following relation:

$$dudv = \overline{V} d\overline{V} d\theta \tag{4.11}$$

where $\overline{V} = \sqrt{u^2 + v^2}$.

With this relation, the expressions for the number density and the velocities at point (X, Y) are:

$$n(X,Y) = \int_\Omega \frac{\beta}{\pi} \exp(-\beta(u^2+v^2)) dudv = \frac{\theta_2 - \theta_1}{2\pi} \tag{4.12}$$

$$\frac{U(X,Y)}{\sqrt{2RT_0}} = \frac{\sqrt{\pi}(\sin\theta_2 - \sin\theta_1)}{2(\theta_2 - \theta_1)} \tag{4.13}$$

$$\frac{V(X,Y)}{\sqrt{2RT_0}} = \frac{\sqrt{\pi}(\cos\theta_1 - \cos\theta_2)}{2(\theta_2 - \theta_1)} \tag{4.14}$$

From the above results, it is informative to obtain the exact solutions of properties along the centerline, which is important to many applications. Along the centerline $Y = 0$, where $\theta_1 = -\theta_2$:

$$n(X,0) = \frac{1}{\pi} \arctan(\frac{H}{X}) \tag{4.15}$$

$$\frac{U(X,0)}{\sqrt{2RT_0}} = \frac{\sqrt{\pi}\sin(\arctan(H/X))}{2\arctan(H/X)} \tag{4.16}$$

$$V(X,0) = 0 \tag{4.17}$$

When X increases from 0 to infinity, the number density decreases from $\frac{1}{2}$ to 0 and the speed ratio increases from $\frac{1}{\sqrt{\pi}}$ to $\frac{\sqrt{\pi}}{2}$. It should be pointed out that this speed ratio is obtained by a thermal speed characterized by the temperature at the slit, not the local temperature.

Several properties of (4.12)– (4.14) are:

1. Flow symmetries are preserved: $n(X,-Y) = n(X,Y)$, $U(X,-Y) = U(X,Y)$, $V(X,-Y) = -V(X,Y)$.

2. On the slit where $X = 0$, $-H < Y < H$: $-\theta_1 = \theta_2 = \frac{\pi}{2}$, $n(0, Y) = \frac{1}{2}$, $V(0, Y) = 0$, $U(0, Y) = \sqrt{2RT_0/\pi}$. The nonzero velocity along the X direction does not contradict the zero mean velocity distribution boundary condition at the slit.

3. On locations above the slit: $X = 0, X > H$: $\theta_1 = \theta_2 = \frac{\pi}{2}$, the following relations hold: $n(0, Y) = 0$, $V(0, Y) = 0$, $U(0, Y) = 0$. Hence, the two edge-points are discontinuity points because of abrupt changes of number density.

4. The mass flux relation through the slit: $n(0, Y) = \frac{1}{2}$ and $U(0, Y) = \sqrt{2RT_0/\pi}$ for $-H < Y < H$, $-\theta_1 = \theta_2 = \frac{\pi}{2}$, hence the mass flow rate out of the slit $= \frac{1}{4} m n_0 \sqrt{8RT_0/\pi}$, which is a well-known kinetic flow result.

5. At the exit tip point: $n(0, H) = \frac{1}{4} = \frac{1}{2} n(0, 0), U(0, H) = V(0, H) = \sqrt{2RT_0/\pi} = U(0, 0)$. Obviously, number density and velocities along the vertical line passing the exit tip are not continuous.

6. Depending on the distance from point (X, Y) to the origin, the flow field can be classified into four regions: near field and inside core region, near field and outside core region, far field inside core region and far field outside core region. The last region is the largest where the slit effects are quite minor, and the velocities in this region have a relation $U(X, Y)/V(X, Y) \propto /(\theta_1 + \theta_2) \approx 1/\alpha$, where α is the angle subtended from the point to the two exit edge points. This relation indicates that the streamlines in that region are almost straight.

4.3.2 DSMC Simulation and Discussions

The above set of analytical solutions is validated by comparisons with a numerical simulation. Because the flows are free molecular, the DSMC method [12] is ideal to

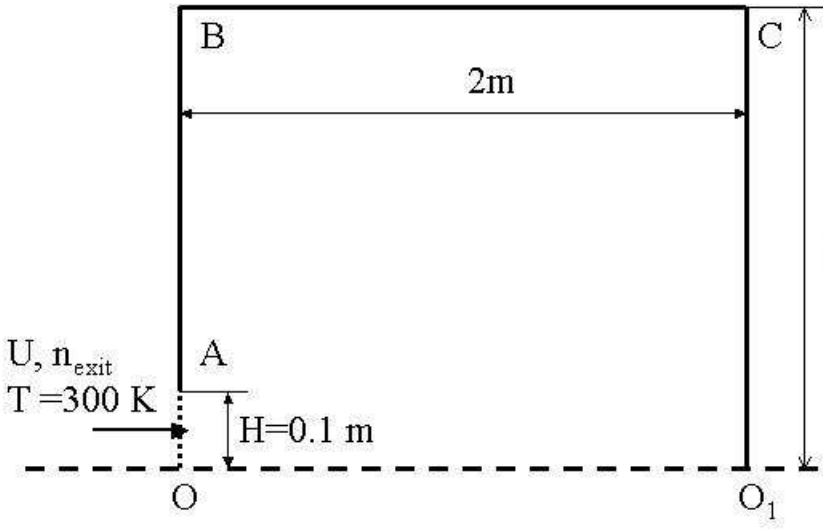

Figure 4.2: Numerical Simulation Domain For Cases 1 and 5 (not in scale).

provide accurate solutions. In the simulation, gaseous xenon flows out of a slit with a semi-height $H = 0.1$ m. In the simulation, the number density at the slit is set to a value corresponding to $Kn = 20$ with a characteristic length $2H$=0.2 m. To compare with the analytical results, all DSMC simulations in this chapter are performed with no collisions.

The simulation domain used for this case is a square with a side length of 2 meters. As illustrated by Figure 4.2, there are three kinds of boundary conditions in these simulations. OO_1 is a symmetric boundary condition; OA is an inlet boundary condition where particles are introduced into the simulation and their thermal velocities are characterized by a temperature T=300 K; Sides $AB - BC - CO_1$ are outlet boundary conditions and when particles cross on these sides, they are removed from the simulation.

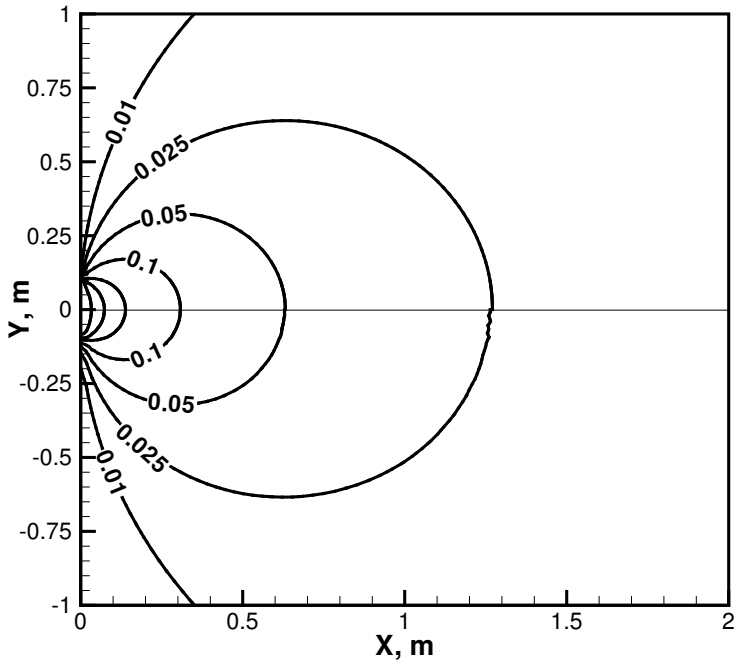

Figure 4.3: Case 1: Contours of Number Density (U_0=0, Top: Analytical, Bottom: DSMC without Collisions).

A mesh of 75 by 60 cells along the X-axis and Y-axis directions is adopted. In this study, collisions are omitted. The main reason for adopting such a dense mesh is to provide high spatial resolution for comparison with analytical results.

MONACO [23] is used to perform this simulation and approximately one million particles are employed in the final sampling stage. The simulation takes approximately 30 hours on a parallel machine with two processors.

Figure 4.3 shows a comparison of number density contours obtained with the analytical results and a DSMC simulation. The average exit velocity U_0 is set to zero. Figures 4.4 and 4.5 show two comparisons of velocity contours along the X and Y directions. The comparison indicates that for this true effusion problem these results are almost identical. Both theoretical and numerical results indicate that there is an exit effect dominating the area close to the exit, while in the far field,

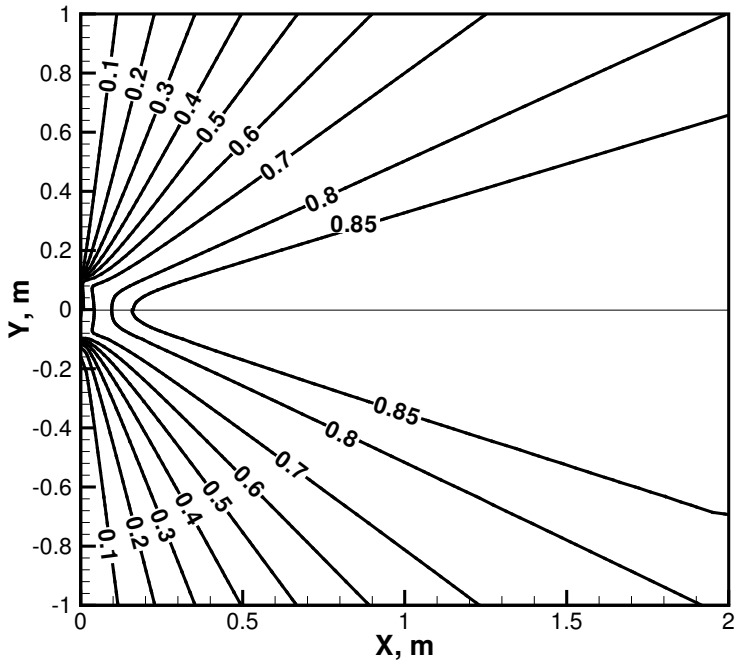

Figure 4.4: Case 1: Contours of $\frac{U(X,Y)}{\sqrt{2RT_0}}$ (U_0=0, Top: Analytical, Bottom: DSMC without Collisions).

the velocity contours are essentially straight lines. Notice that in Equations (4.13) and (4.14), the denominator is zero along the vertical line $X = 0, Y > H$, hence it is a singularity line. The accumulation of contour lines along this singularity line, shown in the analytical contour results of V, is not physical.

Figure 4.6 shows comparisons between analytical results and simulation results of velocity and number density distributions along lines Y=0 and $Y = H$. It clearly confirms the previous discussion that the velocity at the slit center and the tip point are the same but the number density at the tip point is only half of the value at the slit center.

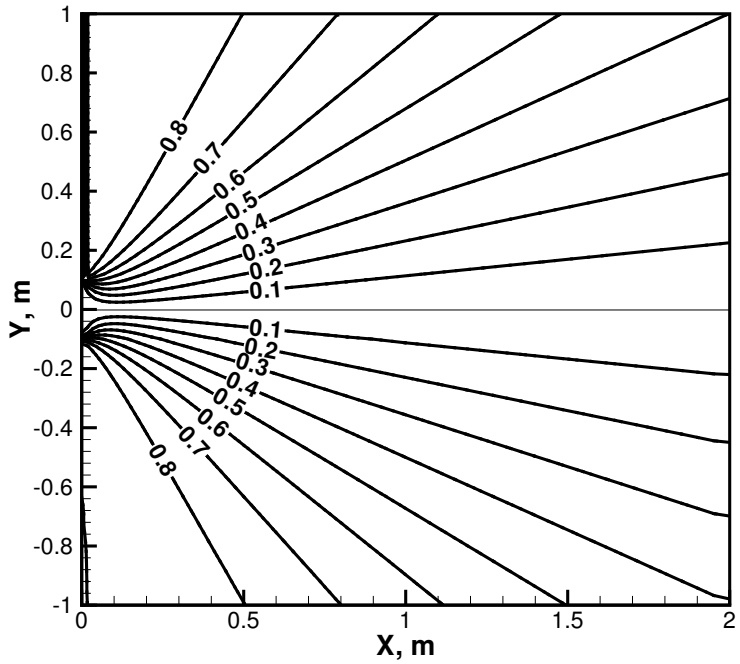

Figure 4.5: Case 1: Contours of $\frac{V(X,Y)}{\sqrt{2RT_0}}$ (U_0=0, Top: Analytical, Bottom: DSMC without Collisions).

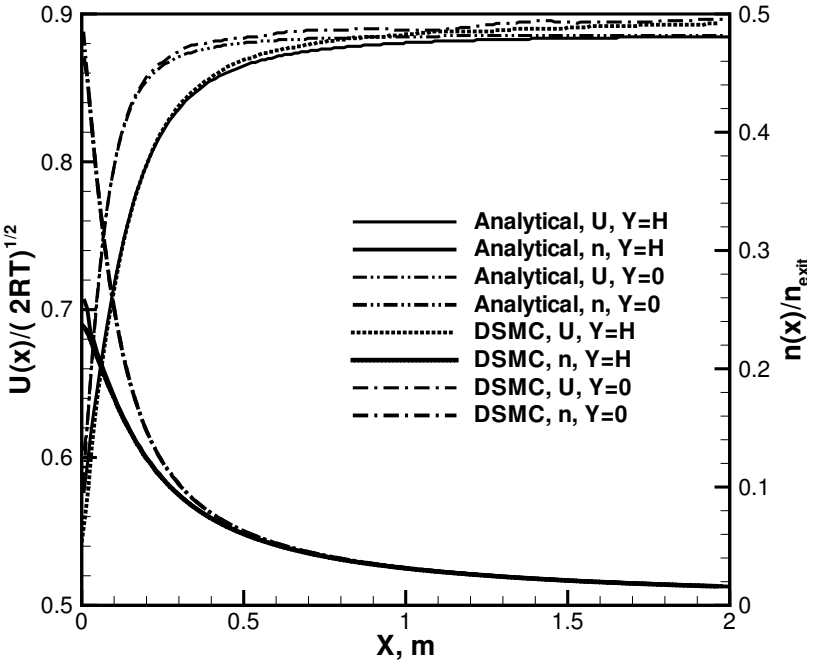

Figure 4.6: Case 1: Number Density and $\frac{U(X,Y)}{\sqrt{2RT_0}}$ Along Y=0 and $Y = H(U_0$=0).

4.4 Problem Two: Free Molecular Effusion Flow From a Rectangular Exit 2H by 2L with a Zero Average Exit Velocity(U_0=0)

4.4.1 Analytical Results

Suppose there is a rectangular exit, which is characterized by a width of $2L$ and a height of $2H$, and the average exit velocity is zero. Suppose there is a point (X, Y, Z) in front of the exit, where $Y > 0$ and $Z > 0$, then from any point $(0, y, z)$ on the exit, particles can only arrive at point (X, Y, Z) if their velocity components follow the relation:

$$\frac{X}{u} = \frac{Y - y}{v} = \frac{Z - z}{w} \tag{4.18}$$

where $X > 0, Y > 0, Z > 0$.

From this relation, the number density and velocity integrals can be greatly simplified with the following change of integral variables:

$$dvdw = \begin{vmatrix} \frac{\partial v}{\partial y} & \frac{\partial v}{\partial z} \\ \frac{\partial w}{\partial y} & \frac{\partial w}{\partial z} \end{vmatrix} dydz = \begin{vmatrix} \frac{-u}{X} & 0 \\ 0 & \frac{-u}{X} \end{vmatrix} dydz = \frac{u^2}{X^2} dydz \tag{4.19}$$

Obviously with this relation, the rectangle edges define an integral domain and the number density and the velocity components can be derived. The integral processes are lengthy and can be found in Appendix C. The final number density result is:

$$\begin{aligned} n(X, Y, Z) = \ & \frac{1}{4\pi} \Bigg[\arctan \frac{(L-Y)(H-Z)}{X\sqrt{X^2+(L-Y)^2+(H-Z)^2}} + \arctan \frac{(L-Y)(H+Z)}{X\sqrt{X^2+(L-Y)^2+(H+Z)^2}} \\ & + \arctan \frac{(L+Y)(H-Z)}{X\sqrt{X^2+(L+Y)^2+(H-Z)^2}} + \arctan \frac{(L+Y)(H+Z)}{X\sqrt{X^2+(L+Y)^2+(H+Z)^2}} \Bigg] \end{aligned} \tag{4.20}$$

The velocities along the X, Y, Z directions are:

$$\begin{aligned}\frac{U(X,Y,Z)}{\sqrt{2RT_0}} = \quad & \frac{1}{4n\pi\sqrt{\pi}}\Bigg[\frac{H-Z}{\sqrt{(H-Z)^2+X^2}}(\arctan\frac{L-Y}{\sqrt{(H-Z)^2+X^2}}+\arctan\frac{L+Y}{\sqrt{(H-Z)^2+X^2}}) \\ & +\frac{H+Z}{\sqrt{(H+Z)^2+X^2}}(\arctan\frac{L-Y}{\sqrt{(H+Z)^2+X^2}}+\arctan\frac{L+Y}{\sqrt{(H+Z)^2+X^2}}) \\ & +\frac{L-Y}{\sqrt{(L-Y)^2+X^2}}(\arctan\frac{H-Z}{\sqrt{(L-Y)^2+X^2}}+\arctan\frac{H+Z}{\sqrt{(L-Y)^2+X^2}}) \\ & +\frac{L+Y}{\sqrt{(L+Y)^2+X^2}}(\arctan\frac{H-Z}{\sqrt{(L+Y)^2+X^2}}+\arctan\frac{H+Z}{\sqrt{(L+Y)^2+X^2}})\Bigg]\end{aligned} \tag{4.21}$$

$$\begin{aligned}\frac{V(X,Y,Z)}{\sqrt{2RT_0}} = \quad & \frac{X}{4n\pi\sqrt{\pi}}\Bigg[\frac{1}{\sqrt{(L-Y)^2+X^2}}(\arctan\frac{H-Z}{\sqrt{(L-Y)^2+X^2}}+\arctan\frac{H+Z}{\sqrt{(L-Y)^2+X^2}}) \\ & -\frac{1}{\sqrt{(L+Y)^2+X^2}}(\arctan\frac{H-Z}{\sqrt{(L+Y)^2+X^2}}+\arctan\frac{H+Z}{\sqrt{(L+Y)^2+X^2}})\Bigg]\end{aligned} \tag{4.22}$$

$$\begin{aligned}\frac{W(X,Y,Z)}{\sqrt{2RT_0}} = \quad & \frac{X}{4n\pi\sqrt{\pi}}\Bigg[\frac{1}{\sqrt{(H-Z)^2+X^2}}(\arctan\frac{L-Y}{\sqrt{(H-Z)^2+X^2}}+\arctan\frac{L+Y}{\sqrt{(H-Z)^2+X^2}}) \\ & -\frac{1}{\sqrt{(H+Z)^2+X^2}}(\arctan\frac{L-Y}{\sqrt{(H+Z)^2+X^2}}+\arctan\frac{L+Y}{\sqrt{(H+Z)^2+X^2}})\Bigg]\end{aligned} \tag{4.23}$$

Note that symmetry is sustained in the above solutions. Suppose $X > 0, Y > 0$ and $Z > 0$:

$$n(X,Y,Z) = n(X,-Y,Z) = n(X,Y,-Z) = n(X,-Y,-Z) > 0$$

$$U(X,Y,Z) = U(X,-Y,Z) = U(X,Y,-Z) = U(X,-Y,-Z) > 0$$

$$V(X,Y,Z) = -V(X,-Y,Z) = V(X,Y,-Z) = -V(X,-Y,-Z) > 0$$

$$W(X,Y,Z) = -W(X,Y,-Z) = W(X,-Y,Z) = -W(-X,-Y,-Z) > 0$$

Along the exit centerline where $Y = Z = 0$:

$$n(X,0,0) = \frac{1}{\pi}\arctan\frac{HL}{X\sqrt{X^2+H^2+L^2}} \tag{4.24}$$

$$\frac{U(X,0,0)}{\sqrt{2RT_0}} = \frac{1}{n\pi\sqrt{\pi}}\left[\frac{H}{\sqrt{H^2+X^2}}\arctan\frac{L}{\sqrt{X^2+H^2}}+\frac{L}{\sqrt{X^2+L^2}}\arctan\frac{H}{\sqrt{X^2+L^2}}\right] \tag{4.25}$$

$$V(X,0,0) = W(X,0,0) = 0 \tag{4.26}$$

These centerline results contain H and L, and are quite different from the standard results of free molecular flow through a small circular orifice. When X changes from 0 to ∞, n changes from $\frac{1}{2}$ to 0, while $U(0,0,0) = \frac{1}{\sqrt{\pi}}$ with $H = L$.

Another two interesting locations are the rectangle corner and an edge midpoint:

$$n(X,L,H) = \frac{1}{4\pi}\arctan\left(\frac{4HL}{X\sqrt{X^2+4L^2+4H^2}}\right) \tag{4.27}$$

$$\begin{aligned}\tfrac{U(X,L,H)}{\sqrt{2RT_0}} = \;& \tfrac{1}{2n\sqrt{\pi}^3}\left[\tfrac{H}{\sqrt{4H^2+X^2}}\arctan\tfrac{2L}{\sqrt{4H^2+X^2}}\right.\\ & \left.+\tfrac{L}{\sqrt{4L^2+X^2}}\arctan\tfrac{2H}{\sqrt{4L^2+X^2}}\right]\end{aligned} \tag{4.28}$$

$$n(X,0,H) = \frac{1}{2\pi}\arctan\frac{2HL}{X\sqrt{X^2+L^2+4H^2}} \tag{4.29}$$

$$\begin{aligned}\tfrac{U(X,0,H)}{\sqrt{2RT_0}} = \;& \tfrac{1}{2n\sqrt{\pi}^3}\left(\tfrac{2H}{\sqrt{4H^2+X^2}}\arctan\tfrac{L}{\sqrt{4H^2+X^2}}\right.\\ & \left.+\tfrac{L}{\sqrt{L^2+X^2}}\arctan\tfrac{2H}{\sqrt{L^2+X^2}}\right)\end{aligned} \tag{4.30}$$

$$n(X,L,0) = \frac{1}{2\pi}\arctan\frac{2HL}{X\sqrt{X^2+4L^2+H^2}} \tag{4.31}$$

$$\begin{aligned}\tfrac{U(X,L,0)}{\sqrt{2RT_0}} = \;& \tfrac{1}{2n\sqrt{\pi}^3}\left(\tfrac{H}{\sqrt{H^2+X^2}}\arctan\tfrac{2L}{\sqrt{H^2+X^2}}\right.\\ & \left.+\tfrac{2L}{\sqrt{4L^2+X^2}}\arctan\tfrac{H}{\sqrt{4L^2+X^2}}\right)\end{aligned} \tag{4.32}$$

Immediately, it can be shown that on the exit center and exit tip: $n(0,L,H) = \frac{1}{4}n(0,0,0) = \frac{1}{2}n(0,0,H)$ and $U(0,L,H) = U(0,0,0)$ if $H = L$.

4.4.2 DSMC Simulations and Discussions

A three-dimensional DSMC simulation is performed to simulate the effusion flow from a rectangular exit with $2L = 2\times0.2$ m by $2H = 2\times0.2$ m. Due to the symmetry in the geometry configuration, only a quarter of the exit is included in the simulation

domain. The simulation domain is a cubic shape with side length of 1 meter. A mesh containing about 0.5 million tetrahedral cells is used to represent the whole domain, and in the final sampling state, about 6 million particles are maintained. Again, the collision function in MONACO is turned off.

Figure 4.7 shows the number density contours in the plane Y=0, the solid contours are the analytical results obtained in this study while the dashed contours are the DSMC results. At the exit, both the analytical and DSMC results yield the same value of $\frac{1}{2}$. Figures 4.8 and 4.9 show contours of $U(X, 0, Z)$ and $W(X, 0, Z)$ in the plane Y=0. In general, both comparisons are quite satisfactory. In all of these results, the exit effects are well captured. This is the only three-dimensional simulation in the six problems discussed in this chapter, and the simulation cost is quite expensive. The comparison can be further improved by a larger scale of sampling. The contours of number density and velocities in the plane $Z = 0$ have similar patterns so they are omitted here.

In addition to the contours, comparisons along the X direction can provide more informative results. Figure 4.10 shows profiles along one horizontal line passing through the exit corner ($Y = L$, $Z = H$). In general, the number density distribution fits better, while the velocities yield larger discrepancies. It is also noted that the number density at X=0 is close to $\frac{1}{8}$ instead of $\frac{1}{2}$ as predicted by Equation (4.27). This is physically correct, because any point inside the domain has a full neighborhood of 2π, but on the corner, only $\frac{\pi}{2}$ is available. It is expected that the points on an edge but not on a corner will have a density value of $\frac{1}{4}$. Correspondingly, from Equation (4.27), it is possible to prove that the corner point velocity in the X direction has the same value as that for the exit center point.

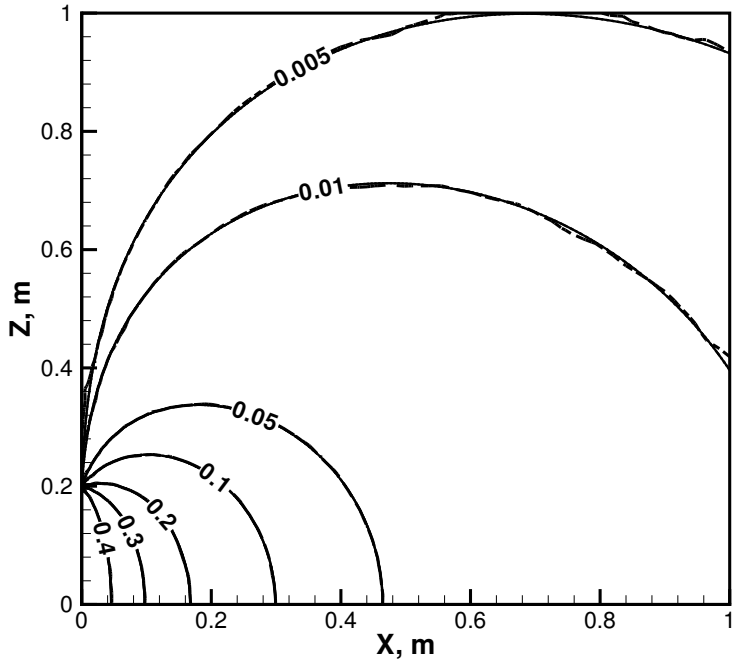

Figure 4.7: Case 2: Contours of Number Density (U_0=0, Solid: Analytical, Dashed: DSMC without Collisions).

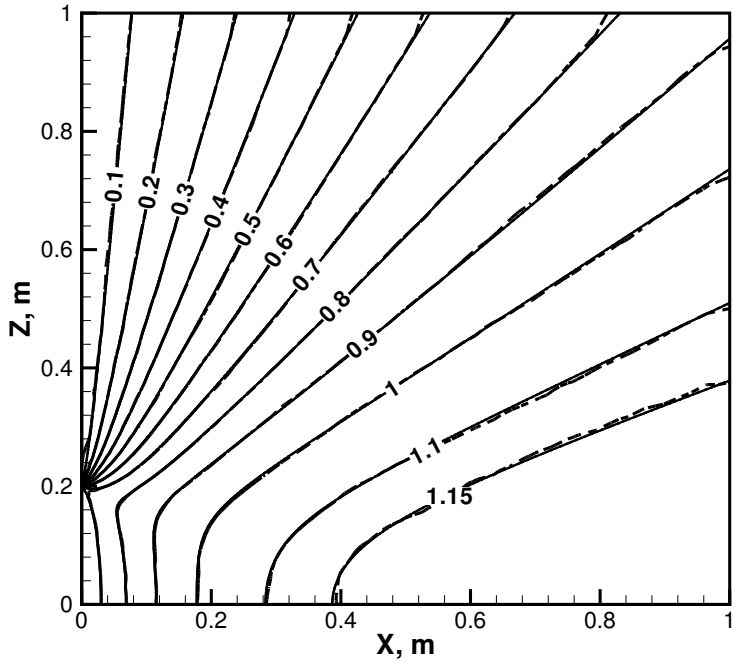

Figure 4.8: Case 2: Contours of $\frac{U(X,0,Z)}{\sqrt{2RT_0}}$ (U_0=0, Solid: Analytical, Dashed: DSMC without Collisions).

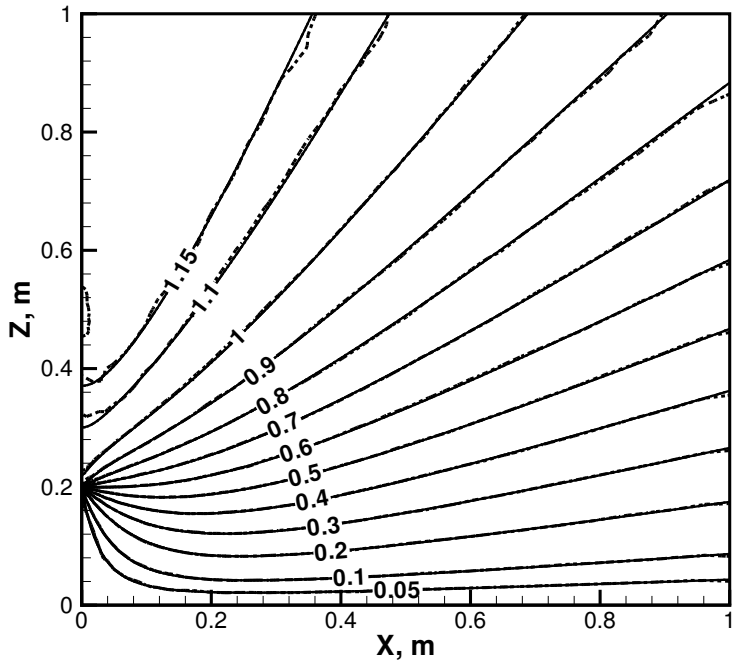

Figure 4.9: Case 2: Contours of $\frac{W(X,0,Z)}{\sqrt{2RT_0}}$ (U_0=0, Solid: Analytical, Dashed: DSMC without Collisions).

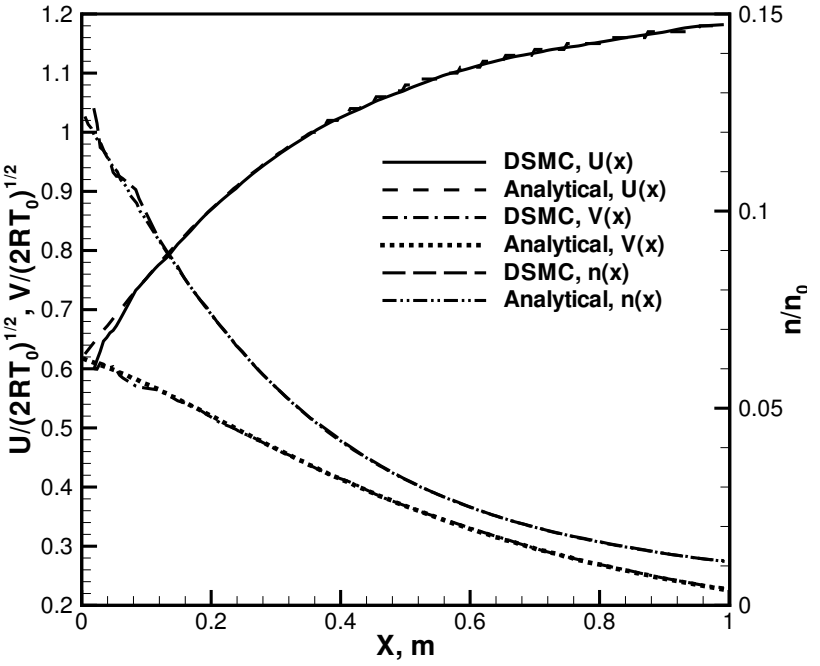

Figure 4.10: Case 2: Profiles of $\frac{U(X,L,H)}{\sqrt{2RT_0}}$ and $n(X, L, H)$ (U_0=0).

4.5 Problem Three: Free Molecular Effusion Flow From a Concentered Rectangular Exit 2H by 2L and $2H_1$ by $2L_1$, with a Zero Average Exit Velocity(U_0=0)

4.5.1 Analytical Results

The solutions to this problem can be obtained from the previous solutions using the fact that free molecular flow out of a concentered rectangular exit is equivalent to a large rectangular source minus a smaller rectangular sink. The final number density result is:

$$\begin{aligned} n(X,Y,Z) = \; & \frac{1}{4\pi}\Bigg[\arctan\frac{(L-Y)(H-Z)}{X\sqrt{X^2+(L-Y)^2+(H-Z)^2}} + \arctan\frac{(L-Y)(H+Z)}{X\sqrt{X^2+(L-Y)^2+(H+Z)^2}} \\ & + \arctan\frac{(L+Y)(H-Z)}{X\sqrt{X^2+(L+Y)^2+(H-Z)^2}} + \arctan\frac{(L+Y)(H+Z)}{X\sqrt{X^2+(L+Y)^2+(H+Z)^2}} \\ & - \arctan\frac{(L_1-Y)(H_1-Z)}{X\sqrt{X^2+(L_1-Y)^2+(H_1-Z)^2}} - \arctan\frac{(L_1-Y)(H_1+Z)}{X\sqrt{X^2+(L_1-Y)^2+(H_1+Z)^2}} \\ & - \arctan\frac{(L_1+Y)(H_1-Z)}{X\sqrt{X^2+(L_1+Y)^2+(H_1-Z)^2}} - \arctan\frac{(L_1+Y)(H_1+Z)}{X\sqrt{X^2+(L_1+Y)^2+(H_1+Z)^2}}\Bigg] \end{aligned} \tag{4.33}$$

The velocities along the X, Y, Z directions are:

$$\begin{aligned} \frac{U(X,Y,Z)}{\sqrt{2RT_0}} = \; & \frac{1}{4n\pi\sqrt{\pi}}\Bigg[\frac{H-Z}{\sqrt{(H-Z)^2+X^2}}\left(\arctan\frac{L-Y}{\sqrt{(H-Z)^2+X^2}} + \arctan\frac{L+Y}{\sqrt{(H-Z)^2+X^2}}\right) \\ & + \frac{H+Z}{\sqrt{(H+Z)^2+X^2}}\left(\arctan\frac{L-Y}{\sqrt{(H+Z)^2+X^2}} + \arctan\frac{L+Y}{\sqrt{(H+Z)^2+X^2}}\right) \\ & + \frac{L-Y}{\sqrt{(L-Y)^2+X^2}}\left(\arctan\frac{H-Z}{\sqrt{(L-Y)^2+X^2}} + \arctan\frac{H+Z}{\sqrt{(L-Y)^2+X^2}}\right) \\ & + \frac{L+Y}{\sqrt{(L+Y)^2+X^2}}\left(\arctan\frac{H-Z}{\sqrt{(L+Y)^2+X^2}} + \arctan\frac{H+Z}{\sqrt{(L+Y)^2+X^2}}\right) \\ & - \frac{H_1-Z}{\sqrt{(H_1-Z)^2+X^2}}\left(\arctan\frac{L_1-Y}{\sqrt{(H_1-Z)^2+X^2}} + \arctan\frac{L_1+Y}{\sqrt{(H_1-Z)^2+X^2}}\right) \\ & - \frac{H_1+Z}{\sqrt{(H_1+Z)^2+X^2}}\left(\arctan\frac{L_1-Y}{\sqrt{(H_1+Z)^2+X^2}} + \arctan\frac{L_1+Y}{\sqrt{(H_1+Z)^2+X^2}}\right) \\ & - \frac{L_1-Y}{\sqrt{(L_1-Y)^2+X^2}}\left(\arctan\frac{H_1-Z}{\sqrt{(L_1-Y)^2+X^2}} + \arctan\frac{H_1+Z}{\sqrt{(L_1-Y)^2+X^2}}\right) \\ & - \frac{L_1+Y}{\sqrt{(L_1+Y)^2+X^2}}\left(\arctan\frac{H_1-Z}{\sqrt{(L_1+Y)^2+X^2}} + \arctan\frac{H_1+Z}{\sqrt{(L_1+Y)^2+X^2}}\right)\Bigg] \end{aligned} \tag{4.34}$$

$$\begin{aligned}\frac{V(X,Y,Z)}{\sqrt{2RT_0}} = \frac{X}{4n\pi\sqrt{\pi}}\Bigg[&\frac{1}{\sqrt{(L-Y)^2+X^2}}\left(\arctan\frac{H-Z}{\sqrt{(L-Y)^2+X^2}}+\arctan\frac{H+Z}{\sqrt{(L-Y)^2+X^2}}\right)\\ &-\frac{1}{\sqrt{(L+Y)^2+X^2}}\left(\arctan\frac{H-Z}{\sqrt{(L+Y)^2+X^2}}+\arctan\frac{H+Z}{\sqrt{(L+Y)^2+X^2}}\right)\\ &-\frac{1}{\sqrt{(L_1-Y)^2+X^2}}\left(\arctan\frac{H_1-Z}{\sqrt{(L_1-Y)^2+X^2}}+\arctan\frac{H_1+Z}{\sqrt{(L_1-Y)^2+X^2}}\right)\\ &+\frac{1}{\sqrt{(L_1+Y)^2+X^2}}\left(\arctan\frac{H_1-Z}{\sqrt{(L_1+Y)^2+X^2}}+\arctan\frac{H_1+Z}{\sqrt{(L_1+Y)^2+X^2}}\right)\Bigg]\end{aligned} \tag{4.35}$$

$$\begin{aligned}\frac{W(X,Y,Z)}{\sqrt{2RT_0}} = \frac{X}{4n\pi\sqrt{\pi}}\Bigg[&\frac{1}{\sqrt{(H-Z)^2+X^2}}\left(\arctan\frac{L-Y}{\sqrt{(H-Z)^2+X^2}}+\arctan\frac{L+Y}{\sqrt{(H-Z)^2+X^2}}\right)\\ &-\frac{1}{\sqrt{(H+Z)^2+X^2}}\left(\arctan\frac{L-Y}{\sqrt{(H+Z)^2+X^2}}+\arctan\frac{L+Y}{\sqrt{(H+Z)^2+X^2}}\right)\\ &-\frac{1}{\sqrt{(H_1-Z)^2+X^2}}\left(\arctan\frac{L_1-Y}{\sqrt{(H_1-Z)^2+X^2}}+\arctan\frac{L_1+Y}{\sqrt{(H_1-Z)^2+X^2}}\right)\\ &+\frac{1}{\sqrt{(H_1+Z)^2+X^2}}\left(\arctan\frac{L_1-Y}{\sqrt{(H_1+Z)^2+X^2}}+\arctan\frac{L_1+Y}{\sqrt{(H_1+Z)^2+X^2}}\right)\Bigg]\end{aligned} \tag{4.36}$$

Along the exit centerline where $Y = Z = 0$:

$$n(X,0,0) = \frac{1}{\pi}\left[\arctan\frac{HL}{X\sqrt{X^2+H^2+L^2}} - \arctan\frac{H_1L_1}{X\sqrt{X^2+H_1^2+L_1^2}}\right] \tag{4.37}$$

$$\begin{aligned}\frac{U(X,0,0)}{\sqrt{2RT_0}} = \frac{1}{n\pi\sqrt{\pi}}\Big[&\frac{H}{\sqrt{H^2+X^2}}\arctan\frac{L}{\sqrt{X^2+H^2}}+\frac{L}{\sqrt{X^2+L^2}}\arctan\frac{H}{\sqrt{X^2+L^2}}\\ &-\frac{H_1}{\sqrt{H_1^2+X^2}}\arctan\frac{L_1}{\sqrt{X^2+H_1^2}}-\frac{L_1}{\sqrt{X^2+L_1^2}}\arctan\frac{H_1}{\sqrt{X^2+L_1^2}}\Big]\end{aligned} \tag{4.38}$$

These centerline results contain H, L, H_1 and L_1, and they are quite different from the standard results of free molecular flow through a small circular orifice. When X changes from 0 to ∞, n changes from $\frac{1}{2}$ to 0, while $U(0,0,0) = \frac{1}{\sqrt{\pi}}$ with $H = L$ and $H_1 = L_1$.

4.5.2 DSMC Simulations and Discussions

A three-dimensional DSMC simulation is performed to simulate the effusion flow from a concentered rectangular exit with $2L = 2 \times 0.2$ m by $2H = 2 \times 0.2$ m and $2L_1 = 2 \times 0.05$ m by $2H_1 = 2 \times 0.05$ m. Due to the symmetry in the geometry

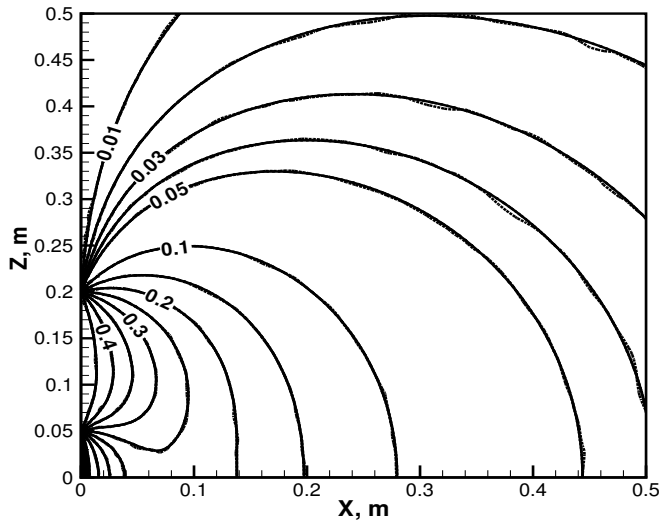

Figure 4.11: Case 3: Contours of Number Density ($H = L = 0.2m$, $H_1 = L_1 = 0.05m$, U_0=0, Solid: Analytical, Dashed: DSMC without Collisions).

configuration, only a quarter of the exit is included in the simulation domain. The simulation domain is a cubic shape with side length of 1 meter. A tetrahedral mesh of 2 million cells is used to represent the whole domain, and in the final sampling state, about 6 million particles are maintained. As usual, the collision function in MONACO was turned off.

Figure 4.11 shows the number density contours in the plane Y=0, the solid contours are the analytical results obtained in this study while the dashed contours are the DSMC results. At the exit, both the analytical and DSMC results yield the same value of $\frac{1}{2}$. Figures 4.12 and 4.13 show contours of $U(X, 0, Z)$ and $W(X, 0, Z)$ in the plane Y=0. In general, both comparisons are quite satisfactory. In all of these results, the exit effects are well captured. The contours of number density and velocities in the plane $Z = 0$ have similar patterns so they are omitted here.

In addition to the contours, comparisons along the X direction can provide more informative results. Figure 4.14 shows profiles of number density along one horizontal

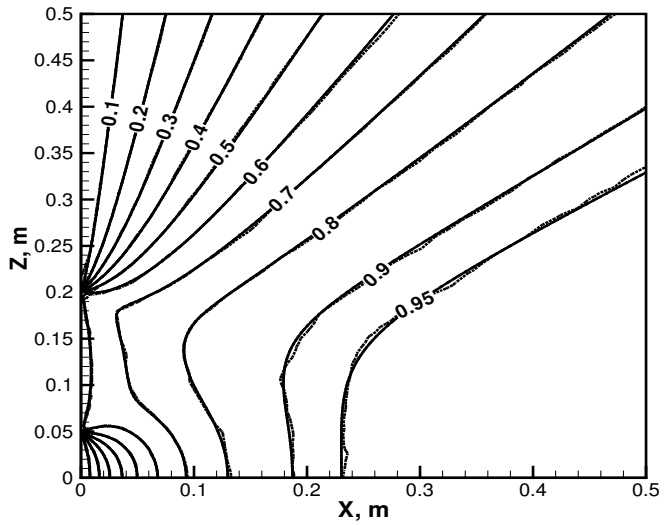

Figure 4.12: Case 3: Contours of $\frac{U(X,0,Z)}{\sqrt{2RT_0}}$ ($H = L = 0.2m$, $H_1 = L_1 = 0.05m$, U_0=0, Solid: Analytical, Dashed: DSMC without Collisions).

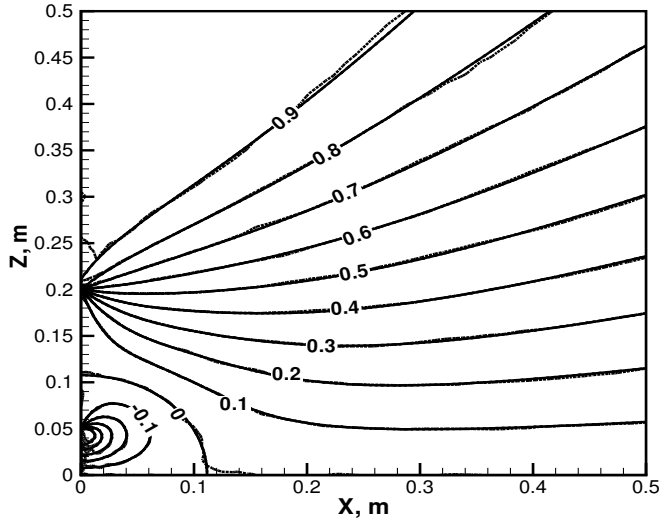

Figure 4.13: Case 3: Contours of $\frac{W(X,0,Z)}{\sqrt{2RT_0}}$ ($H = L = 0.2m$, $H_1 = L_1 = 0.05m$, U_0=0, Solid: Analytical, Dashed: DSMC without Collisions).

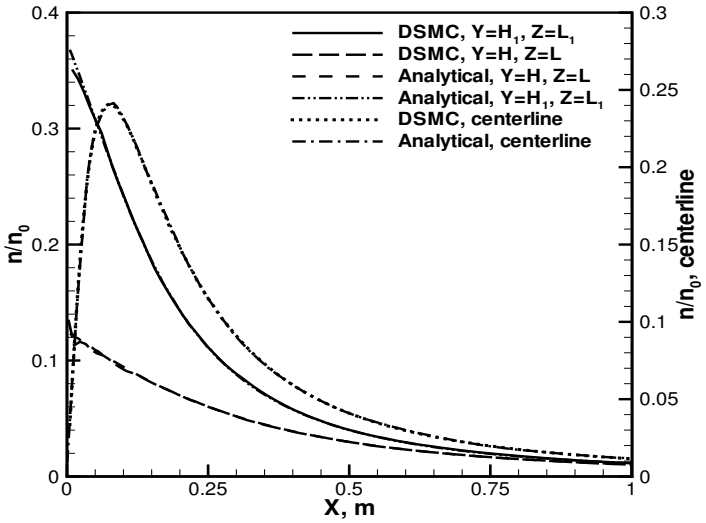

Figure 4.14: Case 3: Profiles of n/n_0 ($H = L = 0.2m$, $H_1 = L_1 = 0.05m$, U_0=0).

line passing the exit corners ($Y = L$, $Z = H$ and $Y = L_1$, $Z = H_1$) and exit centerline. In general, the number density distribution fits quite accurately, and at the outer exit corner the density is about $\frac{1}{8}$ while at the inner corner the value is $\frac{3}{8}$. This is physically correct, because the inner exit corner has a 3 times larger neighborhood than the outer exit corner point. It is possible to further obtain some specific properties, such as the location on the axis with the highest number density, but these derivation processes involve finding roots from complex equations, and they are omitted in this paper.

4.6 Problem Four: Free Molecular Effusion Flow Out of a Circular Exit with a Zero Average Speed (U_0=0)

4.6.1 Analytical Results

Suppose the average velocity at the circular exit is zero. From any point $(0, y, z)$ on the exit which is characterized by a radius of R, only particles with the following

special velocity components can arrive at a point $(X, 0, Z)$ in front of the exit:

$$\frac{X}{u} = \frac{Y - y}{v} = \frac{Z - z}{w} \tag{4.39}$$

where $X > 0, Y > 0, Z > 0$.

Combined with geometry relations:

$$z = r\sin\theta = Z - Xw/u, y = r\cos\theta = Y - Xv/u \tag{4.40}$$

where $0 \leqslant r \leqslant R$, $0 \leqslant \theta \leqslant 2\pi$, the integrals for the number density and the velocities can be simplified using the following variable change:

$$dvdw = \begin{vmatrix} \frac{\partial v}{\partial r} & \frac{\partial v}{\partial \theta} \\ \frac{\partial w}{\partial r} & \frac{\partial w}{\partial \theta} \end{vmatrix} drd\theta = \frac{u^2}{X^2} r dr d\theta \tag{4.41}$$

The major derivation steps for the number density and velocity distributions are summarized in Appendix D. The final results for number density at a point $(X, 0, Z)$ in front of the exit is:

$$n(X,0,Z) = \frac{1}{2} - \frac{X}{4\pi}\int_{-\pi}^{\pi}\left[\frac{(X^2+Z^2-ZR\sin\theta)d\theta}{(X^2+Z^2\cos^2\theta)\sqrt{X^2+Z^2+R^2-2RZ\sin\theta}}\right] \tag{4.42}$$

An option to further simplify the above expression is to expand with a series of trigonometric functions. However, this treatment does not save much evaluation cost, and to maintain higher accuracy, this format is kept and a numerical evaluation is performed.

Similarly, the velocity along the axial direction is:

$$\begin{aligned} \frac{U(X,0,Z)}{\sqrt{2RT_0}} = \; & \frac{X^2}{2\pi n\sqrt{\pi}}\left(\frac{\pi}{X\sqrt{X^2+Z^2}} - \frac{\pi}{\sqrt{(X^2+Z^2+R^2)^2-4R^2Z^2}} + \int_{-\pi}^{\pi}\Bigg[\right. \\ & \frac{Z\sin\theta}{2(X^2+Z^2\cos^2\theta)^{3/2}}\arctan\frac{Z\sin\theta}{\sqrt{X^2+Z^2\cos^2\theta}} + \frac{Z\sin\theta(R-Z\sin\theta)d\theta}{2(X^2+Z^2+R^2-2RZ\sin\theta)(X^2+Z^2\cos^2\theta)} \\ & \left. + \frac{Z\sin\theta d\theta}{2(X^2+Z^2\cos^2\theta)^{3/2}}\arctan\frac{R-Z\sin\theta}{\sqrt{X^2+Z^2\cos^2\theta}}\Bigg]d\theta\right) \end{aligned} \tag{4.43}$$

$$\begin{aligned}\frac{W(X,0,Z)}{\sqrt{2RT_0}} = \; & \frac{1}{2\pi n\sqrt{\pi}}\int_0^{2\pi}\left(\frac{-(Z/2)\cos(2\theta)d\theta}{[X^2+R^2+Z^2-2RZ\sin\theta]}-\right. \\ & \frac{\sin(\theta)d\theta}{\sqrt{X^2+Z^2\cos^2\theta}}(\arctan\frac{R-Z\sin\theta}{\sqrt{X^2+Z^2\cos^2\theta}}+\arctan\frac{Z\sin\theta}{\sqrt{X^2+Z^2\cos^2\theta}})+ \\ & +\frac{\sin\theta(X^2+2Z^2\cos^2\theta)d\theta}{2(X^2+Z^2\cos^2\theta)^{3/2}}(\arctan\frac{R-Z\sin\theta}{\sqrt{X^2+Z^2\cos^2\theta}}+\arctan\frac{Z\sin\theta}{\sqrt{X^2+Z^2\cos^2\theta}}) \\ & \left.+\frac{\sin\theta(X^2+2Z^2\cos^2\theta)(R-Z\sin\theta)d\theta}{2(X^2+Z^2\cos^2\theta)(X^2+Z^2+R^2-2RZ\sin\theta)}+\frac{Z\sin^2\theta(X^2+2Z^2\cos^2\theta)d\theta}{2(X^2+Z^2\cos^2\theta)(X^2+Z^2)}\right)\end{aligned} \tag{4.44}$$

Along the X-axis passing through the exit center, the number density and velocity variations are:

$$n(X,0,0) = \frac{1}{2} - \frac{X}{2\sqrt{X^2+R^2}} \tag{4.45}$$

$$\frac{U(X,0,0)}{\sqrt{2RT_0}} = \frac{1}{\sqrt{\pi}}\left(1+\frac{X}{\sqrt{X^2+R^2}}\right) \tag{4.46}$$

when X changes from 0 to ∞, n changes from $\frac{1}{2}$ to 0, while $\frac{U(X,0,0)}{\sqrt{2RT_0}}$ changes from $\frac{1}{\sqrt{\pi}}$ to $\frac{2}{\sqrt{\pi}}$.

4.6.2 Simulations and Discussions

An axi-symmetric DSMC simulation is performed to validate the analytical results obtained in this case. The simulation domain size is 0.8 m by 0.8 m, and a rectangular mesh of 28,800 cells is adopted mainly to provide high resolution. The circular exit diameter is set to 0.1 m and the number density at the exit is set to a value resulting in a Knudsen number of 20 based on the characteristic length of the exit diameter. In the final sampling stage, about 2 million particles are maintained in the simulation domain. By turning off the collision function in MONACO, the simulation results are expected to be close to these analytical results. The gas translational temperature at the exit is set to 300 K.

Figures 4.15 and 4.16 show the analytical results of number density and $\frac{U(X,0,Z)}{\sqrt{2RT_0}}$ at plane Z=0. The flow patterns are quite similar to Case 1, effusion flow from a thin slit. Figure 4.17 shows a comparison of $\frac{W(X,0,Z)}{\sqrt{2RT_0}}$. The comparison shows exactly

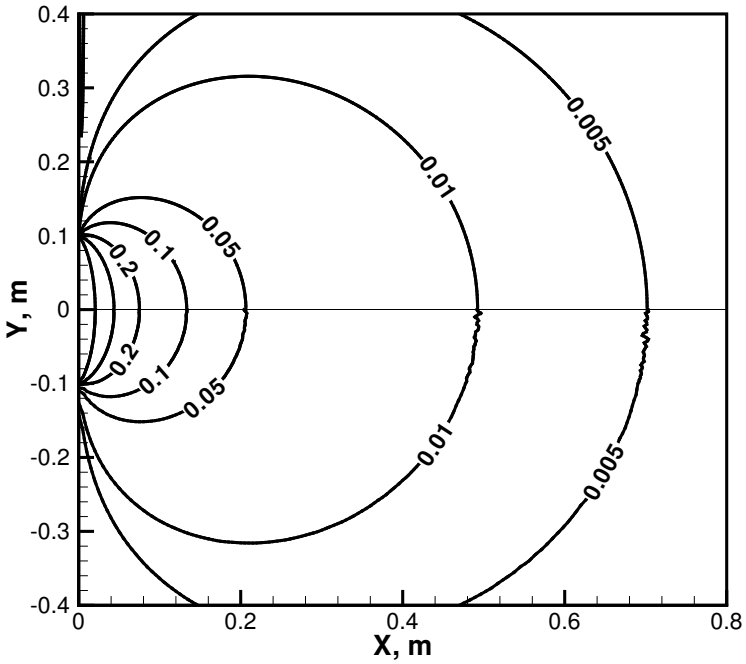

Figure 4.15: Case 4: Contours of Number Density(R=0.1 m, U_0=0, Top: Analytical, Bottom: DSMC without Collisions).

the same flow patterns, and almost identical results. These velocity results indicate clearly the finite geometry exit has an influence around the exit.

Figures 4.18 and 4.19 show variations of number density and velocity along two horizontal lines, one passing through the exit center and the other passing the edge of this exit. It is interesting to recognize that the number density at $(0, R)$ is close to $\frac{1}{4}$, almost half of the value at the exit center, but the circular curvature resulted in some effects on the number density. This is physically correct due to the reason discussed previously.

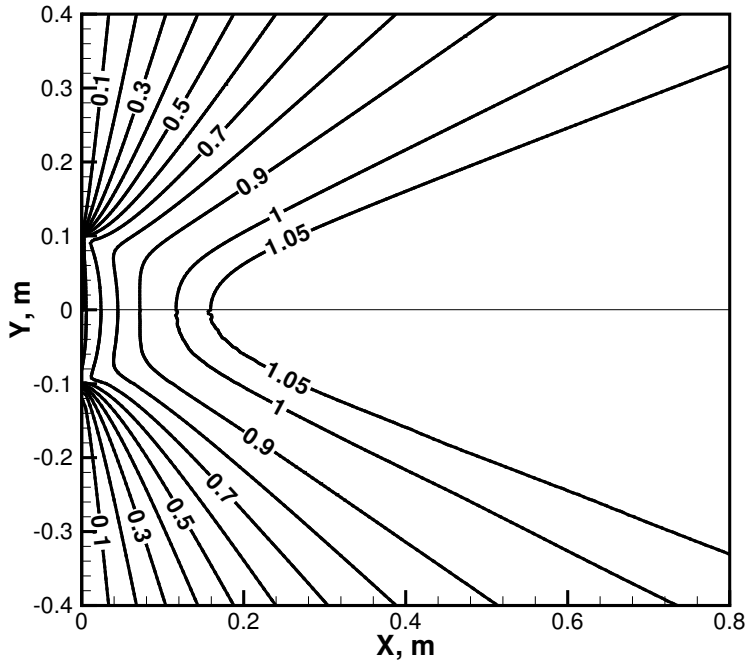

Figure 4.16: Case 4: Speed Ratio $\frac{U(X,Y,0)}{\sqrt{2RT_0}}$ (R=0.1 m, U_0=0, Top: Analytical, Bottom: DSMC).

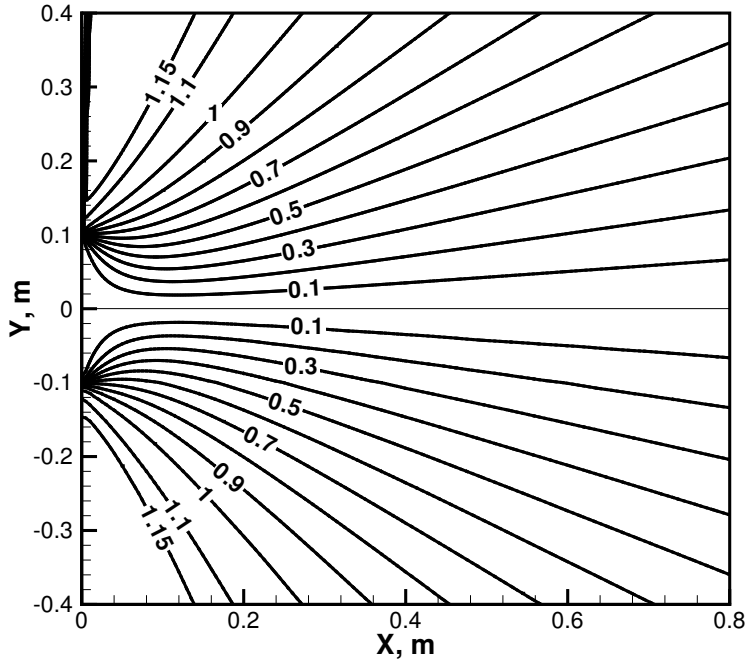

Figure 4.17: Case 4: Speed Ratio $\frac{W(X,Y,0)}{\sqrt{2RT_0}}$ (R=0.1 m, U_0=0, Top: Analytical, Bottom: DSMC).

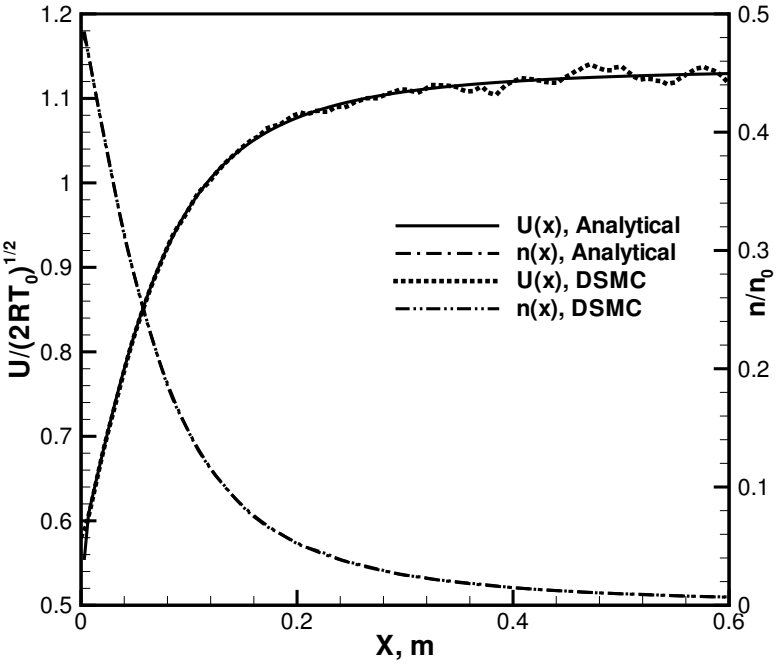

Figure 4.18: Case 4: Normalized Number Density and Velocity along Centerline (R=0.1 m, U_0=0).

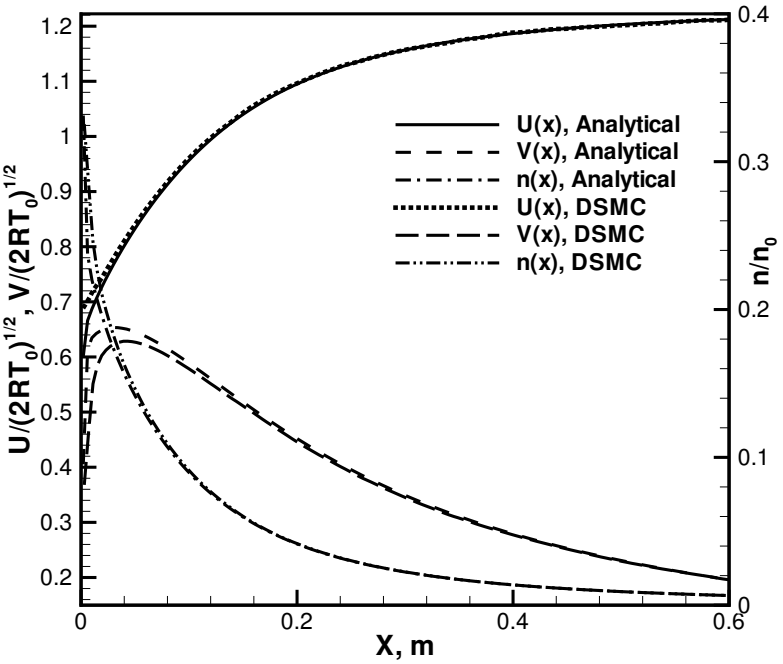

Figure 4.19: Case 4: Normalized Number Density and Velocity along Exit Tip (R=0.1 m, U_0=0).

4.7 Problem Five: Free Molecular Effusion Flow Out of an Annular Exit with a Zero Average Exit Velocity($U_0 = 0$)

4.7.1 Analytical Results

An annulus is a common shape for the exit of the acceleration channel of Hall thrusters. Though this shape is characterized by two parameters of inner and outer radius of R_1 and R_2, Equations (4.39)– (4.41) are still correct for this situation. The only difference in the derivation process is the integral domain $r \in [R_1, R_2]$ for an annular exit instead of $r \in [0, R]$ for a circular exit. Hence, by observing the integral domains, the free molecular flow out of an annulus can be considered as a large circular source of R_2 minus a small circular sink of R_1. The derivation process is similar to Case 3 and is omitted here.

The number density and velocities at a point $(X, 0, Z)$ are:

$$\begin{aligned} n(X,0,Z) = \; & -\frac{X}{4\pi}\int_{-\pi}^{\pi}\left[\frac{d\theta}{\sqrt{X^2+Z^2+R_2^2-2R_2Z\sin\theta}} - \frac{Z\sin\theta(R_2-Z\sin\theta)d\theta}{(X^2+Z^2\cos^2\theta)\sqrt{X^2+Z^2+R_2^2-2R_2Z\sin\theta}}\right] \\ & +\frac{X}{4\pi}\int_{-\pi}^{\pi}\left[\frac{d\theta}{\sqrt{X^2+Z^2+R_1^2-2R_1Z\sin\theta}} - \frac{Z\sin\theta(R_1-Z\sin\theta)d\theta}{(X^2+Z^2\cos^2\theta)\sqrt{X^2+Z^2+R_1^2-2R_1Z\sin\theta}}\right] \end{aligned} \tag{4.47}$$

$$\begin{aligned} \frac{U(X,0,Z)}{\sqrt{2RT_0}} = \; & \frac{X^2}{2\pi n\sqrt{\pi}}\left(\frac{\pi}{\sqrt{(X^2+Z^2+R_1^2)^2-4R_1^2Z^2}} - \frac{\pi}{\sqrt{(X^2+Z^2+R_2^2)^2-4R_2^2Z^2}} + \int_{-\pi}^{\pi}\Bigg[\right. \\ & \frac{Z\sin\theta(R_2-Z\sin\theta)d\theta}{2(X^2+Z^2+R_2^2-2R_2Z\sin\theta)(X^2+Z^2\cos^2\theta)} - \frac{Z\sin\theta(R_1-Z\sin\theta)d\theta}{2(X^2+Z^2+R_1^2-2R_1Z\sin\theta)(X^2+Z^2\cos^2\theta)} \\ & +\frac{Z\sin\theta d\theta}{2(X^2+Z^2\cos^2\theta)^{3/2}}\arctan\frac{R_2-Z\sin\theta}{\sqrt{X^2+Z^2\cos^2\theta}} \\ & \left.-\frac{Z\sin\theta d\theta}{2(X^2+Z^2\cos^2\theta)^{3/2}}\arctan\frac{R_1-Z\sin\theta}{\sqrt{X^2+Z^2\cos^2\theta}}\Bigg]d\theta\right) \end{aligned} \tag{4.48}$$

$$\begin{aligned}\frac{W(X,0,Z)}{\sqrt{2RT_0}} = \; & \frac{1}{2\pi n\sqrt{\pi}}\int_0^{2\pi}\left[\frac{-(Z/2)\cos(2\theta)d\theta}{[X^2+R_2^2+Z^2-2R_2Z\sin\theta]}+\frac{(Z/2)\cos(2\theta)d\theta}{[X^2+R_1^2+Z^2-2R_1Z\sin\theta]}\right.\\ & -\frac{\sin(\theta)d\theta}{\sqrt{X^2+Z^2\cos^2\theta}}\left(\arctan\frac{R_2-Z\sin\theta}{\sqrt{X^2+Z^2\cos^2\theta}}-\arctan\frac{R_1-Z\sin\theta}{\sqrt{X^2+Z^2\cos^2\theta}}\right)\\ & +\frac{\sin\theta(X^2+2Z^2\cos^2\theta)d\theta}{2(X^2+Z^2\cos^2\theta)^{3/2}}\left(\arctan\frac{R_2-Z\sin\theta}{\sqrt{X^2+Z^2\cos^2\theta}}-\arctan\frac{R_1-Z\sin\theta}{\sqrt{X^2+Z^2\cos^2\theta}}\right)\\ & \left.+\frac{\sin\theta(X^2+2Z^2\cos^2\theta)(R_2-Z\sin\theta)d\theta}{2(X^2+Z^2\cos^2\theta)(X^2+Z^2+R_2^2-2R_2Z\sin\theta)}-\frac{\sin\theta(X^2+2Z^2\cos^2\theta)(R_1-Z\sin\theta)d\theta}{2(X^2+Z^2\cos^2\theta)(X^2+Z^2+R_1^2-2R_1Z\sin\theta)}\right]\end{aligned} \tag{4.49}$$

From the above relation, the centerline variations are:

$$n(X,0,0) = \frac{X}{2\sqrt{X^2+R_1^2}} - \frac{X}{2\sqrt{X^2+R_2^2}} \tag{4.50}$$

$$\frac{U(X,0,0)}{\sqrt{2RT_0}} = \frac{X}{\sqrt{\pi}}\left(\frac{1}{\sqrt{X^2+R_1^2}}+\frac{1}{\sqrt{X^2+R_1^2}}\right) \tag{4.51}$$

Obviously, when X changes from 0 to ∞, the centerline number density increases from 0 to a specific value, then decreases slowly to zero, while the speed ratio $\frac{U(X,0,0)}{\sqrt{2RT_0}}$ increases from 0 to $\frac{1}{2\sqrt{\pi}}$.

4.7.2 Simulations and Discussions

An axi-symmetric DSMC simulation without collisions is performed to validate these analytical results. The inner and outer radii of the annulus are set to $R_1 = 0.2$ m and $R_2 = 0.4$ m, respectively. About 19,200 rectangular cells are used to represent a square simulation domain of 1.2 m by 1.2 m. As usual, the temperature at the exit is set to 300 K while the number density is set to a value achieving a Knudsen number of 20 based on a characteristic length of $R_2 - R_1$. At the final sampling stage, about 1.2 million particles are maintained.

Figure 4.20 shows contours of number density, the bottom contours are the analytical results and the top contours represent are DSMC results. In the whole simulation domain, the comparison shows almost identical results. Figures 4.21 and 4.22 show

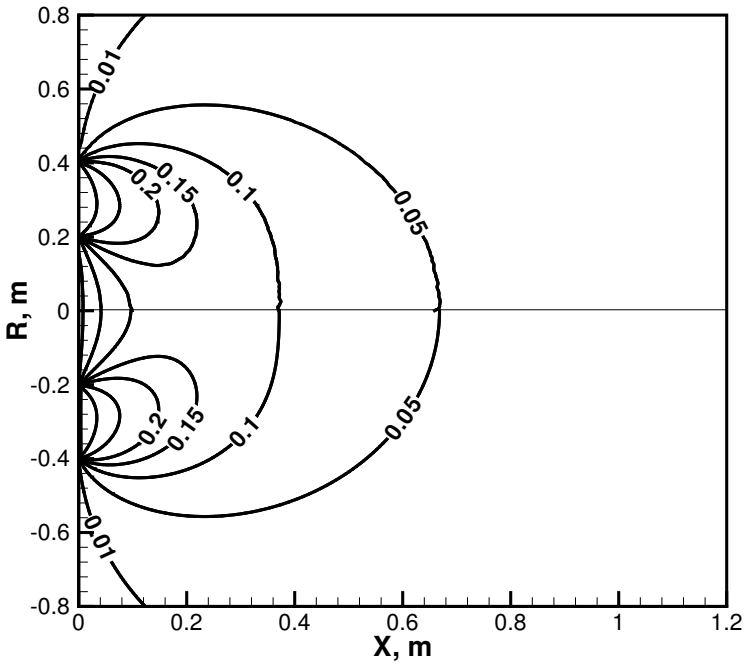

Figure 4.20: Case 5: Contours of Normalized Number Density (R_1=0.2 m, R_2=0.4 m, U_0=0, Bottom: Analytical, Top: DSMC).

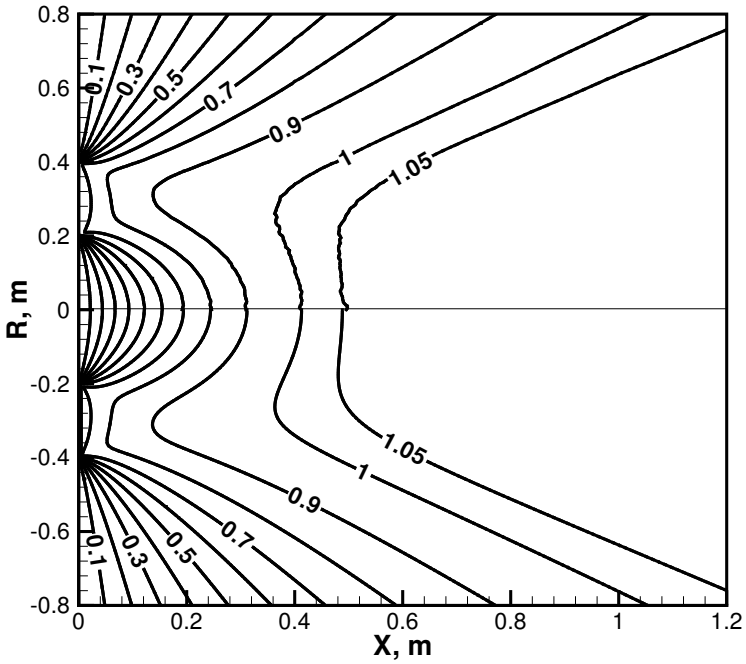

Figure 4.21: Case 5: Contours of $\frac{U(X,0,R)}{\sqrt{2RT_0}}$(R_1=0.2 m, R_2=0.4 m, U_0=0, Bottom: Analytical, Top: DSMC).

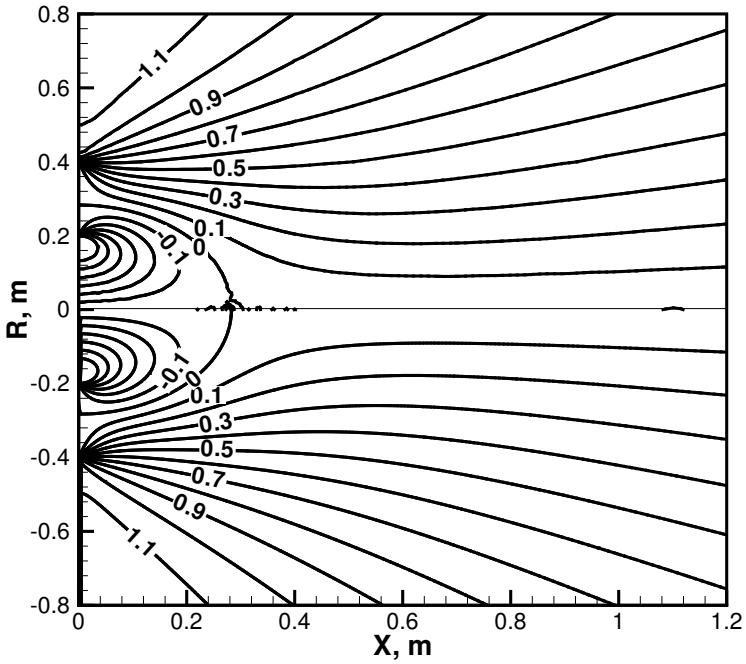

Figure 4.22: Case 5: Contours of $\frac{W(X,0,R)}{\sqrt{2RT_0}}$ (R_1=0.2 m, R_2=0.4 m, U_0=0, Bottom: Analytical, Top: DSMC).

the contours of velocities. Both comparisons are quite satisfactory as well. In all of these three results, both the exit region and the slow "cavity" region in the center, which is characterized by negative W_z, are clearly captured. There are two branches of zero-value lines for W_z, one is along the axis, while the other curved branch starts from a point inside the exit and ends on the axis. The intersection point of the two branches can be found analytically from Equations (4.49). At the specific point,

$$\frac{\partial W(X,0,Z)}{\partial Z}|_{Z=0} = 0 \tag{4.52}$$

From this condition, it is quite easy to show that $X = \sqrt{R_1 R_2}$ is the intersection point on the axis.

Figures 4.23, 4.24, 4.25 and 4.26 are number density and velocity variations along four horizontal lines with different radius to the axis: $r = R_2$, $r = \frac{1}{2}(R_2+R_1)$, $r = R_1$ and $r = 0$. It is quite evident that the number density at the exit tips are close to

$\frac{1}{4}$ while on the exit center point the value is $\frac{1}{2}$. Generally, theoretical velocities and number densities match the results from numerical simulation.

One important result can be obtained for the location on the axis where the peak number density occurs. From Equation (4.47):

$$\frac{\partial n(X,0,0)}{\partial X} = \frac{\partial}{\partial X}\left(\frac{X}{2\sqrt{X^2+R_1^2}} - \frac{X}{2\sqrt{X^2+R_2^2}}\right) = 0 \tag{4.53}$$

This leads to:

$$X = \sqrt{\frac{R_2^2 R_1^{4/3} - R_1^2 R_2^{4/3}}{R_2^{4/3} - R_1^{4/3}}} = \frac{R_1^{2/3} R_2^{2/3}}{\sqrt{R_1^{2/3} + R_2^{2/3}}} = \frac{\kappa^{2/3} R_1}{\sqrt{1+\kappa^{2/3}}} \tag{4.54}$$

$$n_{max} = \frac{1}{2}(\kappa^{2/3}-1)(1+\kappa^{2/3}+\kappa^{4/3})^{-1/2} \tag{4.55}$$

where $\kappa = R_2/R_1 > 1$. Further notice that Equation (4.54) is an increasing function of κ, then a range of X can be decided as:

$$R_1/\sqrt{2} < X < \kappa^{1/3} R_1 = (R_1^2 R_2)^{1/3} < \frac{2R_1 + R_2}{3} \tag{4.56}$$

It is interesting to notice that this distance is less than the average value of the inner and outer radius.

These relations, Equations (4.54)– (4.55), contain only the inner radius and outer radius of the annulus. This is because the derivation is based on a free molecular flow assumption without collision effects, hence the final expression contains only geometry factors, which is quite expected and reasonable. For an annulus with $R_1 = 0.2$ m and $R_2 = 0.4$ m, the highest number density along the centerline is 0.1299 at $X = 0.196$ m, which is shown in Figure 4.26. The DSMC simulation without collisions predicts an exact value at the same location.

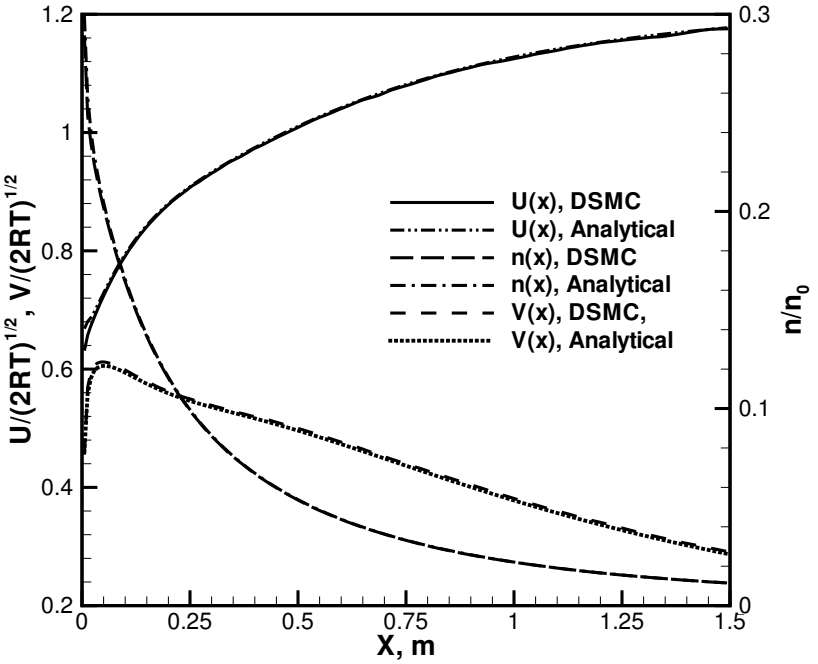

Figure 4.23: Case 5: Number Density and Normalized Velocities along $r = R_2$ (R_1=0.2 m, R_2=0.4 m, U_0=0).

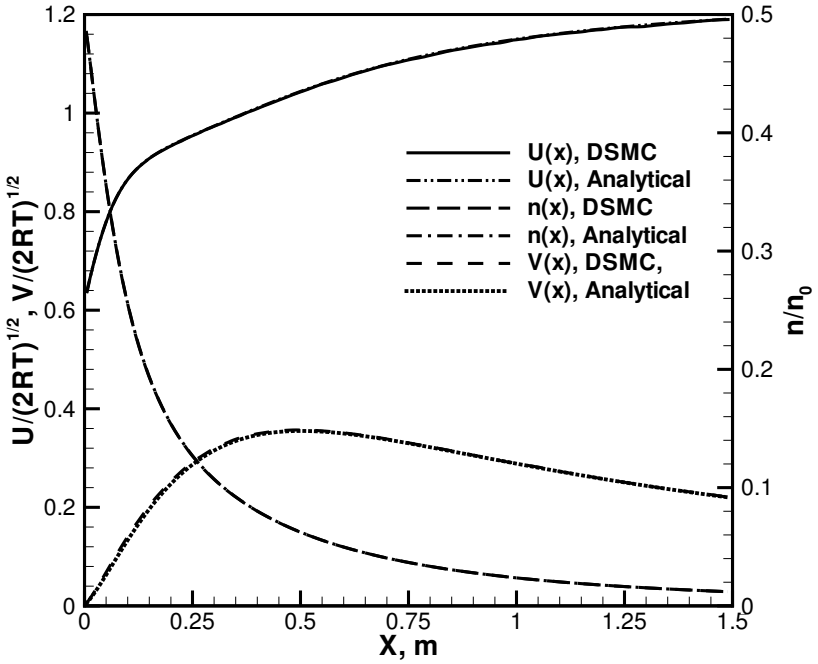

Figure 4.24: Case 5: Number Density and Normalized Velocities along $r = \frac{R_2+R_1}{2}$ (R_1=0.2 m, R_2=0.4 m, U_0=0).

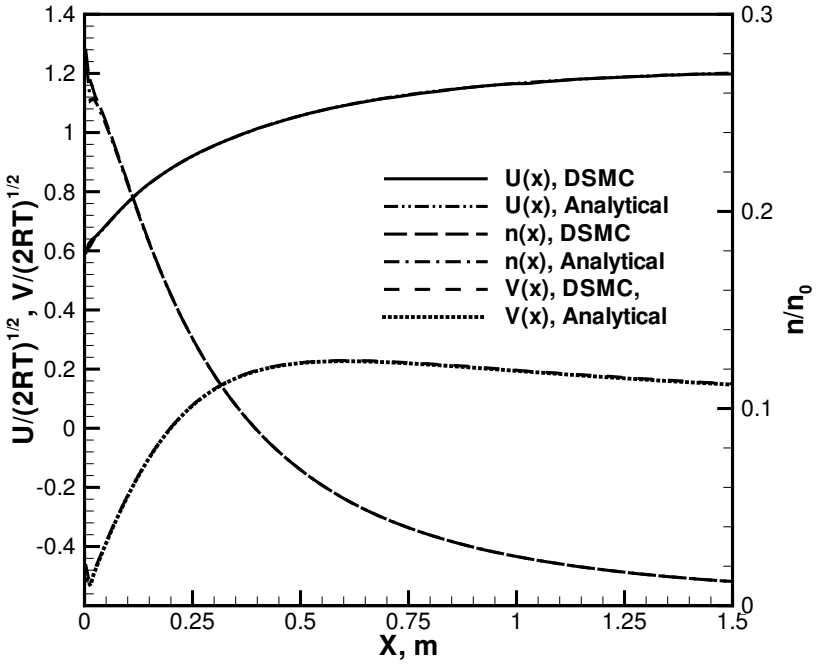

Figure 4.25: Case 5: Number Density and Normalized Velocities along $r = R_1$ (R_1=0.2 m, R_2=0.4 m, U_0=0).

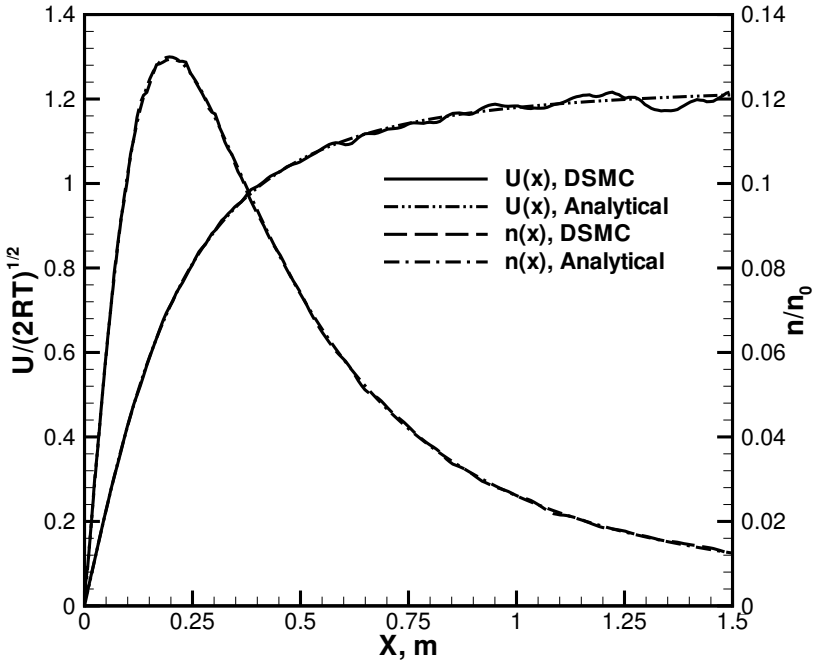

Figure 4.26: Case 5: Number Density and Normalized Velocities along $r = 0$ (R_1=0.2 m, R_2=0.4 m, U_0=0).

4.8 Problem Six: Free Molecular Flow Out of a Thin Slit with a Non-zero Average Speed ($U_0 > 0$)

4.8.1 Analytical Results

Varsigma [40] discussed the jet flow out of a point source with a non-zero average exit velocity. In this section, the finite width of the slit, H, is considered.

Consider the velocity space for a point (X, Y) in front of the slit. The velocity distribution at the point still follows Equation (4.2), but the integral domain changes significantly because of the non-zero average velocity at the slit. With this change, from any point $(0, h)$ on the slit, particles can arrive at the point (X, Y) if and only if their velocity components satisfy the following relation:

$$\tan(\theta) = \frac{Y - h}{X} = \frac{v}{u + U_0}, -H < y < H. \tag{4.57}$$

To compare the difference in the integral domains, for this case, the velocity distribution function does not shift to the right with a value of U_0. Hence, $u + U_0$ represents a particle's real velocity along the X-direction. Obviously the non-zero average velocity U_0 does not destroy the one-to-one mapping relation between velocity phase spaces.

The two integral domain boundaries are:

$$\tan(\theta_2) = \frac{Y + H}{X} \tag{4.58}$$

$$\tan(\theta_1) = \frac{Y - H}{X} \tag{4.59}$$

Figure 4.27 shows the effect of the non-zero exit velocity on the integral domain in velocity space. On the left side is a case of zero average exit velocity and the right side is a case of non-zero average exit velocity. In both plots, region "Aoa" represents an integral domain for a point (X, Y) out of the plume core $(Y > H)$, and region "Bob"

represents an integral domain for a point in the plume core ($Y < H$). The integral domain widens as the point (X, Y) becomes closer to the slit. It is immediately observed that there are several changes between these two integral domains: The existence of a nonzero U_0 translates the integral domain to the left, without any effects on the slopes of the two domain boundaries. The two boundaries shift up or down, resulting in different effects on the points inside the plume core ($Y < H$) and outside the plume core ($Y > H$): if the point is inside the core, the number density increases for the case of a non-zero average exit velocity because of a larger integral domain including regions close to the origin with the highest probability; while the number density at a point outside the plume core decreases because the origin point is excluded from the integral domain. Physically this is reasonable: with a higher average exit velocity, more particles are injected into the simulation domain, while there is less time for particles to diffuse vertically outside the core region while they flow downstream quite quickly. Hence, a non-zero average exit velocity results in a higher density at points inside the plume core and a lower density at points outside the core region.

Suppose the average velocity at the slit exit is greater than zero. Notice $\theta_2 > \theta_1$, $0 < \theta_2 < \pi/2$ and $-\pi/2 < \theta_1 < \pi/2$, the number density and velocities at any point (X, Y) in front of the slit can be derived and are described in Appendix E. The final results are:

$$\begin{aligned} n(X,Y) = \quad & \tfrac{\exp(-\beta {U_0}^2)}{2\pi}(\theta_2 - \theta_1) + \tfrac{1}{4}\left(erf(\sqrt{\beta} U_0 \sin\theta_2) - \tfrac{\theta_1}{|\theta_1|} erf(\sqrt{\beta} U_0 \sin|\theta_1|) \right) \\ & + \tfrac{\sqrt{\beta/\pi}}{2} \int_{\theta_1}^{\theta_2} \exp(-\beta {U_0}^2 \sin^2\theta) U_0 \cos\theta erf(\sqrt{\beta} U_0 \cos\theta) d\theta \end{aligned} \tag{4.60}$$

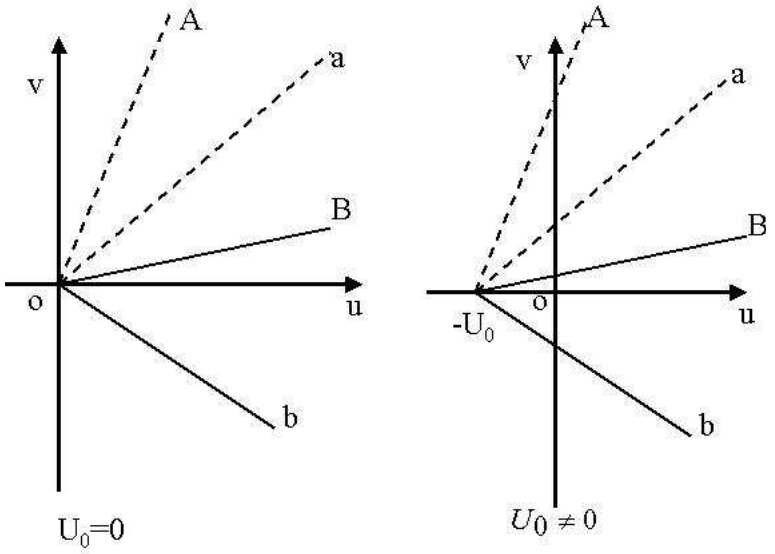

Figure 4.27: Effect on Velocity Space by the Average Exit Velocity.

$$\begin{aligned}\frac{U(X,Y)}{\sqrt{2RT_0}} = \; & \frac{\exp(-\beta {U_0}^2)}{2n\pi\sqrt{2RT_0}}\Bigg[\int_{\theta_1}^{\theta_2}\left(\frac{\sqrt{\pi/\beta}}{2}\exp(\beta {U_0}^2\cos^2\theta)\cos\theta(1+erf(\sqrt{\beta}U_0\cos\theta))\right)d\theta \\ & +\frac{U_0(\theta_2-\theta_1)}{2}+\frac{U_0(\sin(2\theta_2)-\sin(2\theta_1))}{4} \\ & +\sqrt{\beta\pi}\int_{\theta_1}^{\theta_2}\left({U_0}^2\cos^3\theta(1+erf(\sqrt{\beta}U_0\cos\theta))\exp(\beta {U_0}^2\cos\theta)\right)d\theta\Bigg] \end{aligned} \tag{4.61}$$

$$\begin{aligned}\frac{V(X,Y)}{\sqrt{2RT_0}} = \; & \frac{1}{4\sqrt{\pi}n}\Big[\exp(-\beta {U_0}^2\sin^2\theta_1)\cos\theta_1(1+erf(\sqrt{\beta}U_0\cos\theta_1)) \\ & -\exp(-\beta {U_0}^2\sin^2\theta_2)\cos\theta_2(1+erf(\sqrt{\beta}U_0\cos\theta_2))\Big] \end{aligned} \tag{4.62}$$

This set of solutions includes two types of factors: geometry factors represented by θ_1 and θ_2 and other factors involving complex nonlinear relations with U_0, the average exit velocity at the slit.

From Equations (4.60)– (4.62), it can be proved that: $n(X,-Y) = n(X,Y)$, $U(X,-Y) = U(X,Y)$, $V(X,-Y) = -V(X,Y)$. These results can be obtained with aid from the fact that for points (X,Y) and $(X,-Y)$, the integral domains in velocity

space are symmetric about the u-axis.

It is also evident that these solutions are totally compatible with the previous solutions to Case 1. When the average velocity is zero, this current set of general solutions degenerates to the special solutions obtained for the first problem. Another interesting comparison is the quantities on the exit center and exit tip. Though it is difficult to obtain the values at these two points, the integral domain has some simple property: on the exit center, the integral domain is from $-\frac{\pi}{2}$ to $\frac{\pi}{2}$, while at the exit tip, the integral domain is from 0 to $\frac{\pi}{2}$. Hence, it can be concluded from Equations (4.60)– (4.61) that the number density at the exit tip is half of the value on the exit center, while the velocity along the X direction has the same value.

Because this case has a non-zero average exit velocity, it is worthy to investigate several kinds of approximations under special conditions, at least for the number density expressions. Equations (4.60) can be simplified under different conditions by removing the integral expressions and several simplifications are listed here for reference.

In the far field, because $\tan(\theta_2-\theta_1) = \frac{\tan\theta_2-\tan\theta_1}{1+\tan\theta_2\tan\theta_1}$, hence, $\theta_2-\theta_1 = \arctan(\frac{2HX}{X^2+Y^2-H^2})$ $\approx \frac{2Hr\cos\alpha}{r^2-H^2}$, which is quite small:

$$\begin{aligned} n(X,Y) &= \frac{Hr\cos\alpha}{r^2-H^2}\left[\sqrt{\frac{\beta}{\pi}}(1+erf(\sqrt{\beta}U_0\cos\alpha))\exp(-\beta {U_0}^2\sin^2\alpha)U_0\cos\alpha \right. \\ &\quad \left. + \frac{\exp(-\beta {U_0}^2)}{\pi}\right] \end{aligned} \tag{4.63}$$

Equations (4.60) and (4.63) indicate that there are cosine factors in the expression, quite similar to the solutions obtained by Varsigma [40] for flows through an orifice with high speed.

Further, if the average velocity at the slit is large, the plume is confined to a small region close to the X-axis. Hence, with a high average exit speed and a small

α for points inside the core region, the results further take new formats:

$$n(X,Y) = \frac{2HX}{X^2+Y^2-H^2}\left(\frac{\exp(-\beta {U_0}^2)}{2\pi} + \frac{\sqrt{\beta/\pi}U_0 X}{\sqrt{X^2+Y^2}}\right) \tag{4.64}$$

With a low average exit speed, since $erf(x) \approx \frac{2x}{\sqrt{\pi}}$ and $\exp(-x) \approx 1-x$,

$$n(X,Y) = \frac{\theta_2-\theta_1}{2\pi} + \frac{\sqrt{\beta/\pi}U_0(\sin\theta_2 - \sin\theta_1)}{2} + \frac{\sin(2\theta_2)-\sin(2\theta_1)}{4\pi}\beta {U_0}^2 \tag{4.65}$$

4.8.2 Numerical Simulations and Discussions

Though the Equations (4.60)– (4.62) involve several integral terms that cannot be explicitly removed, numerical evaluations are convenient via a computer. The subroutine for the error function can be found in [44]. The simulation domain and mesh are the same as the first case discussed previously, and the collision function in MONACO is turned off.

If the exit average velocity $U_0 = 0$, the boundary line between the flow field and a vacuum is the vertical line above the slit. When the average exit velocity at the exit increases, the boundary line begins to decline towards the plume core, though it still starts with the upper tip $(0, H)$. Hence, there will be a larger void region connected with point $(0, H)$ and residing above the slit. This presents a problem for evaluation of the analytical results because the number density is a component of the denominators in the velocities expressions, and in the analytical vacuum region, the numerical error may exceed the small analytical magnitudes of the number densities. For simulation results from the DSMC method, this is not a problem because the evolution of velocities does not involve a denominator of number density. For the analytical solutions to the fifth problem, an effective boundary line of $n/n_0 = 0.0001$ is introduced to represent the plume edge, and the comparisons are restricted to areas within this boundary. Figure 4.28 shows several such effective boundary lines

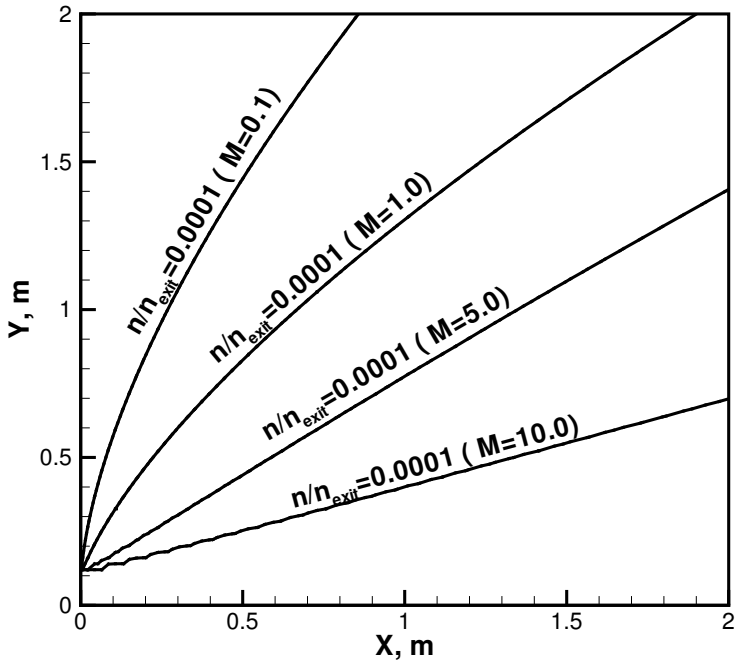

Figure 4.28: Case 6: Analytical Plume Boundary Lines ($H = 0.1m$).

with different average exit velocities at the slit. It indicates that as the average exit velocity increases, the plume region narrows since particles have less time to diffuse vertically. When the exit speed is high enough, the flow field is confined to a narrow region close to the plume core.

Figure 4.29 shows a comparison of number density contours with the DSMC results evaluated at Kn=20. By turning off the collision function in the DSMC method, the results are expected to be close to free molecular. Generally the comparison shows almost identical results.

Figures 4.30 and 4.31 show the corresponding simulation results of velocity contours. The Knudsen number is set to 20 and the average exit velocity at the slit is the sonic speed. Due to the singularity problem mentioned earlier, the analytical results are not valid beyond the boundary line hence they are omitted here. Compared with Figures 4.4 and 4.5 from Case 1, it can be observed that the flow patterns

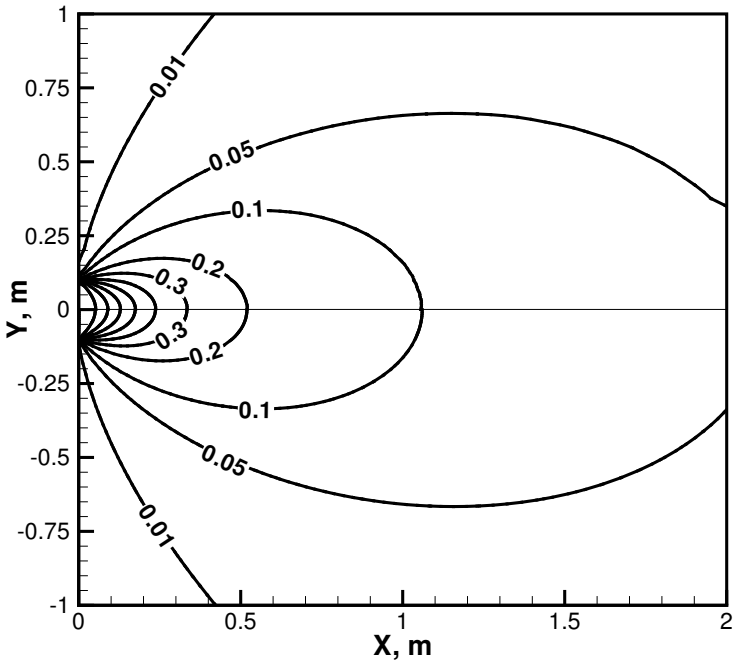

Figure 4.29: Case 6: Contours of $n(X, Y)$ (H=0.1 m, $U_0 = \sqrt{\gamma RT_0}$, Top: DSMC, Bottom: Analytical).

are the same, including a narrow zone where exit effects dominate, straight contour lines in the far field and the same variation trends. Figures 4.4, 4.5, 4.30 and 4.31 strongly indicate that the solutions to these two flow problems are closely related. Figure 4.32 shows a comparison of number density distribution along the plume centerline $Y = 0$ and the slit tip $Y = H$. An average exit velocity $U_0 = \sqrt{\gamma RT}$ results in a density value close to 0.9 at the exit center, which is illustrated on the starting point of one curve. This value is much higher than 0.5 for the true effusion problem discussed here as Case 1. Point $(0, H)$ is a singularity point and its number density value is close to half of the centerline value. The comparison of number density along line $Y = H$ indicates that in general the numerical and analytical results agree quite well. This plot also indicates that with this exit velocity, at downstream locations about $X = 5H$, these two number density distributions merge into one.

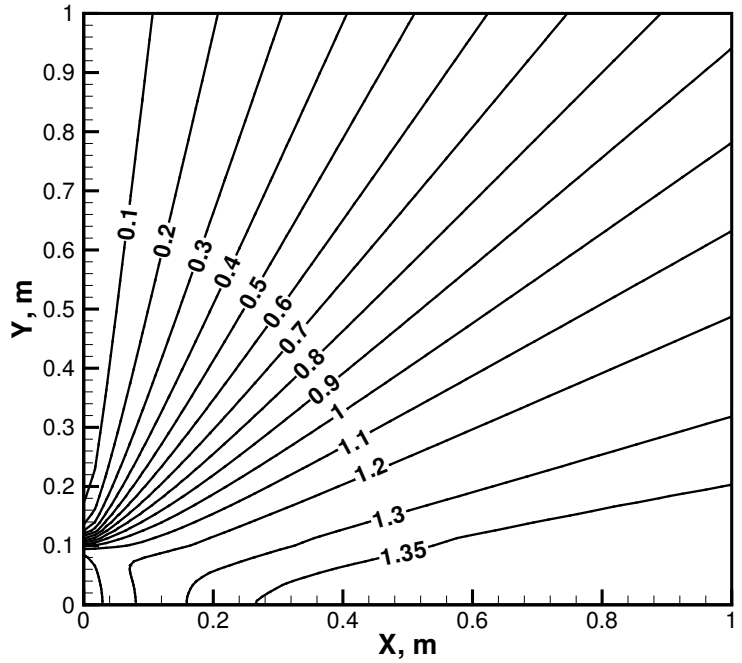

Figure 4.30: Case 6: Contours of $\frac{U(X,Y)}{\sqrt{2RT_0}}$ (DSMC, H=0.1 m, $U_0 = \sqrt{\gamma RT_0}$).

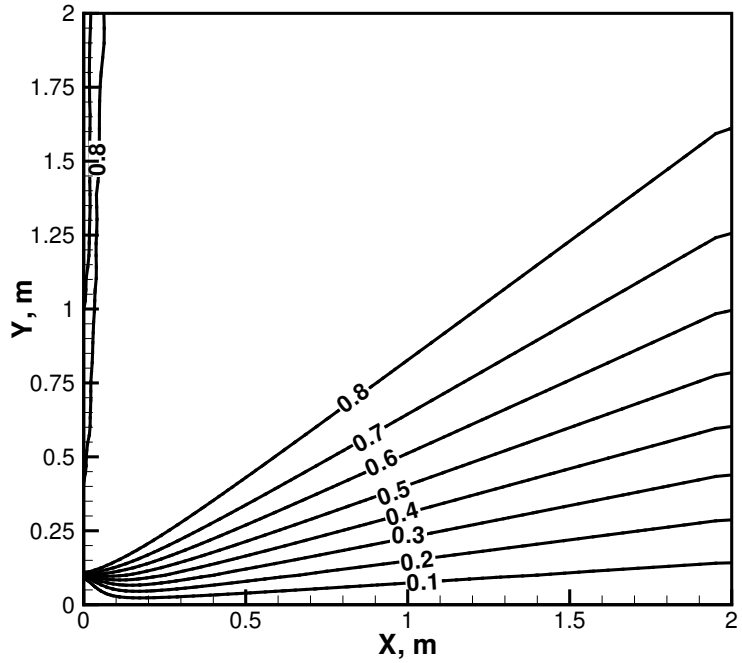

Figure 4.31: Case 6: Contours of $\frac{V(X,Y)}{\sqrt{2RT_0}}$ (DSMC, H=0.1 m, $U_0 = \sqrt{\gamma RT_0}$).

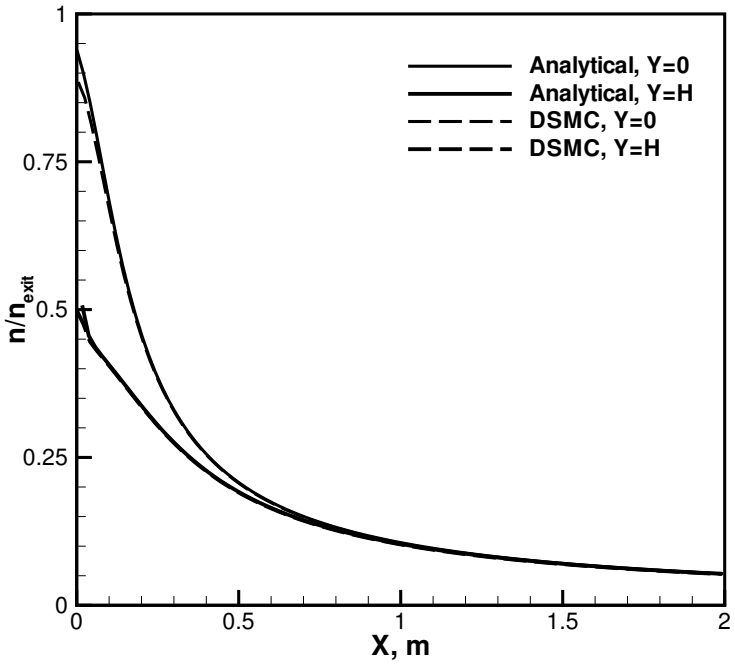

Figure 4.32: Case 6: Comparisons of Number Density along Y=0 and Y=H ($U_0 = \sqrt{\gamma RT_0}$, H=0.1 m).

Figures 4.33 and 4.34 show comparisons of velocities along the centerline Y=0 and the slit tip $Y = H$. It is evident that the numerical results for velocity along the Y direction have a perfect agreement.

Figures 4.35 and 4.36 compare different profiles of number densities along the plume centerline with different average exit velocities $U_0 = 0.1\sqrt{\gamma RT_0}$ and $U_0 = 3\sqrt{\gamma RT_0}$. The Knudsen numbers are set to 20 and these distributions are obtained from different approximations, exact solution and numerical simulations. The comparisons clearly indicate that for both low speed and high speed:

i). The exact solutions agree with the DSMC results;

ii). The low speed simplification agrees with the exact solution quite well for $U_0 = 0.1\sqrt{\gamma RT_0}$;

iii). Surprisingly, the high speed approximation and the far field approximation

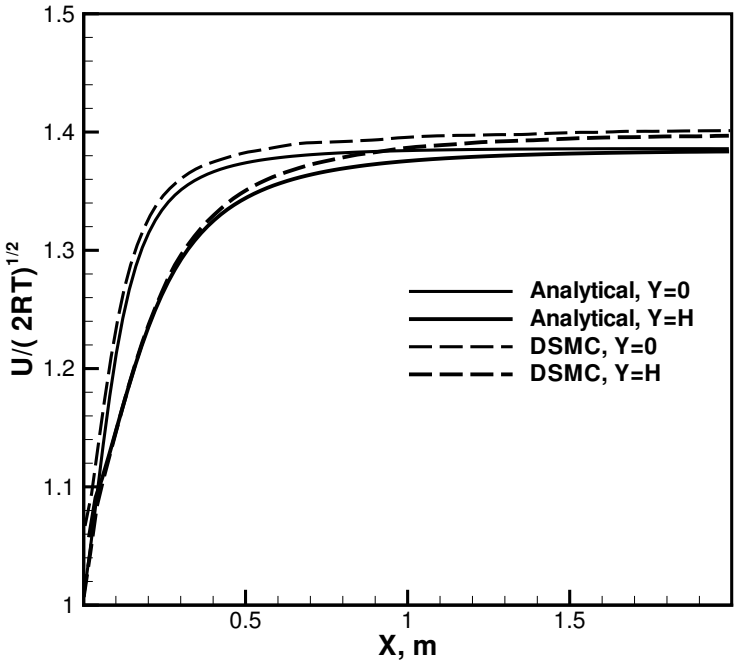

Figure 4.33: Case 6: Comparisons of $\frac{U(X,Y)}{\sqrt{2RT_0}}$ along Y=0 and Y=H ($U_0 = \sqrt{\gamma RT_0}$, H=0.1 m).

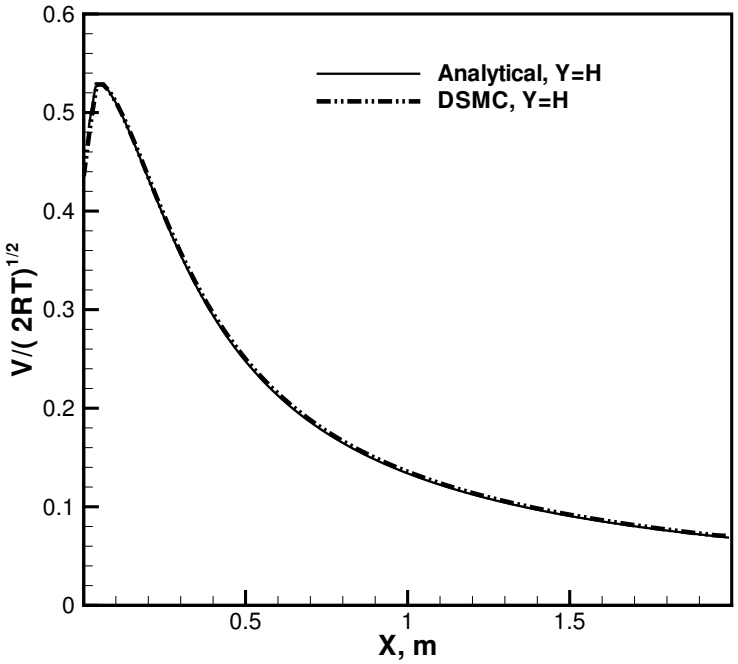

Figure 4.34: Case 6: Comparisons of $\frac{V(X,Y)}{\sqrt{2RT_0}}$ along Y=H ($U_0 = \sqrt{\gamma RT}$, H=0.1 m).

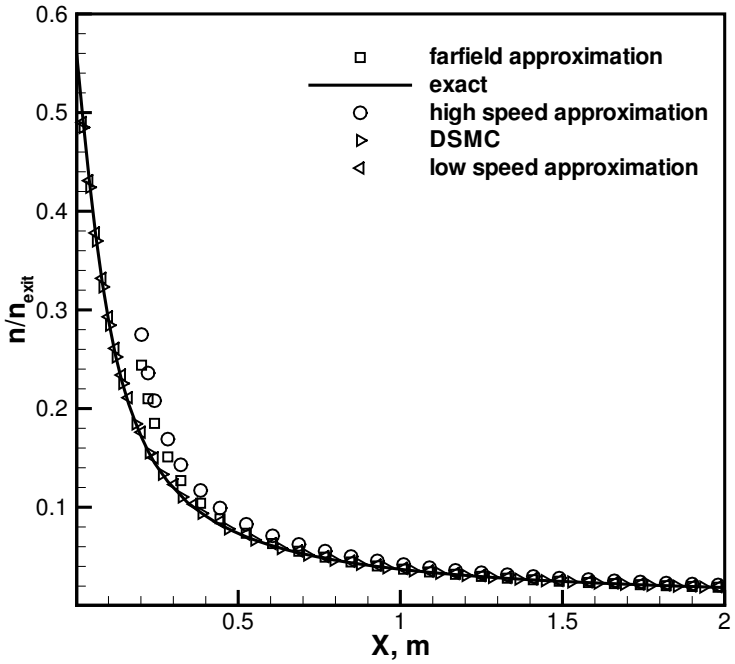

Figure 4.35: Case 6: Comparisons of Number Density along Y=0 (R=0.1 m, $U_0 = 0.1\sqrt{\gamma RT_0}$).

agree quite well for $U_0 = 0.1\sqrt{\gamma RT_0}$ as well;

iv). For $U_0 = 3\sqrt{\gamma RT_0}$, after certain distances down stream of a few slit widths, the far field and the high speed approximations predict quite similar values to the exact analytical and numerical results.

It can be concluded that for number density distributions, over a wide range of average exit velocities, these approximations yield quite good agreement.

4.9 Summary

In this chapter, six fundamental free molecular flows out of an exit with different geometries were investigated analytically. The important relations of velocity-positions, Equations (4.8), (4.18), (4.39) and (4.57), provided one-to-one mapping relations between velocity spaces for a specific point in front of the exit and a point on the exit. These four relations validated Equation (4.7) and provided integral

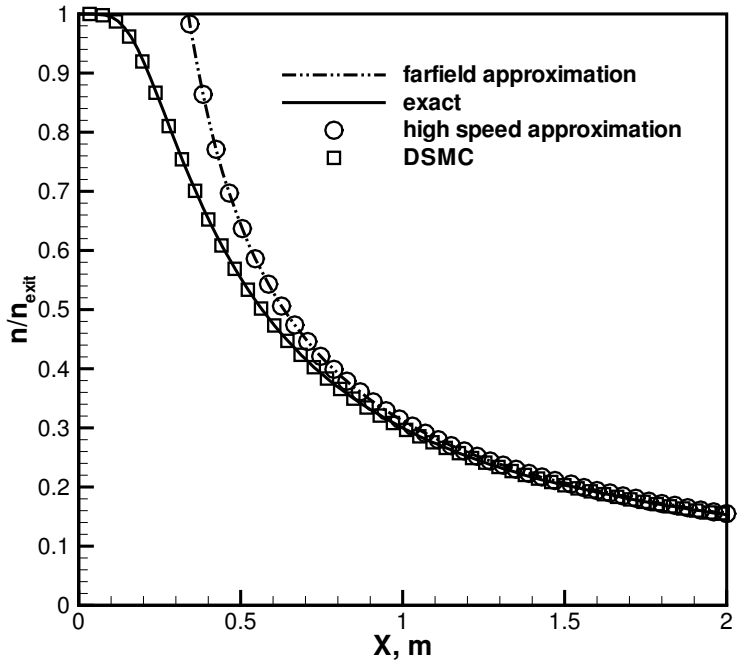

Figure 4.36: Case 6: Comparisons of Number Density along Y=0 (R=0.1 m, $U_0 = 3\sqrt{\gamma RT_0}$).

domains for all six problems.

Analytical exact solutions or exact expressions with detailed exit geometries were obtained. The first five cases belong to a category of true effusion problems with a zero average exit velocity. Their flowfields were associated with geometry factors and no collisions effects were considered. The last problem was of significant importance, because it is the case closest to true plume flows. The analytical results of the last problem indicated that the solutions were composed of two factors: one factor representing simple geometry relations and the other factor representing complex nonlinear effects from the average exit velocity at the slit.

These results included accurate geometry factors, hence they were expected to yield more accurate results than existing models in the literature. These analytical results clearly captured all features of the whole flow field.

Several particle simulations were performed with the DSMC method to validate the analytical solutions obtained in this chapter, and in these simulations, the collision functions were turned off. Generally, simulations for all these six cases yield good agreement with the analytical results, most of the results are essentially identical. It can be concluded that the general treatment of these six free molecular flows from different exit shapes are valid.

This study is an initial effort to provide analytical results to describe the free molecular plume flows from electric propulsion thrusters. It provided a solid basis for further analytical studies, such as plume flows out of a circular or annular thruster with a non-zero average velocity at the thruster exit.

CHAPTER V

PARTICLE SIMULATIONS OF PLASMA PLUME FLOWS FROM A CLUSTER OF THRUSTERS

5.1 Introduction

Hall thrusters represent a very efficient form of electric propulsion devices widely used on spacecraft for primary propulsion and on-orbit applications such as station keeping [38]. In general, Hall thrusters are replacing chemical thrusters in specific applications because of several merits. Hall thrusters can create higher specific impulse, obtain electricity input directly in space through solar cells, and do not require carrying oxidizerStuhlinger:1964. High power electric propulsion systems are being investigated due to improvements in solar cell technology and due to renewed interest in nuclear power.

The development of high-power Hall thrusters falls into two categories: one case involves investigating single, monolithic thrusters, while the second case involves clustering several small thrusters. Generally, clustering is favorable because of several merits including a cheaper manufacturing cost, less demanding requirement from test facilities, more robustness and an ability to tolerate failure of single thrusters.

There are several major interests in numerical simulation of plasma flows from

a cluster of Hall thrusters. One interest is to investigate the plume interactions, especially in the complex and important near field locations. The performance of a thruster in a cluster may be different from a stand alone situation. Another interest is to estimate plume impingement, which involves high-energy ions and Charge Exchange (CEX) ions, onto sensitive spacecraft surfaces such as solar arrays. When a fast ion collides with a slow neutral, one or two electrons may transfer from the neutral to the ion, resulting in a slow ion and a fast neutral. Under the influence of the electric field, this ion may drift behind the thruster. Severe impingement of ions onto spacecraft surfaces may result eventually in failure of devices or even a final failure of the whole mission. If severe impingement is predicted, then a change of design philosophy must be considered to reduce the impingement.

To accurately simulate the plasma plumes from a cluster of Hall thrusters requires an accurate modeling of the complex physical plume mechanism on three-dimensional meshes. A plasma plume is a complex rarefied flow with several species: atoms, positively charged ions and negatively charged electrons. Traditionally, the computational simulation of plasma plume flows into vacuum is performed with a hybrid particle-fluid approach. The direct simulation Monte Carlo (DSMC) method [12] models the collisions of the heavy particles (ions and atoms) while the Particle In Cell (PIC) method [16] models the transport of the ions in electric fields. The electrons are modeled using a fluid description because they adjust their velocities more quickly with their significantly lighter mass.

For the fluid electron model, the Boltzmann relation, Equation (2.6), is usually adopted to compute the plasma potential. The Boltzmann relation requires that the electrons be collisionless, isothermal, un-magnetized. A recently proposed detailed fluid electron model by Boyd and Yim [17] was based on the conservation laws for

electrons and is capable of providing accurate and detailed distributions for electron temperature, plasma potential and electron velocity stream functions. This model was successfully applied in a simulation of an axi-symmetric plasma plume firing from a 200 W class Hall thruster. This model was briefly reviewed in Chapter II. Taccogna [54] proposed a similar model with a further consideration of magnetic field effects and performed an axi-symmetric simulation of plasma flows out of a Hall plasma thruster.

In this study, three-dimensional plasma plumes from one, a cluster of two, and a cluster of four 200 W class Hall thrusters are simulated with the DSMC-PIC methods. These simulations adopt the detailed fluid electron model [17] and a modified treatment of backpressure with a consideration of facility effects is performed on three-dimensional unstructured meshes. It is significant to mention that in the literature there are no other studies that have reported any similar work with such a detailed treatment. As to three-dimensional plume simulations, in the past, Roy [47] performed a calculation of ion thruster bacflow contaminations while Hammel [28] reported a DSMC-PIC simulation of plasma plume flows out of an nozzle. For both of these two works, the Boltzmann relations is adopted as the fluid electron model.

Section 5.2 briefly introduces background information from experiments, Section 5.3 reviews the steps for a general DSMC-PIC hybrid method with several numerical implementation issues, and finally Section 5.4 presents three three-dimensional simulations and a discussion of results.

5.2 Background

The devices considered in the present study are a cluster of four BHT-200 Hall thrusters manufactured by Busek, Co. Each thruster is operated at 200 W with a

nominal thruster level of 13 mN. The cluster of BHT-200 thrusters has been investigated experimentally [8] [60].

The data in [8] were taken in the Large Vacuum Test Facility (LVTF), in the Plasmadynamics and Electric Propulsion Laboratory (PEPL) at the University of Michigan. As illustrated by Figure 3.1, the LVTF is a large cylindrical vacuum chamber with a diameter of 6 meters and a length of 9 meters. Figure 5.1 is a photograph of the thrusters in operation. These four thrusters are configured in a 2 by 2 grid with a center-to-center distance of 0.115 m. As shown in the same photograph, there are four cathode-neutralizers located either above or at the bottom of each thruster, and there is a 7 mm conic cap on the front face of each thruster to protect it against ion sputtering. In operation, different numbers of thrusters in this cluster can be turned on, and in [8], measurements are collected with one, two and four thruster(s) in operation. Hence, to compare with the experimental measurements and to understand the clustering effects, in this study, three particle simulations are performed. In these simulations, only one plume from the thruster is simulated, and the full plume field for the cases of two and four thrusters in operation are obtained by reflections due to the symmetric configuration. For example, in the simulation of a cluster of four thrusters, the simulation domain is a quarter of cylinder with vertical and horizontal symmetric planes, this symmetric configuration reduces the mesh size for a cluster of four thrusters compared to that for a cluster of two thrusters and one thruster. Hence, the simulation of 4 thrusters in operation is the most economic.

In operation, gaseous xenon effuses from the upstream end of the acceleration channel. Some of these xenon atoms are ionized and then accelerated by the imposed electric field in the rest of the acceleration channel. A current of electrons is emitted

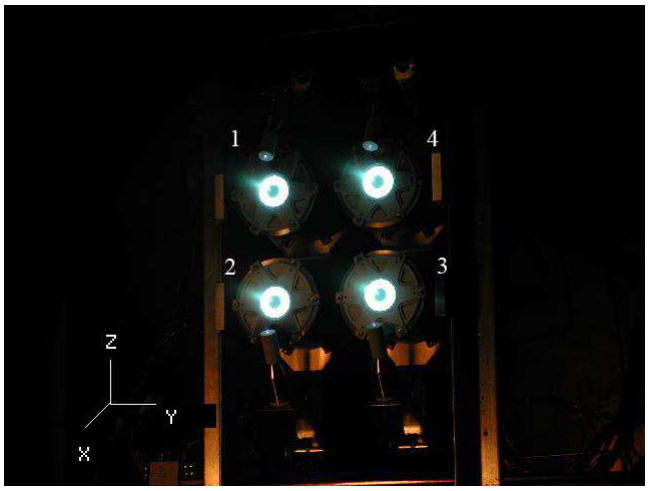

Figure 5.1: Four BHT-200 Hall Thrusters in Operation(Courtesy of PEPL).

from the cathode. One fraction of these electrons are accelerated while traveling along the electric field towards the anode and are trapped by the magnetic field, their high kinetic energy ionizes a fraction of xenon atoms, and eventually, these electrons are depleted at the thruster anode. The rest of the electrons emitted from the cathode travel downstream into the plume to neutralize it.

In the following simulations, the same thruster numbering as [8] is adopted: the upper left, lower left, lower right and upper right thrusters are named as thruster 1, 2, 3 and 4 respectively. The origins of the simulation system are the cluster center, the midpoint between two thrusters and a thruster center for the cases of 4, 2 and 1 thruster(s) in operation, correspondingly. The X-axis direction of the coordinate system used in this simulation is along the plume direction, while the Y and Z axes are the horizontal and vertical lines perpendicular to the plume directions. Figure 5.2 illustrates these coordinates.

The total pumping speed in the LVTF with four of the seven cryopumps in operation for these experiments was 140,000 l/s on xenon resulting in a backpressure

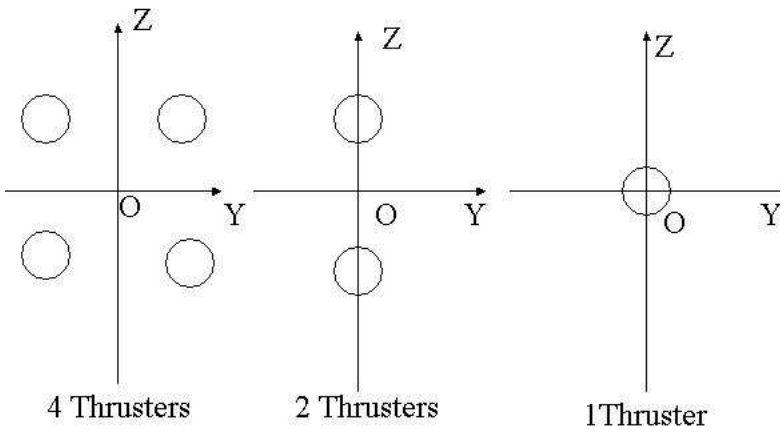

Figure 5.2: Illustration of Simulation Coordinates for 3D Simulations.

of 1.1×10^{-6} or 3.6×10^{-6} Torr for single and four thruster(s) in operation [8], respectively. Faraday probes were used to measure angular profiles of ion current density. A retarding potential analyzer was also used to measure the ion energy distribution function in the plume far field. In addition, a floating emissive probe and a triple Langmuir probe were used to measure the plasma potential, the electron number density and the electron temperature.

Xenon is usually employed for the propellant in Hall thrusters. A plume from a plasma thruster consists of light electrons with thermal speeds of 1×10^6 m/s, and heavier ions or neutrals, such as fast single or double charged ions, Xe^+, Xe^{++}, slow neutral xenon, and fast neutral xenon and slow ions due to CEX.

5.3 Simulation Methods and Numerical Implementation Issues

5.3.1 General Steps for the DSMC-PIC Methods

For particle simulations of plasma plume flow, heavy neutrals and ion particles are simulated with the DSMC [12] and the PIC [16] methods, while the electrons are modeled as a fluid because electrons can adjust themselves more quickly. The hybrid DSMC-PIC simulation can be summarized with the following steps:

Step 1. (PIC): Allocate the charge of each ion inside a cell onto the cell nodes.

Step 2. (Fluid): Calculate plasma potential ϕ using a fluid electron model.

Step 3. (PIC): Calculate ionization in all cells. A fraction of neutrals will be changed to ions.

$$\Delta n_i = C_i n_a n_i \Delta t \tag{5.1}$$

Step 4. (PIC): Calculate the electric field on each node with the relation:

$$\overrightarrow{E} = - \bigtriangledown \phi \tag{5.2}$$

Step 5. (DSMC, PIC): Sample quantities inside each cell.

Step 6. (DSMC): Perform momentum exchange and CEX collisions inside each cell.

Step 7. (DSMC, PIC): Introduce new particles (ions and neutrals) into the simulation domain from inlet boundaries.

Step 8. (PIC): Calculate the ion acceleration based on its location inside its cell.

Step 9. (DSMC, PIC): Move all particles with the time step. When particles move across an outer boundary, they are removed from the simulation; when a neutral particle collides with thruster walls, it rebounds back into the simulation domain with a thermal velocity characterized by the wall temperature of 300 K; when an ion

collides with the wall, it loses its charge and rebounds as a neutral.

In this study, magnetic field effects are neglected because the magnetic field leakage is only expected to be significant right next to the thruster.

5.3.2 General Finite Element Solver for Poisson Equations

Each of Equations (2.7), (2.11) and 2.12 can be expressed as a general Poisson equation [57]:

$$-\bigtriangledown(P(x,y,z)\cdot\bigtriangledown Q(x,y,z)) = S(x,y,z) \tag{5.3}$$

where $P(x,y,z)$ is a distribution of coefficients, $Q(x,y,z)$ is a distribution of the primary variable to be solved and $S(x,y,z)$ is a known distribution of source terms.

For a two-dimensional or axi-symmetric simulation on a structured mesh, an Alternative Direction Implicit(ADI) iterative solver [44] is usually adopted for simplicity. However, there are several drawbacks for the ADI method:

i). It is not applicable, or is very difficult to implement, on unstructured meshes.

ii). For a structured mesh, depending on the geometry of the simulation, the ADI method needs to be applied on each sub-domain separately with artificial inner boundaries which may result in inaccuracy in the simulation results. This precludes the application of ADI to complex geometries, even with structured meshes.

iii). The treatment of boundaries is not natural. This may result in inaccuracies for the source terms on the first layer of nodes on boundaries. At the thruster exit, the gradients are significant and a mistreatment of boundary source conditions will spread the effects into the whole flow domain because of the elliptical property of these equations. The first three layers of nodes close to the boundaries will be heavily affected.

To simulate flows with very complex geometry, an unstructured mesh must be

adopted and this actually precludes the ADI method. To address the above problems, a general purpose finite element solver applicable to two- and three-dimensional structured and unstructured meshes is developed to solve the above three equations. Compared with the ADI method, the finite element method is applicable on structured and unstructured meshes and can integrate the boundary conditions more naturally and accurately.

The discrete, stiff matrix for a triangular cell can be found in [57], and a quadrilateral cell can be simply assembled as two triangles. For a three-dimensional tetrahedral cell with volume V and node coordinates of $x_i, y_i, z_i, i = 1, 2, 3, 4$, suppose a general linear solution in the cell by interpolating values on the four element nodes:

$$u(x, y, z) = u_e(x, y, z) = a_0 + a_1 x + a_2 y + a_3 z \tag{5.4}$$

The coefficients a_0, a_1, a_2, a_3 can be solved via the following group of equations:

$$\begin{pmatrix} 1 & x_1 & y_1 & z_1 \\ 1 & x_2 & y_2 & z_2 \\ 1 & x_3 & y_3 & z_3 \\ 1 & x_4 & y_4 & z_4 \end{pmatrix} \begin{pmatrix} a_0 \\ a_1 \\ a_2 \\ a_3 \end{pmatrix} = \begin{pmatrix} u_1 \\ u_2 \\ u_3 \\ u_4 \end{pmatrix} \tag{5.5}$$

Finally, after discretization, on a single tetrahedral cell, with an aid of a geometry

matrix B_e:

$$B_e = \frac{1}{6V}\begin{pmatrix} -\begin{vmatrix} 1 & y_2 & z_2 \\ 1 & y_3 & z_3 \\ 1 & y_4 & z_4 \end{vmatrix} & \begin{vmatrix} 1 & y_1 & z_1 \\ 1 & y_3 & z_3 \\ 1 & y_4 & z_4 \end{vmatrix} & -\begin{vmatrix} 1 & y_1 & z_1 \\ 1 & y_2 & z_2 \\ 1 & y_4 & z_4 \end{vmatrix} & \begin{vmatrix} 1 & y_1 & z_1 \\ 1 & y_2 & z_2 \\ 1 & y_3 & z_3 \end{vmatrix} \\ \begin{vmatrix} 1 & x_2 & z_2 \\ 1 & x_3 & z_3 \\ 1 & x_4 & z_4 \end{vmatrix} & -\begin{vmatrix} 1 & x_1 & z_1 \\ 1 & x_3 & z_3 \\ 1 & x_4 & z_4 \end{vmatrix} & \begin{vmatrix} 1 & x_1 & z_1 \\ 1 & x_2 & z_2 \\ 1 & y_4 & z_4 \end{vmatrix} & -\begin{vmatrix} 1 & x_1 & z_1 \\ 1 & x_2 & z_2 \\ 1 & x_3 & z_3 \end{vmatrix} \\ -\begin{vmatrix} 1 & x_2 & y_2 \\ 1 & x_3 & y_3 \\ 1 & x_4 & y_4 \end{vmatrix} & \begin{vmatrix} 1 & x_1 & y_1 \\ 1 & x_3 & y_3 \\ 1 & x_4 & y_4 \end{vmatrix} & -\begin{vmatrix} 1 & x_1 & y_1 \\ 1 & x_2 & y_2 \\ 1 & x_4 & z_4 \end{vmatrix} & \begin{vmatrix} 1 & x_1 & y_1 \\ 1 & x_2 & y_2 \\ 1 & x_3 & y_3 \end{vmatrix} \end{pmatrix}$$

Equation (5.3) changes to:

$$B_e^T B_e \{u_{ne}\} - \frac{1}{20}\begin{bmatrix} \frac{1}{10} & \frac{1}{20} & \frac{1}{20} & \frac{1}{20} \\ \frac{1}{20} & \frac{1}{10} & \frac{1}{20} & \frac{1}{20} \\ \frac{1}{20} & \frac{1}{20} & \frac{1}{10} & \frac{1}{20} \\ \frac{1}{20} & \frac{1}{20} & \frac{1}{20} & \frac{1}{10} \end{bmatrix} \{s_{ne}\} = 0 \tag{5.6}$$

where u_{ne} and s_{ne} are the unknown variables and known source terms on the four element nodes.

A Dirichlet boundary condition

$$U = U_b(x, y, z)$$

can be achieved by directly arranging values in the complete source terms and the corresponding rows and columns in the global stiff matrix. A Neumann boundary

condition

$$\frac{\partial U}{\partial n} = G(x, y, z)$$

along face $n_1 n_2 n_3$ can be integrated by adding three extra terms $\frac{1}{3} S_{123} G_{n1}$, $\frac{1}{3} S_{123} G_{n2}$ and $\frac{1}{3} S_{123} G_{n3}$ into the source terms. Usually $G(x, y, z) = 0$ means a natural boundary condition, and a surface with such a boundary condition will not contribute any effect to the global stiff matrix and global source terms, hence this element surface can be omitted. There are boundary conditions $\partial^2 \Psi / \partial n^2 = 0$ for the electron stream functions, therefore fortunately, the surface element contribution to the whole matrix and source terms is zero as well. At the initialization stage, MONACO scans all boundary element surfaces, collects the boundary conditions, stores them into three arrays. When the finite element solver is called to solve these equations, the solver directly obtains boundary information from these arrays.

The final complete stiff matrix is sparse, symmetric and positive definite. These novel properties are not naturally guaranteed by a finite difference method or a finite volume method. To fully take advantage of these properties, an efficient storage scheme [44] is adopted which only requires a cost of $O(n)$ where n is the total node number. The iterative conjugate gradients method [44] is adopted to solve the final linear equations. This method fully takes advantage of the sparse, symmetric and positive definite properties of the global stiff matrix.

5.3.3 Derivative Calculation on an Unstructured Mesh

Several situations will require the calculation of derivatives on a node. Two situations are Step 2 to calculate the source terms for Equations 2.7, 2.11, 2.12, and Step 3 to calculate the electric field from a potential field. Besides accuracy, one requirement for the optimal calculation scheme is to be applicable on both serial and

parallel machines.

There are several options to calculate derivatives on unstructured meshes. One of them is the least square method [28]. The basic idea of the least square method can be illustrated with an example to calculate the electric field from a potential field: assume the unknown gradients on one node are $\overrightarrow{E}(x, y, z) = (E_x, E_y, E_z)$, if there are N nodes connected to this node with differences of plasma potential $d(\phi)_i$ and distance vectors dX_i, then they form $N \times 3$ relations which are overdetermined:

$$ME = d\phi \tag{5.7}$$

where M is an $N \times 3$ matrix, E is a 3×1 vector, and $d\phi$ is an $N \times 1$ vector. By multiplying by a transposed matrix M^T on both sides, this overdetermined matrix is transformed to a 3×3 matrix and the equations are solvable.

One tetrahedral cell is enough to decide the derivatives on a specific cell node. This scheme includes the effects from all nodes connected to a specific node, hence, it yields accurate results. The least square method is also applicable on parallel machines. The only extra cost of this scheme is, at the beginning of a simulation, a table of node connection relations must be gathered and saved for the whole simulation process.

5.3.4 Weighting Schemes

A weighting scheme is a crucial step for a successful DSMC-PIC simulation with the detailed fluid electron model. In Step 1, the ion number density at a specific node must be accurately estimated by weighting the charge of ions in all cells connected with this node. In Step 8, the acceleration for a particle is interpolated from the electric field values on the same nodes. Generally, these two weighting schemes are preferably the same, and the closer a particle to a node, the more influence this

particle will have on or from the node. In Step 3, a correct ionization source term requires both valid charge density and valid neutral density allocated from particles to cell nodes as well.

Usually for charge allocation, there exists two categories of weighting schemes. The first category of weighting schemes is based on areas or volumes. In these methods, a particle's charge is allocated to cell nodes by the areas or volumes formed by the particle's position in the cell nodes. The particle's position in a cell has an important influence on the weight of its charge to be assigned on different cell nodes. This scheme is expected to yield a higher accuracy and is very widely used in PIC simulations. For example, Ruyten [48] presented a well-used scheme for structured axi-symmetric meshes illustrated by Figure 5.3:

$$S_j = \frac{(r_{j+1} - r)(2r_{j+1} + 3r_j - r)}{2(r_{j+1}^2 - r_j^2)} \tag{5.8}$$

$$S_{j+1} = \frac{(r - r_j)(2r_{j+1} + 3r_j - r)}{2(r_{j+1}^2 - r_j^2)} \tag{5.9}$$

$$S_i = \frac{x_{i+1} - x}{x_{i+1} - x_i} \tag{5.10}$$

$$S_{i+1} = \frac{x - x_i}{x_{i+1} - x_i} \tag{5.11}$$

$$W(i, j) = S_i S_j \tag{5.12}$$

$$W(i, j+1) = S_i S_{j+1} \tag{5.13}$$

$$W(i+1, j) = S_{i+1} S_j \tag{5.14}$$

$$W(i+1, j+1) = S_{i+1} S_{j+1} \tag{5.15}$$

This scheme works accurately on cylindrical coordinates with structured rectangular cells by satisfying both charge conservation and charge density conservation. In the literature, there are reports that use similar weighting schemes on unstructured

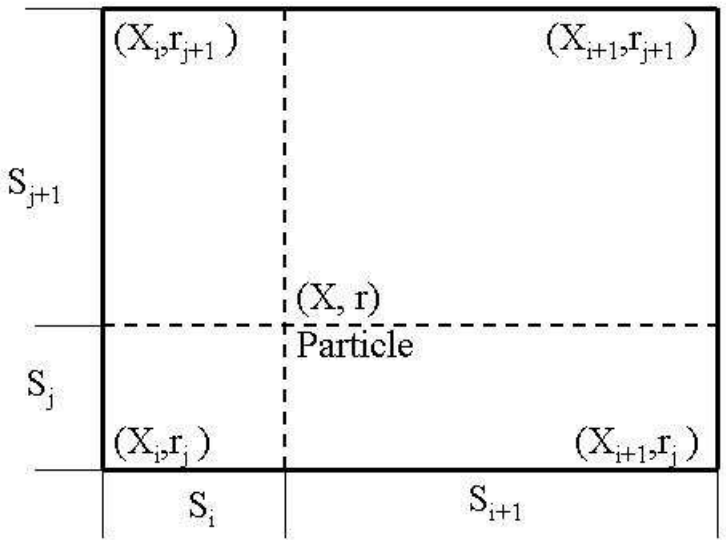

Figure 5.3: Particle Positions and Weighting Factors in Ruyten's Density Conservation Scheme.

meshes based on volumes and areas. However, it will be shown later this is not a proper scheme for a DSMC-PIC simulation of plasma flows on unstructured meshes, especially with the detailed fluid electron model or ionization effects. The other category of weighting schemes is expected to have a lower degree of accuracy since a particle's position in a cell does not have an influence on its weights to different nodes, and density is not conserved. In this type of method, the charge density on a specific node is calculated by summing up all particles' charge inside a closed volume enclosing the node, then dividing by the volume. This closed volume can either be all the cells connected to this node, or, a fraction of these cells. Generally this category of weighting scheme does not have problems associated with the first category, and it can be used for a DSMC-PIC simulation with unstructured meshes.

There are two problems associated with the weighting schemes based on areas

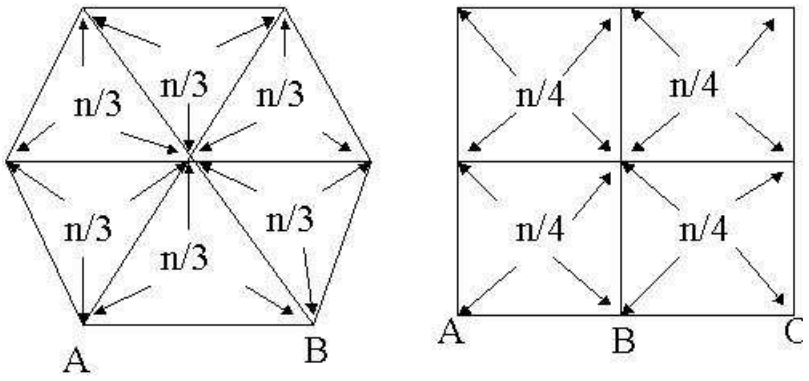

Figure 5.4: Effects of Weighting Scheme by Area/Volume on Unstructured Meshes.

or volumes on an unstructured mesh. Suppose there are a large number of particles in each cell and the average number density is n. Weighting by areas or volumes, similar to Ruyten's scheme, will approximately distribute the ion or neutral density equally onto the nodes forming this cell. Consider Figure 5.4, for a two-dimensional mesh, on the right, the center node is shared by four cells, and the total charge number density at the center node is $n/4 \times 4 = n$. While for the unstructured mesh on the left, the total charge number density will be $n/3 \times 6 = 2n$. While for three-dimensional unstructured tetrahedral cells, usually there are about 16 or more cells connected to an inner node, hence the number density at that node will be calculated as $n/4 \times 16 = 4n$. It is obvious that, for an unstructured mesh, if the weighting scheme by areas or volumes is applied, for a two-dimensional situation with triangles the charge density at one node will be two times higher than its real value, while for an unstructured three-dimensional situation, the estimated charge density will be four or five times higher than the real charge density, depending on how many neighboring cells are connected to this specific node. Another problem is associated with the weighting scheme by areas or volumes. In Figure 5.4, the

number density at a boundary node may be incorrect. For example, if node B in the picture on the right is on a boundary, then with a weighting scheme based on areas or volumes, the number density on node B will be $n/4 \times 2 = n/2$. Compensations will be necessary to correct the number density for all the boundary nodes on the inlets, outlet, walls and symmetric axis. Failure to perform compensation may result in some subtle problems in the simulation results. For example, on the symmetric line of an axi-symmetric simulation, E_y is usually correctly forced to be zero, but, some properties such as E_x on the axis and E_y on the layer of nodes next to the axis, and source terms on the axis will not be correct if the density on the axis is not compensated. Theoretically, a compensation of two times on the axis is only approximately correct for the axi-symmetric situation due to radial effects.

If the Boltzmann relation, Equation (2.6), is used to compute the plasma potential, the overestimated charge density may not result in significant problems. The mistake in plasma potential is globally offset by the logarithm function in Equation (2.6), and this error is further canceled in the calculation of the electric field by Equation (5.2). As a result, even though the number density and the plasma potential are calculated incorrectly by the weighting scheme of areas or volumes, the electric field is almost correct. This is the possible reason why there are no reports of this problem in the literature. However, weighting by areas or volumes for an unstructured mesh is not a correct approach and should be avoided.

For the detailed fluid electron model, which includes detailed physical terms and the potential is calculated by Equation (2.11), this mistake will create a false potential field. Further, for the ionization source term in Equation (5.1), both the charge density and the neutral density on a node will be overestimated, and a minimum of $4 \times 4 - 1 = 15$ times higher source term will be calculated for the ionization

process in Step 2. In the near field, the neutral number density is usually much higher than the ion number density, hence, an overestimated ionization rate will trigger a positive feedback for the ion number density. Finally, in the near field, a false high accumulation of ion number density will be generated and completely corrupt the potential field. For the detailed fluid electron model, where the potential calculation is more sensitive than the Boltzmann relation, the weighting scheme by areas or volume will trigger a chain reaction in ionization and finally invalidate the simulation. Hence, the first category of weighting schemes based on areas or volumes, is totally unusable on unstructured meshes for this detailed fluid model with ionization effects.

For the second category of weighting schemes, usually a correct charge allocation is always expected. In the literature, one option to calculate the charge density on a specific node is by summing up all particles inside the cells around the node then dividing by the total volume of all cells surrounding the node:

$$n = \sum_{j=0}^{N} N_j / \sum_{j=0}^{N} V_j \tag{5.16}$$

In [28], another scheme is reported which is similar but more accurate than Equation (5.16) and requires a high quality mesh. The total charge of a particle is assigned to the closest node from this particle. Though this scheme is physically accurate, there are situations when the nearest node to the particle is not one of the cell nodes forming the cell where the particle is located, such as regions near boundaries with boundary constraints.

The most common defect for the second category of weighting scheme is that it requires much cross node transportation on a parallel machine and it will be quite inefficient. The charge and neutral allocation scheme adopted in this study is a simple

one. First, the cell average values are calculated and then these values are averaged onto the nodes in the current processor. Suppose there are N cells connected to a node in one computer processor, and the jth cell has an average charge density n_j, then the charge density n on the node can be expressed as:

$$n = \sum_{j=0}^{N} n_j / N \tag{5.17}$$

This scheme does not require a complete list of cell average values for all cells physically connected to a node, but only cells in the same computer processor, hence, it is efficient on a parallel machine without significant loss of accuracy. The interpolation of electric field with the weighting scheme by areas or volumes is still correct and no change is necessary.

To effectively suppress statistical scatter in the charge density, this study further adopts a relaxation in charge and neutral density on a node:

$$n_{new} = 0.1 n_{alloc} + 0.9 n_{old} \tag{5.18}$$

where n_{new} is the current charge or neutral number density, n_{alloc} is the density obtained from the just mentioned allocation scheme, and n_{old} is the charge or neutral number density used in the last time step. For steady flow simulations, this treatment is effective in reducing statistical scatter.

5.3.5 Collision Dynamics

The DSMC method uses particles to simulate collision effects in rarefied gas flow by collecting groups of particles into cells that have a size of the order of a mean free path. In Step 6, pairs of particles inside a cell are selected at random and a collision probability is evaluated that is proportional to the product of the relative velocity and the collision cross section for each pair. The probability is compared

with a random number to determine if that collision occurs. If so, some form of collision dynamics is performed to alter the properties of the colliding particles. The No Time Counter(NTC) method [12] is adopted to determine if a collision occurs in this study. A special treatment to handle collisions between particles of different weights will be presented later.

There are two types of collisions that are important in these Hall thruster plumes: elastic, or momentum exchange(MEX) collisions and charge exchange (CEX)collisions. The elastic collisions involve only exchange of momentum between the participating particles. For atom-atom collisions, the Variable Hard Sphere [12] model is employed and the collision cross-section of xenon is:

$$\sigma_{el}(Xe, Xe) = \frac{2.12 \times 10^{-18}}{g^{2\omega}} m^2 \tag{5.19}$$

where g is the relative velocity and ω=0.12 is related to the viscosity temperature exponent for xenon. For atom-ion elastic interactions, one common choice is to use the following cross section of Dalgarno et al. [22]:

$$\sigma_{el}(Xe, Xe^+) = \frac{2.12 \times 10^{-18}}{g} m^2 \tag{5.20}$$

Another choice, which is adopted in this study, is to set the MEX cross section equal to the CEX cross section.

In all elastic interactions, the collision dynamics is modeled using isotropic scattering together with conservation of linear momentum and energy to determine the post-collision velocities of the colliding particles. Charge exchange concerns the transfer of one or more electrons between an atom and an ion. For singly and doubly charged ions, the following cross sections measured by Pullins et al. [45] and Miller et al. [35] are used:

$$\sigma_{el}(Xe, Xe^+) = 1.0 \times 10^{-20}(87.3 - 13.6 \log(\frac{m_c g^2}{2e}))m^2 \tag{5.21}$$

$$\sigma_{el}(Xe, Xe^{++}) = 1.0 \times 10^{-20}(45.7 - 13.6\log(\frac{m_c g^2}{2e}))m^2 \tag{5.22}$$

where m_c is the reduced mass.

5.3.6 Boundary Conditions

When an ion particle hits a wall, it loses its charge and reflects diffusely as a neutral particle with a thermal velocity characterized by a wall temperature of 300 K. For the thrusters in this study, the front wall and the center protection cap are dielectric, and the sheath voltage is significant. The sheath voltage for the front wall can be estimated by a transformation of Equation (2.9):

$$\phi_w = \phi_0 + \left(\frac{\overrightarrow{j}}{\sigma} - \frac{k \bigtriangledown (n_e T_e)}{e n_e}\right) \cdot d\overrightarrow{l} \tag{5.23}$$

where ϕ_0 is the potential at the node next to the wall. For other wall locations, a potential of 0 Volt is appropriate. The gradient of electron temperature is set to zero at each wall.

Several macroscopic properties of the plasma are required as boundary conditions for the computations. Specifically, the plasma potential, the electron stream function and the electron temperature are required for all boundaries. Table 5.1 summarizes the boundary conditions for the stream function, the plasma potential and the electron temperature, most of these values are the same as Reference [17]. As to electron stream functions, an essential requirement is, at both thruster exit and the cathode exit, two Neumann boundary conditions must be specified to satisfy the current density relations: $\frac{\partial \Psi}{\partial n} = \frac{J_a}{e}$ and $\frac{\partial \Psi}{\partial n} = \frac{J_c}{e}$, correspondingly.

At the thruster exit, for all heavy species, the number density, velocity and temperature are required. The setup employs a mixture of analysis and estimation based on experimental data of the mass flow rate from anodes and cathodes, thrust, and

total ion current. The neutrals are assumed to exit the thruster and cathodes at the sonic speed corresponding to assumed values for their temperature. Finally, a divergence angle of $\theta_+ = 30$ degree for the outer edge and $\theta_- = 20$ degree for the inner edges of the exit channel are assumed. The thruster and cathode wall temperature are set to 300 K.

Boundary	Outflow	Wall	Thruster Exit	Cathode	Symmetric Plane
$\phi(V)$	2	0 or Eqn.(5.23)	93.0	7.0	$\frac{\partial \phi}{\partial n} = 0$
$\Psi(m^{-1}s^{-1})$	$\frac{\partial^2 \Psi}{\partial n^2} = 0$	0	$\frac{\partial \Psi}{\partial n} = \frac{J_c}{e}$	$\frac{\partial \Psi}{\partial n} = \frac{J_a}{e}$	$\frac{\partial \Psi}{\partial n} = 0$
Te(eV)	0.6	1	6.0	2.0	$\frac{\partial Te}{\partial n} = 0$

Table 5.1: Boundary Conditions for the Detailed Electron Fluid Model.

5.3.7 Backpressure Treatment

Hall thrusters are designed for use in space, where almost perfect vacuum exists, but they are tested in ground vacuum chambers such as the LVTF, where a finite background chamber pressure always exists and that may result in adverse effects on the performance of thrusters. Meanwhile, according to the discussions in chapter III, the semi-decaying period for the evolution of background gas in a cylindrical chamber can be expressed as:

$$\tau_d = \frac{V\sqrt{2\pi m}}{\alpha s_p \sqrt{kT_w}} = \frac{L\sqrt{2\pi}}{\alpha s \sqrt{RT_w}} \tag{5.24}$$

For the LVTF, the semi-decaying period is on the order of one second with a chamber length of 9 meters, 4 thrusters and 4 pumps in operation. Because a DSMC-PIC simulation must use small time steps such as 1×10^{-7} sec, it takes over 50 million time steps for the chamber background flow to reach a steady state. Further, considering the space discretization cost, a full scale three-dimensional DSMC-PIC simulation is

impossible. In this study, the three-dimensional simulation is limited to a reduced scale of a cylindrical domain close to the thruster clusters. With this simplified approach to simulate the plume flow inside a vacuum chamber, the background flow must be properly estimated and included in the simulations.

As discussed in Chapter III, there are several key vacuum facilities effects that have effects on the backpressure in a vacuum chamber, such as the vacuum pump sticking coefficient, the vacuum pump area, and the chamber side wall. Among these facility effects, the vacuum pump sticking coefficient has the most important effects. For the experimental measurements in [8], four two-sided cryogenic pumps in LVTF were operated. As pointed out in [9], propellant frost will build up on cryopump surfaces and eventually will limit the pumping speed, hence, even though the nominal sticking coefficient for xenon on steel is high at 15 K, in real experimental operation, the sticking coefficient for pumps may be much lower. From the results in Chapter III, the number density, backpressure, average velocity and velocity distribution function at the pre-pump region are Equations (3.21), (3.25), (3.27)and (3.23).

Experimental measurements [8] indicated there was a backpressure of 4.78×10^{-4} Pa with four thrusters and four vacuum pumps (s=0.1460) in operation. With a mass flow rate of 0.833 mg/sec from each anode and 0.098 mg/sec from each cathode, the pump absorption coefficient computed from Equation (3.25) is 0.39, which is consistent with the conclusions in Chapter III based on other measurements [59] in the LVTF. The mean background flow velocity computed with Equation (3.27) is about 6.0 m/sec with four thrusters and four pumps in operation.

In the particle simulations, the most convenient treatment of background pressure is to adopt static background particles: inside each cell, there are a few particles with velocities sampled from a zero-centered Maxwellian velocity distribution func-

tion. These particles participate in collisions with normal particles and change the velocities of other particles, but their positions and velocities do not change. In this study, a similar background particle treatment is adopted with few modifications in Chapter III. The number density calculated from Equations (3.25) is slightly less than the values obtained directly by $n = P_b/(kT_w)$, and their velocities are assigned from Equation (3.23), not a zero-centered Maxwellian distribution. There is a net average velocity towards the thrusters for the background particles. Because Equations (3.25) and (3.26) consider multiple factors from pumps such as the pump area and the absorption coefficient, thruster effects such as the mass flow rate, the chamber effects such as the backpressure and properties of the propellant, it is reasonable to expect a more accurate result than the traditional treatment of background static particles with assigned velocities sampled from a zero-centered Maxwellian distribution.

5.3.8 Particle Weight

In this study, the inlet boundary conditions have quite different scales. For the cathode, the diameter is about 5.08×10^{-4} m, though the neutral number density at the cathode exit is greater than that at the anode exit, the fluxes of ions and neutrals from the cathode are smaller than those from the anode. To address this problem, particle weighting is enabled in MONACO. Each particle introduced at the cathode and anode is assigned with a relative weight ratio W_p. The real particle weight is decided by multiplying this W_p with the local cell weight ratio W_c. When particles travel from one cell into another, a clone process is performed based on the two cell weight ratios, and this particle's relative ratio does not change. Background static particles are assigned with weight ratios as well.

This treatment effectively resolves the problem of different fluxes from cathodes and anodes. One issue for this different particle weighting is collisions, and it is handled using the following procedure: when two particles collide, the heavier particle is split into two particles: one split particle has the same weight ratio as the other particle and a collision is performed between these two particles with the same weight; the other split particle keeps the rest of the weight and does not participate in collision. This treatment is quite similar to [18], which reported a simulation of flows with trace species.

One issue should be handled carefully. In axi-symmetric simulations and three-dimensional simulations, cell volumes change dramatically. For example, in the former case, cells at a large radius have a large volume while cells around the axis have quite small volumes. In these three-dimensional simulations, cells at the outer boundary and cells around the cathodes have quite different cell volumes. The relative particle weights for the background static particles are quite different, and can be much smaller than those for a normal particle. When a normal particle and a background static particle collide, if the normal particle's weight ratio is greater than the static particle, then a split of the normal particle should be processed. Failure to perform this process results in a false velocity change for the normal particle.

This splitting scheme is quite effective for the problems in this study. One side-effect of this scheme is it results in an increasing number of low-weight particles due to collisions. For neutral particles, a special process is implemented to reduce their number: if a neutral particle's relative weight W_p is larger than a threshold value W_{thresh}, it is kept in the simulation without a weight change; otherwise, it is either discarded from the simulation, or kept in the simulation statistically by changing its relative weight ratio to the threshold value. For ion particles, they

are essential to the simulations, hence their weights are unchanged and all ions are kept in the simulation. For DSMC-PIC simulations with background static particles representing a finite backpressure, the process is like a slow diffusion process: a large amount of slow ions slowly diffusing in the simulation domain. This represents a problem to be addressed in a future study.

5.3.9 Code Implementation

In this study, there are some concrete code implementations and re-engineering to improve MONACO interface and structure, and they are summarized in Appendix F.

5.4 Simulations and Results

In this study, three DSMC-PIC particle simulations are performed to simulate plume flows from one, two and four BHT200 thrusters. Due to the setup symmetry, only one thruster is needed in the simulation and the results for cases with two and four thrusters in operation are obtained by symmetric reflections.

A specific PIC module is implemented in MONACO. Three unstructured meshes are generated with the software Hypermesh [5]. The very detailed geometries of the 7 mm conic cap and the small cathode are included in the meshes. The cathode exit plane is an orifice with a diameter of 5.08×10^{-4} m. It is a challenge for meshing and the circular cathode exit plane is simplified with six triangles by conserving the same exit area. Later simulation results indicate that the cathode has important effects on the flowfield, hence, the preservation of the cathode geometry is quite essential. All simulations use three static background particles per cell and all time steps are set to 2×10^{-7} second.

Table 5.2 lists several details for these simulations. The finite element solver is called every 10 time steps for Equations (2.7), (2.11), (2.12) and takes a significant

fraction of the simulation time. The simulations take 40,000 time steps to reach a steady stage and another 20,000 time steps for sampling.

Ths	Domain (cylinder)	Triangular cells	Tetra-hedrons	Particles (million)	Time (Hours)	Machine
1	Full	32,550	971,796	10.8	230	Parallel, 8 CPUs
2	1/2	34,058	829,243	6.3	160	Parallel, 8 CPUs
4	1/4	41,972	556,796	5.2	120	PC, 2.1GHz

Table 5.2: Simulation Details.

5.4.1 Axi-symmetric Benchmarks:Current Density for Single BHT200

To confirm the validity of new code implementation, an axi-simulation of the plasma plume flow from a single BHT200 without background was performed and the results were compared with another hybrid code, which was well-tested in the past. Most results from both codes were compared and in general, the comparisons were quite satisfactory. Among these results, the most sensitive benchmarks are the current density at constant radius from the thruster center. And Figures 5.5 and 5.6 are two comparisons of the current density results sampled from a fixed radius of 25cm or 50cm in front of the thruster center. Both of the results show almost identical results from these two codes.

5.4.2 Comparison With Measurements

Electron Temperature

Figures 5.7– 5.9 show contours of electron temperature with 1, 2 and 4 thrusters in operation. With more thrusters in operation, the contours extend further down-stream. Figures 5.10 and 5.11 shows comparisons of electron temperature along several thruster centerlines and two cluster centerlines. It is significant to mention

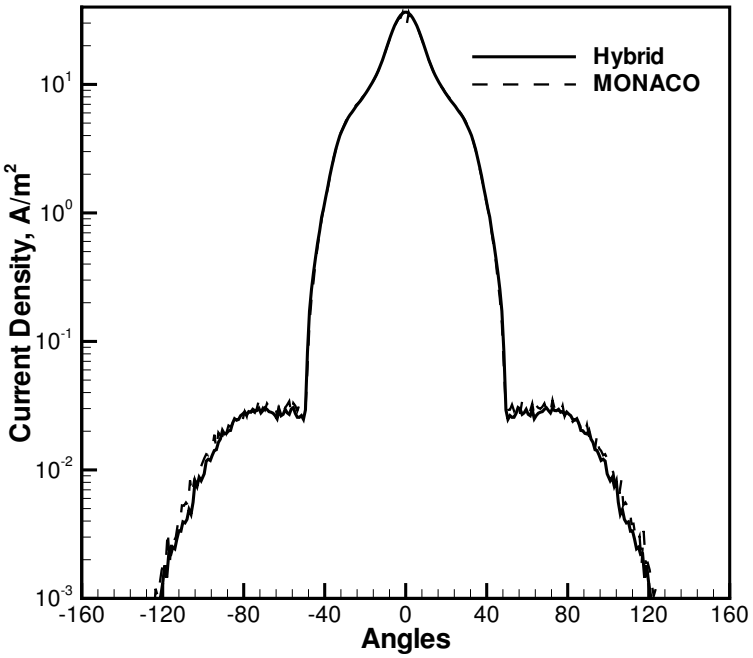

Figure 5.5: Comparison of Current Density Cross Fixed Radius from the Thruster Center(R=25cm, 1 Thruster in Operation, without backpressure).

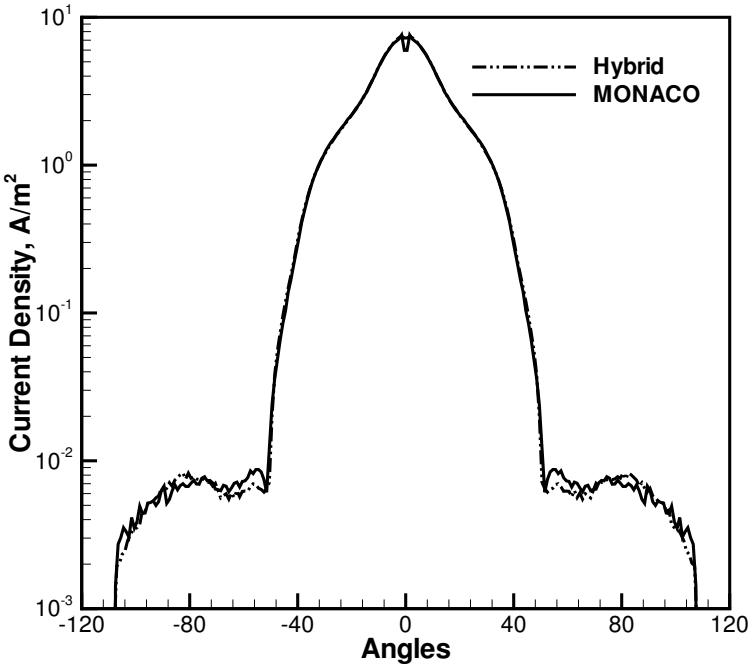

Figure 5.6: Comparison of Current Density Cross Fixed Radius from the Thruster Center(R=50cm, 1 Thruster in Operation, without backpressure).

that the Boltzmann relation assumes a constant electron temperature and cannot predict any variation. The detailed fluid electron model yields a non-constant electron temperature field that is more physically reasonable. In Figure 5.10, the circles represent experimental measurements along the centerline of a thruster acceleration channel with one thruster in operation. The solid line represents the corresponding simulation result with one thruster in operation. The comparison indicates that the numerical simulation results are close to the experimental measurement data. It is also evident that with several thrusters in operation, the centerline electron temperature is slightly different in the near field and has a large difference in the far field. With more thrusters in operation, cluster centerline values and thruster centerline values merge at a short distance from the thrusters, correspondingly. The closer to the thruster exit, the higher the electron temperature, and the simulation results predict that the electron temperature from different plumes merge at station X=0.08 m. The experimental data was obtained with a triple Langmuir probe. This is one of the most important results in this study because these results clearly indicate the superiority of this detailed electron model over the Boltzmann relation, and it clearly displays the clustering effects as well.

Plasma Potential

Figure 5.12 shows contours of plasma potential in the plane y=0 with 4 thrusters in operation. In the near field, the plumes are well separated while at a short distance from the thruster exit plane they merge into one plume. Compared with the electron temperature results, the plasma potential merges at a further downstream station, X=0.15 m.

Figures 5.13, 5.14, 5.15 and 5.16 present comparisons of plasma potential along

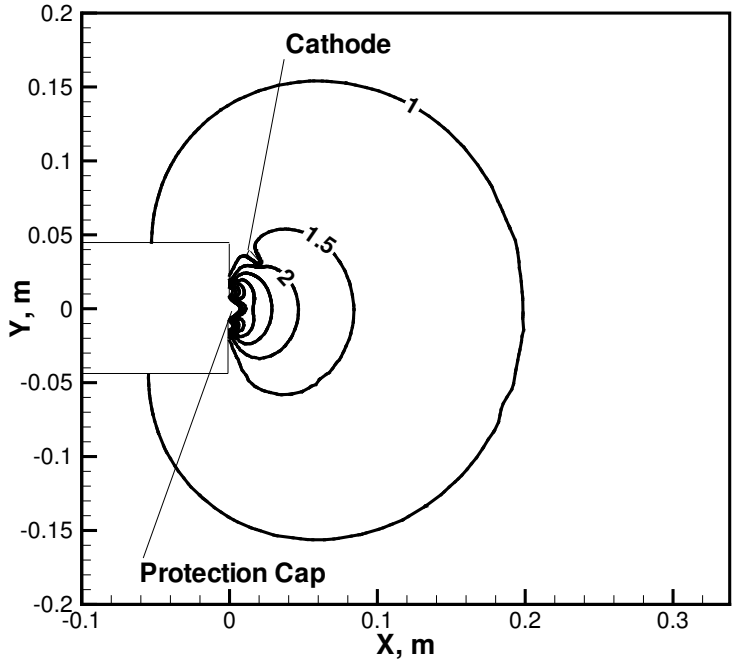

Figure 5.7: Contours of Electron Temperature (eV) in the Plane Through Thruster 1 (increment=0.5 eV, 1 Thruster in Operation).

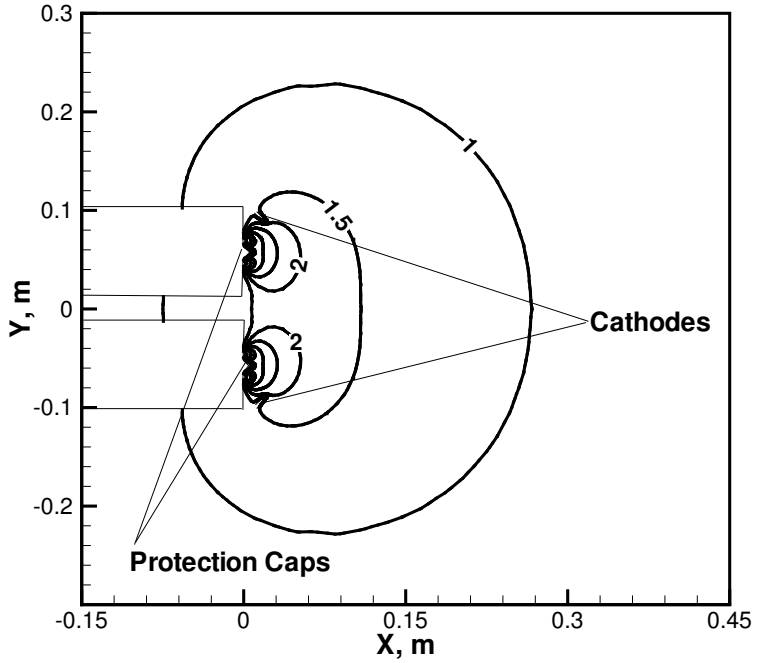

Figure 5.8: Contours of Electron Temperature (eV) in the Plane Through Thrusters 3 and 4 (increment=0.5 eV, 2 Thrusters in Operation).

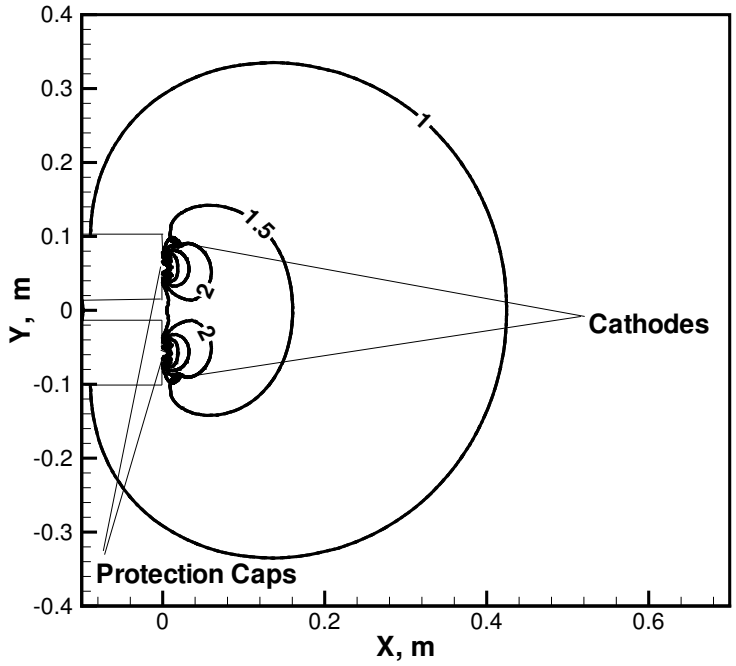

Figure 5.9: Contours of Electron Temperature (eV) in the Plane Through Thrusters 3 and 4 (increment=0.5 eV, 4 Thrusters in Operation).

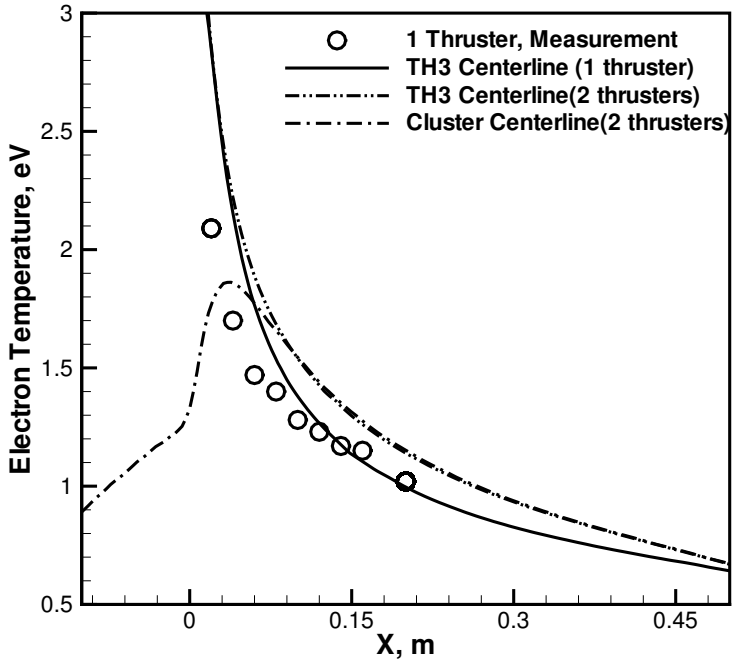

Figure 5.10: Profiles of Electron Temperatures (eV) along Different Centerlines(I).

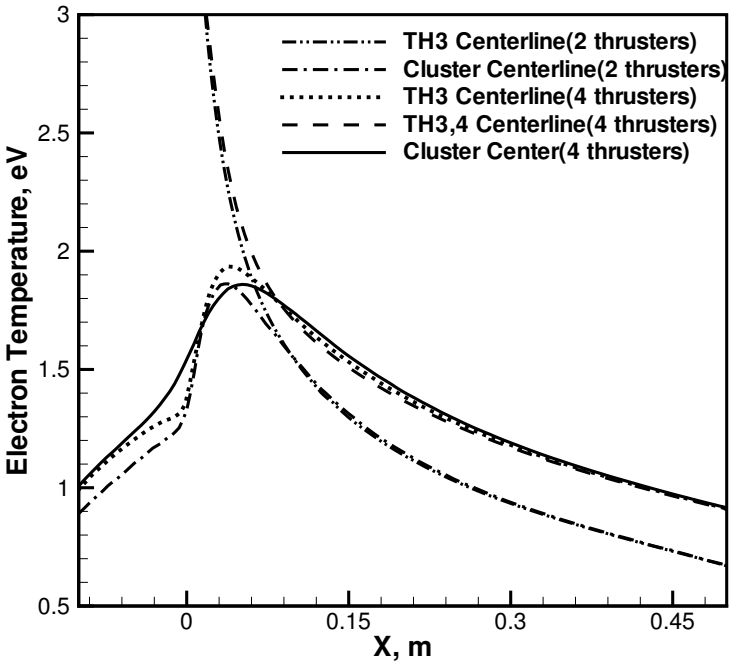

Figure 5.11: Profiles of Electron Temperatures (eV) along Different Centerlines(II).

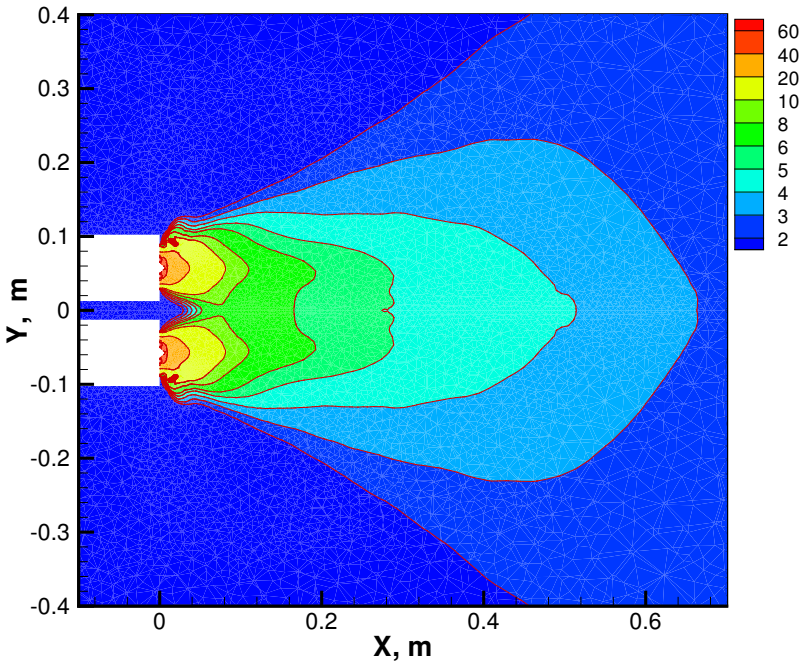

Figure 5.12: Contours of Plasma Potential(V) in a Plane Through Thrusters 3 and 4 (4 Thrusters in Operation).

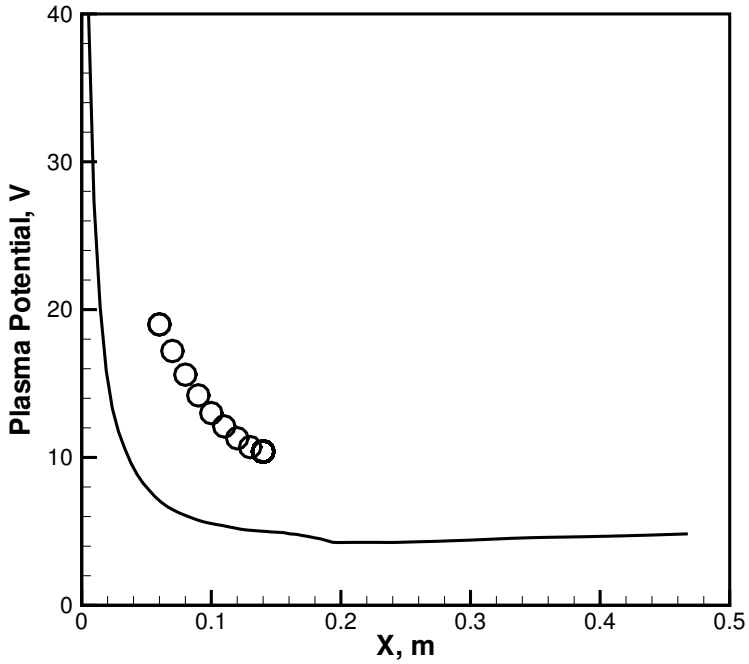

Figure 5.13: Profiles of Plasma Potential(V) along Centerline (I)(1 Thruster in Operation).

different centerlines and at the station X=0.05 m. The experimental data in these three pictures were obtained with one or two thrusters in operation. In general, these simulations yield lower plasma potentials than the experimental measurements, especially for the situation of one thruster in operation. This defect is possibly related with linear finite element used in this study and the sparse mesh in 3D simulations, this problem will be explained in detail at the end of this chapter. Figure 5.15 shows that the plasma potentials along different centerlines converge into one universal distribution at about X=0.15 m, which indicates that the four or two plume flows merge into one. These three figures also indicate that the numerical simulation predicts lower potential peak values than the experimental measurements at specific locations. However, they predict a matching distribution along the centerline passing through the middle point of two thrusters, and the general shape of the computed

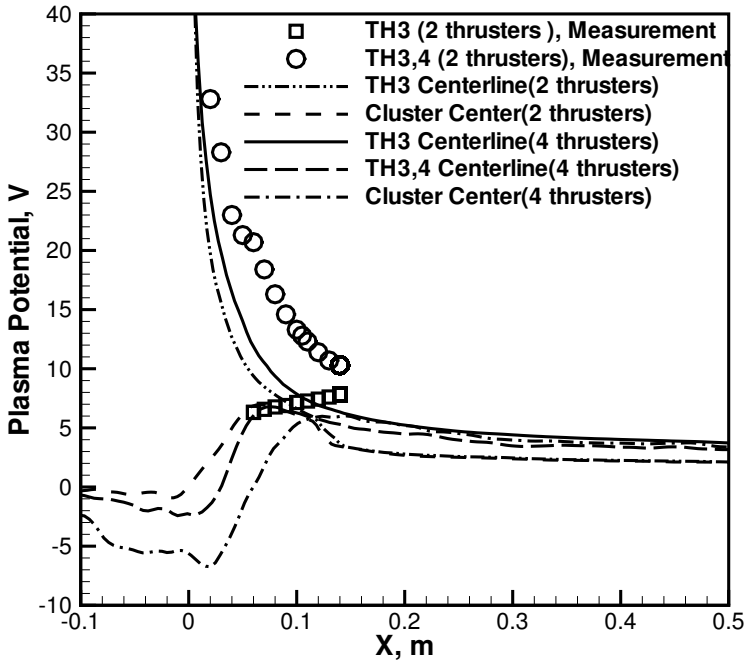

Figure 5.14: Profiles of Plasma Potential (V) along Centerlines(II).

potential profile at X=0.05 m fits the experimental measurement as well.

Electron Number Density

Figures 5.17– 5.19 show the ion number density contours in plane y=0 with 1, 2 and 4 thrusters in operation. This plane intersects the 7 mm conic protection caps and the cathodes. These figures indicate that there is a high ion number density accumulated next to the protection cap, and the plumes from different thrusters eventually merge into one. The bulges in the outer region of the contours close to the thrusters result from the CEX effects and a large density of slow ions exists in these regions. These figures evidently indicate the cathode and cluster effects: the flowfield of one thruster is not symmetric about its axis and the plumes from different thrusters interact. Another observation is that the value of ion number density around the cathode is much higher than the value when one or two thrusters are in operation. Though these simulations include the ion flux from the cathodes,

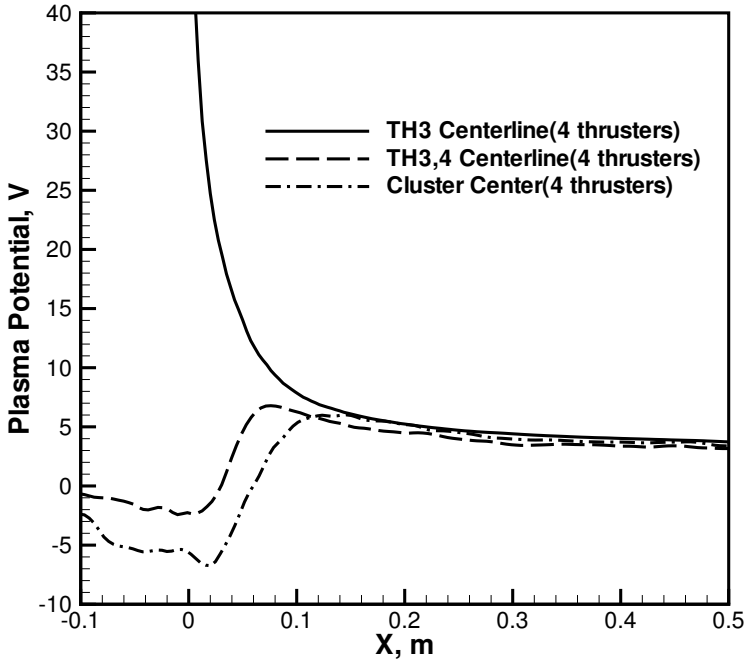

Figure 5.15: Profiles of Plasma Potential (V) along Centerlines(III).

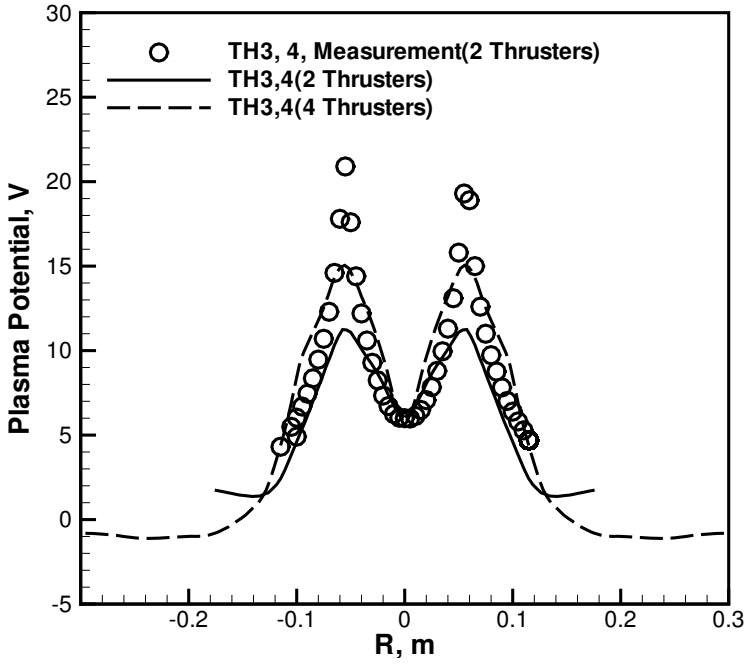

Figure 5.16: Plasma Potential(V) at Station X=5 cm and through the Horizontal line.

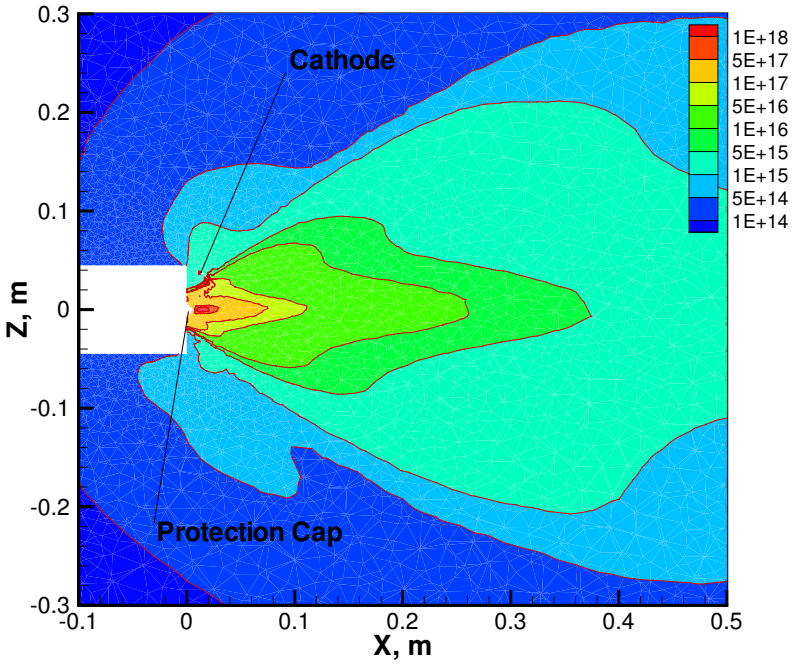

Figure 5.17: Contours of Ion Number Density (m^{-3}) in the Plane through Thruster 1 (1 Thruster in Operation).

the flux amount is quite small. The physical explanation for this phenomenon is that neutrals emitted by the cathode collide with the plume beam, then due to CEX effects, one fraction of the slow ions reflects upward and forward. Further, the three cases also indicate that with more ions coming out from two or four thrusters, the plume cores extend significantly downstream, and finally they merge into one plume again.

Figures 5.20, 5.21 and 5.22 show electron number densities along different centerlines and at station X=0.20 m. Figure 5.20 and 5.21indicate that the number densities from all four plumes merge into one at the station around X=0.20 m while two plumes merge into one at the station around X=0.50 m. Electron number density obtained from a Langmuir probe contains significant experimental uncertainty [29]. Three different profiles of measured data by Brian Beal are shown representing two

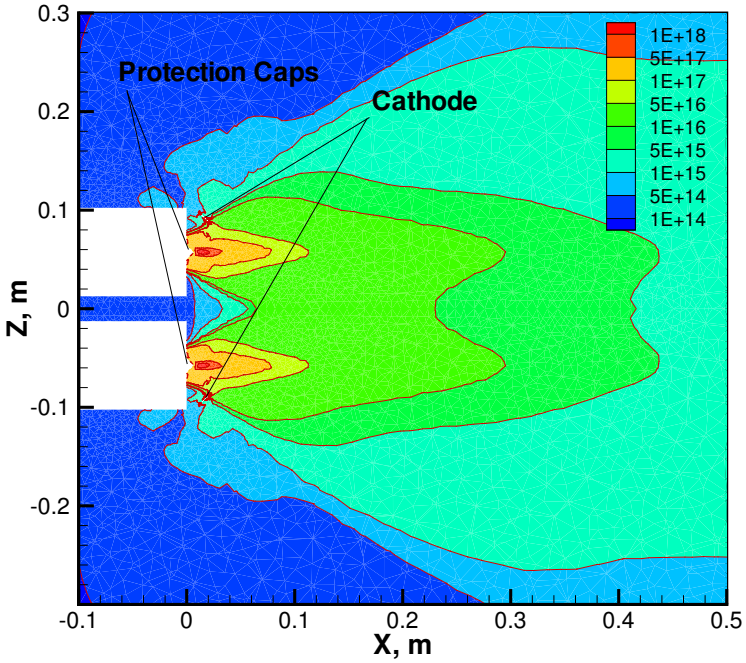

Figure 5.18: Contours of Ion Number Density (m^{-3}) in the Plane through Thrusters 3 and 4 (2 Thrusters in Operation).

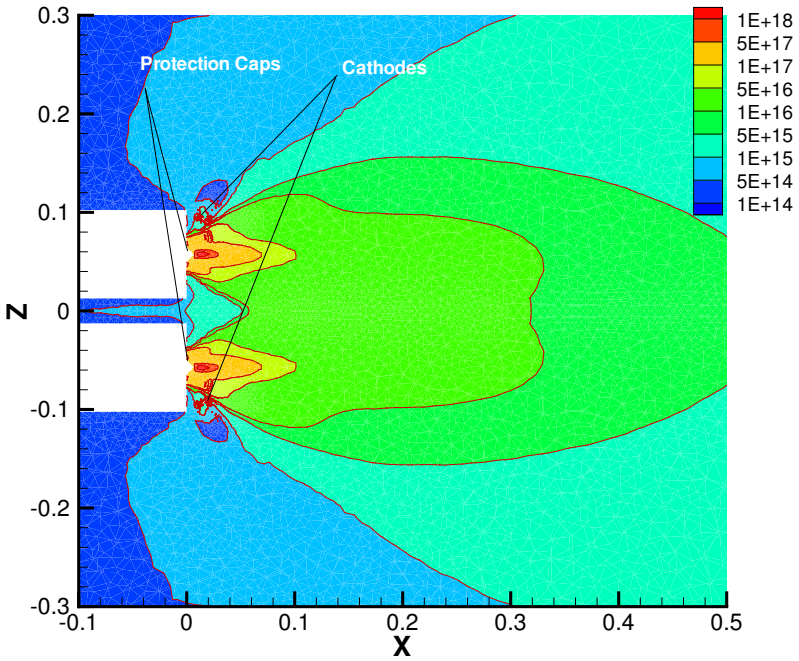

Figure 5.19: Contours of Ion Number Density (m/s) in Plane Y=0 cm (4 Thrusters in Operation).

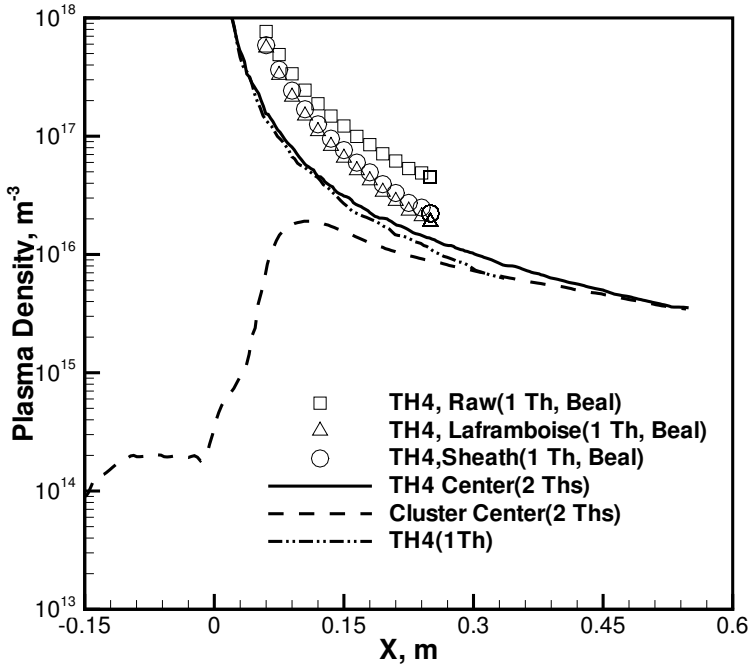

Figure 5.20: Profiles of Electron Density (m^{-3}) along Different Centerlines.

different corrections to the raw data. The profile labeled "sheath" assumes that the probe collection radius is increased by a sheath of five Debye lengths, thus leading to a reduction in plasma density. The profile labeled "Laframboise" incorporates corrections due to the slightly different voltages applied to each of the three probes in the instrument. The correction is sensitive to the ratio of electron to ion temperature, and a ratio of one is assumed in the corrected data shown here. Comparisons indicate that in general the numerical results predict significantly lower values than the experiments. However, the sheath and Laframboise corrected data yield better agreement with the simulation data.

5.4.3 Clustering Effect

It is interesting to observe some topographic patterns formed by clustering thrusters in the near field number density. Figure 5.23 shows the ion number density at station X=2 cm with 4 thrusters in operation. Figure 5.24 shows the corresponding

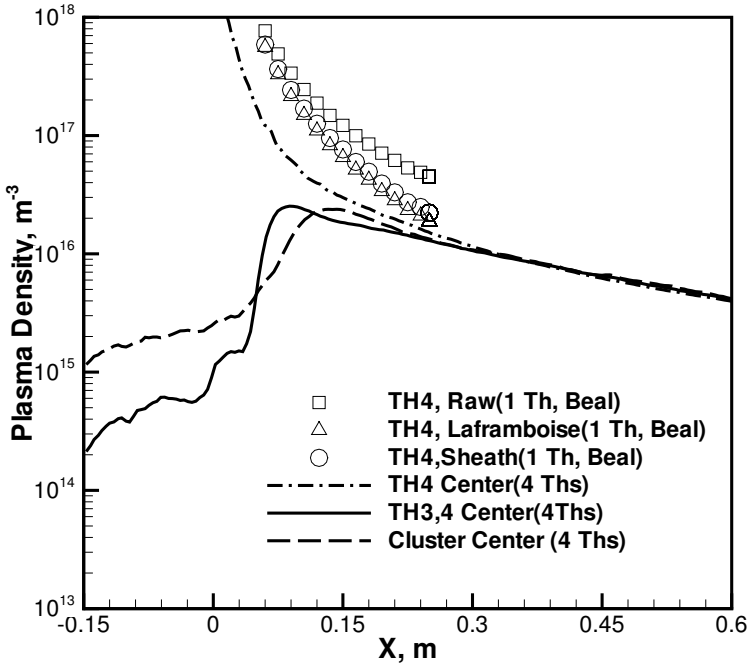

Figure 5.21: Profiles of Electron Density (m^{-3}) along Different Centerlines.

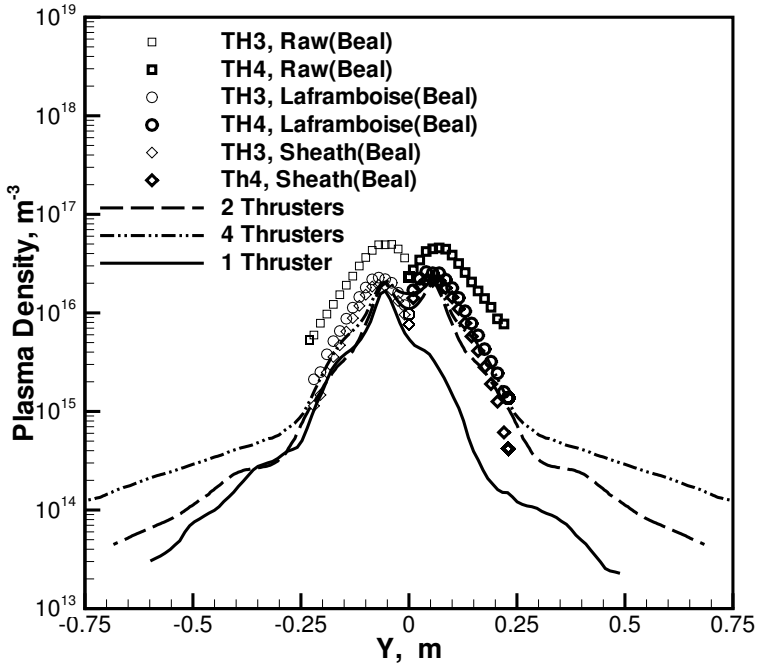

Figure 5.22: Profiles of Electron Density (m^{-3}) at Station X=20 cm and Passing Through Thruster Centerlines.

plasma potential. Note that the contour increments are not uniform in both results. Figure 5.23 indicates that with a cluster of four thrusters in operation, a special three-dimensional structure occurs in the ion number densities. With two thrusters in operation, the middle point between the two thrusters is an unstable saddle point which has a lower potential than the plume core, but a higher potential value than the far field. Hence, slow ions diffuse along all directions, there exists two spots close to the cathodes with relatively high density of slow ions due to the CEX effects. However, with four thrusters in operation, the topographic pattern of ion density in the near field is quite different. The four thruster centers represent high potential values because of the large amount of ions in the plume cores. When CEX happens, slow ion particles may freely diffuse away along the electric field direction opposite to the cluster center, hence low ion densities exist along four major diffusion directions of 45 degree, 135 degree, 225 degree and 315 degree, as indicated by Figure 5.23. Meanwhile, a portion of slow ions may travel along the electric field direction to the cluster center, which has a relatively lower potential value than the plume core and a zero value of electric field. With more slow ions accumulated at the cluster center, a special cusp shape is formed at the cluster center. There are slow ions coming from the four thruster plume beams, and at the same time, there are slow ions escaping through the four low potential gaps between the thrusters, i.e. 0 degree, 90 degree, 180 degree and 270 degree. These escaping slow ions form a special pattern of a four-leaved clover. There are four small secondary leaves in the contours as well, which are generated by the cathode. A relatively large amount of slow ions are created around the cathodes, without electric field effect, they should diffuse upwards or downwards. However, with the effects of the electric field, these slow ions diffuse outside along the four directions with the strongest electric field strength: 45 degree,

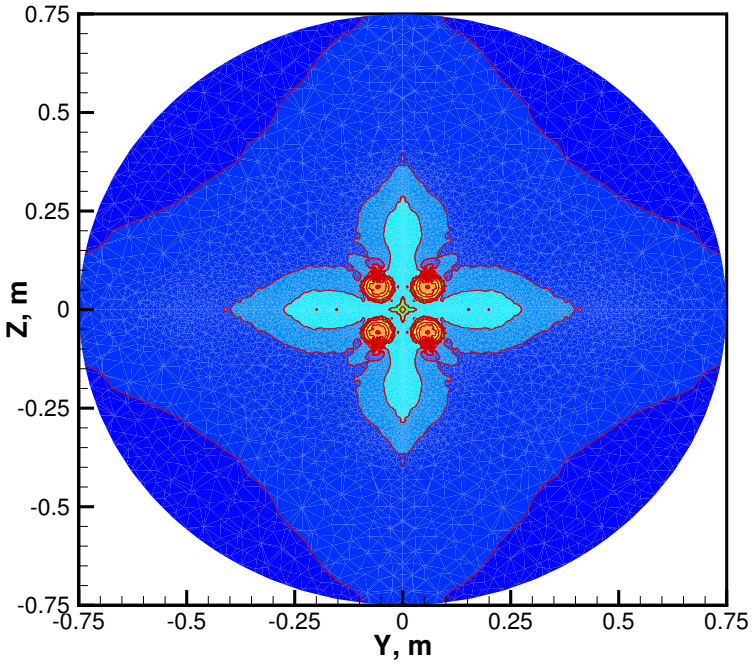

Figure 5.23: Contours of Ion Number Density (m^{-3}) at Station X=2 cm (4 Thrusters in Operation).

135 degree, 225 degree and 315 degree. In the near field, a special topography is formed: four strong plume cores with a low potential at the cluster center, 4 major leaves and 4 secondary leaves represent diffusion directions for the slow ions. Further downstream, the strengths of these four beams decrease quickly and eventually merge into one plume. Probably Figure 5.23 is one of the most interesting results obtained in this study, and it clearly illustrates the CEX effects, clustering effects and cathode effects. In the corresponding neutral number density contours, Figure 5.25, neutral particles simply diffuse along all directions, and no special topography is found.

Figure 5.26 shows several profiles of ion density along different centerlines. It is evident that with four thrusters in operations, a fraction of slow ions originally diffusing radially is trapped at the cluster center and due to electric field effects, these slow ions flow backwards and escape to the back of the thruster. Hence, a severe

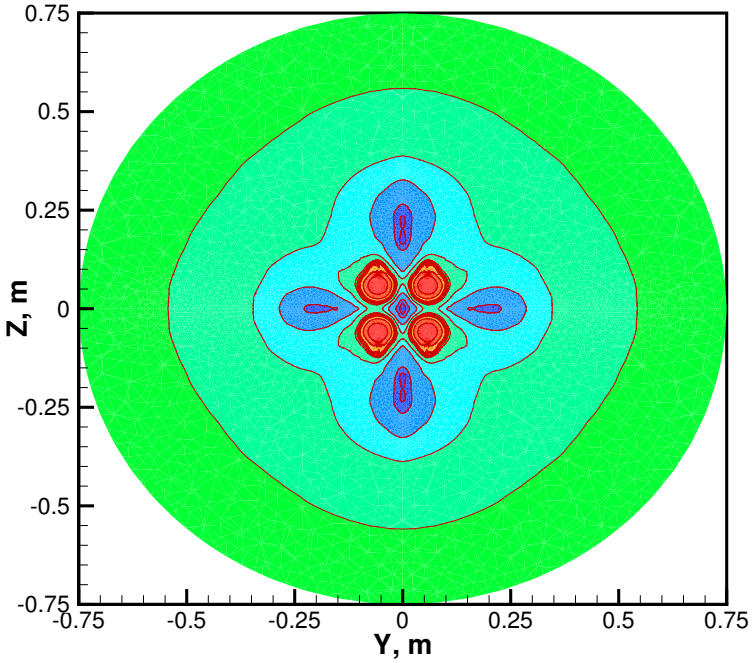

Figure 5.24: Contours of Plasma Potential (V) at Station X=2 cm (4 Thrusters in Operation).

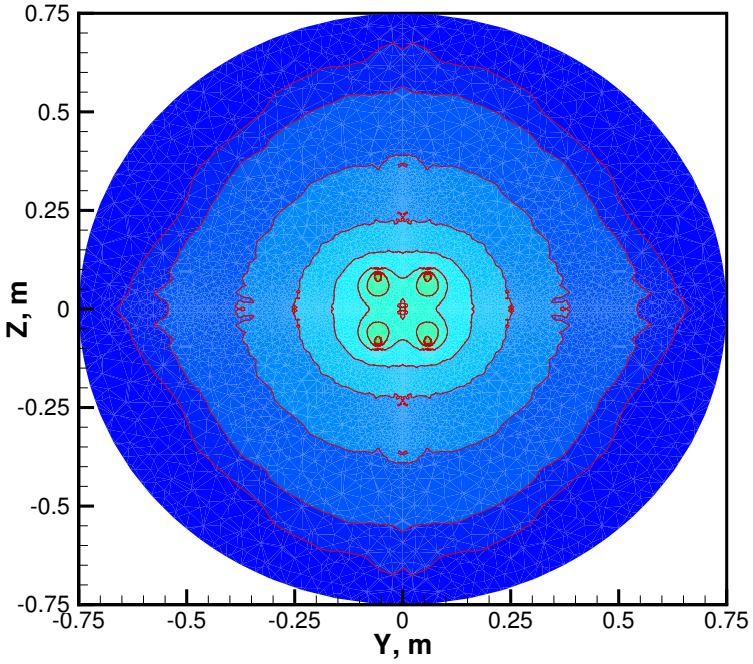

Figure 5.25: Contours of Neutral Number Density (m^{-3}) at Station X=2 cm (4 Thrusters in Operation).

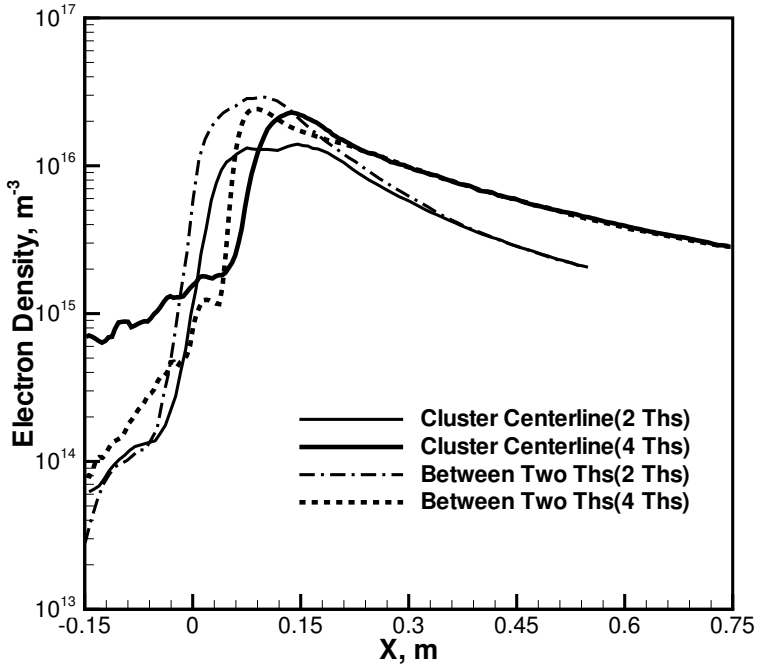

Figure 5.26: Distribution of Electron Number Density (m^{-3}) along Lines Passing Through the Cluster Center and Midpoint of Two Thrusters(Two or Four Thrusters in operation).

impingement at the back of the cluster is expected because of a higher ion number density.

5.4.4 Cathode Effects

Cathode effects can be illustrated by velocity and number density contours. Figures 5.27 – 5.30 show several contours of ion and atom velocity in a vertical plane that includes the cathode for one and two thrusters in operation. These figures illustrate that the cathode has several effects on the ion and atom velocity distributions. The existence of a cathode in all of these plots results in special areas around the cathodes. In the near field close to the thruster exit, the ion velocity is accelerated by the strong electric field, while further down stream, the ion velocity changes slowly because of CEX effects. The latter effect is clearly illustrated by the contours of neu-

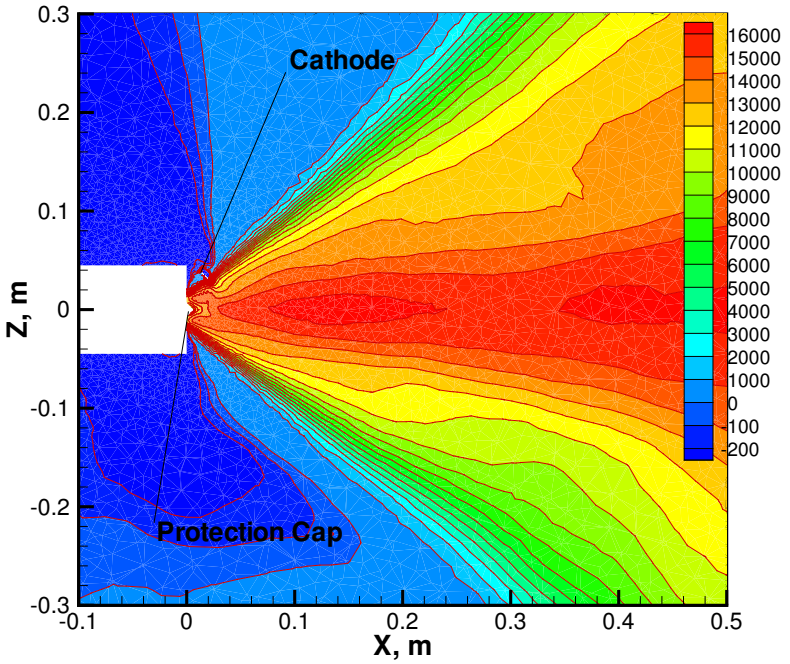

Figure 5.27: Contours of Ion Velocity(m/s) along X Direction Passing Through Thruster 1 (1 Thrusters in Operation).

tral velocity where accelerations occur downstream. The neutral density around the thruster is high, but quickly decreases in all directions. With a decreasing percentage of slow neutrals, the percentage of fast neutrals, as a result of CEX effects, increases at the same time. As a net effect, the neutral velocity is accelerated downstream. The corresponding results for four thrusters in operation are quite similar with the situation of two thrusters in operation, hence they are omitted. Figures 5.31– 5.32 clearly show the cathode effects. These figures indicate that it is important to include the cathode in a plume flow simulation.

5.4.5 Analysis of Neutral Flow

The neutral number density can be predicted with a simple free molecular flow model. Because the neutral flow is highly rarefied, the Knudsen number for neutrals is about 55 for a channel height of 7.5 mm. Hence the neutral number density

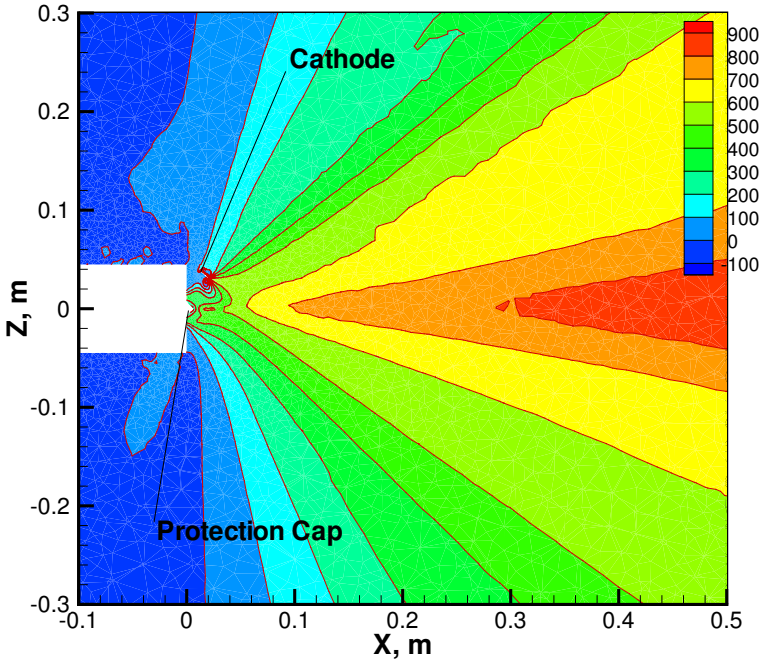

Figure 5.28: Contours of Neutral Velocity(m/s) along X Direction in the Plane Through Thruster 1 (1 Thruster in Operation).

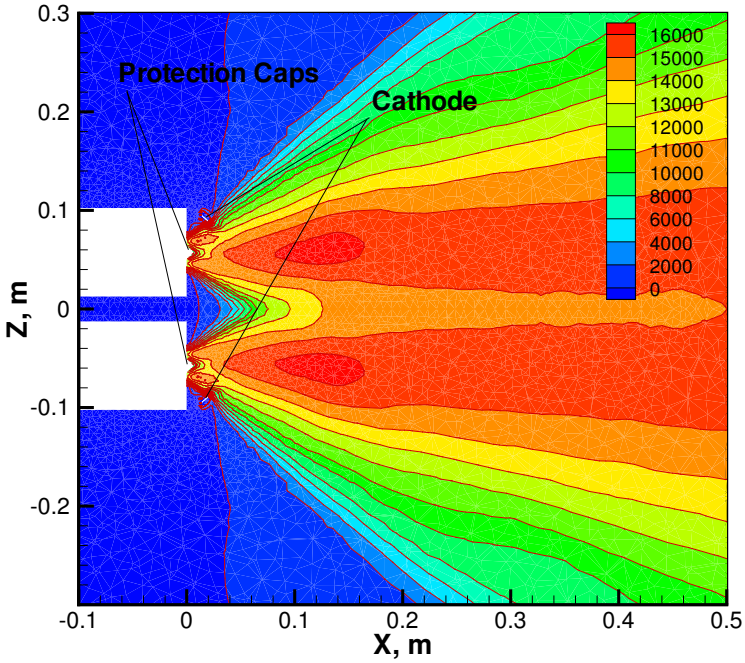

Figure 5.29: Contours of ion Velocity(m/s) along X Direction Passing Through Thrusters 3 and 4 (2 Thrusters in Operation).

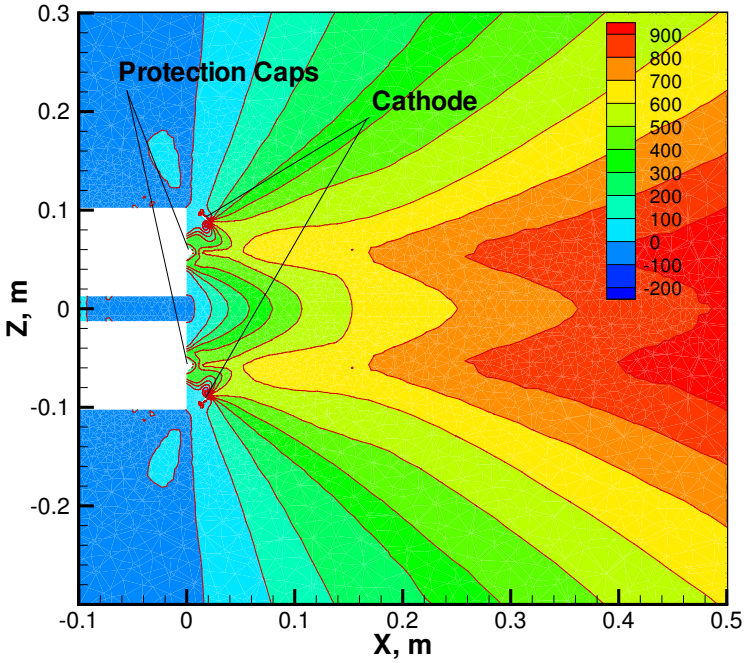

Figure 5.30: Contours of Neutral Velocity(m/s) along X Direction Passing Through Thrusters 3 and 4 (2 Thrusters in Operation).

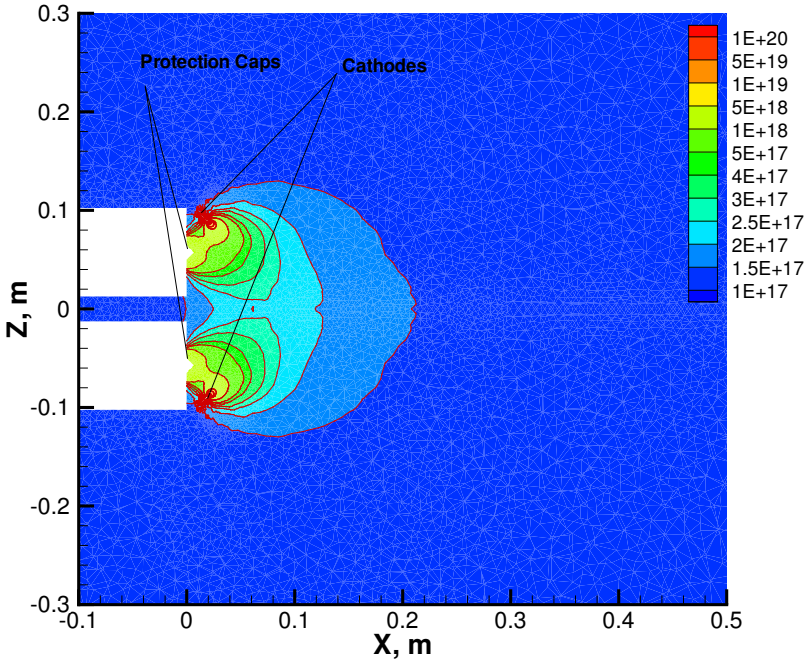

Figure 5.31: Contours of Neutral Number Density (m^{-3}) in Plane Y=0 cm (4 Thrusters in Operation).

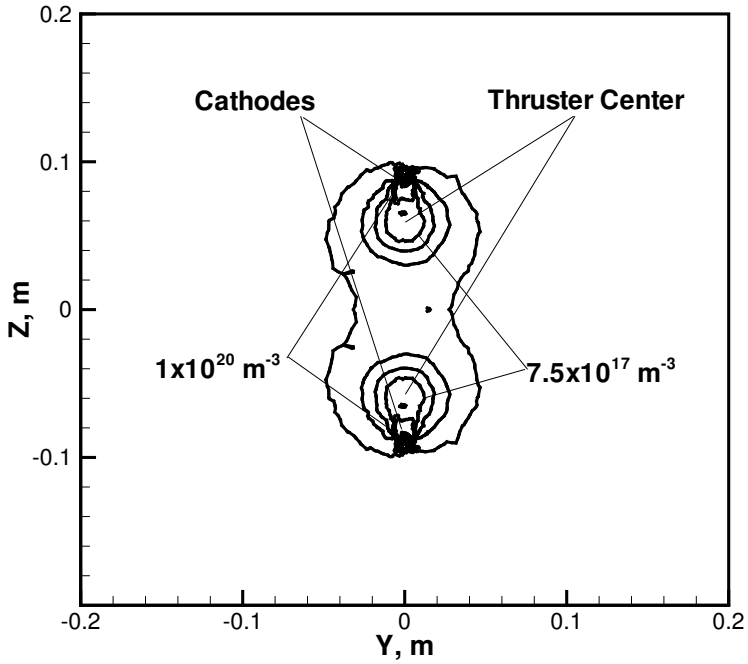

Figure 5.32: Contours of Neutral Number Density (m^{-3}) at Station X=2 cm (2 Thrusters in Operation).

distribution, with four thrusters in operation, can be approximated by a free molecule flow model with zero mean velocity from four small annular sources for the thrusters and four small orifices for the cathodes. At any specific point with coordinates (x, y, z) in front of the thrusters, the velocity phase at that point can only have non zero values within specific solid angles from the four ring sources of thrusters and four small orifices for the cathodes. The number density distribution at any point can be estimated by the solid angles at that point subtended by these four ring sources and four cathodes. The derivation process is straightforward but tedious and the final expression for the solid angle is listed in Appendix G.

With four thrusters in operation, the final expression for the number density at

any point in front of the thruster cluster is:

$$\begin{aligned} n(x,y,z) = \quad & n_{back} + \tfrac{x(R^2-r^2)n_a}{4\pi}(F(A_1,A_2)+F(A_3,A_4)+F(A_5,A_6)+F(A_7,A_8)) \\ & +\tfrac{n_c}{4\pi}(H(n_{x1},n_{y1},n_{z1},b,a,d)+H(n_{x2},n_{y2},n_{z2},b,-a,d) \\ & +H(n_{x3},n_{y3},n_{z3},b,-a,-d)+H(n_{x4},n_{y4},n_{z4},b,a,-d) \end{aligned} \tag{5.25}$$

With two thrusters or one thruster in operation, the corresponding results are a fraction of Equation (5.25).

Figure 5.33 presents the comparison between the simulation results and the analytical results along different centerlines with 4 thrusters in operation. Both the simulation results and the analytical results present the same trends: The neutral number density along the cluster centerline and the centerline of vertical/horizontal planes first increases quickly then decreases slowly with a maximum value at a specific distance from the thruster; the maximum value along the cluster centerline is further downstream from the thruster face and is smaller than the value on the centerline between two thrusters. The difference between simulation and analytical results can be explained by the following factors omitted in this crude analytical model: wall effects, the MEX and the CEX effects and the non-zero mean velocity at the exit planes of anodes and cathodes. Especially, the wall effect is significant in the very near field because the thruster wall area is large, and the non-zero average speed may have significant effects as well. Despite these factors, the comparison still yields a certain agreement.

The cathode is included in this simulation essentially as a source located off the thruster wall, while for the axi-symmetric simulation in [17], the cathode was treated as an annulus on the thruster front face without mass flux. In addition, the protection cap was not included in [17]. Due to these differences, though most of

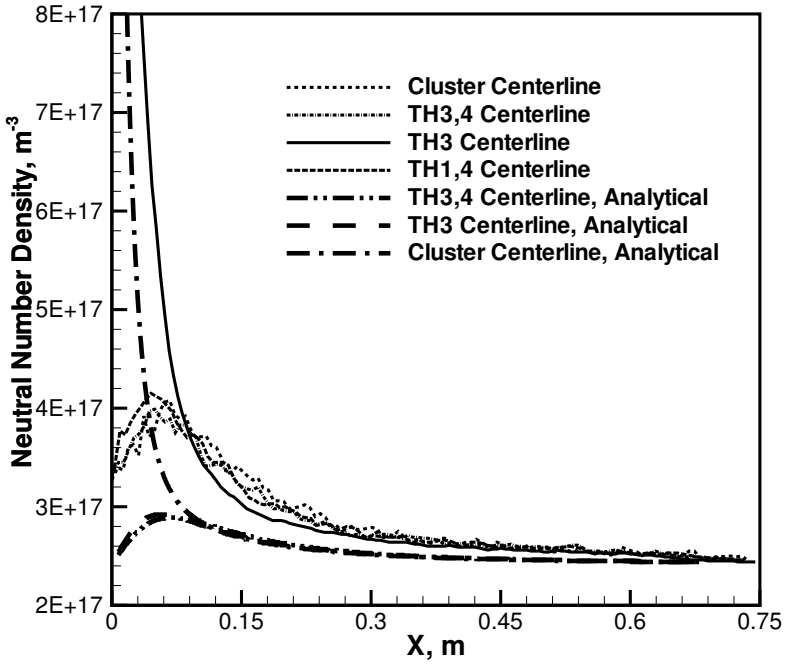

Figure 5.33: Distribution of Neutral Number Density (m^{-3}) along Different Centerlines(4 Thrusters).

the parameters are the same, these three-dimensional simulations yield some results that are different from the axi-symmetric simulation in [17].

Here are two comments to end this discussion of results. The first comment is about the drawbacks of axi-symmetric simulations. Firstly, with more than one thruster in operation, axi-symmetric simulation is completely not applicable. Secondly, in simulation of a single thruster, the three-dimensional cathode is usually either completely omitted or simplified as a ring source. However, from this study, it is evident that the cathode position, angle, and amount of flux have significant effects on the flowfield. Hence, these three-dimensional simulations should be superior to over an axi-symmetric simulation. The second comment is about one defect in this study. For the right hand side terms in Equations (2.7), (2.11) and (2.12), several second order derivatives are involved, but the finite element adopted in this study

employs a linear element. This problem is not severe because the derivation calculation scheme in this study permits a degree of resolution for these second derivatives, and the source term is weak.

5.5 Conclusions

In this study, a comprehensive three-dimensional DSMC-PIC package with a general purpose finite element solver and a detailed electron fluid model was developed and applied to simulate the plasma plumes from a cluster of four Hall thrusters with different numbers of thrusters in operation. Several major implementation issues were reviewed and the backpressure was modeled using the results from Chapter III.

Generally, the simulation results yield some detailed flow patterns, and some results matched the available experimental measurements or analytical results. The cluster effects are evidently captured. From the results along different centerlines, different properties of the plumes merge into one plume at different locations from X=0.05 m to X=0.60 m. The simulations also showed that the cathodes have significant effects on the plume flows. The CEX effect is clearly illustrated in the simulation results as well.

CHAPTER VI

SUMMARY, CONCLUSIONS AND FUTURE WORK

This thesis includes three pieces of work:

1. Vacuum chamber facility effects;

2. Analytical free molecular flow solutions;

3. Three-dimensional particle simulations of plasma flows from a cluster of Hall thrusters with the DSMC-PIC methods on unstructured meshes.

The following sections summarize these studies, list the major conclusions and suggest possible long term and short term works for the future.

6.1 DSMC-PIC Simulations of Plasma Plume Flows From a Cluster of Hall Thrusters

6.1.1 Summary and Conclusions

As the centerpiece of this thesis, several DSMC-PIC particle simulations were performed for the plume flows from a cluster of four Hall thrusters with different numbers of thrusters in operation. These simulations adopted a detailed fluid electron model to describe electron properties, including the electron velocity stream

function, the plasma potential and the electron temperature. A general purpose finite element solver was developed to solve these important electron properties. Several implementation issues were reviewed as well.

One important finding through this study was, it is not proper to allocate charge or neutral number density to nodes based on areas or volumes on unstructured meshes. This problem was hidden and unnoticed on unstructured meshes if the Boltzmann relation was used to compute the plasma potential. For the detailed electron model, especially when including ionization effects, this scheme resulted in a serious problem.

The geometries of a cathode and a protection cap were included in the simulations. Another novel treatment in the simulations was that the facility effects and backpressure flow were considered by using the analytical results obtained in Chapter III.

The simulations were compared with available experimental data, and they indicated the cathode had important effects on some flow property distributions. They also clearly displayed CEX effects and the clustering effects. There exist complex three-dimensional near field structures in the ion number density with four Hall thrusters in operation. With four thrusters in operation, a severe impingement is expected right behind the cluster center. Compared with axi-symmetric simulations, these three-dimensional simulations had several improvements, and when compared with the Boltzmann relation, the detailed fluid electron model displayed much superiority in predicting the electron temperature as well.

6.1.2 Future Work

There are several tasks to be considered as future projects:

1. Include magnetic field effects in plume flow simulations. With this implementation, the modeling package MONACO-PIC will be more complete and applicable to more plasma plume simulations.

2. Implementation of higher order finite element solver. As pointed out in Chapter V, several second order derivatives were involved on the right hand side of source terms but the current finite element solver adopted a linear element. This problem was alleviated by two facts: first these source terms were usually weak; second, the least-square derivative calculation method on an unstructured mesh partially took consideration of these second derivatives. However, since in three-dimensional simulations, the mesh is usually more sparse than axi-symmetric simulations, implementation of a higher order finite element solver will provide more accurate results.

3. Full scale three-dimensional simulation of plasma flows. As discussed in Chapter III, a full scale three-dimensional simulation of plasma plume flow inside a large vacuum chamber required a huge number of time steps. This simulation involves background flow and plasma plume flows, and it was a multiple timescale problem coupled in space as well. This problem represents a great challenge for particle simulations.

4. Further improvements in the experimental version of MONACO. DSMC-PIC simulations are generally complex and there are no standards to follow yet. This experimental version of MONACO just provided a platform and many further improvements can be implemented. For example, in the simulations with background static particles, a large amount of slow ions were created due to different particle weights and the splitting scheme. Seeking a more effective

solution to reduce the slow ion number will improve the performance of the package.

6.2 Vacuum Chamber Facility Effects

6.2.1 Summary and Conclusions

To understand the facility effects and the topography of background gas in a vacuum chamber is important to the electric propulsion community. Chapter III concentrated on this problem. The study was based on the fact that the background flows in a vacuum chamber equipped with one-sided or two-sided cryogenic pumps were free molecular. With several other assumptions, the background flow in a large vacuum chamber were simplified through five different free molecular flows between two plates, with or without a consideration of sidewall effects. The first model was based on mass conservation, with a consideration of the mass flow into the chamber via thrusters and that out of the chamber via pumps; while the other four models were based on an analysis of the flux relations in two directions and several number density relations at both vacuum chamber ends and the pumps.

The major conclusions from this study are:

1. No matter how efficiently the pumps work, there is always a finite background pressure existing in a vacuum chamber. The backpressure is decided by many factors, including the mass flow rate from thrusters, the propellant properties, the chamber wall temperature, the cryogenic pump sticking coefficient, the pump size, the chamber wall temperature and possibly the pump temperature.

2. There exists a semi-decaying period for the unsteady flow evolution. An unsteady process takes three or four such semi-decaying periods to reach a steady state, which presents a serious problem for a full scale three-dimensional par-

ticle simulation of plume flows in a vacuum chamber. The existence of this semi-decaying period fact was confirmed by particle simulations of background flow in a vacuum chamber equipped with one-sided pumps.

3. Generally, the flow inside a vacuum chamber does not follow a zero-centered Maxwellian velocity distribution. The highest background average flow velocity can reach over 100 m/s for gaseous xenon. Hence, the traditional treatment of stationary background flows in DSMC-PIC simulations of plasma flows firing from thrusters is not always accurate. Several suggestions were proposed to improve the background flow treatment in particle simulations.

4. The cryogenic pump sticking coefficient in the LVTF, PEPL is close to 0.40 on average. Depending on different working conditions, the actual value can vary within a small range.

5. For vacuum chambers equipped with two-sided pumps, kinetic models with diffusive or reflective pump wall conditions yielded almost the same results for the vacuum pump sticking coefficient, the average backpressure and the average background velocity. Because a real wall reflection is always between completely reflective and completely diffusive, these two models predict very accurate results.

6. For vacuum chambers equipped with one-sided pumps, sidewall effects can be analyzed by further introducing a transportation coefficient χ, which can be evaluated numerically for chambers with different cross-section shapes. Both analytical solutions and numerical simulations indicated that the sidewall may have a different role in deciding the average background pressure with different values of the pump sticking coefficient, α.

7. Usually, pumps are operated at low temperature, and the large amount of slow particles reflected from the pump are confined locally around the pumps. To estimate the average background pressure in a large chamber, numerical simulations indicate that the treatment of setting T_p/T_w to unity is a reasonable approach to obtain the average background pressure and average velocity in the vacuum chamber.

This study provides five sets of analytical free molecular flow solutions to evaluate the background pressure and the average background flow velocities with facility effects, including the vacuum pump sticking coefficient, the pump area and the sidewall length effects. Chapter III presented several principles to study these types of problems as well. Following these principles can aid investigations of background flows in other types of large vacuum chambers with complex geometry configurations. The study in this work may apply to other chambers with different cross section shapes and other usages as well, such as materials processing.

6.2.2 Future Work

There are several assumptions adopted during the analysis of the background flow in vacuum chambers equipped with one-sided pumps or two-sided pumps. Though the assumptions are correct for these types of chambers discussed in this study, there are more complicated vacuum chambers where the above assumptions are not valid. Several such special conditions are:

1. Unlike the assumption in this study that plume flows reflect at a chamber end without pumps, plume flows may directly impinge on vacuum pumps in other types of chambers.

2. Unlike the assumption in this study that particles cannot consecutively hit a

pump, in several chamber configurations, particles can.

3. Unlike the assumption in this study that vacuum pumps are located on or close to one chamber end, several vacuum chambers have distributed pumps on both chamber ends and side walls.

Obviously, these assumptions will significantly complicate the analysis process.

6.3 Analytical Solutions to Free Molecular Effusion Flows

6.3.1 Summary and Conclusions

Chapter IV presented an initial effort to analytically study free molecular plasma plume flows by neglecting the electric field and collisions. This study reinterpret an important observation found by Narasimha with a new relation of velocities and positions. To arrive at a specific point in front of the exit by starting from a point on the exit, a necessary and sufficient condition is, the particle's velocity components satisfy the relation of velocities and positions. This relation takes different formats in the flow problems studied in this chapter. It provided a one-to-one relation between velocity spaces and hence provided a complete support to Narasimha's observation, provided integral domain boundaries to evaluate number density and velocities, and for specific cases, it provided integral variable changes to simplify the integral process.

Free molecular flows out of a thin slit, a rectangular exit, a concentered rectangular exit, a circular exit and an annular exit with a zero average exit velocity, and free molecular flows out of a thin slit with a nonzero average exit velocity were studied. Exact solutions were obtained for the first two cases but only exact expressions were obtained for the other three cases. However, evaluation of these exact expressions was straightforward.

DSMC simulations were performed to validate these analytical results. To compare with the analytical free molecular flow solutions, the collision function in the DSMC simulations was disabled. Most comparisons were quite satisfactory or even identical. These flows shared the same patterns: there was a region around the exit where the exit effect was quite significant, and in the far field, the stream lines were almost straight. For the last case, analytical results indicated that as the average exit velocity increased, the plume flows were confined in a narrower region around the axis.

6.3.2 Future Work

Other free molecular flows should be investigated analytically and numerically as consecutive problems. Though the results to these problems will be closer to real plume flows, they will be complex as well:

1. Free molecular flows out of a rectangular exit, with a non-zero average exit speed.

2. Free molecular flows out of a circular exit, with a non-zero average exit speed.

3. Free molecular flows out of an annular exit, with a non-zero average exit speed.

Studies of these problems will provide complete and concrete analytical solutions, at the kinetic level, to analyze plasma plume flows in space.

APPENDICES

APPENDIX A

Nomenclature

a_i	coefficient for the ith node in a tetrahedral cell
b, a, d	x, y, z distances from a cathode to the cluster center
B_e	geometry matrix for a single tetrahedral cell
c_e	mean electron thermal velocity
C_i	ionization coefficient
d	atomic diameter
D	chamber diameter
e	unit charge
$\overrightarrow{E}$	electric field vector
$f(C)$	velocity distribution function
F_{X+}	mass flux rate passing station through X from one side
F_{X-}	mass flux rate passing station through X from the other side

$G(x, y, z)$	value for Neumann boundary condition
g	relative velocity
H, L	chamber length
h_c	combustion enthalpy
J	free charge current density
J_A	anode electron current density
J_C	cathode current density
k	Boltzmann constant
Kn	Knudsen number
$\dot{m}$	mass flux rate into vacuum chamber
m	atomic mass, or mean mass of exhaust products
m_c	reduced mass
n	plasma number density, or number of nodes
n_a	neutral number density from anode
n_c	neutral number density from cathode
n_{in}	number density for flux into the vacuum chamber
n_x, n_y, n_z	normal of cathode exit plane
n_{X+}	number density for particles passing through station X from one side

n_{X-}	number density for particles passing through station X from the other side
$\overrightarrow{n}$	surface normal
p_e	electron pressure
P_b	chamber backpressure
$P(x, y, z)$	variable for the generalized Poisson equations
$Q(x, y, z)$	coefficients for the generalized Poisson equations
$\overrightarrow{r}$	distance vector between two points
R_c	cathode orifice radius
R	gas constant, or circle radius
$R_{1,}\, R_2$	inner and outer radius for an annular exit
r	distance between two points
s	area ratio, $= S_p/S_c$
S_p	pump surface area
s_{ne}	source term on cell nodes
S_c	chamber cross-sectional area
$S(x, y, z)$	source terms for the generalized Poisson equations
T	temperature
T_H	heavy particle temperature

T_p	pump plate temperature
$\widetilde{T}_{pw}$	temperature ratio, $= T_p/T_w$
u_e	linear variable inside a tetrahedral cell
u_{ex}	average exit velocity
u_{ne}	variable value on tetrahedral cell nodes
U, V, W	mean velocity
U_0	mean inlet velocity
$U_b(x, y, z)$	value for Dirichlet boundary condition
V	cell or chamber volume
V_e	electron velocity vector
V_w	thermal velocity, $\sqrt{2kT_w/\pi m}$
V_p	thermal velocity, $\sqrt{2kT_p/\pi m}$
v_{th}	thermal speed
x_i, y_i, z_i	node coordinates
α	pump sticking coefficient
β	$= (2RT)^{-1}$
χ	particle conductance percentage from one chamber end to the other end
δ	molecular distance

ϵ_i	ionization energy for xenon, =12.7 eV
ϵ	particle conductance percentage from chamber wall to one chamber end
γ	specific heat ratio
κ_e	electron thermal conductivity
κ	ratio of annulus inner and outer radius,$=R_2/R_1$
λ	mean free path
λ_d	Debye length
ν_e	electron collision frequency, $= \nu_{ei} + \nu_{en}$
ν_{ei}	ion-electron collision frequency
ν_{en}	neutral-electron collision frequency
ω	viscosity temperature exponent
ω_p	plasma frequency
Ω	solid angle in velocity phase space or physical space
ϕ	plasma potential
ψ	electron velocity stream function
ρ	background density
ρ_0	initial background density
σ	plasma conductivity

σ_i	reference cross section for xenon
σ_{el}	reference cross section for elastic collisions
τ	mean collision time
θ_+	divergence angle for the outer channel edge
θ_-	divergence angle for the inner channel edge
τ_d	semi decaying period

subscript

$_{back}$	background
$_c$	chamber
$_e$	electron
$_i$	ion
$_n$	neutral
$_{ref}$	reference value
$_w$	wall

APPENDIX B

Integrals Used In This Dissertation

$erf(x) = \frac{2}{\sqrt{\pi}} \int_0^x \exp(-x^2)dx, erf(\infty) = 1$

$\int \frac{1}{(u^2+a^2)^{3/2}}du = \frac{u}{a^2(u^2+a^2)^{1/2}} + C$

$\int \frac{1}{(u^2+a^2)^2}du = \frac{u}{2a^2(a^2+u^2)} + \frac{1}{2a^3}\arctan(\frac{u}{a}) + C$

$\int \frac{1}{u^2+a^2}du = \frac{1}{a}\arctan(\frac{u}{a}) + C$

$\int_{-\pi}^{\pi} \frac{c^2\sin^2\theta}{a^2+c^2\cos^2\theta}d\theta = 2\pi\sqrt{1+c^2/a^2} - 2\pi$

$\int \frac{1}{a+b\cos\theta}d\theta = \frac{2}{\sqrt{a^2-b^2}}\arctan(\sqrt{\frac{a-b}{a+b}}\tan\frac{\theta}{2}) + C$

$\int \frac{1}{a^2\cos^2\theta+b^2\sin^2\theta}d\theta = \frac{1}{ab}\arctan(\frac{b\tan u}{a}) + C$

$\int \frac{1}{a+b\sin\theta}d\theta = \frac{2}{\sqrt{a^2-b^2}}\arctan\frac{a\tan(u/2)+b}{\sqrt{a^2-b^2}} + C$

$\int_{-\pi}^{\pi} \frac{\sin\theta}{a+b\sin\theta}d\theta = \int_{-\pi}^{\pi}(\frac{1}{b} - \frac{a}{b(a+b\sin\theta)}d\theta) = \frac{2\pi}{b}(1 - \frac{a}{\sqrt{a^2-b^2}}), (a > 0)$

$\int_{-\pi}^{\pi} \frac{\sin^2\theta}{a+b\sin\theta}d\theta = \frac{2a\pi}{b^2}(\frac{a}{\sqrt{a^2-b^2}} - 1), (a > b > 0)$

$\int_A^B \frac{1}{(x^2+a^2)\sqrt{x^2+a^2+b^2}}dx = \frac{1}{ab}\big[\arctan(\frac{bB}{a\sqrt{a^2+b^2+B^2}}) - \arctan(\frac{bA}{a\sqrt{a^2+b^2+A^2}})\big]$

APPENDIX C

Derivations for Free Molecular Flow Out of a Rectangular Slit, $U_0 = 0$

$$n(X,Y,Z) = (\tfrac{\beta}{\pi})^{3/2} \int_0^\infty du \int_{-H}^{+H} dz \int_{-L}^{+L} dy \tfrac{u^2}{X^2} \exp(-\beta u^2 \tfrac{X^2+(Y-y)^2+(Z-z)^2}{X^2})$$

$$= (\tfrac{\beta}{\pi})^{3/2} X^{-2} \int_{-H}^{+H} dz \int_{-L}^{+L} dy \sqrt{\pi} \tfrac{X^3}{4\beta^{3/2}(X^2+(Y-y)^2+(Z-z)^2)^{3/2}}$$

$$= \tfrac{X}{4\pi} \int_{-H}^{+H} \left[\tfrac{(L-Y)dz}{(X^2+(Z-z)^2)\sqrt{X^2+(L-Y)^2+(Z-z)^2}} + \tfrac{(L+Y)dz}{(X^2+(Z-z)^2)\sqrt{X^2+(L+Y)^2+(Z-z)^2}} \right]$$

$$= \tfrac{1}{4\pi} \left[\arctan \tfrac{(L-Y)(H-Z)}{X\sqrt{X^2+(L-Y)^2+(H-Z)^2}} + \arctan \tfrac{(L-Y)(H+Z)}{X\sqrt{X^2+(L-Y)^2+(H+Z)^2}} \right]$$

$$+ \tfrac{1}{4\pi} \left[\arctan \tfrac{(L+Y)(H-Z)}{X\sqrt{X^2+(L+Y)^2+(H-Z)^2}} + \arctan \tfrac{(L+Y)(H+Z)}{X\sqrt{X^2+(L+Y)^2+(H+Z)^2}} \right]$$

$$\tfrac{U(X,Y,Z)}{\sqrt{2RT_0}} = \tfrac{1}{n\sqrt{2RT_0}} (\tfrac{\beta}{\pi})^{3/2} \int_0^\infty du \int_{-H}^{+H} dz \int_{-L}^{+L} dy \tfrac{u^3}{X^2} \exp(-\beta u^2 \tfrac{X^2+(Y-y)^2+(Z-z)^2}{X^2})$$

$$= \tfrac{X^2}{2n\pi\sqrt{\pi}} \int_{-H}^{+H} dz \int_{-L}^{+L} [X^2 + (Y-y)^2 + (Z-z)^2]^{-2} dy$$

$$= \tfrac{X^2}{2n\pi\sqrt{\pi}} \int_{-H-Z}^{H-Z} \left[\tfrac{L-Y}{2[X^2+z^2][X^2+(L-Y)^2+z^2]} + \tfrac{L+Y}{2[X^2+z^2][X^2+(L+Y)^2+z^2]} \right.$$

$$\left. + \tfrac{1}{2\sqrt{(X^2+z^2)^3}} \arctan \tfrac{L-Y}{\sqrt{X^2+z^2}} + \tfrac{1}{2\sqrt{(X^2+z^2)^3}} \arctan \tfrac{L+Y}{\sqrt{X^2+z^2}} \right] dz$$

$$= \tfrac{1}{4n\pi\sqrt{\pi}} \left(\tfrac{H-Z}{\sqrt{(H-Z)^2+X^2}} (\arctan \tfrac{L-Y}{\sqrt{(H-Z)^2+X^2}} + \arctan \tfrac{L+Y}{\sqrt{(H-Z)^2+X^2}}) \right.$$

$$+ \tfrac{H+Z}{\sqrt{(H+Z)^2+X^2}} (\arctan \tfrac{L-Y}{\sqrt{(H+Z)^2+X^2}} + \arctan \tfrac{L+Y}{\sqrt{(H+Z)^2+X^2}})$$

$$+ \tfrac{L-Y}{\sqrt{(L-Y)^2+X^2}} (\arctan \tfrac{H-Z}{\sqrt{(L-Y)^2+X^2}} + \arctan \tfrac{H+Z}{\sqrt{(L-Y)^2+X^2}})$$

$$\left. + \tfrac{L+Y}{\sqrt{(L+Y)^2+X^2}} (\arctan \tfrac{H-Z}{\sqrt{(L+Y)^2+X^2}} + \arctan \tfrac{H+Z}{\sqrt{(L+Y)^2+X^2}}) \right)$$

$$\frac{V(X,Y,Z)}{\sqrt{2RT_0}} = \frac{1}{n\sqrt{2RT_0}}\left(\frac{\beta}{\pi}\right)^{3/2}\int_0^{\infty} du \int_{-H}^{+H} dz \int_{-L}^{+L} dy \frac{u^3}{X^2}\frac{Y-y}{X}\exp\left(-\beta u^2 \frac{X^2+(Y-y)^2+(Z-z)^2}{X^2}\right)$$

$$= \frac{1}{n\pi\sqrt{2RT_0}}\left(\frac{\beta}{\pi}\right)^{3/2}\int_{-H}^{+H} dz \int_{-L}^{+L} \frac{X^4}{2\beta^2[X^2+(Y-y)^2+(Z-z)^2]^2}\frac{Y-y}{X^3}dy$$

$$= \frac{X}{4n\pi\sqrt{\pi}}\int_{-H}^{+H}\left(\frac{1}{X^2+(L-Y)^2+(Z-z)^2} - \frac{1}{X^2+(L+Y)^2+(Z-z)^2}\right)dz$$

$$= \frac{X}{4n\pi\sqrt{\pi}}\left[\frac{1}{\sqrt{(L-Y)^2+X^2}}\left(\arctan\frac{H-Z}{\sqrt{(L-Y)^2+X^2}} + \arctan\frac{H+Z}{\sqrt{(L-Y)^2+X^2}}\right)\right.$$

$$\left. - \frac{1}{\sqrt{(L+Y)^2+X^2}}\left(\arctan\frac{H-Z}{\sqrt{(L+Y)^2+X^2}} + \arctan\frac{H+Z}{\sqrt{(L+Y)^2+X^2}}\right)\right]$$

$$\frac{W(X,Y,Z)}{\sqrt{2RT_0}} = \frac{1}{n\sqrt{2RT_0}}\left(\frac{\beta}{\pi}\right)^{3/2}\int_0^{\infty} du \int_{-H}^{+H} dz \int_{-L}^{+L} dy \frac{u^3}{X^2}\frac{Z-z}{X}\exp\left(-\beta u^2 \frac{X^2+(Y-y)^2+(Z-z)^2}{X^2}\right)$$

$$= \frac{1}{n\pi\sqrt{2RT_0}}\left(\frac{\beta}{\pi}\right)^{3/2}\int_{-H}^{+H} dz \int_{-L}^{+L} \frac{X^4}{2\beta^2[X^2+(Y-y)^2+(Z-z)^2]^2}\frac{Z-z}{X^3}dy$$

$$= \frac{X}{4n\pi\sqrt{\pi}}\int_{-L}^{+L}\left(\frac{1}{X^2+(Y-y)^2+(Z-H)^2} - \frac{1}{X^2+(Y-y)^2+(Z+H)^2}\right)dy$$

$$= \frac{X}{4n\pi\sqrt{\pi}}\left[\frac{1}{\sqrt{(H-Z)^2+X^2}}\left(\arctan\frac{L-Y}{\sqrt{(H-Z)^2+X^2}} + \arctan\frac{L+Y}{\sqrt{(H-Z)^2+X^2}}\right)\right.$$

$$\left. - \frac{1}{\sqrt{(H+Z)^2+X^2}}\left(\arctan\frac{L-Y}{\sqrt{(H+Z)^2+X^2}} + \arctan\frac{L+Y}{\sqrt{(H+Z)^2+X^2}}\right)\right]$$

APPENDIX D

Derivations for Free Molecular Flow Out of a Circular Slit, $U_0 = 0$

$$n(X,0,Z) = \int_0^\infty du \int_0^R dr \int_0^{2\pi} \frac{ru^2}{X^2}\left(\frac{\beta}{\pi}\right)^{3/2} \exp\left(-\beta u^2 \frac{X^2+(Y-y)^2+(Z-z)^2}{X^2}\right) d\theta$$

$$= \int_0^R dr \int_0^{2\pi} \frac{r\sqrt{\pi}}{4X^2}\left(\frac{\beta}{\pi}\right)^{3/2} \left[\beta \frac{X^2+(Y-y)^2+(Z-z)^2}{X^2}\right]^{-3/2} d\theta$$

$$= \int_0^R dr \int_0^{2\pi} \frac{Xr}{4\pi}\left[X^2+Z^2+r^2-2rZ\sin\theta\right]^{-3/2} d\theta$$

$$= \frac{X}{4\pi}\int_0^{2\pi}\left[\frac{1}{\sqrt{X^2+Z^2}} - \frac{1}{\sqrt{X^2+Z^2+R^2-2RZ\sin\theta}} + \left(\int_0^R \frac{Z\sin\theta}{(X^2+Z^2+r^2-2rZ\sin\theta)^{3/2}} dr\right)\right] d\theta$$

$$= \int_0^{2\pi}\left[\frac{1}{\sqrt{X^2+Z^2}} - \frac{1}{\sqrt{X^2+Z^2+R^2-2RZ\sin\theta}} + \left(\int_0^R \frac{Z\sin\theta}{(X^2+Z^2+r^2-2rz\sin\theta)^{3/2}} dr\right)\right] d\theta$$

$$= \frac{X}{2\sqrt{X^2+Z^2}} - \frac{X}{4\pi}\int_{-\pi}^{\pi} \frac{d\theta}{\sqrt{X^2+Z^2+R^2-2RZ\sin\theta}} + \frac{X}{4\pi}\int_{-\pi}^{\pi} \frac{Z^2\sin^2\theta d\theta}{\sqrt{X^2+Z^2}(X^2+Z^2\cos^2\theta)}$$

$$+\frac{X}{4\pi}\int_{-\pi}^{\pi} \frac{Z\sin\theta(R-Z\sin\theta)d\theta}{(X^2+Z^2\cos^2\theta)\sqrt{X^2+Z^2+R^2-2RZ\sin\theta}}$$

$$= \frac{1}{2} - \frac{X}{4\pi}\int_{-\pi}^{\pi}\left[\frac{d\theta}{\sqrt{X^2+Z^2+R^2-2RZ\sin\theta}} - \frac{Z\sin\theta(R-Z\sin\theta)d\theta}{(X^2+Z^2\cos^2\theta)\sqrt{X^2+Z^2+R^2-2RZ\sin\theta}}\right]$$

$$\frac{U(X,0,Z)}{\sqrt{2RT_0}} = \frac{1}{n\sqrt{2RT_0}}\int_0^\infty udu \int_0^R dr \int_0^{2\pi} \frac{ru^2}{X^2}\left(\frac{\beta}{\pi}\right)^{3/2} \exp\left(-\beta u^2 \frac{X^2+(Y-y)^2+(Z-z)^2}{X^2}\right) d\theta$$

$$= \int_0^R dr \int_0^{2\pi} \frac{X^2}{2\beta^2 n\sqrt{2RT_0}}\left(\frac{\beta}{\pi}\right)^{3/2} r\left[X^2+r^2+Z^2-2rZ\sin\theta\right]^{-2} d\theta$$

$$= \int_{-Z\sin\theta}^{R-Z\sin\theta} dr \int_0^{2\pi} \frac{X^2}{2\pi n\sqrt{\pi}} \frac{r+Z\sin\theta}{[X^2+r^2+Z^2-2rZ\sin\theta]} d\theta$$

$$= \frac{1}{2\pi n\sqrt{\pi}}\int_{-\pi}^{\pi}\left(\frac{X^2 d\theta}{2(X^2+Z^2)} - \frac{X^2 d\theta}{2(X^2+Z^2+R^2-2RZ\sin\theta)} + \frac{Z\sin\theta d\theta}{2(X^2+Z^2\cos^2\theta)}\times\right.$$

$$\left[\frac{R-Z\sin\theta}{X^2+Z^2\cos^2\theta+(R-Z\sin\theta)^2} + \frac{\arctan((R-Z\sin\theta)/\sqrt{X^2+Z^2\cos^2\theta})}{(X^2+Z^2\cos^2\theta)^{1/2}}\right.$$

$$+\frac{Z\sin\theta}{X^2+Z^2\cos^2\theta+(-Z\sin\theta)^2}+\frac{\arctan((Z\sin\theta)/\sqrt{X^2+Z^2\cos^2\theta})}{(X^2+Z^2\cos^2\theta)^{1/2}}\Big]\Bigg)$$

$$=\frac{X^2}{2\pi n\sqrt{\pi}}\Bigg(\frac{\pi}{X^2+Z^2}-\frac{\pi}{\sqrt{(X^2+Z^2+R^2)^2-4R^2Z^2}}+\int_{-\pi}^{\pi}\Big[\frac{Z^2\sin^2\theta d\theta}{2(X^2+Z^2)(X^2+Z^2\cos^2\theta)}$$

$$\frac{Z\sin\theta(R-Z\sin\theta)d\theta}{2(X^2+Z^2+R^2-2RZ\sin\theta)(X^2+Z^2\cos^2\theta)}+\frac{Z\sin\theta(R-Z\sin\theta)d\theta}{2(X^2+Z^2\cos^2\theta)^{3/2}}\arctan\frac{R-Z\sin\theta}{\sqrt{X^2+Z^2\cos^2\theta}}$$

$$+\frac{Z\sin\theta}{2(X^2+Z^2\cos^2\theta)^{3/2}}\arctan\frac{Z\sin\theta}{\sqrt{X^2+Z^2\cos^2\theta}}\Big]\Bigg)$$

$$=\frac{X^2}{2\pi n\sqrt{\pi}}\Bigg(\frac{\pi}{X\sqrt{X^2+Z^2}}-\frac{\pi}{\sqrt{(X^2+Z^2+R^2)^2-4R^2Z^2}}+$$

$$+\int_{-\pi}^{\pi}\Big[\frac{Z\sin\theta}{2(X^2+Z^2\cos^2\theta)^{3/2}}\arctan\frac{Z\sin\theta}{\sqrt{X^2+Z^2\cos^2\theta}}+$$

$$+\frac{Z\sin\theta(R-Z\sin\theta)d\theta}{2(X^2+Z^2+R^2-2RZ\sin\theta)(X^2+Z^2\cos^2\theta)}+\frac{Z\sin\theta d\theta}{2(X^2+Z^2\cos^2\theta)^{3/2}}\arctan\frac{R-Z\sin\theta}{\sqrt{X^2+Z^2\cos^2\theta}}\Big]d\theta\Bigg)$$

$$\frac{W(X,0,Z)}{\sqrt{2RT_0}}=\frac{1}{n\sqrt{2RT_0}}\int_0^{\infty}wdu\int_0^R dr\int_0^{2\pi}\frac{ru^2}{X^2}(\frac{\beta}{\pi})^{3/2}\exp(-\beta u^2\frac{X^2+(Y-y)^2+(Z-z)^2}{X^2})d\theta$$

$$=\int_0^R dr\int_0^{2\pi}\frac{X}{2\beta n\sqrt{2RT_0}}(\frac{\beta}{\pi})^{3/2}r(Z-r\sin\theta)[X^2+r^2+Z^2-2rZ\sin\theta]^{-2}d\theta$$

$$=\int_{-Z\sin\theta}^{R-Z\sin\theta}dr\int_0^{2\pi}\frac{X}{2\pi n\sqrt{\pi}}\frac{(X+Z\sin\theta)(-X\sin\theta+Z\cos^2\theta)}{[X^2+r^2+Z^2\cos^2\theta]^2}d\theta$$

$$=\int_{-Z\sin\theta}^{R-Z\sin\theta}dr\int_0^{2\pi}\frac{X}{2\pi n\sqrt{\pi}}\frac{XZ\cos(2\theta)+\sin\theta(-X^2+Z^2\cos^2\theta)}{[X^2+r^2+Z^2\cos^2\theta]^2}d\theta$$

$$=\frac{X}{2\pi n\sqrt{\pi}}\Bigg[\int_0^{2\pi}(\frac{-(Z/2)\cos(2\theta)d\theta}{[X^2+(R-Z\sin\theta)^2+Z^2\cos^2\theta]}+\frac{(Z/2)\cos(2\theta)d\theta}{[X^2+Z^2]^2})$$

$$+\int_{-Z\sin\theta}^{R-Z\sin\theta}\frac{-\sin\theta}{[X^2+r^2+Z^2\cos^2\theta]^2}drd\theta+\int_{-Z\sin\theta}^{R-Z\sin\theta}\frac{X^2\sin\theta+2Z^2\sin\theta\cos^2\theta}{[X^2+r^2+Z^2\cos^2\theta]^2}drd\theta\Bigg]$$

$$=\frac{1}{2\pi n\sqrt{\pi}}\Bigg[\int_0^{2\pi}\frac{-(Z/2)\cos(2\theta)d\theta}{[X^2+R^2+Z^2-2RZ\sin\theta]}-$$

$$\frac{\sin(\theta)d\theta}{\sqrt{X^2+Z^2\cos^2\theta}}(\arctan\frac{R-Z\sin\theta}{\sqrt{X^2+Z^2\cos^2\theta}}+\arctan\frac{Z\sin\theta}{\sqrt{X^2+Z^2\cos^2\theta}})+$$

$$+\frac{\sin\theta(X^2+2Z^2\cos^2\theta)d\theta}{2(X^2+Z^2\cos^2\theta)^{3/2}}(\arctan\frac{R-Z\sin\theta}{\sqrt{X^2+Z^2\cos^2\theta}}+\arctan\frac{Z\sin\theta}{\sqrt{X^2+Z^2\cos^2\theta}})$$

$$+\frac{\sin\theta(X^2+2Z^2\cos^2\theta)(R-Z\sin\theta)d\theta}{2(X^2+Z^2\cos^2\theta)(X^2+Z^2+R^2-2RZ\sin\theta)}+\frac{Z\sin^2\theta(X^2+2Z^2\cos^2\theta)d\theta}{2(X^2+Z^2\cos^2\theta)(X^2+Z^2)}\Bigg]$$

APPENDIX E

Derivations for Free Molecular Flow Out of a Slit, $U_0 > 0$

$$n(X,Y) = \int_{-U_0}^{+\infty} du \int_{(u+U_0)\tan\theta_1}^{(u+U_0)\tan\theta_2} \frac{\beta}{\pi} \exp(-\beta(u^2+v^2))dv$$

$$= \int_0^{+\infty} V dV \int_{\theta_1}^{\theta_2} \frac{\beta}{\pi} \exp(-\beta({U_0}^2 + V^2 - 2U_0 V\cos\theta))dv$$

$$= \frac{\exp(-\beta{U_0}^2)}{\pi} \int_0^{+\infty} \int_{\theta_1}^{\theta_2} \frac{d\exp(-\beta V^2)}{-2} \exp(2\beta U_0 V\cos\theta)d\theta$$

$$= \frac{\exp(-\beta{U_0}^2)}{2\pi}[(\theta_2-\theta_1) + 2\int_0^{+\infty}\int_{\theta_1}^{\theta_2} \beta U_0\cos\theta\exp(-\beta V^2 + 2\beta U_0 V\cos\theta)dV d\theta]$$

$$= \frac{\exp(-\beta{U_0}^2)}{2\pi}[(\theta_2-\theta_1) + 2\int_{\theta_1}^{\theta_2} \beta U\cos\theta\exp(\beta{U_0}^2\cos^2\theta)d\theta \int_{-U_0\cos\theta}^{+\infty}\exp(-\beta t^2)dt]$$

$$= \frac{\exp(-\beta{U_0}^2)}{2\pi}[(\theta_2-\theta_1) + \sqrt{\frac{\pi}{\beta}}\int_{\theta_1}^{\theta_2}\exp(\beta{U_0}^2\cos^2\theta)\beta U\cos\theta[1+erf(\sqrt{\beta}U_0\cos\theta)]d\theta]$$

$$= \frac{\exp(-\beta{U_0}^2)}{2\pi}(\theta_2-\theta_1) + \frac{1}{4}(erf(\sqrt{\beta}U_0\sin\theta_2) - sgn(\theta_1)erf(\sqrt{\beta}U_0\sin|\theta_1|))$$

$$+\frac{\sqrt{\beta/\pi}}{2}\int_{\theta_1}^{\theta_2}\exp(-\beta{U_0}^2\sin^2\theta)U_0\cos\theta erf(\sqrt{\beta}U_0\cos\theta)d\theta$$

$$\frac{V(X,Y)}{\sqrt{2RT_0}} = \frac{1}{n\sqrt{2RT_0}}\int_{-U}^{\infty} v du \int_{(u+U_0)\tan\theta_1}^{(u+U_0)\tan\theta_2}\frac{\beta}{\pi}\exp(-\beta(u^2+v^2))dv$$

$$= \frac{1}{n\sqrt{2RT}}\int_0^{\infty} V^2 dV \int_{\theta_1}^{\theta_2}\frac{\beta}{\pi}\sin\theta\exp(-\beta({U_0}^2+V^2-2U_0V\cos\theta))dv$$

$$= \frac{1}{4\sqrt{\pi}n}\Bigg[\exp(-\beta{U_0}^2\sin^2\theta_1)\cos\theta_1(1+erf(\sqrt{\beta}U_0\cos\theta_1))$$

$$-\exp(-\beta{U_0}^2\sin^2\theta_2)\cos\theta_2(1+erf(\sqrt{\beta}U_0\cos\theta_2))\Bigg]$$

$$\frac{U(X,Y)}{\sqrt{2RT_0}} = \frac{1}{n\sqrt{2RT_0}} \int_{-U_0}^{\infty}(u+U_0)du \int_{(u+U_0)\tan\theta_1}^{(u+U_0)\tan\theta_2} \frac{\beta}{\pi}\exp(-\beta(u^2+v^2))dv$$

$$= \frac{1}{n\sqrt{2RT_0}} \int_0^{+\infty} V^2 dV \int_{\theta_1}^{\theta_2} \frac{\beta}{\pi}\cos\theta\exp(-\beta({U_0}^2+V^2-2U_0V\cos\theta))dv$$

$$= \frac{\beta}{n\pi\sqrt{2RT_0}}\exp(-\beta{U_0}^2)\int_0^{\infty}\int_{\theta_1}^{\theta_2}\frac{d\exp(-\beta V^2)}{-2\beta}V\cos\theta\exp(2\beta U_0V\cos\theta)dVd\theta$$

$$= \frac{\exp(-\beta{U_0}^2)}{2\pi n\sqrt{2RT_0}}\int_0^{\infty}\int_{\theta_1}^{\theta_2}\cos\theta(1+2\beta U_0V\cos\theta)\exp(-\beta V^2+2\beta U_0V\cos\theta)d\theta$$

$$= \frac{\exp(-\beta{U_0}^2)}{2\pi n\sqrt{2RT_0}}[\int_{\theta_1}^{\theta_2}\exp(\beta{U_0}^2\cos^2\theta)\cos\theta\frac{\sqrt{\pi/\beta}}{2}(1+erf(\sqrt{\beta}U_0\cos\theta))$$

$$+\int_0^{+\infty}2\beta UV\cos^2\theta\exp(-\beta V^2+2\beta U_0V\cos\theta)dV]d\theta$$

$$= \frac{\exp(-\beta{U_0}^2)}{2n\pi\sqrt{2RT_0}}\left[\int_{\theta_1}^{\theta_2}\left(\frac{\sqrt{\pi/\beta}}{2}\exp(\beta{U_0}^2\cos^2\theta)\cos\theta(1+erf(\sqrt{\beta}U_0\cos\theta))\right)d\theta\right.$$

$$+\frac{U_0(\theta_2-\theta_1)}{2}+\frac{U_0(\sin(2\theta_2)-\sin(2\theta_1))}{4}$$

$$\left.+\sqrt{\beta\pi}\int_{\theta_1}^{\theta_2}\left(U_0^2\cos^3\theta(1+erf(\sqrt{\beta}U_0\cos\theta))\exp(\beta{U_0}^2\cos\theta)\right)d\theta\right]$$

The following relation is used in the derivation process for $U(X,Y)$:

$$\int_0^{\infty}\int_{\theta_1}^{\theta_2}2\beta U_0V\cos^2\theta\exp(-\beta V^2+2\beta U_0V\cos\theta)dVd\theta$$

$$= \int_0^{\infty}\int_{\theta_1}^{\theta_2}-(d\exp(-\beta V^2))U_0\cos^2\theta\exp(2\beta U_0V\cos\theta)d\theta$$

$$= \int_{\theta_1}^{\theta_2}(U_0\cos^2\theta+\int_0^{\infty}2{U_0}^2\cos^3\theta\beta\exp(-\beta V^2+2\beta U_0V\cos\theta)dV)d\theta$$

$$= \frac{U_0(\theta_2-\theta_1)}{2}+\frac{U_0(\sin(2\theta_2)-\sin(2\theta_1))}{4}$$

$$+\sqrt{\beta\pi}\int_{\theta_1}^{\theta_2}{U_0}^2\cos^3\theta(1+erf(\sqrt{\beta}U_0\cos\theta))\exp(\beta{U_0}^2\cos\theta)d\theta$$

APPENDIX F

Code Implementation

The DSMC-PIC simulations of the plume flows out of a cluster of thrusters, which were discussed in Chapter V, were performed with an experimental version of MONACO. This short Appendix is devoted to a review of the many new features and changes in this experimental version of the code.

F.1 Problems

As reviewed in Chapter II, MONACO-V3.0 is a flexible DSMC simulation package written in C language with many features including:

1. capable of performing 2D/AXI/3D simulations.
2. capable of using structured/unstructured meshes, hence, flows with quite complicated geometries can be simulated.
3. capable of simulating flows with multiple species and chemical reactions.
4. good data structure with effective performance on serial and parallel machines.

However, even with these excellent features, MONACO-V3.0 is not a perfect particle simulation package. There are some issues in adding new modules into it due to problems in its structural design.

The most severe problem for MONACO-V3.0 is a lack of control layer and separations between code functionalities and code interfaces. In essence, though with many good features, MONACO-V3.0 is a process oriented package instead of an object oriented package. To maintain the original modules' capabilities with an introduction of a new module, a new compilation variable will have to be added to achieve conditional code compilation, and new information will be presented in the code and increase the difficulties of code readability and maintainability. In a large research group with many group members working on different derivative methods from the standard DSMC method, such as the PIC method, the Information Preservation(IP) method, two-phase flow with gases and solid particles and hybrid methods with CFD, different versions of MONACO must be kept. This presents a significant problem of maintainability.

F.2 Solutions

To solve the structural problem, while adding a PIC module into MONACO, several special remedies are introduced. These remedies include adopting two important design patterns in software engineering, Singleton and Facade [26].

Singleton The intent of this pattern is to ensure a class only has one instance, and provide a global point of access to it. It serves as a global variable making an object accessible anywhere in the code. Because the Singleton class encapsulates its sole instances, it can have strict control over how and when clients access it. Because this pattern reduces name space, it is an improvement over global variables, as it avoids polluting the name space with global variables that store sole instances. More detailed discussions and examples can be found in Reference [26].

Facade This pattern provides a unified interface to a set of interfaces in a sub-

system. Facade defines a higher-level interface that makes the subsystem easier to use. This facade introduces a facade object that provides a single simplified interface to the more general facilities of a subsystem, which will minimize the communication and dependencies between systems. This pattern provides a simple default view of the subsystem that is good enough for most clients. It can add layers to the subsystems which can have different usage. Hence, facade can be used to define an entry point to each level and it shields clients from subsystem components, thereby reducing the number of objects that clients deal with and making the subsystem easier to use. This pattern increases the ease of use and generality of software and results in the subsystem being more reusable and easier to customize. More detailed discussions and examples can be found in Reference [26].

F.3 Implementations

Several essential modifications are implemented in this experimental version of MONACO, including utilizations of the Singleton and Facade patterns:

1. C++ classes are introduced. Hence, a true Object Oriented Programming style is achieved.

2. Several control classes, simulation engines, are introduced to provide as a major control layer in the code. Exactly one instance of this control class is initialized. Meanwhile, this control class is a derived class from a base class which can trace back to an abstract class as shown in Figure F.1. During the simulation, the control code initializes an engine object by a control card in a parameter file, as shown in the code in Figure F.2. This treatment results in a Singleton pattern and avoids a busy interface and compilation variables.

3. The most base class, AbstractEngine, provides all kinds of interfaces that will

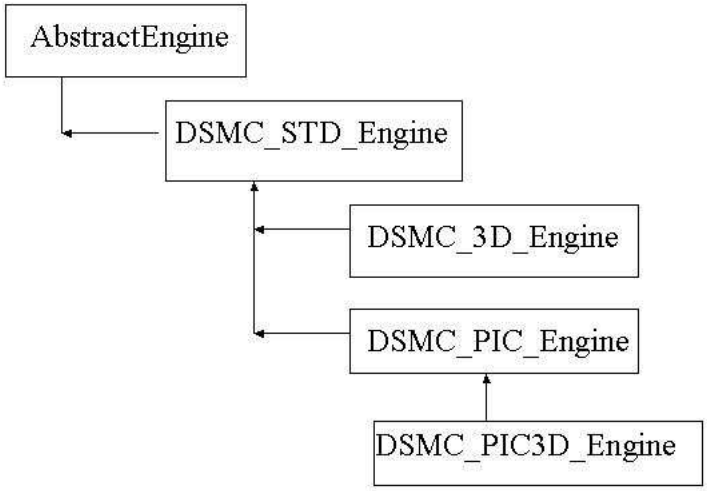

Figure F.1: Relations Among Different Classes of Simulation Engines.

```
AbsEngine *Engine_PTR =NULL;
int main(int argc, char *argv[])
{
  ....
  if( mode ==1 || mode ==2)
        Engine_PTR =new  DSMC_STD_Engine();
  else if( mode ==3)
        Engine_PTR =new  DSMC_3D_Engine();
  else if(mode ==4)
        Engine_PTR =new  DSMC_PIC_Engine();
  else if(mode==5)
        Engine_PTR =new  DSMC_PIC3D_Engine();
  Engine_PTR->InitCells(…);
  …..
  return 1;
}
```

Figure F.2: Part of Major Control Code.

be used in the simulation. The interface types are defined as pure virtual without function bodies. Hence, this class achieves the Facade pattern. For example, in Figure F.2, with different simulation methods, there are different cell initialization functions wrapped in different classes, such as a standard two-dimensional DSMC simulation and an axi-symmetric DSMC-PIC simulation. In the new experimental version of MONACO, different function bodies are provided for the two corresponding classes, with the same interface, i.e. function names and parameter list are defined in class AbstractEngine. With a different configuration of parameters, MONACO can perform different types of simulations without a recompilation. With this approach, interfaces and functionalities are clearly separated, and information hiding is achieved.

4. All the functions in all classes but AbstractEngine are defined as virtual. Hence, unless a concrete function body is declared in a current class, by default, MONACO will locate a function body for this current class from its base classes. This treatment ensures a compact code with better maintainability and ease of use.

5. Most old functions in MONACO-V3.0, are kept as global methods and they are called inside the engine classes with wrappers. This arrangement ensures the validity of the new experimental version of MONACO by essentially using old functions and avoiding a busy interface.

6. All the good features of MONACO-V3.0 are preserved. After re-engineering, this experimental version can run on serial machines and parallel machines with unstructured or structured meshes. The update with C++ and classes does not corrupt the merits of MONACO-V3.0.

7. Particle weight are enabled. Particles are assigned a relative weight ratio when they enter the simulation domain at inlets via cathodes and anodes.

8. Implemented various sampling tools. Current density at different angles of fixed radius, energy spectrum on special points can be obtained with these tools.

9. Card controlling is achieved. Usually in DSMC-PIC simulations, there are many combinations of parameters and options, hence, like a general feature of a commercial solver, control cards are enabled with a configuration file. This provides many dynamic controls which can be conveniently turned on and off. For example, the following card defines an ion velocity profile at the thruster exit, parameters such as the outer divergence angle and inner divergence angles can be easily changed outside the code while a simulation is performing. By remove the $, this card is disabled and the ion velocity will assume a default profile defined in another basic input file.

$THRUSTER_EXIT_PROFILE 30.0 20.0 2 0.01125 3.75e-3

10. Many frequently used functions are declared as inline functions to achieve higher performance.

These changes significantly improved the architecture of MONACO, and enhanced its readability, maintainability and ease of use. Meanwhile, this version has achieved good expansion capabilities for the future. Theoretically, DSMC and all its derivative methods, can be united with ease in this experimental version of MONACO. The only necessary step to add a new method is to consider a proper existing class to derive from, and add a new class into MONACO with different new functions sharing the same interfaces defined in class AbstractEngine.

APPENDIX G

Derivations for Neutral Number Density Distribution

$$
\begin{aligned}
\Omega = \;& \textstyle\sum_0^4 \int \frac{x}{R_i^3} ds_i + \sum_0^4 \int \frac{(x-b)n_{xj}+(y-a_i)n_{xj}+(z-d_j)n_{xj}}{R_j^3} ds_j \\
= \;& \textstyle\sum_{i=0}^4 \int_0^{2\pi} \frac{x}{R_i^3} d\theta + \sum_0^4 \int \frac{(x-b)n_{xj}+(y-a_i)n_{xj}+(z-d_j)n_{xj}}{R_j^3} ds_j \\
= \;& \textstyle\frac{x(R^2-r^2)}{2} \int_0^{2\pi} \frac{d\theta}{(x^2+(y-(a+\frac{R+r}{2}\cos\theta)^2+(z-(a+\frac{R+r}{2}\sin\theta)^{3/2}} \\
& + \textstyle\frac{x(R^2-r^2)}{2} \int_0^{2\pi} \frac{d\theta}{(x^2+(y-(-a+\frac{R+r}{2}\cos\theta)^2+(z-(a+\frac{R+r}{2}\sin\theta)^{3/2}} \\
& + \textstyle\frac{x(R^2-r^2)}{2} \int_0^{2\pi} \frac{d\theta}{(x^2+(y-(a+\frac{R+r}{2}\cos\theta)^2+(z-(-a+\frac{R+r}{2}\sin\theta)^{3/2}} \\
& + \textstyle\frac{x(R^2-r^2)}{2} \int_0^{2\pi} \frac{d\theta}{(x^2+(y-(-a+\frac{R+r}{2}\cos\theta)^2+(z-(-a+\frac{R+r}{2}\sin\theta)^{3/2}} \\
& + H(n_{x1}, n_{y1}, n_{z1}, b, a, d) + H(n_{x2}, n_{y2}, n_{z2}, b, -a, d) \\
& + H(n_{x3}, n_{y3}, n_{z3}, b, -a, -d) + H(n_{x4}, n_{y4}, n_{z4}, b, a, -d) \\
= \;& x(R^2-r^2)\big(F(A_1, A_2) + F(A_3, A_4) + F(A_5, A_6) + F(A_7, A_8)\big) \\
& + H(n_{x1}, n_{y1}, n_{z1}, b, a, d) + H(n_{x2}, n_{y2}, n_{z2}, b, -a, d) \\
& + H(n_{x3}, n_{y3}, n_{z3}, b, -a, -d) + H(n_{x4}, n_{y4}, n_{z4}, b, a, -d)
\end{aligned}
$$

where

$$H(n_x, n_y, n_z, b, a, d) = \begin{cases} \frac{\pi R_c^2((x-b)n_x+(y-a)n_y+(z+b)n_z)}{((x-b)^2+(y-a)^2+(z+d)^2)^{3/2}}, & S > 0 \\ 0, & S < 0 \end{cases}$$

$$S = (x-b)n_x + (y-a)n_y + (z-d)n_z, F(A_i, A_j) = E(\sqrt{\frac{2A_j}{A_i + A_j}})/(A_i + A_j)^{3/2}$$

$E(x)$ is the complete elliptical integrals, and

$$A_1 = (y-a)^2 + (\tfrac{R+r}{2})^2 + x^2 + (z-a)^2, A_2 = (R+r)\sqrt{(y-a)^2 + (z-a)^2}$$

$$A_3 = (y+a)^2 + (\tfrac{R+r}{2})^2 + x^2 + (z-a)^2, A_4 = (R+r)\sqrt{(y+a)^2 + (z-a)^2}$$

$$A_5 = (y-a)^2 + (\tfrac{R+r}{2})^2 + x^2 + (z+a)^2, A_6 = (R+r)\sqrt{(y-a)^2 + (z+a)^2}$$

$$A_7 = (y+a)^2 + (\tfrac{R+r}{2})^2 + x^2 + (z-a)^2, A_8 = (R+r)\sqrt{(y+a)^2 + (z+a)^2}$$

The above derivation process uses the elliptical calculus formula [21]:

$$\int_{-\pi/2}^{\pi/2} \frac{d\theta}{(a + b\sin\theta)^{3/2}} = \frac{2}{(a+b)^{3/2}} E(\sqrt{\frac{2b}{a+b}})$$

BIBLIOGRAPHY

BIBLIOGRAPHY

[1] E. Ahedo, P. Martinez-Cerezo and M. Martinez-Sanchez. One-dimensional Model of the Plasma Flow in a Hall Thruster. *Physics of Plasma*, Vol.8, pp.3058–3068, 2001.

[2] B. J. Alder and T. E. Wainwright. Studies in Molecular Dynamics. *Journal of Chemical Physics*, 27:1208–1209, 1957.

[3] B. J. Alder and T. E. Wainwright. Studies in Molecular Dynamics.(I) General Method. *Journal of Chemical Physics*, 31:459–466, 1959.

[4] M. P. Allen and D. J. Tildesley. *Computer Simulation of Liquids.* Oxford University Press, New York, 1987.

[5] Altair Engineering Inc. Version 6.0. Troy, Michigan, 2003.

[6] O. Atoks, N. R. Aluru and U. Ravaioli. Application of a Parallel DSMC Technique to Predict Flow Characteristics in Microfluidic Filters. *Journal of Microelectromech. Systems*, Vol.10, pp.538–549, 2001.

[7] D. Baganoff and J. D. McDonald. A Collision-Selection Rule for a Particle Simulation Method Suited to Vector Computers. *Physics of Fluids*, 2(7):1248–1259, July 1990.

[8] B. E. Beal. *Clustering of Hall Effect Thrusters for High-Power Electric Propulsion.* Ph.D. thesis, Department of Aerospace Engineering, University of Michigan 2004.

[9] L. Biagioni, L. Boccaletto, L. Marcuccio, S. Nicolini, D., Servi and M. Andrenucci. A Large Space Simulator for Electric Propulsion Testing: Design Requirements and Engineering Analysis. AIAA Paper 2000-3750, July 2000.

[10] G. A. Bird. Forty Years of DSMC. *Rarefied Gas Dynamics:22nd International Symposium,* edited by T. J. Bartel and M.A. Gallis, pp.372-380, 2001.

[11] G. A. Bird. Monte Carlo Simulation in an Engineering Context. *Progress in Astronautics and Aeronautics*, Vol.74, pp.239–255, 1998.

[12] G. A. Bird. *Molecular Gas Dynamics and the Direct Simulation of Gas Flows.* Oxford University Press, New York, 1994.

[13] G. A. Bird. Breakdown of Translational and Rotational Equilibrium in Gaseous Expansions. *AIAA Journal*, 8:1998–2003, 1970.

[14] G. A. Bird. Direct Simulation and the Boltzmann Equation. *Physics of Fluids*, 13(11):2676–2681, Nov. 1970.

[15] G. A. Bird. Monte-Carlo Simulation in an Engineering Context. *Proceedings of the 12th International Symposium on Rarefied Gas Dynamics*, Charlottesville, Virginia, pp.239–255, 1981.

[16] C. K. Birdsall and A. B. Langdon. *Plasma Physics Via Computer Simulation*. Adam Hilger, 1991.

[17] I. D. Boyd and J. T.Yim. Modeling of the Near Field Plume of a Hall Thruster. *Journal of Applied Physics*, May 2004, v.95 i.9. pp.4575-4584.

[18] I. D. Boyd. Conservative Species Weighting Scheme for the Direct Simulation Monte Carlo Method. *Journal of Thermophysics and Heat Transfer*, Vol.10, No.4, pp.579-585, 1996.

[19] I. D. Boyd. Analysis of Rotational Nonequilibrium in Standing Shock Waves of Nitrogen. *AIAA Journal*, 28(11):1997–1999, Nov. 1990.

[20] I. D. Boyd. Rotational-Translational Energy Transfer in Rarefied Nonequilibrium Flows. *Physics of Fluids A*, 2(3):447–452, Mar. 1990.

[21] P. Byrd and M. Friedman. *Handbook of Elliptic Integrals For Engineering and Physicists*. Springer-Verlag, 1954.

[22] A. Dalgarno, M. R.C. McDowell and A. Williams. The Mobilities of Ions in Unlike Gases.

[23] S. Dietrich and I. D. Boyd. Scalar and Parallel Optimized Implementation of the Direct Simulation Monte Carlo Method. *Journal of Computational Physics*, 126:328–342, 1996.

[24] F. Dyson. *Disturbing the Universe*. Harper and Row, 1979. Proceedings of the Royal Society, Vol.250, 1958, pp.411-425.

[25] J. Fan. A Generalized Soft-Sphere Model for Monte Carlo Simulation. *Physics of Fluids*, Vol.14, pp.4256–4265, 2002.

[26] E. Gamma, R. Helm, R. Johnson and J.Vlissides. *Design Patterns-Elements of Reusable Object-Oriented Software*. Addison-Wesley, 20th printing, 2000.

[27] T. I. Gombosi. *Gaskinetic Theory*. Cambridge University Press, New York, 1994.

[28] J. R. Hammel. *Development of An Unstructured 3-D Direct Simulation Monte Carlo/Particle-In-Cell code and the Simulation of Microthruster Flows*. M.S. Dissertation, Mechanical Engineering Dept., Worcester Polytechnic Institute, Worcester, MA, 2002.

[29] W. A. Hargus. The Air Force Clustered Hall Thruster Program. AIAA Paper 2002–3678, July 2002.

[30] J. M. Harlie. *Molecular Dynamics Simulation: Elementary Methods*. Wiley-Interscience, New York, 1993.

[31] M. S. Ivanov, S. F. Gimelshein. Computational Hypersonic Rarefied Flows. *Annual Review of Fluid Mechanics*, Vol.30, pp.469–505, 1998.

[32] A. J. Jamison, A. D. Ketsdever and E. P. Muntz. Gas Dynamic Calibration of a nano-Newton thrust stand. *Rev. Sci. Instrum.*, 73, pp.3629-3673, 2002.

[33] K. Koura and H. Matsumoto. Variable Soft Sphere Molecular Model for Air Species. *Physics of Fluids A*, 4(5):1083–1085, May 1992.

[34] H. W. Liepmann. Gas Kinetics and Gas Dynamics of Orifice Flow. *Journal of Fluid Mechanics*, Vol.10, pp.65–79, 1961.

[35] S. Miller, D. J. Levandier, Y. Chiu and R. A. Dressler. Xenon Charge Exchange Cross Sections for Electrostatic Thruster Models. *Journal of Applied Physics*, Vol. 19, 2002, pp.984-991..

[36] M. Mitcher and C. H. Kruger. *Partially Ionized Gases*. Wiley, 1973.

[37] E. P. Muntz. Rarefied Gas Dynamics. *Annual Review of Fluid Mechanics*, Vol.21, pp.387–417, 1989.

[38] R. Myers. Overview of Electric Propulsion Activities in industry. AIAA Paper 2000–3147, July 2000.

[39] R. Narasimha. Orifice Flow of High Knudsen Number. *Journal of Fluid Mechanics*, Vol.10, October, pp.371–384, 1961.

[40] R. Narasimha. Collisionless Expansion of Gases into Vacuum. *Journal of Fluid Mechanics*, Vol.12, pp.294–308, 1962.

[41] R. Narasimha. *Some Flow Problems in Rarefied Gas Dynamics*. Ph.D. thesis, California Institute of Technology, Pasadena, CA, 1961.

[42] A. Nrotenberg and H. Weitzner. Nearly Free Flow Through an Orifice. *Physics of Fluids*, Vol.12, pp.1573–1581, 1969.

[43] E. S. Oran, C. K. Oh and B. Z. Cybyk. Direct Simulation Monte Carlo:Recent Advances and Applications. *Annual Review of Fluid Mechanics*, Vol.30, pp.403–441, 1998.

[44] W. H. Press, S. A. Vetterling, W. T. Flannery and B. P. Flannery. *Numerical Recipes in C*. Cambridge University Press, New York, 1994.

[45] S. H. Pullins, Y. Chiu, D. J. Levandier and R. A. Dresseler. Ion Dynamics in Hall Effect and Ion Thruster -Xenon Symmetric Charge Transfer. AIAA Paper 2000-0636, Jan. 2000.

[46] R. S. Roy. *Numerical Simulation of Ion Thruster Plume Backflow for Spacecraft Contamination Assessment*. Ph.D. thesis, Massachusetts Institute of Technology 1995.

[47] R. S. Roy, D. E. Hastings and S. Taylor. Three-Dimensional Plasma Particle-In-Cell Calculations of Ion Thruster Backflow Contamination. *Journal of Computational Physics*, Vol.128, pp.6–18, 1996.

[48] W. M. Ruyten. Density-Conservation Shape Factors for Particles Simulations in Cylindrical and Spherical Coordinates. *Journal of Computational Physics*, 105:224–232, 1993.

[49] F. Sharipov. Numerical Simulation of Rarefied Gas Flow Through a Thin Orifice. *Journal of Fluid Mechanics*, Vol.518, pp.35–60, 2004.

[50] T. B. Smith. *Deconvolution of Ion Velocity Distributions From Laser-Induced Fluorescence Spectra of Xenon Electrostatic Thruster Plumes*. Ph.D. thesis, Department of Aerospace Engineering, University of Michigan, 2003.

[51] J. S. Sovey, R. H. Vetrone, S. P. Grisnik, R. M. Myers and J. E. Parkes, Test Facilities for High-Power Electric Propulsion. *Journal of Propulsion and Power*, Vol.10, No.1, pp.342–372, 1994.

[52] E. Stuhlinger. *Ion Propulsion for Space Flight*. McGraw-Hill, 1964.

[53] P. Szwemin, K. H. Szymanski and S. Jousten. Monte Carlo Study of a New PTB Primary Standard for Very Low Pressure. *Metrologia*, Vol.36, No.1, pp.562–564, 1999.

[54] E. Taccogna, S. Longo and M. Capitelli. *Very-near-field Plume Simulation of a Stationary Plasma Thruster. Eur.Phys. Appl. Phys* Vol.28, pp.113-122, 2004.

[55] D. B. VanGilder. *Numerical Simulation of The Plume of Electric Propulsion Thrusters*. Ph.D. thesis, Cornell University, 2000.

[56] W. G. Vincenti and C. H. Kruger, Jr. *Introduction to Physical Gas Dynamics*. Krieger Publishing, Malabar, Florida, 1986.

[57] R. Vichnevetsky. *Computer Methods for Partial Differential Equations*. Prentice-Hall, 1981.

[58] P. Vijayakumar, Q. Sun, and I. D. Boyd. Detailed Models of Vibrational-Translational Energy Exchange for the Direct Simulation Monte Carlo Method. *Physics of Fluids*, 11(8):2117–2126, Aug. 1999.

[59] M. W. Walker, A. D. Gallimore, I. D. Boyd and C. Cai. Vacuum Chamber Pressure Maps of a Hall Thruster Cold-Flow Expansion. *Journal of Propulsion and Power*, Vol.20, No.6, pp.1127–1131, 2004.

[60] M. L. Walker. *Effects of Facility Backpressure on the Performance and Plume of a Hall Thruster*. Ph.D. thesis, Department of Aerospace Engineering, University of Michigan, Ann Arbor, 2004.

[61] D. R. Willis. Mass Flow Through a Circular Orifice and a Two-Dimensional Slit at High Knudsen Numbers. *Journal of Fluid Mechanics*, Vol.21, pp.21–32, 1965.

ABSTRACT

THEORETICAL AND NUMERICAL STUDIES OF PLUME FLOWS
IN VACUUM CHAMBERS

by

Chunpei Cai

Chairperson: Professor Iain D. Boyd

This thesis consists of three parts: a study of facility effects on the background flow in large vacuum chambers; an analytical study of free molecular flows out of exits with different shape representing thruster plumes; and particle simulations of plasma plume flows from a cluster of Hall thrusters.

The first part of this thesis discusses the facility effects on large vacuum chambers, which is quite important to the Electric Propulsion (EP) community. Based on the fact that the background flows in large vacuum chambers equipped with cryogenic pumps are free molecular, five models are proposed to study the average background pressure and flow velocity and their relation to several facility effects, such as pump sticking coefficient, pump size, wall and pump temperatures, and chamber sidewall length. The analysis are based on the mass flow rates into and out of the chamber, the fluxes along two directions and various number density relations at various

stations such as chamber ends and vacuum pumps. As an unsteady process, a background flow evolves exponentially and there exists a semi-decaying period. This semi-decaying period is of the order of seconds and presents a challenge to a full-scale three-dimensional particle simulation of plasma plume flows in a chamber. The background flow in a large vacuum chamber can not be considered to follow a zero-centered Maxwellian distribution and some modifications of backpressure for particle simulations are proposed. Analysis of existing experimental measurement data indicates that on average, the pump sticking coefficient for the Large Vacuum Test Facility, in the University of Michigan is about 0.4. Generally, background pressures decrease as pump sticking coefficients or pump areas increase. Vacuum chamber sidewall length has a different effect when combined with a large pump sticking coefficient or a small pump sticking coefficient. Numerical simulations prove the validity of several results. This study provides five sets of exact analytical free molecular flow solutions, including detailed velocity probability distribution functions for background flow particles. The general principles and processes can be used to guide studies of other types of vacuum chambers with more complex configurations.

The second part of the thesis develops several sets of analytical solutions to free molecular flows out of exits with different shapes. It is demonstrated that the plasma plume flows expanding into vacuum can be studied analytically as a combination of several free molecular flows, if the electric field and collision effects are omitted. There exists a unique relation of velocity and positions. A particle's velocity components satisfying this condition is the necessary and sufficient condition that the particle can arrive at a specific point in front of the thruster exit while starting from one specific location on the exit. Free molecular flows out of a thin slit, a rectangular slit, a concentered rectangular exit, a circular exit and an annular exit with a zero average

exit velocity, and free molecular flows out of a thin slit with a nonzero average exit flow velocity are studied. Six sets of exact analytical solutions or exact analytical expressions are obtained for the number density and velocity distributions in front of the exits. The solutions to the last problem include both geometry factors and the nonzero average exit velocity factors.

The last part of the thesis presents several three-dimensional particle simulations of plasma plume flows from a cluster of Hall thrusters. A detailed electron fluid model is used to solve important electron properties such as plasma potential and electron temperature. A finite element solver is developed to solve the equations of the electron properties on unstructured meshes. Several important implementation issues are discussed and one significant finding is that the class of particle-to-node weighting schemes based on areas or volumes on an unstructured mesh is inaccurate. This problem is not obvious if the Boltzmann relation is used to determine the plasma potential; however, if the detailed electron model is used to calculate the plasma potential, especially when ionization effects are included in the simulation, then the class of allocation schemes yields invalid results. The other significant treatment that distinguishes these simulations is that background static particles representing the backpressure are assigned velocities sampled from a distribution that takes into consideration the facilities effects. These simulations indicate that the plume flows from a cluster of four thrusters form complex three-dimensional near field structures. For example, the contours of electron number densities in the near field include a special four-leaved clover shape with another four secondary leaves. Compared with the Boltzmann relation, this study indicates that the detailed electron model is more comprehensive. Effects due to clustering and the cathodes are clearly demonstrated by the simulation results. Even though three-dimensional

simulations are more expensive and complex, they have many advantages over axi-symmetric simulations.